Università degli Studi di Genova

Scuola di Scienze Matematiche, Fisiche e Naturali

Thesis for the Doctoral degree in Physics

XXXV cycle

Consequences of interactions in quantum Hall edge channels

January 2023

PhD candidate Giacomo Rebora

Supervisor Dr. Dario Ferraro

Referee Dr. Flavio Ronetti (Université d'Aix-Marseille)

Referee Prof. Roberta Citro (Università di Salerno)

Contents

Acronyms

QO Quantum Optics

EQO Electron Quantum Optics

HBT Hanbury Brown-Twiss

HOM Hong-Ou-Mandel

QH Quantum Hall

2DEG Two-Dimensional Electron Gas

QPC Quantum Point Contact

1D One-Dimensional

IQH Integer Quantum Hall

FQH Fractional Quantum Hall

QD Quantum Dot

TLL Tomonaga Luttinger Liquid

EMP Edge-Magnetoplasmon

Introduction

Quantum Optics (QO) is a branch of physics dealing with light and light-matter interaction at the quantum level. The striking ability in generating, manipulating and measuring quantum states of the electromagnetic field achieved in the last decades has provided some simple yet fundamental tests for the quantum mechanical behavior of single-photon states [1].

In a similar fashion, the progresses in the experimental control of individual electronic degrees of freedom ballistically propagating in mesoscopic devices led to the birth of a new branch of condensed-matter physics known as Electron Quantum Optics (EQO) [2]. It aims at reproducing quantum-optical experiments and set-ups in solid state devices. Major achievements in this context were the realization of the electronic equivalent of the Hanbury-Brown and Twiss (HBT) interferometer [3], which allows to access the granular nature of the particles, and of the Hong-Ou-Mandel (HOM) experiment [4], able to provide information about the statistical properties of the colliding particles.

The full correspondence between QO and EQO is built on few but necessary ingredients: fermionic waveguides, electronic beamsplitters and single electron sources. The first ones are provided by one-dimensional topological edge states emerging in the Quantum Hall (QH) effect [5, 6], both in the integer and in the fractional regimes. By applying a strong perpendicular magnetic field to a Two-Dimensional Electron Gas (2DEG), bulk conduction is suppressed but metallic states appear at the edge of the Hall bar. Chirality of edge states, forced by the direction of the magnetic field, forbids electronic backscattering, thus providing efficient waveguides of electrons. In QO experiments, photon beams are manipulated with the help of beamsplitters. In QH systems, a negative gate voltage can partially deplete the underlying 2DEG, deviating the path of the edge states. This constriction is called Quantum Point Contact (QPC) and allows to control the reflection and transmission of the fermionic beam impinging on the barrier. Finally, two main recipes have been proposed to add a single electron on top of the filled Fermi sea in fermionic systems. First, the so-called driven mesoscopic capacitor [7], which consists of a quantum dot subjected to a rectangular drive and connected to 2DEG through an additional QPC, allows to inject separately an electron and a hole into the system. Alternatively, one can excite a single electron above the Fermi sea by applying a well defined voltage pulses to a quantum conductor as suggested by L. Levitov and coworkers [8, 9, 10].

Despite evident similarities with conventional QO, EQO brings into play new features that are inherently characteristic of electronic system. Firstly, single-photon states are usually created on a real quantum mechanical vacuum (*i.e.* zero-particle state), while single-electron states are always generated on top of the filled Fermi sea. Therefore, the contribution of the Fermi sea to the dynamics of the system have to be carefully taken into account in the framework of EQO. Nevertheless, a fermionic

analogue of R. J. Glauber's theory of optical coherence [11] has been developed circumventing this complication through correlation functions [12] and leading to a better understanding of the experimental results [13, 14, 15].

Even more importantly, electrons strongly differ from photons due to their statistics and their charged nature. These lead to many-body effects which strongly affect the dynamics of excitations and play a major role in various experimental situations. Due to their One-Dimensional (1D) nature, QH edge channels are prone to emphasize interaction effects. In one dimensional systems, the motion of an electron interacting with its neighbors strongly affects the latter, so that the Fermi liquid paradigm does not hold. Contrary to two and three dimensional systems, the picture of quasi-free quasi-particles is not accurate. It is replaced by the Luttinger liquid theory, that relies on bosonic collective excitations. For example, in the Integer Quantum Hall (IQH) effect, at filling factor higher than one, transport occurs along several co-propagating channels on each edge. As they are very close by one another, they are coupled by interchannel Coulomb interaction, which leads to the appearance of new collective propagation modes. Various experiments have been carried out to investigate the coupling between edge channels and their effect on the relaxation and decoherence of electronic excitations. This coupling has been shown to be responsible for the loss of the visibility of the interference pattern in Mach-Zehnder interferometers at filling factor $\nu = 2$ [16]. Indeed, at $\nu > 1$, interactions dramatically change the nature of excitations, leading to energy exchange between the channels and to charge fractionalization [17, 18]. Proceeding even further, the Fractional Quantum Hall (FQH) effect is another paradigmatic example of the consequences of electron-electron interactions since it takes its roots in the strong correlations among electrons [19]. From these statements, we immediately understand that the electronic interactions in QH edge channels cannot be neglected and must inevitably be added to the EQO puzzle.

An open problem of the EQO field with respect to conventional QO is the real time detection of the signal, which is still out of reach for nowadays electronics and only recently has been addressed [20, 21]. The more reliable experimental strategy to overcome this problem consists in measuring current-current correlations (*i.e.* noise) over a wide range of frequencies, in such a way to reconstruct the time evolution through Fourier transform [22]. Moreover, noise is an inescapable ingredient of any electronic device. While at first it may be regarded as a nuisance, it has now been accepted as a key tool to improve our understanding of nanoscale conductors and their dynamics. Electronic noise is typically broken down into two contributions associated with different underlying physical phenomena. Thermal (or Johnson-Nyquist) noise is an equilibrium property, arising at a finite temperature from the thermal motion of electrons [23, 24]. Shot noise manifests itself in a non-equilibrium situation, when current flows through a conductor, as a consequence of electrons being transmitted or reflected predominantly on a given side of the device [25]. Moreover, using atomic-scale metallic junctions [26], it was recently showed that under a temperature rather than a voltage bias, a finite non-equilibrium noise signal could be measured paving the way toward new properties of strongly interacting systems. Then, its analysis allows to access the out-of-equilibrium properties of the considered mesoscopic system. Furthermore, the study of finite frequency noise reveals even more interesting in the light of recent experiments [27, 28, 29] underlying the deep connections between this quantity and the quantum fluctuations of the microwave radiation emitted by driven mesoscopic devices.

The main purpose of this Thesis is to understand what are the consequences of un-

avoidable electronic interactions in edge channels of the QH effect, both in the integer and fractional regimes, on current-current fluctuations. This theoretical analysis can pave the way to new experimental EQO applications. The present Thesis is divided in five Chapters.

In **Chapter 1** we present the field of EQO carefully discussing its building blocks. Starting from the electronic waveguides guaranteed by the QH effect and we describe the action of a the QPC. Two types of single electron sources are then discussed, both from a theoretical and an experimental point of view. A particular attention is devoted to minimal excitation states of quantum conductors, usually called levitons. In the second part of this Chapter, we discuss the physics of noise in mesoscopic systems introducing the scattering formalism which allow us to deal with different types of noise in non-interacting systems.

In **Chapter 2** we present interacting 1D fermionic systems. After a general introduction to the bosonization precedure, we exploit the hydrodynamical model following the seminal work of X. G. Wen. This allows us to deal with a large class of interacting QH states in both the integer and the fractional regime. In the former case, we will phenomenologically consider possible dissipative effects observed in recent experiments.

Chapter 3 is devoted to the theoretical investigation of HOM interferometry in a QH system with filling factor $\nu = 2$, namely the physics of colliding identical excitations. We show that the injected electronic wavepackets fractionalize before partitioning at a QPC due to interactions. Moreover, we demonstrate that, when the injection occurs through time-dependent voltage pulses arbitrarily shaped, the HOM noise always vanishes for a symmetric device. In addition, we propose a direct measurement of the strength of interactions.

Electron-electron interactions naturally leads to non-linearities in the current-voltage characteristic in a QPC geometry. The main task of **Chapter 4** is to understand the consequences of these peculiar correlations on the quantum properties of the microwaves emitted by a QH device in presence of interactions. We connect the quantum features of the emitted radiation, such as squeezing, to the current fluctuations and we compare two different periodic drives, respectively a cosine pulse and a Lorentzian one. Interestingly, we observe that the Lorentzian drive is characterized by a more robust squeezing effect even in presence of interaction. Furthermore, we report recent experimental results along this direction.

Finally, in **Chapter 5** we originally investigate the current fluctuations due to a temperature bias, instead of a voltage one. We study the noise associated to the flowing between two different FQH edge states, with filling factors belonging to the Laughlin sequence, coupled through a QPC and connected to two reservoirs placed at different temperatures. We solve exactly the problem for all couplings and for all temperatures in the case of a specific combination of filling factors. Moreover, we generalize our approach to a generic junction and we derive a universal expression which connects the out-of-equilibrium noise to the equilibrium one up to the first order in the temperature mismatch. Starting from recent theoretical result, this analysis allows to better understand the transport properties of strongly interacting systems and to move toward more involved investigation concerning the statistics of their emergent excitations.

This Thesis is based on the following publications co-authored by myself:

1. G. Rebora, M. Acciai, D. Ferraro and M. Sassetti, *Collisional interferometry of levitons in quantum Hall edge channels at* $\nu = 2$, Phys. Rev. B **101**, 245310

(2020).

2. G. Rebora, D. Ferraro, R.H. Rodriguez, F.D. Parmentier, P. Roche and M. Sassetti, *Electronic wave-packets in integer quantum Hall edge channels: relaxation and dissipative effects*, Entropy **23**, 138 (2021).

3. G. Rebora, D. Ferraro and M. Sassetti, *Suppression of the radiation squeezing in interacting quantum Hall edge channels*, New J. Phys. **23**, 063018 (2021).

4. G. Rebora, J. Rech, D. Ferraro, T. Jonckheere, T. Martin and M. Sassetti, *Delta-T noise between fractional quantum Hall edge states at different filling factor*, arXiv:2207.00454 (2022).

The other work not included in this Thesis is:

5. G. Rebora, M. Acciai, D. Ferraro and M. Sassetti, *Radiation squeezing in interacting quantum Hall edge channels*, Il Nuovo Cimento C **6**, 178 (2022).

Chapter 1

Electron Quantum Optics

In this Chapter, we discuss the field of EQO with a particular insight on the necessary ingredients to develop it and on the typical quantity investigated in experiments, namely the current flucuations (noise). We will focus on the QH effect in the integer and fractional regimes where topologically protected chiral edge channels behave as electronic waveguides. By introducing the QPC, we present the electronic counterpart of the photonic beamsplitter. Then we discuss the physics of single-electron sources, which represents a fundamental building block to make EQO possible. We conclude discussing the noise as a tool to extract information about the dynamics of mesoscopic systems, with an overview of the different sources of fluctuation. Here, we focus on the scattering matrix formalism valid for non-interacting systems that will allow us to deal with some notable examples in EQO experiments.

1.1 From Quantum Optics to Electron Quantum Optics

Quantum transport is a central topic of mesoscopic physics that deals with electronic transport in a regime where the effects of quantum mechanics cannot be neglected. Here, the wave nature of electrons cannot be ignored: transport is influenced by electronic phase coherence. This requires that the inelastic scattering length ℓ, which characterizes the distance over which an electron can propagate without experiencing an inelastic collision, is larger than the sample size L.

As suggested by the name, EQO is inspired to a great deal by conventional quantum optics with photons. The essential tools to build a quantum optic set-up are coherent sources to generate single-photon states, waveguides to control their propagation and beamsplitters that can be used to partition incoming waves and recombine them to perform interferometric experiments. QO is a well established field started in the 60s, with the seminal works of Glauber [11, 30], that has reached such a maturity level that it is now possible to generate, manipulate and probe states of the quantum electromagnetic field involving one to few photons per mode. The experimentalists were able to build single photon sources and to prove the coherence of single photon wave packets. In this framework, the well-known HBT interferometer [3] intended to study the intensity correlations of a photon beams received by two detectors. Moreover, the famed HOM experiment [4] probed the bunching behavior of two photons impinging on a half silvered mirror, as a function of the time delay between the two photonic pulses. This HOM experiment has now become a paradigm of modern quantum mechanics.

Since the birth of mesoscopic physics in the early eighties [31, 32, 33], scientists tried to make parallels between electron flow in solid state devices and photon beams in QO.

The electronic analog of a beamsplitter is the so-called QPC, which has been originally developed as a way to create 1D electronic systems starting from a 2DEGs [34, 35]. If an electron is created in the channel and sent towards the constriction, the QPC will act as a beamsplitter. Indeed, the excitation will be transmitted or reflected with a certain probability. Moreover, in the ballistic regime, there are systems where electrons can propagate along veritable waveguides. Such waveguides are naturally provided by topologically protected edge channels in the QH effect [5].

This has inspired R. Landauer [36], M. Büttiker [37] and many other to develop a scattering approach to quantum transport in which a quantum conductor is seen as a scatterer, thus exploiting the analogy with optics. However, many problems related to the difficulty of mapping photons to electrons come out. First of all, electrons are fermions while photons are bosons and this difference in the particles statistics can strongly affect the dynamics. Moreover, whereas photons are emitted in vacuum, we always have to remember the presence of the underlying Fermi sea when we think of electrons propagating in solid-state devices. Last but not least, electrons do interact with each other and this can lead to new and interesting effects and produce a richer phenomenology. This is still not the end of the story since, until fifteen years ago, the quantum electronics relied on sources, such as constant voltage bias, that send continuous streams of electrons in which no quasi-particle could be singularized. Therefore, the quantum transport appear as a complicated many-body problem from the start.

Things changed when technological progress made it possible to access the GHz frequency range in quantum transport experiments [38]. This allowed to probe the dynamical timescales of the quantum conductor itself such as the electronic ballistic time of flight across the conductor[1]. In 2007, a source able to inject coherent single-electron excitations within a quantum Hall edge channel was realized [7]. This opened a new era for quantum electronics based on the study of quantum electrical currents carrying one to few electronic excitations per period. Single electron sources together with quantum point contacts and topological edge channels are then fundamental ingredients in order to build up the EQO and we will address them in the first part of this Chapter.

In the second part of the Chapter, we point out the importance of noise measurements by showing that quantum fluctuations contains information which cannot be extracted from simpler quantities, such as the average electrical current. Through the scattering matrix formalism, we will deal with different sources of noise, concluding with some notable examples of experiments in the EQO framework.

1.2 Edge channels in the quantum Hall effect

In this Section, we introduce the main ideas behind the discovery of the quantum Hall effect. In the first part, the phenomenology of the IQH effect is presented. This peculiar physical phenomenon can be explained in terms of a quantum mechanical treatment of non-interacting electrons in a magnetic field. Then, we take into account the FQH effect, limitedly to the Laughlin sequence, which can be explained by taking into account electron-electron interactions. These two effects are crucial for the second EQO's building block since they allow to obtain actual waveguides for electrons in solid state devices.

[1] Typically of the order of tens to hundreds of pico-seconds for a micrometer-long ballistic conductor.

1.2.1 Integer quantum Hall effect

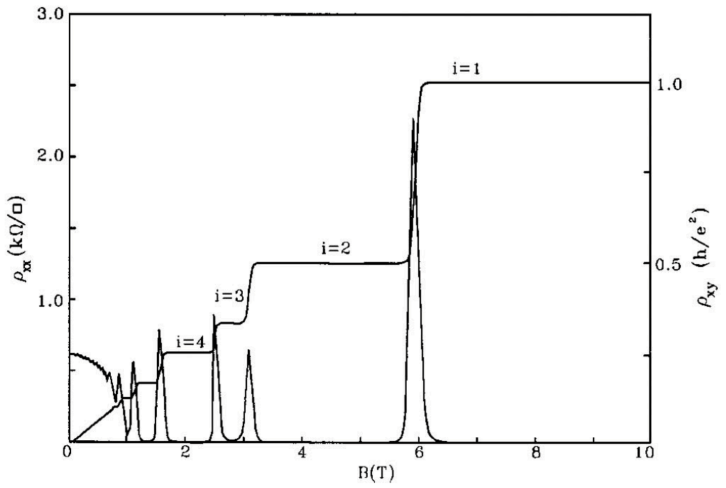

Figure 1.1: Measurements of longitudinal resistivity ρ_{xx} and Hall resistivity ρ_{xy} as a function of the magnetic field for the states of the IQH effect. The Hall resistance shows well defined plateaus. Taken from Ref. [39].

A very convenient platform for electronic rails can be exploited when a 2DEG is exposed to a high magnetic field at low temperature: it enters the IQH effect regime and conducting edge channels arise at the boundary of the 2DEG. This so-called IQH regime was discovered by K. von Klitzing in 1980 [5]. He was awarded the Nobel prize five years later. The most striking manifestation of this effect is that the transverse conductance of the sample becomes quantized in units of e^2/h, displaying plateaus at the values

$$G_H = \frac{1}{R_H} = n\frac{e^2}{h}, \qquad n \in \mathbb{N}, \tag{1.1}$$

and the longitudinal conductance vanishes (see Fig. 1.1). Then, the bulk of the 2DEG becomes insulating and electronic transport occurs only along 1D channels located at the edges of the sample. Here h is the Planck's constant, $-e$ the electron charge and the integer number n is called filling factor and counts the number of the filled Landau levels (see below).

Transport in the IQH effect can be understood semi-classically by considering the cyclotron motion of electrons in the 2DEG in presence of a perpendicular magnetic field. This semi-classical motion of electrons is depicted in Fig. 1.2: electrons in the bulk move in closed cyclotron orbits with a fixed center of motion, and therefore cannot travel from one end of the sample to the other. The cyclotron orbits of electrons near the edges, on the other hand, are interrupted by the edges, so that electrons bounce forward along the so-called skipping orbits. Because of the fixed direction of rotation imposed by the magnetic field, all electrons on one edge propagate in the same direction (in Fig. 1.2 electrons in the upper edge propagate from left to right), whereas electrons near the other edge propagate in the opposite direction: electronic transport in the IQH regime is therefore chiral. Due to chirality, these channels have the notable property of being topologically protected in such a way that backscattering is forbidden. The word topological is borrowed from mathematics, where it denotes global properties which are insensitive to local details. It is used in this context to emphasize that the

edge states protection is very robust and independent of the sample's details such as disorder and impurities. The discovery of the IQH effect has been a real revolution in condensed matter physics: it was indeed the first example of a topological state and changed our understanding of the phases of matter, paving the way to the search for topological materials [40, 41, 42].

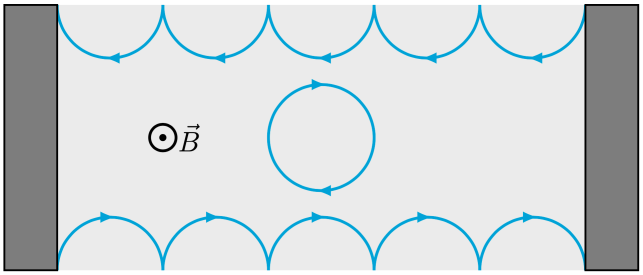

Figure 1.2: Semi-classical picture of the IQH effect: electrons move in cyclotrons orbits. These orbits are interrupted on the edges and electrons bounce forward, all in the same direction. Transport occurs at the edge of the sample and is chiral.

The above semi-classical argument can be made rigorous and there are different ways of quantitatively discussing the edge channels. In the following we just sketch one of them and refer the reader to the literature for further details [43, 44, 45, 46]. We assume to work in the continuum limit, neglecting the lattice potential[2]. Therefore we can consider free electrons moving in the xy plane (L_x and L_y being the sizes of the sample in the two directions), under a perpendicular magnetic field $\vec{B} = B\hat{z}$. The Hamiltonian is $H = (\vec{p} + e\vec{A})^2/(2m_e)$, with $\vec{p} = -i\hbar(\partial_x, \partial_y, 0)$, $\vec{A}$ the magnetic vector potential and m_e the electron mass. The spectrum of the system is given by the Landau levels [48]

$$E_n = \hbar\omega_c\left(n + \frac{1}{2}\right) \tag{1.2}$$

where $0 \leq n \in \mathbb{N}$ and $\omega_c = eB/m_e$ is the cyclotron frequency. These levels are highly degenerate and can accomodate $N_{deg} = \varphi/\varphi_0$ electrons, with $\varphi = BL_xL_y$ the magnetic flux through the sample and $\varphi_0 = h/e$ the flux quantum. In order to prove this, we have to compute the wavefunctions of the problem. Unlike the energy spectrum in Eq. (1.2), they do depend on the particular gauge choice for the vector potential $\vec{A}$, which needs to be specified. In the Landau gauge $\vec{A} = -By\,\hat{y}$, suitable to study translationally invariant systems, the wavefunctions must have the form

$$\phi_{n,k}(x, y) = e^{ikx}Y_{n,k}(y) \tag{1.3}$$

because the Hamiltonian does not depend on x. By assuming periodic boundary conditions in the $\hat{x}$ direction, the momentum k is quantized in the usual way

$$k = \frac{2\pi r}{L_x}, \qquad r \in \mathbb{Z}. \tag{1.4}$$

[2]This approximation works if the lattice spacing u is smaller with respect to the magnetic length ℓ_B [47]. The typical lattice spacing is of the order of few nanometers and the magnetic length is $\ell_B \approx 26\,\text{nm}$. Therefore the condition $u < \ell_B$ is quite well satisfied for all possible experimentally accessible magnetic fields. Indeed, the maximum value for the magnetic field in non-destructive experiments is $B \approx 45\,\text{T}$ in the continuous regime and $B \approx 80\,\text{T}$ in the pulsed regime.

By using the expression in Eq (1.3), the Hamiltonian becomes

$$H = \frac{p_y^2}{2m_e} + \frac{1}{2}\omega_c(y - k\ell_B^2), \tag{1.5}$$

where $\ell_B = \sqrt{\hbar/eB}$ is called the magnetic length. The above result describes a harmonic oscillator, whose potential is centered at the position $y_k = k\ell_B^2$. Therefore, the wavefunctions $Y_{n,k}(y)$ in Eq. (1.3) are given by [49]

$$Y_{n,k}(x,y) = \mathcal{N}\exp\left[-\frac{(y - k\ell_B^2)^2}{2\ell_B^2}\right]\mathcal{H}_n(y - k\ell_B^2) \tag{1.6}$$

where $\mathcal{N}$ is a normalization factor and $\mathcal{H}_n$ are the Hermite polynomials [50]. The important thing to notice about this expression is that the spatial localization of the states depends on k: each wavefunction is localized around $y_k = k\ell_B^2$. Thus, by imposing that $|y_k| < L_y/2$ (meaning that the center of each harmonic oscillator has to be inside the sample) and using Eq. (1.4), one finds $|r| < L_x L_y/(4\pi\ell_B^2)$. Thus, the number of states in each Landau level is given by $N_{deg} = \varphi/\varphi_0$, as stated above. An important quantity in the QH effect is the filling factor[3] ν, defined as the fraction of filled Landau levels. If we denote by N the total number of electron in the system, the filling factor is clearly given by

$$\nu = \frac{N}{N_{deg}} = \frac{hn_e}{eB} \tag{1.7}$$

with n_e the electron density in the system. The last ingredient we need in order to explain edge states is a confining potential in the $\hat{y}$ direction to describe the finiteness of the sample. Thus we add to the Hamiltonian a term $U_c(y_k)$, with the properties of being zero inside the sample and increasing at its edges (*i.e.* at $y = \pm L_y/2$) to keep the electrons confined. By recalling that the wavefunctions without the confining potential are localized around y_k , the confining potential can be adiabatically approximated as

$$U_c = U_c(y_k) + O(|\partial_y U_c(y)|) \tag{1.8}$$

and the energy of each eigenstate in Eq. (1.6) will be raised by the quantity $U_c(y_k)$. As a consequence, Landau levels corresponding to states close to the edges are bent, so that the spectrum as a function of k assumes the structure sketched in Fig. 1.3.

From this picture we can finally understand the conductance quantization from an edge perspective: when the Fermi energy lies in the gap between the first and second Landau levels, it intersects the bent spectrum in two points, roughly at $k \approx \pm L_y/(2\ell_B^2)$. The group velocity is given by

$$v_g = \frac{1}{\hbar}\frac{\partial E}{\partial k_y} = \frac{1}{\hbar}\frac{\partial E}{\partial y_k}\frac{\partial y_k}{\partial k} = \frac{\ell_B^2}{\hbar}\frac{\partial E}{\partial y_k}. \tag{1.9}$$

This let us state that

$$v_g(y_k) = -v_g(-y_k) \tag{1.10}$$

which means that in the bulk the group velocity is zero while the group velocities on the edge are non vanishing and opposite: a right-moving state has a positive group

[3] Here we use the letter ν for the filling factor, differently from the letter n used in Eq. (1.1). The reason for this is that the filling factor ν in (1.7) can also assume fractional values.

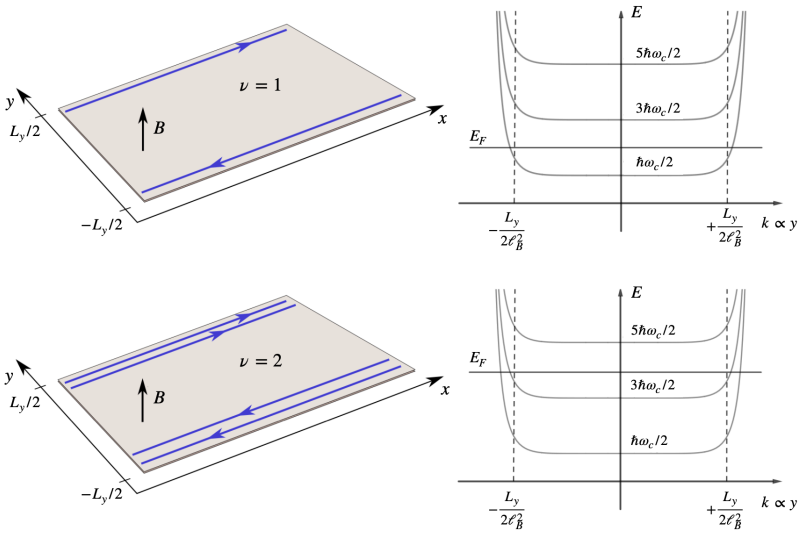

Figure 1.3: Bending of the Landau levels of Eq. (1.2) at the edge of the sample due to the confining potential $U_c(y)$. When n Landau levels are filled (*i.e.* the filling factor is $\nu = n$), the Fermi energy intersects the spectrum in n couples of points and n chiral channels emerge at each edge of the Hall bar (the cases $n = 1$ and $n = 2$ are shown here).

velocity and a left-moving one has a negative group velocity. Moreover, given the proportionality between k and y, we know that those states are located at the edges of the sample (near $y = \pm L_y/2$) and, therefore, spatially separated. The situation at filling factor $\nu = 1$ we have just described is represented in Fig. 1.3 (top left), where it can be seen that a conduction channel appears at the edges of the Hall bar, while the bulk is insulating. The right-moving channel is located on the upper edge of the sample, because the state with positive group velocity in the bent spectrum is at $k = +L_y/(2\ell_B^2)$. Conversely, for the same reason, the left-moving channel is located on the lower edge of the sample. The bottom part of Fig. 1.3 shows the case of filling factor $\nu = 2$. Here, the Fermi level intersects the spectrum four times and consequently four edge states are formed, two right-moving and two left-moving. Therefore, two copropagating channels emerge at each edge of the sample. The spatial separation of edge edge states with different chiralities has the important consequence that backscattering between them is exponentially suppressed with the transverse size of the sample L_y and in practice is forbidden; therefore, electrons move chirally along the edges in perfectly transmitting channels. From the Landauer picture of quantum transport [51, 52], we know that each of such channels bears a conductance quantum $G_Q = e^2/h$. Moreover, from Fig. 1.3, it is obvious that when an integer number of Landau levels is filled, *i.e.* $\nu = n \in \mathbb{N}$, the Fermi energy intersects the spectrum n times and therefore n channels emerge at each edge. On the whole, the conductance of the system is then nothing but the Hall conductance of Eq. (1.1). Remarkably, disorder effects unavoidably present in realistic samples, actually help (if they are not too strong) stabilizing the edge channels [45] leading to better defined plateaus.

In conclusion, we have seen that the IQH effect naturally provides chiral edge channels which are real one-way waveguides for electrons and, as such, a perfect playground for EQO purposes. Moreover, they have been known almost since the discovery of the IQH effect [5] and the systems where they emerge are experimentally well mastered.

For this reason, the majority of EQO experiments have indeed been performed in IQH edge channels.

1.2.2 Fractional quantum Hall effect

In the previous Section, the main theoretical arguments describing the quantization of quantum Hall resistance at multiple integer values of h/e^2 were presented. Nevertheless, in 1982 D. C. Tsui, H. L. Stormer and coworkers reported an unusual behavior of the Hall resistance [19] (see Fig. 1.4). For a sample with higher mobility and subjected to a more intense magnetic field than those used by von Klitzing, they observed the appearance of a plateau at a fractional filling factor $\nu = 1/3$. Later on, plateaus were measured in correspondence to many other fractional values of Landau level filling: this peculiar phenomenology, which cannot be explained in terms of the physical picture given for the IQH, has been called FQH effect. This new effect gives the possibility to deal with another kind of edge states presenting a fractionally quantized Hall conductance $G_H = \nu e^2/h$, with $\nu \in \mathbb{Q}$ (see Fig. 1.4).

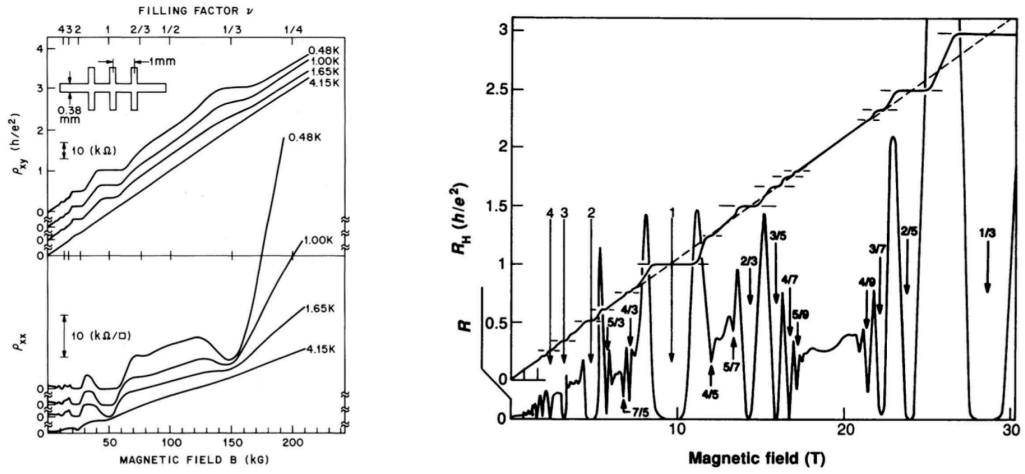

Figure 1.4: FQH states. (Left panel) First observation of a plateau at $\nu = 1/3$ in the Hall resistivity ρ_{xy}. Taken from [19]. (Right panel) Plateaus in the Hall resistance in correspondence of fractional values of filling factors. Taken from [53].

Due to the need of including Coulomb interaction among electrons, the theoretical explanation of the FQH effect is by far harder than for the IQH effect. Nevertheless, a subset of fractional filling factors received an insightful interpretation due to R. Laughlin in 1983, who won the Nobel Prize in 1998 together with D. C. Tsui and H. L. Stormer for his theoretical contribution [39, 54, 55]. The subsequence, of value of filling factor he theoretically described, was named Laughlin sequence and contains all the filling factors of the form

$$\nu = \frac{1}{2p+1}, \qquad p \in \mathbb{N}, \tag{1.11}$$

which includes $\nu = 1/3$, the first observed FQH state. Since in the last Chapter of this Thesis we will deal with the FQH effect, we briefly present these states.

The theoretical framework that successfully explained the IQH regime has been entirely presented in terms of a single-particle picture. The great physical intuition of

Laughlin was that the main element which gives rise to the FQH phenomenology is the Coulomb repulsion between electrons and that one should abandon the physical picture in terms of independent electrons used for the IQH effect [43].

A system of N interacting electrons in a magnetic field can be described by the following Hamiltonian[4]

$$H = \sum_{i=1}^{N} \frac{(\mathbf{p}_i + \frac{e}{c}\mathbf{A}(\mathbf{r}_i))^2}{2m} + \sum_{i \neq k}^{N} \frac{e^2}{\epsilon |\mathbf{r}_i - \mathbf{r}_k|}, \tag{1.12}$$

where ε is the dielectric constant of the material where the FQH state is realized. To deal with this additional contribution, one might think to proceed with a standard perturbative analysis. For a state like $\nu = 1/3$, the degeneracy of the ground state would be $N_{deg} = 3N$. All the possible combination to fill the lowest Landau levels with N electrons are given by

$$\binom{3N}{N} = \frac{(3N)!}{N!(2N)!}, \tag{1.13}$$

which for macroscopic N reaches really huge values. In the framework of the degenerate perturbation theory, one should diagonalize a macroscopically large matrix, which is a task out of reach even for numerical algorithms.

Nevertheless, a qualitative understanding for the stability of states at fractional filling factor can be drawn resorting to a simple picture of interacting electrons. In partially filled Landau levels, there is a huge freedom to fill the Hall bar with electrons. In the presence of repulsion between electrons, our freedom to distribute them is reduced. Let us start focusing on the ideal case of an infinite magnetic field. The magnetic length goes to zero and states are localized: electrons behave like point charge and tend to crystallize by minimizing their interaction energy. A unique ground state is formed, called Wigner crystal [56], which is radically distinct from the FQH phase[5]. When the magnetic field is lowered to finite values, wavefunctions of electron overlap and they cannot form anymore a crystalline structure. For some magic filling factors, they form a strongly correlated quantum liquid, which can be described in terms of an unique many-body wavefunction.

The form of the ground state wavefunction of Laughlin sequence states can be guessed based on generical considerations such as the symmetry of the problem and the Fermi statistics of electrons. The ansatz of Laughlin for the wavefunction of the ground states is the following [58]

$$\psi_{2p+1} = \mathcal{M} \prod_{i<j}^{N} (z_i - z_j)^m e^{-\sum_{k=1}^{N} |z_k|^2} \tag{1.14}$$

where $\mathcal{M}$ is a normalization factor and $z = x + iy$ is a complex spatial coordinate. This many-body wavefunction is built from angular momentum eigenstates $\phi_m(z) \sim z^m e^{-|z|^2}$, in accordance with rotational invariance of Coulomb interaction. Moreover, it satisfies transational invariance with respect to the origin.

The Laughlin wavefunction thus obtained has not been derived mathematically diagonalizing an hamiltonian. Actually, it is a variational wavefunction that satisfy

[4] We neglect the role of lattice potential and disorder, which turn out to be marginal in the description of the FQH effect.

[5] It can be obtained more realistically for sample with a very low density [57].

the symmetry and the constraints of the problem. The variational parameter is given by the integer number m, which is the only elements in Eq. (1.14) not already fixed. The variational wavefunction efficiently approximates the ground state of a Laughlin state with filling factor ν when the value of m is chosen such that

$$m = 2p + 1, \qquad p \in \mathbb{N}, \tag{1.15}$$

which means that $m = 1/\nu$. For such specific value of m, Laughlin wavefunction satisfies Pauli exclusion principle: indeed, when two coordinates z_i and z_j are exchanged, the many-body wavefunction acquires a minus sign, in accordance with Fermi statistics.

The presence of zeros with order $2p + 1$ enforce a separation between electrons, which induces a strong correlation in the system ground state. This correlation increases for higher values of p, meaning that a lower filling factor corresponds to a stronger Coulomb interaction among electrons.

Before concluding this part, it is instructive to point out a relation between the order of zeros in the Laughlin wavefunctions at filling factor ν and the corresponding degeneracy since the zeros are related to the flux quanta. The highest order zero in z_i in Eq. (1.14) has an exponent $(2p+1)(N-1)$, which in the thermodynamic limit, $(N-1) \approx N$, gives

$$(2p+1)N = N_{deg} \rightarrow \frac{N}{N_{deg}} = \nu = \frac{1}{2p+1}. \tag{1.16}$$

We have seen that the FQH effect is a peculiar phase of matter whose description involves necessarily a many-body picture, in contrast with the IQH one, which can be completely understood in terms of free electrons. However, similarly to the IQH regime, the edge states of the FQH provides an interesting alternative to the electronic waveguides needed for EQO as will be clear in the following.

1.3 Quantum point contact

The electronic analog of a beamsplitter can be implemented in a 2DEG in the form of a QPC which consists of a pair of electrostatic gates deposited on the surface of the sample. For our purpose, we assume from now on that the sample shows the QH effect. When a negative voltage is applied on the gates, a constriction is created in the 2DEG between them due to electrostatic repulsion (see Fig. 1.5 where the metallic gates (brown) are polarized by the gate voltage V_g). This constriction gives rise to a potential barrier, the shape of which can be determined from the geometry of the gates. By tuning the gate voltage, one can selectively transmit or reflect each edge channel. In particular, when large negative gate voltages are applied, the potential barrier becomes very large, and no electron can be transmitted. The influence of the gate voltage for a system at filling factor $\nu = 2$ is well illustrated by Fig. 1.5.

At high magnetic field, the description of the transmission through the QPC in terms of spin-degenerate electronic modes is replaced by the description in terms of edge channels following equipotential lines, which are reflected one by one as the QPC gate voltage is swept towards large negative values. This effect was first experimentally demonstrated in [35], see Fig. 1.6 where the conductance at magnetic fields below $B = 1\,\mathrm{T}$ presents steps in units of $2e^2/h$. At high magnetic field, the height of the conductance steps is equal to e^2/h, reflecting the removal of spin-degeneracy. The

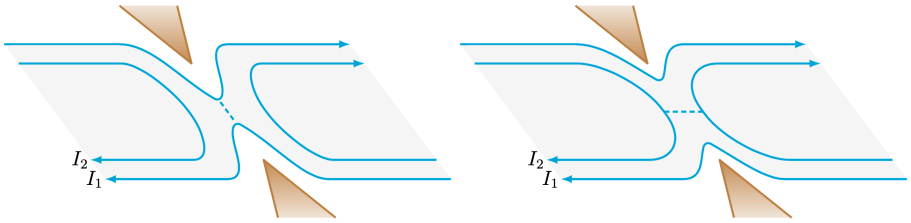

Figure 1.5: QH bar at filling factor $\nu = 2$ in presence of gate voltages. (Left) Set-up 1: the inner channels are fully reflected, and the outer ones are partially transmitted or reflected. (Right) Set-up 2: because of the smaller gate voltage, the outer channels are fully transmitted and the inner ones are partially transmitted or reflected.

number of conductance steps n decreases with the magnetic field, and corresponds to the number of edge channels. Between two conductance plateaus, the conductance G of the QPC is proportional to the transmission probability T:

$$G = \mathsf{T}\frac{e^2}{h}. \tag{1.17}$$

This equation is known as Landauer's formula [59]. R. Landauer has been a pioneer in mesoscopic transport, since he has developed a theory based on the scattering properties of the sample only, as we will see in next Sections. Figure 1.6 therefore demonstrates that one can tune the transmission of a QPC by changing its gate voltage; in particular, when set at the exact half of the opening of the first conductance plateau, the outer edge channel is partially transmitted with a probability $\mathsf{T} = 1/2$, while all other edge channels are fully reflected. The QPC therefore acts as a tunable, channel-selective beamsplitter.

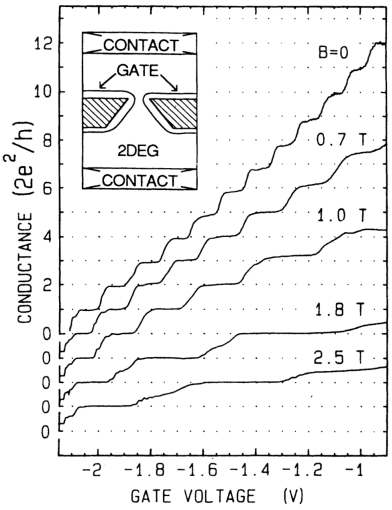

Figure 1.6: Conductance of a QPC as a function of gate voltage: it exhibits steps of value $2e^2/h$, corresponding to the progressive transmission of spin-degenerate edge-states. As the magnetic field is increased, the number of edge states decreases. For high fields, steps at e^2/h start appearing as the spin-degeneracy of Landau levels is lifted. Figure is taken from [35].

QPCs are crucial elements in EQO experiments as they allow to put into evidence

striking phenomena through noise measurements as we will see in the next Sections.

1.4 Single electron sources

It was not until recently, though, that coherent on-demand single-electron sources became available and well established. There are nowadays a few ways of generating and controlling single-electron wavepackets in quantum conductors and they are nicely reviewed in Ref. [60]. In summary, the state of the art concerning single-electron sources is the following.

Mesoscopic capacitor This source is based on a driven Quantum Dot (QD), coupled to a 2DEG in the IQH effect regime and is able to inject single electrons with well defined energy above the Fermi sea. It was the first single-electron source to be implemented.

Leviton source It is based on the application of a properly engineered voltage pulse to a 1D quantum conductor. It has the advantage that it can inject multiple electrons at the same time and its implementation does not require complex nanolithography design.

Dynamical quantum dots This source exploits a QD whose confining potential can be modulated in order to trap and release electrons in a cyclic way. It is typically implemented by relying on two parallel electrostatic gates deposited on top of a 2DEG, with a small opening between them that defines the QD region. This source generates electrons with energy far above the Fermi sea (the typical energy of electrons ejected from the QD is 100 meV, while the Fermi energy is about 10 meV) [61, 62, 63].

Surface acoustic waves Like in the previous case, electrons are first trapped in a QD and then emitted by the application of a surface acoustic wave, generated via the piezo-electric effect, which kicks electrons out of the QD [64, 65]. This source is difficult to implement, but was shown to be very accurate and allows for single shot detection of electrons.

In the following, we will briefly introduce the mesoscopic capacitor [7] and present in more detail the Leviton source [13], the latter being the most relevant one for the purpose of the present Thesis. We refer to the review [60] for further information about the last two entries of the previous list.

1.4.1 Mesoscopic capacitor

In 2007, G. Fève and coworkers at Laboratoire Pierre Aigrain in Paris realized the first on-demand single-electron source. This emitter is based on a driven mesoscopic capacitor [7, 66]. The system is sketched in Fig. 1.7 and is realized in a GaAs/AlGaAs 2DEG in the IQH effect regime. By means of metallic gates a part of the 2DEG is confined and a QD is created, whose transmission is controlled by a gate voltage V_g. A coupling between the QD and the edge states of the 2DEG is therefore present. In particular, the gate potential V_g is set in such a way that inner edge states[6] are fully reflected so that only one edge mode couples to the QD. Finally, an additional top gate

[6]The experiment was performed at filling factor $\nu = 2$, thus two edge channels are present in the Hall bar.

(yellow region above the QD in Fig. 1.7) can be used to shift the chemical potential of the QD with respect to the Fermi level of the 2DEG.

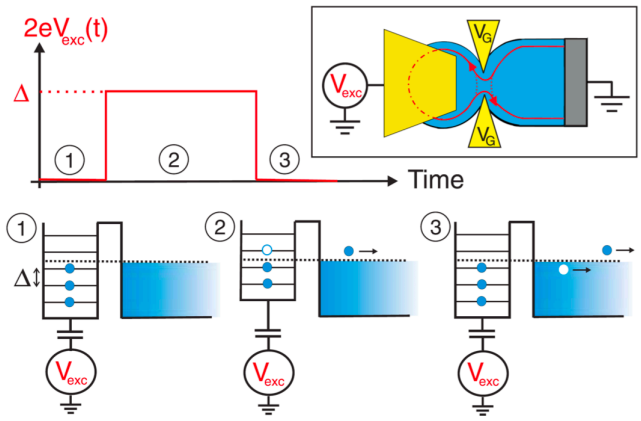

Figure 1.7: Set-up and operating mechanism of a single electron source based on a driven mesoscopic capacitor source. Image taken from [7].

Due to confinement, the spectrum of the QD is made of discrete energy levels, spaced by a characteristic scale Δ. Typical experimental values are $\Delta \approx (2 \div 4)\,\mathrm{K}$ [7], in temperature unit. By acting on the top gate with a rectangular voltage $eV_{exc}(t)$ of amplitude $\Delta/2$, these energy levels are shifted in such a way that the uppermost occupied level of the QD is abruptly brought above the Fermi level (step 1); thus the electron tunnels into the edge state of the 2DEG (step 2), with a typical time scale τ, which is controlled by the transmission D between the dot and the edge mode [67]. Finally, the QD levels are brought back to their original position and an electron tunnels from the edge mode into the dot, *i.e.* a hole is emitted in the 2DEG (step 3). By cyclically repeating this precedure, the periodic emission of single electrons and holes into the edge channel is achieved.

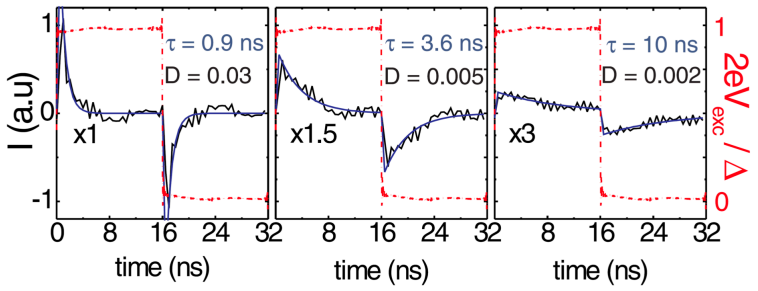

Figure 1.8: Real-time average current describing the emission of single electrons and holes from the mesoscopic capacitor into the edge channel of the 2DEG. Image taken from [7].

Real-time measurements in Fig. 1.8 show an exponentially decreasing average current of the form [7]

$$\langle I(t)\rangle = \pm\frac{e}{\tau}\frac{e^{-t/\tau}}{1+e^{-\mathcal{T}/2\tau}}, \tag{1.18}$$

where $\mathcal{T}$ is the period of the cycle and the plus (minus) sign in front of the previous expression applies in the first (second) half of the cycle. Provided that $\tau \ll \mathcal{T}$, the integral per half-period of the previous relation gives precisely an elementary charge, thus suggesting that a veritable emission of single electrons and single holes is achieved during every period. In order to be completely sure of this statement, one has to go beyond average current measurements, so as to rule out the possibility that the above mentioned quantization is just an average effect (for instance an electron is emitted in the first half period, no electrons in the third, two electrons in the fifth, thus compensating for the missing emission in the third). This can be done by considering current correlations [68, 69]. In particular, it has been shown that the accuracy of the mesoscopic capacitor as a single-electron source strongly depends on its operating regime [70]. In order to fix the ideas, the two extreme conditions are represented in Fig. 1.9. The left panel is the so-called optimal regime, where the energy of the uppermost occupied level of the QD is at $\Delta/2$ below the Fermi level of the 2DEG. In this regime the mesoscopic capacitor operates as a perfect single-electron emitter. This is not the case when the situation is the one represented in the right panel, *i.e.* the so-called resonant regime. Here, there is always a QD level at resonance with the Fermi energy and the device can be shown to produce unwanted electron-hole pair excitations, visible in the noise spectrum [68].

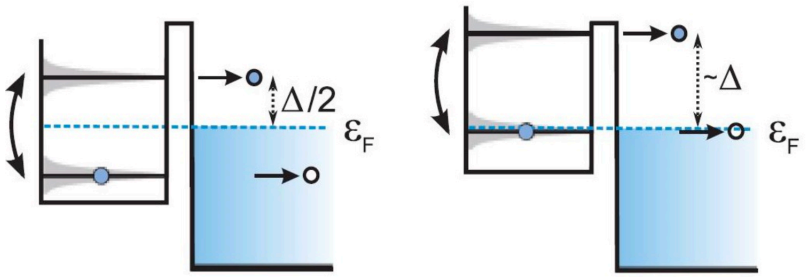

Figure 1.9: Two different operating conditions of the driven mesoscopic capacitor. Left: optimal regime. Right: resonant regime. Image taken from [68].

As a final remark, we emphasize that the mesoscopic capacitor is an emitter providing single electrons with a well defined energy, which is clearly related to the level spacing Δ in the QD. In particular, in the optimal emission regime, the energy of the injected electron is centered at $\varepsilon_0 = \Delta/2$ and distributed as a Lorentzian in energy domain. This leads to the electronic wavefunction

$$\tilde{\varphi}(\varepsilon) = \mathcal{N}_\varepsilon \frac{1}{\varepsilon - \varepsilon_0 + i\gamma}\, \theta(\varepsilon). \tag{1.19}$$

For high enough emission above the Fermi sea it is exponential in the time domain, namely

$$\varphi(t) = \mathcal{N}_t\, e^{-i\hbar/\varepsilon_0} e^{-\gamma t}\, \theta(t). \tag{1.20}$$

Here, $\mathcal{N}_{\varepsilon/t}$ ensures normalization and $\gamma = 1/\tau$ denotes the electron escape rate from the QD. From the above equation and from Fig. 1.8 it is transparent that the emission cannot be well localized in time. We will see in Section 1.4.2 that a complementary source exists, providing a localized emission in time and, consequently, an energy which is not well defined.

1.4.2 Voltage pulse source

A perhaps conceptually simpler way to generate excitations in a 1D quantum conductor exploits the application of a voltage pulse to the system. As the conductance of a ballistic quantum channel is given by (neglecting spin) the conductance quantum $G_Q = e^2/h$, it follows that the charge carried by the excitation generated by $V(t)$ is simply given by

$$Q = \frac{e^2}{h}\int_{-\infty}^{+\infty} V(t)dt. \tag{1.21}$$

Equivalently, the number q of electrons associated with this excitation is

$$q = \frac{Q}{-e} = -\frac{e}{h}\int_{-\infty}^{+\infty} V(t)dt. \tag{1.22}$$

However, this does not mean that any voltage drive such that the previous integral gives $q = n \in \mathbb{N}$ actually injects n electrons into the system. This is because, while on average it is certainly true that n electrons are injected, the integral in Eq. (1.22) tells us nothing about the possible creation of neutral particle-hole pair excitations.

The goal is then to find a shape of $V(t)$ ensuring that no such neutral excitations are created. This seemingly very complicated task has a quite simple solution, first found by L. Levitov and coworkers [8, 9] well before the birth of EQO. The answer is that the voltage pulse has to be a superposition of quantized Lorentzian functions such that

$$V(t) = \mp\frac{2\hbar}{e}\sum_{j=1}^{n}\frac{\tau_j}{\tau_j^2 + (t-t_j)^2}. \tag{1.23}$$

Here, τ_j is a parameter describing the temporal extension of each Lorentzian pulse and t_j is their emission time. When the negative (positive) sign in Eq. (1.23) is chosen, this drive generates n electrons (holes), without any particle-hole pair excitations. After Levitov, such excitations have been dubbed Levitons [13].

We will prove this result in the next Section, which is dedicated to a quite detailed analysis of Levitons in a non-interacting system. At this stage, we just show in Fig. 1.10 a sketch of the experimental implementation [13] which confirmed the theoretical prediction, together with a schematic representation of the main properties of a single-Leviton wavefunction. The experiments considered a periodic train of quantized Lorentzian pulses, applied to a contact connected to a 2DEG. The 1D conductor is created by means of a QPC, with tunable transmission D, as depicted in Fig. 1.10(a). The current fluctuations due to the presence of the QPC are measured in the right contact and allow to probe the cleanness of the produced excitations [9, 10]. From Fig. 1.10(b) we observe that the temporal profile of the current is a Lorentzian, while the energy distribution of the excitation is a decreasing exponential which leaves the Fermi sea untouched. Thus a Leviton with, $n = 1$, is a single-electron excitation on top of the Fermi sea. By referring to Fig. 1.10, the form of the wavefunction associated to the resulting time-resolved minimal excitation is

$$\psi(t) = \mathcal{N}'_t\,\frac{1}{t + i\tau_0} \tag{1.24}$$

while the energy-resolved form is an exponential

$$\tilde{\psi}(\varepsilon) = \mathcal{N}'_\varepsilon\, e^{-\frac{\tau_0}{\hbar}\varepsilon}\,\theta(\varepsilon). \tag{1.25}$$

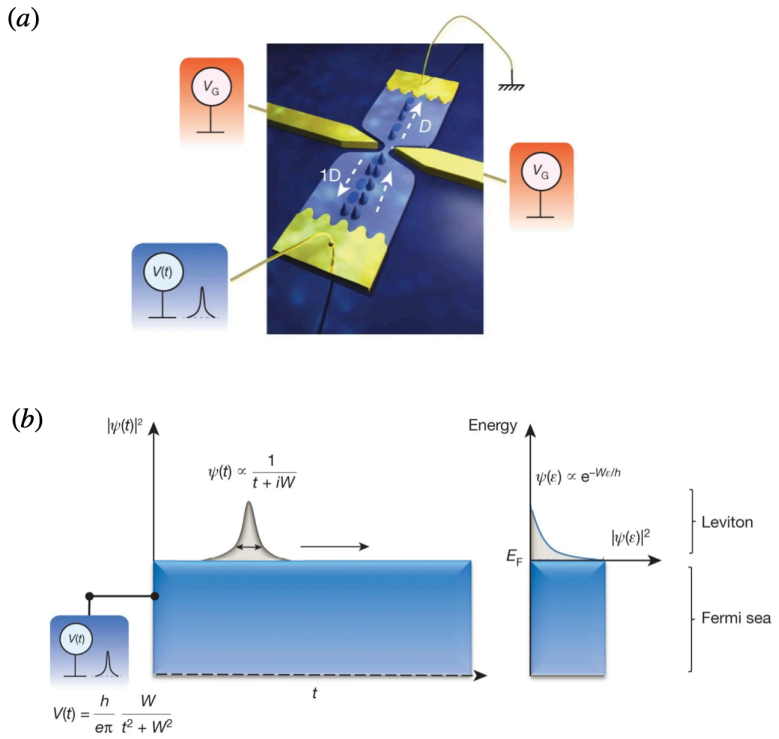

Figure 1.10: (a) Sketch of the experimental set-up: a periodic train of Lorentzian pulses is applied to the left contact. A stream of single electrons is generated in a 1D channel, created in a 2DEG by means of a QPC with tunable transmission D. (b) Sketch of the temporal profile of a Leviton wavefunction and its energy distribution. As we can observe, the Fermi sea is untouched. The temporal extension of the Lorentzian excitation is W which correspond to τ_j of Eq. (1.23) for the j-th electron (*i.e.* $\tau_0 = W$ if we have only one electron). Both images are taken from [13].

1.4.3 Levitons as purely electronic excitations

In this Section, we prove that Lorentizan pulses with quantized area do indeed generate minimal electronic excitations. In this Section, we choose units in which $\hbar = 1$.

As stated at the beginning of the Chapter, here the analysis will be limited to non-interacting electrons. For this reason, we consider the simplest possible 1D conductor, *i.e.* a single QH chiral edge channel. By setting the chemical potential to zero, the Hamiltonian of this system is

$$H_0 = \int_{-\infty}^{+\infty} dx\, \psi^\dagger(x)(-iv_F\partial_x)\psi(x) \tag{1.26}$$

where $\psi(x)$ is the fermionic annihilation field operator, destroying an electron at position x, and v_F is the Fermi velocity along the edge. Note that this Hamiltonian has a linear spectrum

$$\omega(k) = v_F k \tag{1.27}$$

and that its propagation is chiral. Even if the dispersion relation along the edge could deviate from this behavior, it is always possible to assume the linear relation of Eq. (1.27) if we are interested in the low-energy behavior of the system.

In order to find the voltage drive generating minimal excitations, we have first to understand how a generic $V(t)$ influences the time evolution $\psi(x,t)$ of the electron field operator. We consider the situation depicted in Fig. 1.11, where a the time-dependent potential $V(t)$ is applied to the edge channel in the region $x \in (-\infty, 0)$. We describe this with the function $U(x,t) = \Theta(-x)V(t)$, where $\Theta(x)$ is the Heaviside step function. The voltage couples to the charge density on the edge via the Hamiltonian

$$H_U = -e \int_{-\infty}^{+\infty} dx\, U(x,t)\psi^\dagger(x)\psi(x). \tag{1.28}$$

Before finding the time evolution $\psi(x,t)$, we want to better specify the setting of the problem with some general remarks. We assume that at $t = -\infty$ the system is in

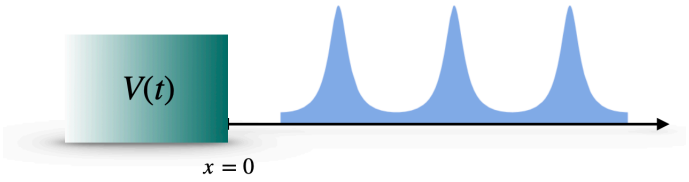

Figure 1.11: Voltage pulse source applied to a chiral edge channel. The potential $V(t)$ is applied uniformly in the spatial region $(-\infty, 0)$ and generates excitations propagating to the right, due to the chirality of the edge mode.

thermal equilibrium, with no applied drive, and thus is characterized by the time-independent equilibrium density matrix ρ_0, stemming uniquely from the Hamiltonian H_0. Then, at $t = -\infty + \kappa$ (with κ an infinitesimal time), the drive $V(t)$ is switched on. In the remainder of this Section, we adopt the Heisenberg picture, so that the time evolution is entirely attributed to operators. As a result, the quantum average of any operator $O(x,t)$ will be performed as

$$\langle O(x,t)\rangle_0 = \mathrm{Tr}[\rho_0\, O(x,t)], \tag{1.29}$$

where the time evolution $O(x,t)$ has to be determined with the full Hamiltonian $H = H_0 + H_U$.

Let us now return to the time evolution of the fermionic field. It is easy to derive the following Heisenberg equation of motion from the Hamiltonian $H = H_0 + H_U$:

$$i(\partial_t + v_F\partial_x)\psi(x,t) = -eU(x,t)\psi(x,t). \tag{1.30}$$

Consider first the simple case of equilibrium, where $U(x,t) = 0$. In this situation, the solution to the above equation is simply

$$\psi(x,t) = \psi(x - v_F t, 0) = \psi\left(0, t - \frac{x}{v_F}\right) \tag{1.31}$$

where we have make explicit the chirality of the propagation. Thanks to the chirality in the time evolution of the equilibrium solution, we can use interchangeably ω and k as conjugate variables. In particular, the usual Fourier representation of the fermionic field as an integral over momenta can also be written as

$$\psi(x - v_F t, 0) = \frac{1}{\sqrt{2\pi v_F}} \int_{-\infty}^{+\infty} d\omega\, e^{-i\left(t - \frac{\omega x}{v_F}\right)} c(\omega), \tag{1.32}$$

where $c(\omega)$ is the operator annihilating an electron at energy ω. These operators satisfy the equilibrium average

$$\langle c^\dagger(\omega)c(\omega')\rangle_0 = \mathrm{Tr}[\rho_0 c^\dagger(\omega)c(\omega')] = \delta(\omega-\omega')f(\omega) \tag{1.33}$$

where

$$f(\omega) = \frac{1}{1+e^{\frac{\omega}{k_B T}}} \tag{1.34}$$

is the Fermi function, T is the temperature and k_B is the Boltzmann constant.

We now come to the general solution of Eq. (1.30) in the presence of the driving term $U(x,t)$. It can be shown that the time evolution $\psi(x,t)$ in this case is given by (see A for details)

$$\psi(x,t) = \psi(x-v_F t,0)e^{ie\int_{-\infty}^{t} dt' U[x-v_F(t-t'),t']}. \tag{1.35}$$

By taking into account the spatial dependence of $U(x,t)$, the previous result can be further written, for $x>0$, as

$$\psi(x,t) = \psi(x-v_F t,0)e^{i\alpha\left(t-\frac{x}{v_F}\right)} \tag{1.36}$$

with

$$\alpha(\tau) = e\int_{-\infty}^{\tau} dt' V(t'). \tag{1.37}$$

Notice that, even in presence of the drive $V(t)$ the time evolution of the fermionic operator is chiral. This is indeed an inherent property of quantum Hall edge states. As a consequence, we can write

$$\psi(x,t) = \frac{1}{\sqrt{2\pi v_F}}\int_{-\infty}^{+\infty} d\omega\, e^{-i\omega\left(t-\frac{x}{v_F}\right)}C(\omega), \tag{1.38}$$

where $C(\omega)$ is again a fermionic operator. Its explicit expression can be obtained in this way. We define the Fourier transform

$$p(\omega) = \int_{-\infty}^{+\infty} d\tau\, e^{i\alpha(\tau)}e^{i\omega\tau} \tag{1.39}$$

and replace Eq. (1.32) to Eq. (1.36), arriving at

$$C(\omega) = \frac{1}{2\pi}\int_{-\infty}^{+\infty} d\omega' p(\omega')c(\omega-\omega'). \tag{1.40}$$

Thus, we see that $C(\omega)$ is built as a superposition of operators $c(\omega)$, shifted at all possible energies ω' and weighted by the (complex) coefficient $p(\omega')$ which depends on the voltage drive. Notice that when $V(t)=0$ we have from Eq. (1.39) $p(\omega)=2\pi\delta(\omega)$ and therefore $C(\omega)=c(\omega)$, as expected.

This discussion shows that the effects of the drive can be included in the new operators $C(\omega)$, which define a modified occupation number distribution

$$F(\omega) = \langle C^\dagger(\omega)C(\omega)\rangle_0 = \mathrm{Tr}[\rho_0 C^\dagger(\omega)C(\omega)]. \tag{1.41}$$

By using Eq. (1.40) and the equilibrium average (1.33), we find

$$F(\omega) = \int_{-\infty}^{+\infty}\frac{d\omega'}{(2\pi)^2}|p(\omega)|^2 f(\omega-\omega'). \tag{1.42}$$

This result tells us that the new occupation number distribution is obtained as a superposition of equilibrium Fermi functions, shifted at all possible energies ω' and weighted by the probability density that the drive creates an excitation at energy ω'. This interpretation of the Fourier transform $|p(\omega)|^2/(2\pi)^2$ as a probability density is supported by the normalization condition

$$\int_{-\infty}^{+\infty} \frac{d\omega}{(2\pi)^2} |p(\omega)|^2 = 1, \tag{1.43}$$

which can be obtained from the definition in Eq. (1.39).

We now have all we need to formalize the request that no holes are generated by the drive $V(t)$. Since a finite temperature naturally generates particle-hole pairs, let us consider the zero temperature limit, where any additional hole is due only by the drive (no holes are present at equilibrium). We can understand how to achieve our goal in two different ways. The first one is to notice that, if $p(\omega') = 0$ for $\omega' < 0$, then from Eq. (1.42) we observe that only upward shifts of the Fermi function $f(\omega)$ are allowed and, since at $T = 0$ we have $f(\omega - \omega') = \theta(\omega' - \omega)$, it is impossible to modify the occupation number at negative energies $\omega < 0$. As a consequence, the Fermi sea remains untouched and no holes are generated. We can arrive at the same conclusion by calculating the number of holes N_h in the system, given by

$$N_h = \int_{-\infty}^{0} d\omega \langle C(\omega) C^\dagger(\omega) \rangle_0 = \int_{-\infty}^{0} d\omega \, F(\omega) \tag{1.44}$$

A straightforward calculation yields

$$N_h = \frac{1}{(2\pi)^2} \int_{-\infty}^{0} d\omega \int_{-\infty}^{\omega} d\omega' |p(\omega')|^2 \tag{1.45}$$

and shows that $N_h = 0 \iff p(\omega) = 0$ for $\omega < 0$, as stated above.

By looking back at the definition (1.39), is it clear that this imposes a constraint on the functional form of $e^{i\alpha(t)}$. In particular, this function must be analytic in the lower complex plane (when t is regarded as a complex variable) and must have at least one pole in the upper part of it to prevent $p(\omega)$ from vanishing everywhere. Finally, being a phase, $|e^{i\alpha(t)}| = 1$. Thus we can consider [10]

$$e^{i\alpha(t)} = \frac{t - t_0 + i\tau_0}{t - t_0 - i\tau_0}, \qquad t_0 \in \mathbb{R}, \ \tau_0 > 0. \tag{1.46}$$

From this we arrive at the final result

$$V(t) = -\frac{i}{e} \frac{d}{dt} \ln e^{i\alpha(t)} = -\frac{2}{e} \frac{\tau_0}{\tau_0^2 + (t - t_0)^2} \tag{1.47}$$

which is precisely what reported in Eq. (1.23), for $n = 1$ (recall that here $\hbar = 1$). The generalization to more electrons is straightforward. We simply have to add more poles in the upper complex plane when constructing the function $e^{i\alpha(t)}$, together with corresponding zeros in the lower plane in order to have a unitary modulus:

$$e^{i\alpha(t)} = \prod_{j=1}^{n} \frac{t - t_j + i\tau_j}{t - t_j - i\tau_j}, \qquad t_j \in \mathbb{R}, \ \tau_j > 0. \tag{1.48}$$

This leads to the complete Eq. (1.27), with the minus sign. Finally, by following the same steps, it is now easy to show that a single-hole excitation is obtained by requiring that $e^{i\alpha(t)}$ has a pole in the lower complex plane, which amounts to reverse the sign of each τ_j.

1.5 The noise is the signal

The conductance G of a sample is an interesting quantity, however, it is only related to the averaged properties of electronic transport. The Landauer's formula (see Eq. (1.17)) is indeed obtained by computing the average current. In this context the time fluctuations of the current around its average value cannot be addressed. These fluctuations are quantified by the so called noise, which is physically very rich, as it encodes properties about the particles correlations and statistics.

Pioneering works on current fluctuations in mesoscopic systems by M. Büttiker, R. Landauer and T. Martin [71, 72, 73, 74] have shown that current noise contains information about the dynamics of charge carriers. On the experimental side, the measurement of partitioned current noise after a quantum point contact has shown that the statistics of electrical current in an ideal quantum conductor is sub-Poissonian [75], as a direct consequence of the Pauli exclusion principle. Current noise measurements in an HBT configuration has also allowed, for example, to measure the charge of fractional excitations in the $\nu = 1/3$ regime [76, 77]. The extraction of the charge of quasiparticle from shot noise measurements illustrated in a spectacular way the relevance of studying the noise to obtain information on the current carriers. The idea behind the sentence "The noise is the signal" [73], expressed by Landauer, is central in the EQO framework and we will refer, for the rest of this thesis, to the current noise as one of the most interesting physical quantities.

Throughout this thesis, we will characterize these fluctuations in terms of the current-current correlation function. Let us consider a conducting system through which a current $I(t)$ flows from the source to the drain electrode. The fluctuations of this current around the expectation value $\langle I(t)\rangle$ are described by the quantity

$$\Delta I(t) = I(t) - \langle I(t)\rangle. \tag{1.49}$$

The characterization of these fluctuations in the time domain is usually done by using the autocorrelation function of the current fluctuations

$$C(t,\tau) = \langle \Delta I(t)\Delta I(t+\tau)\rangle = \langle I(t)I(t+\tau)\rangle - \langle I(t)\rangle\langle I(t+\tau)\rangle. \tag{1.50}$$

In the case of a stationary current the statistical properties of the fluctuations are time-translational invariant and the noise only depends on τ, namely

$$C(\tau) = \langle \Delta I(t)\Delta I(t+\tau)\rangle = \langle \Delta I(0)\Delta I(\tau)\rangle. \tag{1.51}$$

Since the real time detection of the current correlations is extremely difficult in nowadays experiments, techniques based on finite frequency current noise have been developed in order to reconstruct the time behavior of the signals. Therefore, tipically experiments address the noise spectral density which is the Fourier transform of $C(\tau)$, namely[7]

$$S(\omega) = 2\int_{-\infty}^{+\infty} d\tau\, e^{i\omega\tau}\langle \Delta I(\tau)\Delta I(0)\rangle. \tag{1.52}$$

1.5.1 An introduction to scattering formalism

In this Section we present the scattering matrix formalism, which is a very powerful method allowing to tackle a variety of problems regarding transport in mesoscopic

[7] We consider an additional factor 2 in front of the Fourier transform for normalization purposes, as usually done in literature [74].

physics when the interaction between electrons can be neglected. The scattering approach relates transport properties of the system, in particular current and its fluctuations, to its scattering properties, which are assumed to be known from a quantum mechanical calculation. To describe this approach, we'll mainly rely on Ref. [74] and the original paper on the scattering matrix method in the operator formalism by Büttiker [78] although other excellent reviews and books are available in the literature [79, 80, 81].

To fix the ideas, we consider a sample, see Fig. 1.12, connected to two electronic reservoirs by a coherent waveguide (or lead). Electronic reservoirs contain a very large number of particles and are assumed to be described by an equilibrium state with well defined chemical potential $\mu_{L/R}$ and temperature $T_{L/R}$. Electrons in the reservoirs thus are characterized by the Fermi distribution (we recall Eq. (1.34))

$$f_\alpha(E) = \left[e^{(E-\mu_\alpha)/(k_B T_\alpha)} + 1\right]^{-1}, \qquad \alpha = L,\, R. \tag{1.53}$$

Driving the system out of equilibrium corresponds to setting different chemical potentials and/or temperatures in the different terminals. Inside the conductor we assume that only elastic scattering events take place leading to an overall conservation of the energy. Note, however, that there must be some inelastic mechanism inside the reservoirs in order to achieve an equilibrium distribution.

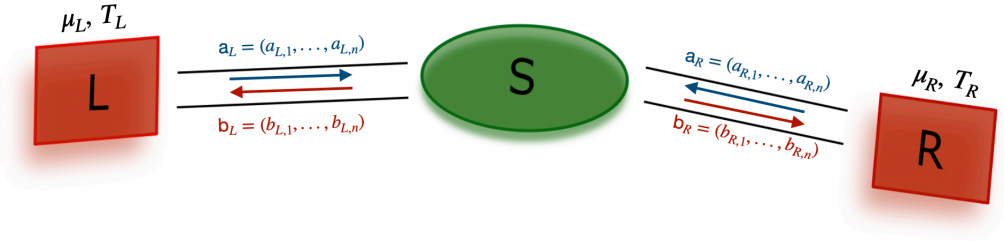

Figure 1.12: Example of two-terminal scattering problem for the case of one transverse channel. The system consists of two reservoirs at different temperatures $T_{L/R}$ and chemical potentials $\mu_{L/R}$ connected to a sample S. The electrons entering the central region from reservoirs (blue) are mixed by the scattering matrix of the system and emerge as new outgoing ones (red).

We assume, without loss of generality, that the transverse (across the leads) and the longitudinal (along the leads) motion of electrons are separable. Due to strong confinement, motion in the transverse directions x, y is quantized and described by the index n (corresponding to the set of orthonormal functions $\chi_{L/R,n}(x,y)$). Let us introduce operators $a_{\alpha,n}(E)$ that annihilate an electron with total energy E in the n-th channel going from terminal α to the central scattering region[8]. They obey conventional anticommutation relations

$$\left\{a_{\alpha,n}(E), a^\dagger_{\beta,m}(E')\right\} = \delta_{\alpha,\beta}\delta_{n,m}\delta(E-E'). \tag{1.54}$$

Note that the total energy E is determined by the sum of energies in the longitudinal and transverse channels, with the transverse energy in n-th channel given by $E_{L,n}$.

[8] To avoid confusion, we label terminals with Greek indices $\{\alpha, \beta, ...\}$ and use Roman indices $\{n, m, ...\}$ for transverse channels.

Similarly, operators $b_{\alpha,n}(E)$ annihilate an electron with energy E in the n-th channel going in the opposite direction. The operators a and b are related via the scattering matrix of the system. Due to the presence of two terminals and N conduction channels per side, the full system is described by the $2N \times 2N$ matrix s. Indeed, one has

$$b_{\alpha,i} = \sum_{\beta=L,R} \sum_{j_1}^{N} s_{\alpha\beta,ij} a_{\beta,j}. \tag{1.55}$$

However, collecting incoming and outgoing operators in vectors $\mathbf{a}_\alpha = (a_{\alpha,1}, ..., a_{\alpha,N})$ and $\mathbf{b}_\alpha = (b_{\alpha,1}, ..., b_{\alpha,N})$ with $i = L, R$ allows for a compact expression of the scattering matrix in terms of a four blocks matrix

$$\begin{pmatrix} \mathbf{b}_L \\ \mathbf{b}_R \end{pmatrix} = \begin{pmatrix} r & t' \\ t & r' \end{pmatrix} \begin{pmatrix} \mathbf{a}_L \\ \mathbf{a}_R \end{pmatrix} = s \begin{pmatrix} \mathbf{a}_L \\ \mathbf{a}_R \end{pmatrix}. \tag{1.56}$$

This structure is peculiar of the considered case but it can be generalized. Here, each block r, t, t' and r' is a $N \times N$ matrix. Coefficients for r are given by $r_{ij} = s_{LL,ij}$ and similar relations hold for the remaining three blocks. Blocks on the diagonal account for the reflection back to the left and right reservoirs respectively, while off-diagonal blocks describe the transport, respectively, from left to right and from right to left. The scattering matrix is in general unitary and additional symmetries (such as time reversal, if present) further constrain the block component of s. If N transverse channels are accessible, the field operator in the left waveguide reads

$$\psi_L(\mathbf{r}, t) = \int_0^{+\infty} dE\, e^{-iEt/\hbar} \sum_{n=1}^{N} \frac{\chi_{L,n}(x, y)}{\sqrt{2\pi\hbar v_{L,n}(E)}} \left[a_{L,n}(E) e^{ik_{L,n}z} + b_{L,n}(E) e^{-ik_{L,n}z} \right] \tag{1.57}$$

with $v_{L,n}(E) = (\hbar/m)k_{L,n}(E)$ and $k_{L,n}(E) = \sqrt{2m(E - E_{L,n})}/\hbar$ for a quadratic dispersion[9]. Note that an analogous relation holds for the right waveguide. However, current conservation allows us to focus solely on the left side of the conductor.

We now give the general results for current and noise in the scattering formalism focusing on the main passages and referring the reader interested in a more detailed discussion to the literature [74, 80, 81]. The 1D current operator in the left lead is obtained by integrating the quantum-mechanical three-dimensional current density [49, 82] in the transverse directions x and y

$$I_L(z, t) = \frac{e\hbar}{2im} \int dx\, dy \left[\psi_L^\dagger(z, t) \partial_z \psi_L(z, t) - \partial_z \psi_L^\dagger(z, t) \psi_L(z, t) \right]. \tag{1.58}$$

Let us insert the field operator Eq. (1.57) into Eq. (1.58). After some algebra, and neglecting the energy depencence of $v_{L,n}(E)$[10], one gets the following position-independent result for the current operator

$$I_L(t) = \frac{e}{h} \sum_{n=1}^{N} \int dE_1 dE_2\, e^{i(E_1 - E_2)t/\hbar} \left[a_{L,n}^\dagger(E_1) a_{L,n}(E_2) - b_{L,n}^\dagger(E_1) b_{L,n}(E_2) \right]. \tag{1.59}$$

[9] The integral in Eq. (1.57) runs from 0 to $+\infty$, as we are dealing with electrons with parabolic dispersion $E = \hbar^2 k^2/(2m)$. Different dispersion relations may lead to different limits of integration.

[10] This is a reasonable assumption in most cases, since only energies in a narrow window around the Fermi level play a relevant role, while $v_{L,n}(E)$ typically varies significantly on a much bigger scale. Therefore, we can safely assume the velocity $v_{L,n}(E) = v_{L,n}(E_F)$ constant.

The expectation value for I_L is found by recalling that particles going from the reservoirs to the scattering region are in an equilibrium state described by Eq. (1.53). Then the operators $a_{\alpha,n}$ obey

$$\langle a^\dagger_{\alpha,n}(E_1)a_{\beta,n'}(E_2)\rangle = \delta_{\alpha,\beta}\delta_{n,n'}\delta(E_1-E_2)f_\alpha(E_1). \tag{1.60}$$

We now write Eq. (1.59) solely in terms of the operators $a_{\alpha,n}$, $a^\dagger_{\alpha,n}$ thanks to Eq. (1.56) and we find

$$\begin{aligned}\langle I_L\rangle &= \frac{e}{h}\sum_{n=1}^{N}\int dE\left[f_L(E) - \sum_{\beta=L,R}\sum_{m=1}^{N} s^*_{L\beta,nm}s_{L\beta,nm}f_\beta(E)\right] = \\ &= \frac{e}{h}\sum_{n=1}^{N}\int dE\left\{\left[1-\sum_{m=1}^{N}|r_{nm}|^2\right]f_L(E) - \sum_{m=1}^{N}|t_{nm}|^2 f_\beta(E)\right\} = \\ &= \frac{e}{h}\int dE\ \mathrm{Tr}(t^\dagger t)\left[f_L(E)-f_R(E)\right],\end{aligned} \tag{1.61}$$

where the last passage follows from the unitarity of the scattering matrix. Indeed from $s^\dagger s = \mathbb{I}$ one finds $r^\dagger r + t^\dagger t = \mathbb{I}$ which leads to $\sum_m(|r_{nm}|^2+|t_{nm}|^2)=1$. We note that Eq. (1.61) is a basis invariant expression. The matrix $t^\dagger t$ can be diagonalized and it has a set of eigenvalues (transmission probabilities) $\mathsf{T}_n(E)$. Then the expression for the current in a mesoscopic two-terminal system, as long as electron-electron interactions do not play a prominent role, is

$$\langle I_L\rangle = \frac{e}{h}\sum_{n=1}^{N}\int dE\ \mathsf{T}_n(E)\left[f_L(E)-f_R(E)\right]. \tag{1.62}$$

Notice that, in an equilibrium configuration with $\mu_L = \mu_R$ and $T_L = T_R$, Fermi distributions in the reservoirs are exactly the same and no current flows though the sample. For the following, to avoid notational confusion, we would like to point out the difference between the transmission coefficient T and the temperature T.

Consider now an out of equilibrium situation, where a voltage bias V is applied on the mesoscopic system. The electrochemical potential in the left reservoir is brought below the Fermi level, namely $\mu_L = E_F - eV$ while $\mu_R = E_F$, with equal temperature T on both sides. As the energy scale set by eV is usually much smaller than E_F, the integral in Eq. (1.62) is dominated by a small energy window of width $\sim eV$ around the Fermi level. Thus, we can neglect the energy dependence of $\mathsf{T}_n(E)$ in this short interval and perform the integration over the Fermi distributions, getting

$$\langle I_L\rangle \approx \frac{e}{h}\sum_{n=1}^{N}\mathsf{T}_n(E_F)\int dE\left[f_L(E)-f_R(E)\right] = \frac{e^2}{h}V\sum_{n=1}^{N}\mathsf{T}_n(E_F), \tag{1.63}$$

where the last passage holds for $E_F \gg \{eV, k_BT\}$. Thus, the conductance $G = \langle I_L\rangle/V$ for a two-terminal mesoscopic system in presence of N conduction channels is generally given by[11]

$$G = \frac{e^2}{h}\sum_{n=1}^{N}\mathsf{T}_n. \tag{1.64}$$

[11] In the following, the notation T_n without the energy argument stands for the n-th transmission eigenvalue evaluated at the Fermi level, *i.e.* $\mathsf{T}_n = \mathsf{T}_n(E_F)$.

Equation (1.64) is known as a multi-channel generalization of the Landauer formula of Eq. (1.17). It relates the conductance of a quantum conductor to the transmission eigenvalues of the available conduction channels.

We are concerned with fluctuations of the current with respect to their average value. We focus on the autocorrelation spectrum of $\Delta I_L = I_L - \langle I_L \rangle$, which is given by

$$S(\omega) = 2 \int_{-\infty}^{+\infty} d\tau \, e^{i\omega\tau} \langle \Delta I_L(0) \Delta I_L(\tau) \rangle \tag{1.65}$$

and we calculate it through the scattering matrix formalism introduced above. Differently from $\langle I_L \rangle$, to find the noise power, we need the four-operator average

$$\langle a^\dagger_{\alpha_1,n_1} a_{\alpha_2,n_2} a^\dagger_{\alpha_3,n_3} a_{\alpha_4,n_4} \rangle \tag{1.66}$$

which can be evaluated recalling Wick's theorem [83]. This leads to

$$\begin{aligned} S(\omega) = & 2\frac{e^2}{h} \int dE \ \mathrm{Tr}(tt^\dagger tt^\dagger) \big\{ f_L(E)[1 - f_L(E - \hbar\omega)] + \\ & + f_R(E)[1 - f_R(E - \hbar\omega)] \big\} + \\ & + 2\frac{e^2}{h} \int dE \ \mathrm{Tr}(rr^\dagger tt^\dagger) \big\{ f_L(E)[1 - f_R(E - \hbar\omega)] + \\ & + f_R(E)[1 - f_L(E - \hbar\omega)] \big\}. \end{aligned} \tag{1.67}$$

The general result for the zero frequency noise power in a two-terminal conductor is

$$\begin{aligned} S(\omega = 0) = & 2\frac{e^2}{h} \sum_{n=1}^{N} \int dE \ \mathsf{T}_n^2(E) \big\{ f_L(E)\big[1 - f_L(E)\big] + f_R(E)\big[1 - f_R(E)\big] \big\} + \\ & + 2\frac{e^2}{h} \sum_{n=1}^{N} \int dE \ \mathsf{T}_n(E)\big[1 - \mathsf{T}_n(E)\big]\big[f_L(E) - f_R(E)\big]^2. \end{aligned} \tag{1.68}$$

In Eq. (1.68), the first two terms are referred to the equilibrium noise since they depend on the Fermi distribution of left and right reservoirs separately. Conversely, the third one can be regarded as the non-equilibrium contribution to the power spectrum since this term never appear in the equilibrium situation when $f_L = f_R$.

From Eq. (1.68), we are then able to evaluate the zero frequency noise $S(0) \equiv S$. Usually it has been investigated in presence of a dc voltage drop of the form $\mu_R = E_F = \mu_L + eV$ and no temperature gradient. In this configuration, through the Landauer framework, the noise can be described as [74, 84]

$$S = 4\frac{e^2}{h} k_B T \sum_{n=1}^{N} \mathsf{T}_n^2 + 2\frac{e^2}{h} eV \coth\left(\frac{eV}{2k_B T}\right) \sum_{n=1}^{N} \mathsf{T}_n(1 - \mathsf{T}_n). \tag{1.69}$$

Instead of a voltage bias, it is possible to consider the system connected to two reservoirs placed at different temperatures T_R and T_L. Then, when a non-zero temperature difference ΔT defined as

$$\Delta T = T_L - T_R \tag{1.70}$$

is applied across the conductor, a similar approximate expression for the current noise can be derived based on the Landauer formalism [26]

$$S \approx 4k_B \bar{T} \frac{e^2}{h} \sum_{n=1}^{N} \mathsf{T}_n + 2\frac{e^2}{h} \frac{k_B (\Delta T)^2}{\bar{T}} \left(\frac{\pi^2}{9} - \frac{2}{3}\right) \sum_{n=1}^{N} \mathsf{T}_n(1 - \mathsf{T}_n) \tag{1.71}$$

where the average temperature

$$\bar{T} = \frac{T_R + T_L}{2} \tag{1.72}$$

between the hot and cold reservoirs has been introduced.

Let's focus on particular cases to fully appreciate the physics contained in Eqs. (1.69) and (1.71) and to highlight the differences between equilibrium and non-equilibrium contributions to the noise.

1.5.2 Equilibrium thermal noise

At finite temperature, electrons are subject to thermal agitation. Consequently, an equilibrium noise arises, as established in the classical regime by J. B. Johnson [23] and H. Nyquist [24] in 1928. It is observed for a zero voltage bias between the leads ($\mu_L = \mu_R$) and a non-zero temperature ($T \neq 0$), or as long as the voltage is much lower than the temperature ($eV \ll k_B T$). Then, from Eq. (1.69), we find

$$S = 4\frac{e^2}{h} k_B T \sum_{n=1}^{N} \mathsf{T}_n = 4 k_B T G, \tag{1.73}$$

which is the famous Johnson-Nyquist relation for the thermal noise. It states that the equilibrium noise S is proportional to the electrical conductance G and this proportionality is given by the temperature T. Notice that the same result can be obtained from Eq. (1.71) when no temperature difference is taken into account.

Thermal noise is an equilibrium statistical property of the system, while the conductance tells us how the conductor reacts and dissipates energy when is driven out of equilibrium by applying a non-zero voltage bias. Therefore, Eq. (1.73) emphasizes a very important relation between equilibrium and non-equilibrium properties of the system. Indeed it shows, in the linear response regime, a remarkably profound link between equilibrium fluctuations and dissipative properties of a system. It was indeed demonstrated that the Johnson-Nyquist formula is nothing but a particular manifestation of the more general relation known as fluctuation-dissipation theorem [85].

Equation (1.73) is a first example of what we can learn from noise measurements. For example, we can measure the electronic temperature of a mesoscopic device by looking at the ratio S/G which is the essence of the noise thermometry technique [86, 87, 88]. However, it is by moving onto non-equilibrium noise in quantum conductor that we can fully appreciate the power behind the Landauer's statement.

1.5.3 Shot noise

Contrary to the Johnson-Nyquist noise, shot-noise is due to an out of equilibrium situation created by a voltage imbalance. It can only be probed when a voltage bias is applied between the leads: $\mu_L - \mu_R = -eV$. Shot noise in an electrical conductor is a consequence of the granularity of the charge. Indeed, an electric current is nothing but the flow of discrete particles with quantized charge which can be different depending on the system we consider. At zero temperature, the auto-correlation noise reads [72, 78, 89, 90]

$$S = 2\frac{e^2}{h} e|V| \sum_{n=1}^{N} \mathsf{T}_n(1 - \mathsf{T}_n) \tag{1.74}$$

which is obtained by exploiting the limit

$$\lim_{x\to\pm\infty} \coth(x) = \pm 1 \tag{1.75}$$

in Eq. (1.69).

This expression reflects the fact that the non-equilibrium shot noise is not simply determined by the conductance of the sample. Instead, it is determined by a sum of products of transmission and reflection probabilities of the channels. When considering a sample with one channel at zero temperature, the average current reads: $\langle I_L\rangle = (2e/h)eV\mathsf{T}$. Thus Eq. (1.74) can be written as

$$S = 2e\langle I_L\rangle(1-\mathsf{T}). \tag{1.76}$$

It is clear that zero-temperature shot noise is always suppressed in comparison with the Poissonian value in which $S = 2e\langle I_L\rangle$. The noise is then said to be sub-Poissonian. In fact, for both open ($\mathsf{T} = 1$) or close ($\mathsf{T} = 0$) channels the particles can only be transmitted, or oppositely reflected, through the mirror and shot noise completely vanishes. Moreover, knowing both the current and the zero-frequency noise gives access to the charge of the carriers. In this way, the fractional charge of the quasi-particles in the FQH effect was measured [76, 91].

Let us remark that the origin of shot noise is much different from the thermal one. The latter is a property of an equilibrium system caused by fluctuations in the occupation number. The former is instead an intrinsically non-equilibrium characteristic which only emerges when we drive a current through the system.

1.5.4 Delta-T noise

Instead of a voltage bias, one can in principle consider the conductor connected to two reservoirs at different temperatures. The presence of a temperature gradient gives rise to an out of equilibrium noise dubbed as delta-T noise which is different from the previous shot noise. It is worth noticing that delta-T noise is purely thermal in origin but it is only generated in a non-equilibrium situation. In recent years, systems connected to reservoirs kept at different temperatures have been experimentally [26, 92, 93, 94] and theoretically considered [95, 96, 97, 98, 99, 100, 101].

When a temperature difference ΔT is applied across the conductor at zero voltage bias, a new expression for the current noise can be derived through the scattering formalism. In order to obtain Eq. (1.71), we recall Eq. (1.68) for the zero frequency noise $S = S_1 + S_2$ with the two components

$$\begin{aligned} S_1 &= 2\frac{e^2}{h}\sum_{n=1}^{N}\mathsf{T}_n^2\int dE\,\big\{f_L(E)\big[1-f_L(E)\big]+f_R(E)\big[1-f_R(E)\big]\big\} \\ S_2 &= 2\frac{e^2}{h}\sum_{n=1}^{N}\mathsf{T}_n\big[1-\mathsf{T}_n\big]\int dE\,\big\{f_L(E)\big[1-f_R(E)\big]+f_R(E)\big[1-f_L(E)\big]\big\}, \end{aligned} \tag{1.77}$$

where we have taken the channels' transmission function as energy independent for sake of simplicity. Based on this approximation, we evaluate S_1 exactly by using identities for the Fermi function

$$\begin{aligned} S_1 =& 2\frac{e^2}{h}\sum_{n=1}^{N}\mathsf{T}_n^2\int dE\,\left[-k_BT_L\frac{\partial f_L(E)}{\partial E}-k_BT_R\frac{\partial f_R(E)}{\partial E}\right] \\ =& 2\frac{e^2}{h}k_B\bar{T}\sum_{n=1}^{N}\mathsf{T}_n^2 \end{aligned} \tag{1.78}$$

with the average temperature being $\bar{T} = (T_R + T_L)/2$. Since we are considering an out-of-equilibrium situation induced by a temperature bias, the second term S_2 can be evaluated by considering the difference

$$S_2 = S_2(\Delta\mu = 0, \Delta T) - S_2(\Delta\mu = 0, \Delta T = 0). \tag{1.79}$$

Here in Eq. (1.79), the first term includes all contributions that depend on the temperature difference while the second term, which is the equilibrium one, is subtracted in order to deal with the out-of-equilibrium contribution. It is worth noticing that in presence of a energy dependent transmission a new term appears and it depends on the derivative of the transmission function at the vicinity of the Fermi energy [97]. Without entering into analytical details which can be found in Ref. [26], the equilibrium contribution is

$$S_2(\Delta\mu = 0, \Delta T = 0) = 4\frac{e^2}{h} k_B \bar{T} \sum_{n=1}^{N} \mathsf{T}_n(1 - \mathsf{T}_n) \tag{1.80}$$

and the temperature-induced term, before the integration, is

$$\begin{aligned} S_2(\Delta\mu = 0, \Delta T) = 2\frac{e^2}{h} \int dE \left[f_L(E) - f_R(E)\right] \times \\ \times \coth\left(\frac{\Delta T}{2k_B T_L T_R}(E - E_F)\right) \sum_{n=1}^{N} \mathsf{T}_n(1 - \mathsf{T}_n). \end{aligned} \tag{1.81}$$

Notice that the equilibrium contribution is the thermal noise obtained in Eq. (1.73). Equation (1.81) can be simplified by Taylor-expanding the $\coth(x)$ function and the difference $(f_L - f_R)$ in terms of the temperature gradient. The solution of this integral depends on the symmetry of the system. If the junction conducts symmetrically in the forward and backward direction, odd powers in ΔT do not contribute and the final result, for non-interacting electronic systems, reads

$$S \approx 4\frac{e^2}{h} k_B \bar{T} \sum_{n=1}^{N} \mathsf{T}_n + 2\frac{e^2}{h} \frac{k_B (\Delta T)^2}{\bar{T}} \left(\frac{\pi^2}{9} - \frac{2}{3}\right) \sum_{n=1}^{N} \mathsf{T}_n\big(1 - \mathsf{T}_n\big). \tag{1.82}$$

This symmetrical set-up has been recently studied for FQH systems in a QPC geometry and it was found that the tunneling of quasiparticles is associated with negative values of the delta-T noise [96]. If the system is no longer symmetric, such as if the system is made by different samples, then odd ΔT powers will appears, affecting the final result. This problem will be addressed in the last Chapter.

1.6 Noise in interferometric set-up

1.6.1 Single particle interferometry

We have already seen that thermal and shot noise provide information about the dissipative properties of a system, the temperature, and the charge of the carriers. Furthermore, it is possible to extrapolate the statistical properties of particles from the study of a particular kind of shot noise, called partition noise. In order to understand the origin of this type of noise, we consider a typical experiment where particles are incident on a target at which they are scattered and then conducted in some sort of optical table, as shown in Fig. 1.13. For the following, we will consider our particles as both bosons or fermions, specifying their nature when necessary.

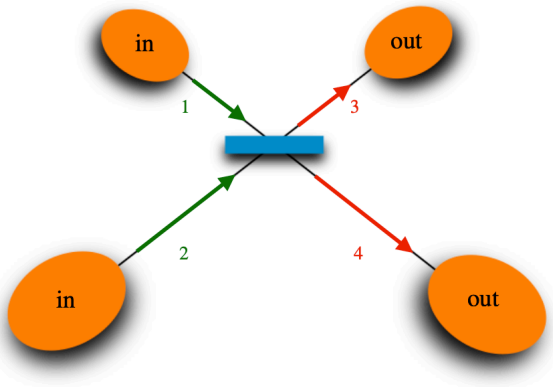

Figure 1.13: Optical like set-up for two particle interferometry. Incoming particles, traveling in input channels 1 and 2, impinge on the beamsplitter in the middle (thin blue layer). They are either reflected (with probability R) or transmitted (with probability $\mathsf{T} = 1 - \mathsf{R}$) into the output channels 3 and 4.

The particles coming from input channels 1 and 2 collide on a central scatter and exit in output 3 and 4. At the barrier the particle is either transmitted with probability T or reflected with probability $\mathsf{R} = 1 - \mathsf{T}$. In the EQO framework, the central scatter is nothing than the QPC introduced in Section 1.3.

We describe incoming particles in second quantization with annihilation a_i and creation $a_i^\dagger$ operators (with $i = 1, 2$) while operators b_j and $b_j^\dagger$ ($j = 3, 4$) describe the outgoing particles. Due to the probabilistic nature of the scattering processes, the relation between input and output operators in a matrix form reads

$$\begin{pmatrix} b_3 \\ b_4 \end{pmatrix} = \begin{pmatrix} \sqrt{\mathsf{R}} & i\sqrt{\mathsf{T}} \\ i\sqrt{\mathsf{T}} & \sqrt{\mathsf{R}} \end{pmatrix} \begin{pmatrix} a_1 \\ a_2 \end{pmatrix} \tag{1.83}$$

where R and T are, respectively, the reflection and transmission coefficients. The occupation number of input and output arms are $n_i = a_i^\dagger a_i$ ($i = 1, 2$) and $n_j = b_j^\dagger b_j$ ($j = 3, 4$). The occupation numbers of output channels are given by:

$$\begin{aligned} n_3 &= \mathsf{R}n_1 + \mathsf{T}n_2 + i\sqrt{\mathsf{RT}}(a_1^\dagger a_2 - a_2^\dagger a_1) \\ n_4 &= \mathsf{T}n_1 + \mathsf{R}n_2 - i\sqrt{\mathsf{RT}}(a_1^\dagger a_2 - a_2^\dagger a_1). \end{aligned} \tag{1.84}$$

The probabilistic scattering of particles induce fluctuations in the occupation number of output arms. For instance, by using Eq. (1.84) and applying repeatedly Wick's theorem, one can compute the auto-correlators and cross-correlator of number occupations in the output arms, which are

$$\langle \Delta n_3^2 \rangle = \langle \Delta n_4^2 \rangle = -\langle \Delta n_3 \Delta n_4 \rangle = \mathsf{RT} \tag{1.85}$$

where we have introduced the notation $\Delta n_i = n_i - \langle n_i \rangle$.

Fluctuations in the detected number of particles described by Eq. (1.85) are called partition noise since they are due only to random partition occuring at the central scatterer. In particular, for the simple case of single particle injection from only one arm, the partition noise is proportional to RT and vanishes both for a completely transparent or reflecting barrier. This can be intuitively understood since there is no partition for the incoming particle as only one output arm is accessible and the

occupation number of the output states cannot fluctuate. However, from these observations no differences between bosons and fermions arise. We then move to the more interesting case of two-particle interferometry.

1.6.2 Two particle interferometry

Consider now a situation where the injection of a particle, either a boson or a fermion, occurs in both channels of the set-up in Fig. 1.13. We must assume that the colliding particles reach the mirror simultaneously, *i.e.* at the same time, in order to observe the effect of multi-particle physics. In this case the average number of particles, detected at both outputs, are $\langle n_3\rangle = \mathsf{R}\langle n_1\rangle + \mathsf{T}\langle n_2\rangle = 1$ and $\langle n_4\rangle = \mathsf{R}\langle n_2\rangle + \mathsf{T}\langle n_1\rangle = 1$. Regardless of the statistics and of the transmission coefficient of the mirror, each detector measures exactly one particle on average. Let's focus on the average $\langle n_3^2\rangle$

$$\begin{aligned}\langle n_3^2\rangle &= \mathsf{R}^2\langle n_1^2\rangle + \mathsf{T}^2\langle n_2^2\rangle + 2\mathsf{RT}\langle n_1 n_2\rangle + \mathsf{RT}\langle a_1^\dagger a_2 a_2^\dagger a_1 + a_2^\dagger a_1 a_1^\dagger a_2\rangle \\ &= 1 + \mathsf{RT}(2 \pm 2)\end{aligned} \tag{1.86}$$

where the upper sign accounts for the bosonic case, while the lower one for fermions. The difference in the sign is due to the fact that $a_i a_i^\dagger = 1 \pm a_i^\dagger a_i$ depending on the statistics. Furthermore if we exchange R with T we obtain the same result meaning that $\langle n_3^2\rangle = \langle n_4^2\rangle$. From the conservation relation $n_1 + n_2 = n_3 + n_4$ we obtain the average value

$$\begin{aligned}\langle n_3 n_4\rangle &= \mathsf{RT}[\langle n_1^2\rangle + \langle n_2^2\rangle - \langle n_1\rangle - \langle n_2\rangle - (2 \pm 2)\langle n_1 n_2\rangle] + \langle n_1 n_2\rangle \\ &= 1 - \mathsf{RT}(2 \pm 2).\end{aligned} \tag{1.87}$$

The final relation about average fluctuations then reads

$$\langle \Delta n_3^2\rangle = \langle \Delta n_4^2\rangle = -\langle \Delta n_3 \Delta n_4\rangle = \mathsf{RT}(2 \pm 2). \tag{1.88}$$

According to this analysis, a very different behavior for bosons and fermions emerges. If we compare the above result with twice the partition noise of a single source, we see that the fluctuations are doubled for the bosonic case and completely suppressed for fermions. Physically, Equation (1.87) is a concise statement of the Pauli principle. For bosons, the probability that the two particles exit on opposite sides, namely $P(1,1) = 1 - 4\mathsf{RT}$, depends on the transmission and reflection coefficient of the scatterer and vanishes for an ideal barrier with $\mathsf{T} = \mathsf{R} = 1/2$. Then, the two particles are preferentially scattered into the same output branch. This effect, which states that photons in a symmetric beamsplitter exits on the same side, is called photon bunching. Differently, for fermions $P(1,1)$ is insensitive to the transmission and reflection probability and it is given by $P(1,1) = 1$. Thus fermions are scattered with probability one into the different output branches. This effect is known as antibunching. Similar considerations also comes from the probabilities of the two particles to be scattered in the same channels $P(2,0) = P(0,2) = 2\mathsf{RT}$ for bosons or $P(2,0) = P(0,2) = 0$ for fermions.

Cross- and auto-correlated noise

In the following we will provide some complementary details about noise calculation in electronic interferometers realized in solid state devices. We consider a QH bar at filling factor $\nu = 1$ (see Fig. 1.14) in a two terminal QPC geometry. Two time-dependent potential $V_{R/L}$ are applied to the reservoirs. In this Section, we will deal

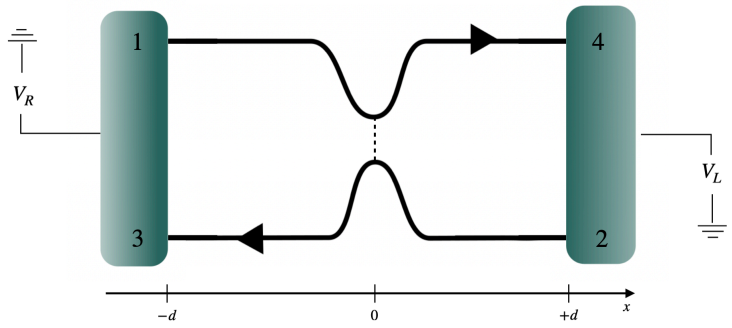

Figure 1.14: Quantum Hall bar at filling factor $\nu = 1$ in a two-terminal QPC geometry. Two time-dependent potentials V_R and V_L are applied to left and right reservoirs, respectively, playing the role of electron sources on demand. The incoming field particles are labelled with 1 and 2 while the outgoing ones with 3 and 4.

with free electrons while in the next Chapters we will study the effects of interactions in such kind of systems. By recalling Eq. (1.36), the fermionic fields incoming into edge states from the two reservoirs are given by

$$\psi^{(in)}_{R/L}(x,t) \equiv \psi_{R/L}(x,t) = e^{ie\int_{-\infty}^{t\mp\frac{x}{v_F}} dt' V_{R/L}(t')} \psi_{R/L}(x \mp v_F t, 0). \tag{1.89}$$

Electronic fields outgoing from the QPC are termed $\psi^{(3/4)}_{L/R}(x,t)$ whether they enter into reservoir as right- or left-movers. They are connected to fermionic fields in Eq. (1.89) by the scattering matrix of Eq. (1.83) which model the QPC between the two edge states. In this way, the fermionic fields $\psi^{(3/4)}_{L/R}$ are expressed as a simple linear combination of $\psi^{(1/2)}_{R/L}$, weighted by the appropriate probability transmission and reflection, T and R, determined by the voltage gate of the QPC. Thus, one has

$$\begin{pmatrix} \psi^{(3)}_R \\ \psi^{(4)}_L \end{pmatrix} = \begin{pmatrix} \sqrt{\mathsf{R}} & i\sqrt{\mathsf{T}} \\ i\sqrt{\mathsf{T}} & \sqrt{\mathsf{R}} \end{pmatrix} \begin{pmatrix} \psi^{(1)}_R \\ \psi^{(2)}_L \end{pmatrix}. \tag{1.90}$$

As argued before, we are interested in using this scattering matrix approach to compute the current noise in single-electron interferometric set-up. We consider a periodic injection of particles so that, the zero-frequency current noise, from Eq. (1.52), is written as

$$\begin{aligned} S_{\alpha,\beta} &= 2\int_{-\frac{\mathcal{T}}{2}}^{+\frac{\mathcal{T}}{2}} dt \int_{-\infty}^{+\infty} dt' \langle \Delta I_\alpha(x_\alpha,t)\Delta I_\beta(x_\beta,t')\rangle = \\ &= 2\int_{-\frac{\mathcal{T}}{2}}^{+\frac{\mathcal{T}}{2}} dt \int_{-\infty}^{+\infty} dt' \langle \Delta I_\alpha(0,t-\xi_\alpha\frac{x_\alpha}{v_F})\Delta I_\beta(0,t'-\xi_\beta\frac{x_\beta}{v_F})\rangle \end{aligned} \tag{1.91}$$

where in the second line we have taken into account the chirality. Notice that α and β can assume the value 3 or 4 and $\xi_{3/4} = \pm 1$. The chiral current operator $I_\alpha(x_\alpha,t)$ enters into the reservoir associated to the label α and x_α indicates the position of such reservoir. It can be easily expressed as a balance of fermionic operators entering or exiting reservoirs as

$$\begin{aligned} I_3(x,t) &= -ev_F\big[:\psi^{\dagger(3)}_L(x,t)\psi^{(3)}_L(x,t): - :\psi^{\dagger(1)}_R(x,t)\psi^{(1)}_R(x,t):\big] \\ I_4(x,t) &= -ev_F\big[:\psi^{\dagger(4)}_R(x,t)\psi^{(4)}_R(x,t): - :\psi^{\dagger(2)}_L(x,t)\psi^{(2)}_L(x,t):\big], \end{aligned} \tag{1.92}$$

where the notation : ... : stands for the normal ordering with respect to the Fermi sea.

The current fluctuations associated to the same reservoir ($\alpha = \beta$) are called auto-correlators, while for different reservoirs ($\alpha \neq \beta$) they are called cross-correlators. The current operator can be recast using Eq. (1.90) thus obtaining

$$\begin{aligned} I_3(x,t) &= -ev_F\big[\mathsf{T}\big(:\psi_L^{\dagger(2)}(x,t)\psi_L^{(2)}(x,t):-:\psi_R^{\dagger(1)}(x,t)\psi_R^{(1)}(x,t):\big)+ \\ &\quad -i\sqrt{\mathsf{RT}}\big(:\psi_R^{\dagger(1)}(x,t)\psi_L^{(2)}(x,t):-:\psi_L^{\dagger(2)}(x,t)\psi_R^{(1)}(x,t):\big)\big] \\ I_4(x,t) &= -ev_F\big[\mathsf{T}\big(-:\psi_L^{\dagger(2)}(x,t)\psi_L^{(2)}(x,t):+:\psi_R^{\dagger(1)}(x,t)\psi_R^{(1)}(x,t):\big)+ \\ &\quad +i\sqrt{\mathsf{RT}}\big(:\psi_L^{\dagger(2)}(x,t)\psi_R^{(1)}(x,t):-:\psi_R^{\dagger(1)}(x,t)\psi_L^{(2)}(x,t):\big)\big]. \end{aligned} \tag{1.93}$$

Let us notice that the two current are related as $I_3(x,t) = -I_4(x,t)$, which is consistent with the charge conservation. As a consequence, the auto-correlators are related to the cross-correlators according to

$$S_{33} = S_{44} = -S_{34} = -S_{43}. \tag{1.94}$$

In the following, for definiteness we focus on the cross-correlator of reservoirs 3 and 4, namely S_{34}, and we use the shorthand notation $S = S_{34}$.

By using the definition of current noise in Eq. (1.91) and the expression for the current I_4 just derived, one finds for the zero-frequency auto-correlator

$$\begin{aligned} S &= -2(ev_F\mathsf{T})^2\int_{-\frac{\mathcal{T}}{2}}^{+\frac{\mathcal{T}}{2}}dt\int_{-\infty}^{+\infty}dt'\sum_{r=L,R}\mathcal{G}_{F,r}^{(e)}(t,t')\mathcal{G}_{F,r}^{(h)}(t,t')+ \\ &\quad -2(ev_F)^2\mathsf{RT}\int_{-\frac{\mathcal{T}}{2}}^{+\frac{\mathcal{T}}{2}}dt\int_{-\infty}^{+\infty}dt'\big[\mathcal{G}_R^{(e)}(t,t')\mathcal{G}_L^{(h)}(t,t')+\mathcal{G}_L^{(e)}(t,t')\mathcal{G}_R^{(h)}(t,t')\big], \end{aligned} \tag{1.95}$$

where we eliminate the dependence on x_α by using the chirality of fermionic fields and we define the Green's functions

$$\begin{aligned} \mathcal{G}_{R/L}^{(e)}(t,t') &= \langle\psi_{R/L}^{\dagger,(1/2)}(0,t)\psi_{R/L}^{(1/2)}(0,t')\rangle \\ \mathcal{G}_{R/L}^{(h)}(t,t') &= \langle\psi_{R/L}^{(1/2)}(0,t)\psi_{R/L}^{\dagger,(1/2)}(0,t')\rangle. \end{aligned} \tag{1.96}$$

Let us comment, that, in analogy with Glauber's coherence theory of photons [11], the first line of Eq. (1.96) can be also termed first order electronic coherence function. This object is the central quantity of EQO [12, 102, 103]. While for photons a single coherence functions is sufficient, in mesoscopic systems one needs two types of coherence functions, respectively, for electrons and holes. Therefore, in addition to first line we have the second one in Eq. (1.96). At equilibrium (*i.e.* when no voltage is applied) these coherence functions are

$$\begin{aligned} \mathcal{G}_{F,R/L}^{(e)}(t,t') &= \int_{-\infty}^{+\infty}\frac{dE}{2\pi v_F}e^{iE(t-t')}f_{R/L}(E) \\ \mathcal{G}_{F,R/L}^{(h)}(t,t') &= \int_{-\infty}^{+\infty}\frac{dE}{2\pi v_F}e^{-iE(t-t')}\big[1-f_{R/L}(E)\big]. \end{aligned} \tag{1.97}$$

where the $f_{R/L}(E)$ is the Fermi distribution given in Eq. (1.53) for the right and left movers respectively.

The first contribution in Eq. (1.95) is given by fluctuations of current in each single channel, while the second one encodes the effects of interplay between the two edge

channels. By exploiting both lines in Eq. (1.97), a straightforward calculation shows that this last contribution is given by

$$2(ev_F\mathsf{T})^2\int_{-\frac{\mathcal{T}}{2}}^{+\frac{\mathcal{T}}{2}}dt\int_{-\infty}^{+\infty}dt'\sum_{r=L,R}\mathcal{G}^{(e)}_{F,r}(t,t')\mathcal{G}^{(h)}_{F,r}(t,t')=4\mathsf{T}^2\frac{e^2}{2\pi}(k_BT). \tag{1.98}$$

The second contribution is strongly dependent on the type of configurations chosen for the voltage drive. In the following, we focus on the situation where a single voltage drive is turned on, namely

$$V_R(t)=V(t),\qquad V_L(t)=0. \tag{1.99}$$

here $V(t)=V_{\rm DC}+V_{\rm AC}(t)$, with $V_{\rm AC}$ a generic function satisfying $\int_{-\mathcal{T}/2}^{+\mathcal{T}/2}\frac{dt}{\mathcal{T}}V_{\rm AC}(t)=0$ with period

$$\mathcal{T}=\frac{2\pi}{\Omega} \tag{1.100}$$

where Ω is the frequency of the drive. This configuration is called Hanbury-Brown-Twiss (HBT) set-up, in analogy with the HBT experiment performed with photons [104]. In this case, when a source of Levitons is applied to the reservoir, a stream of single electrons is partitioned against the QPC. The first experimental evidence of the existence of Levitons were reported by performing noise measurements in this kind of set-up [13]. A second configuration is given by the Hong-Ou-Mandel (HOM) set-up which will be studied in more details in the third Chapter. Here, we qualitatively describe the HOM set-up providing a comparison with its photonic counterpart. In this case, two identical trains of Levitons are generated and delayed by a tunable time shift δ, satisfying

$$V_R(t)=V(t)\qquad V_L(t)=V(t+\delta). \tag{1.101}$$

1.6.3 Hanbury-Brown-Twiss set-up

In the HBT set-up, the noise in Eq. (1.95) becomes

$$\begin{aligned}S^{HBT}=&-4\mathsf{T}^2\frac{e^2}{2\pi}(k_BT)+\\&-(ev_F)^2\,\mathsf{RT}\int_{-\frac{\mathcal{T}}{2}}^{+\frac{\mathcal{T}}{2}}dt\int_{-\infty}^{+\infty}dt'\left[\mathcal{G}^{(e)}_R(t,t')\mathcal{G}^{(h)}_{F,L}(t,t')+\mathcal{G}^{(e)}_{F,L}(t,t')\mathcal{G}^{(h)}_R(t,t')\right].\end{aligned} \tag{1.102}$$

In this configuration, the Green's functions for right-movers are

$$\mathcal{G}^{(e/h)}_R(t,t')=e^{\pm ie\int_t^{t'}d\tau V(\tau)}\langle\psi^{\dagger,(1)}_R(0,t)\psi^{(1)}_R(0,t')\rangle. \tag{1.103}$$

In order to conveniently deal with voltage phases, we introduce the following Fourier decomposition [105]

$$e^{-i\varphi_{\rm AC}(t)}=\sum_{l=-\infty}^{+\infty}p_le^{-il\Omega t} \tag{1.104}$$

where $\varphi_{\rm AC}(t)=e\int_0^t dt'V_{\rm AC}(t')$ is a function with period $\mathcal{T}$. Here, we have introduced the Fourier coefficients

$$p_l=\int_{-\frac{\mathcal{T}}{2}}^{+\frac{\mathcal{T}}{2}}dt\,e^{il\Omega t}e^{-i\varphi_{\rm AC}(t)}=\int_{-\frac{\mathcal{T}}{2}}^{+\frac{\mathcal{T}}{2}}dt\,e^{i(l+q)\Omega t}e^{-\varphi(t)} \tag{1.105}$$

where we defined q the number of particle emitted by $V(t)$ in a period as[12]

$$q = -\frac{e}{h}\int_{-\frac{\mathcal{T}}{2}}^{+\frac{\mathcal{T}}{2}} \frac{dt}{\mathcal{T}}\, V(t) = -\frac{eV_{\mathrm{DC}}}{\hbar\Omega}. \tag{1.106}$$

Equation (1.105) is the probability amplitude for particles to absorb ($l > 0$) or emit ($l < 0$) an energy $l\hbar\Omega$. This allows to interpret the discretization of energy shifts in terms of photons of the electromagnetic field generated by V_{AC}. This kind of energy transfers due to an AC drive are called photo-assisted processes and the coefficients are known as photo-assisted coefficients [105, 106].

By expressing $\mathcal{G}_R^{(e/h)}$ in the Fourier space, one has

$$\begin{aligned}
\mathcal{G}_R^{(e)}(t,t') &= \sum_{l,k} p_k^* p_l e^{-i(l+q)\Omega t'} e^{i(k+q)\Omega t} \int_{-\infty}^{+\infty} \frac{dE}{2\pi v_F}\, e^{iE(t-t')} f_R(E) \\
\mathcal{G}_R^{(h)}(t,t') &= \sum_{l,k} p_k p_l^* e^{i(l+q)\Omega t'} e^{-i(k+q)\Omega t} \int_{-\infty}^{+\infty} \frac{dE}{2\pi v_F}\, e^{iE(t-t')} f_R(E),
\end{aligned} \tag{1.107}$$

one can further simplify the expression in Eq. (1.102). The zero-frequency noise at finite temperature T due to a QPC with transmission T is

$$S^{HBT} = -4\mathsf{T}^2\frac{e^2}{2\pi}(k_B T) - 2\frac{e^2}{2\pi}\mathsf{RT}\sum_l |p_l|^2 (l+q)\hbar\Omega \coth\left(\frac{(l+q)\hbar\Omega}{2k_B T}\right). \tag{1.108}$$

The second contribution is called photo-assisted shot noise and carries information about the properties of the driving voltage due to the presence of the coefficients p_l. At zero temperature, the noise in Eq. (1.108) becomes

$$S^{HBT} = -S_0 \sum_l |p_l|^2 |l+q| \tag{1.109}$$

where we introduced $S_0 = 2(e^2/\mathcal{T})\mathsf{RT}$.

The noise in the HBT geometry was used by the group of D. C. Glattli at CEA Saclay in 2013 to provide the first experimental signatures of the correctness of Levitov's theoretical prediction [13] about the cleaness of the Lorentzian voltage pulses. In particular, they defined an excess noise

$$\Delta S = S^{HBT} - S_{\mathrm{DC}} \tag{1.110}$$

where S_{DC} is the noise due solely to V_{DC} (equivalent to set $p_l = \delta_{l,0}$) whose expression at finite temperature is

$$S_{\mathrm{DC}} = -2\frac{e^2}{2\pi}\mathsf{RT}(eV_{\mathrm{DC}})\coth\left(\frac{eV_{\mathrm{DC}}}{2k_B T}\right). \tag{1.111}$$

At zero temperature, the excess noise reads

$$\Delta S = -S_0 \sum_{l<-q} |p_l|^2 |l+q|. \tag{1.112}$$

This quantity can be experimentally probed and is actually connected to the number of unwanted particle-hole pairs generated by the drive. The key result is the following:

[12] Notice that this notation is the natural extension of Eq. (1.22) to the periodic case.

in a non-interacting system at zero temperature, the number of extra electron-hole pairs is directly proportional to the excess noise ΔS [9, 10]. Therefore, the excess noise ΔS has to vanish for Lorentzian pulses with integer q. From a mathematical point of view, this happens because the Lorentzian drive is the only possible pulse for which $p_l = 0$ for $l < -q$. It is worth noticing that all these considerations are the periodic equivalent of what described in Section 1.4.3 for a Lorentzian single pulse.

A vanishing excess noise was measured in the experiment, whose result is shown in Fig. 1.15. The plots show the excess noise as a function of q, for three kind of signals: a sine, a square wave and a Lorentzian drive. Since the experiment has been done at finite temperature, particle-hole pairs can also be thermally excited and this effect must be taken into account, as here we want to investigate whether such pairs are created as a consequence of the applied drive and not by thermal effect. It is possible to have an estimate of the thermally-excited pairs by generalizing Eq. (1.112) to finite temperatures. The dashed lines in the plots show the expected thermal contribution obtained in such a way. As we can see, the Lorentzian drive is the only one whose excess noise at integer q is entirely due to thermal contributions, this guarantees that no particle-hole pair is generated as an effect of the drive, thus confirming the minimal character of Levitons. The experiment also shows a clear hierarchy between the three different drives, with the square wave being the noisiest one.

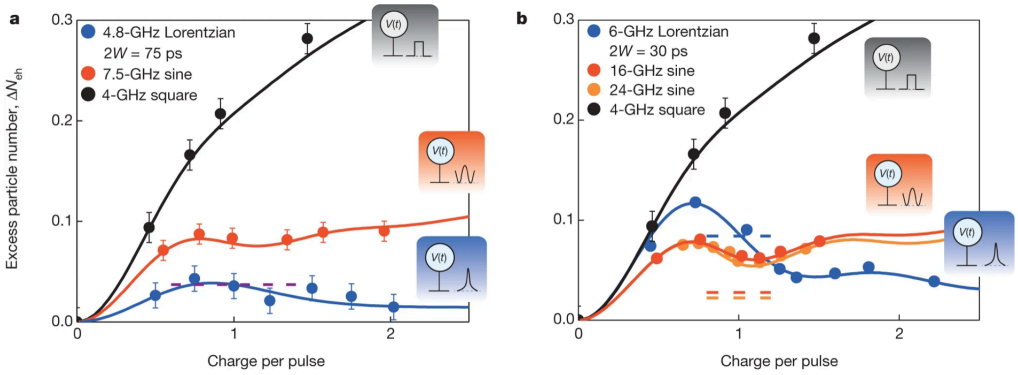

Figure 1.15: Experimental evidence for Levitons. Both panels show excess noise measurements for different kind of drives, as a function of the number of charges per period q. Dashed lines indicate the finite-temperature contribution to the excess noise and show that for a Lorentzian drive this is actually the only contribution, thus confirming the expected behavior of Levitons. Image taken from [13].

1.6.4 Hong-Ou-Mandel set-up

The historical HOM set-up consists in sending two photons on the two input channels of a beamsplitter, and measuring the coincidence rate at the two outputs. Referring to Fig. 1.13, the two outputs arms are 3 and 4 and $n_{3(4)}$ is the number of particles on arms 3 (4). When the time delay δ between arrivals of the photons at the beamsplitter is large, they are transmitted or reflected independently, and the coincidence rate reaches a steady value corresponding to the HBT result. However, when the photons arrive simultaneously at the splitter, they become sensitive to their exchange statistics. As photons are bosons, they tend to bunch and thus exit in the same output of the splitter. Consequently, the coincidence rate between the two outputs drops down to zero according to Eq. (1.88). Its measurement as a function of the time delay between

arrivals at the splitter, or equivalently the difference between the propagation lengths of the input arms, exhibits a so-called HOM dip (see Fig. 1.16 second column).

In the electronic analog of the HOM set-up, two electrons are aimed at a QPC through edge channels of the QH effect. When the time delay between arrivals at the QPC is large, the electrons are partitioned independently and exit in either one or the other output channel. But, when they reach the QPC simultaneously, their fermionic nature forbids them to be superimposed in the same state, in agreement with the Pauli principle. Indistinguishable electrons antibunch: the only possible outcome is to measure one electron in each output arm. For fermions, the coincidence count for indistinguishable particles would thus be doubled compared to the classical case. However, as single shot detection is not available yet for electrons, this antibunching is not probed by coincidence counts but rather by the low frequency fluctuations of the electrical current transmitted in the outputs. Indeed, the number of particles fluctuations $\langle \Delta n_3^2 \rangle = \langle \Delta n_4^2 \rangle$ directly reflect the electronic antibunching. In analogy with the HOM dip observed for bosons, a Pauli dip is expected for fermions (see Fig. 1.16 third column), albeit on a different quantity. According to this, the HBT experiment can be viewed as a peculiar case of HOM interferometry.

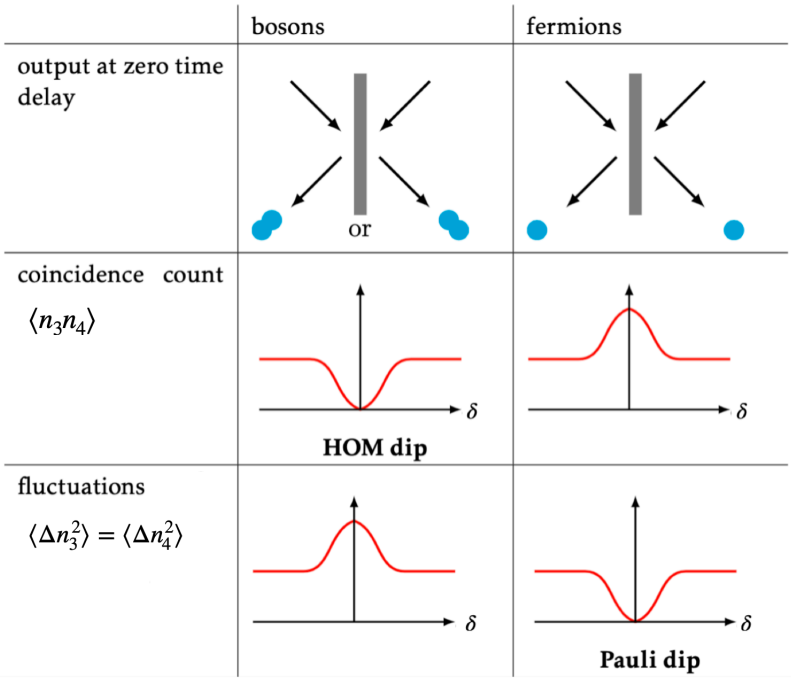

Figure 1.16: Sketch of an HOM experiment. Two indistinguishable particles are partitioned on a splitter. Coincidence counts $\langle n_3 n_4 \rangle$ and number of particles fluctuations $\langle \Delta n_3^2 \rangle$ are recorded as a function of the tunable delay δ. Indistinguishable bosons always exit in the same output, which results in the suppression of the coincidence rate (HOM dip) and the doubling of the fluctuations. An opposite behavior is expected for indistinguishable fermions: antibunching results in the doubling of the coincidence counts and the suppression of the number of particles fluctuations (Pauli dip).

Recalling the set-up in Fig. 1.14: two counter-propagating edge states meet at a QPC. A single electron emitter is connected to each incoming edge state, and single electrons can be injected with a controlled time difference δ in the two edge states. Each source can be alternatively switched off, so that the HBT noise produced by the

other source can be measured. In the HOM set-up, when both sources are on, the current correlations are measured at the two outputs of the QPC, as a function of the time difference between the two injections. The emission of a single electron and then a single hole is repeated periodically and consequently, by properly detuning one source with respect to the other, not only can the interference between two electrons be considered, but also the interference between one electron and one hole. This last case has no counterpart with photons: positive interferences (a peak rather than a dip) are obtained, which depend on the energy overlap between the electrons and holes, and which are strongly affected by temperature [107, 108].

Chapter 2

Switching on interactions

In the previous Chapter, we introduced the field of EQO in a regime where electron-electron interactions have been neglected, insofar as the propagation along the channels was assumed to be interaction free and dissipationless. However, due to their one-dimensional nature, quantum Hall edge channels are prone to emphasize interaction effects. This thesis aims at extending EQO studies to regimes where interaction effects are important. This Chapter is therefore dedicated to a presentation of interacting fermionic systems in 1D. After a general introduction to the bosonization procedure, we exploit the hydrodynamical Wen model. This allows us to deal with a large class of interacting QH states in both the integer and fractional regime. In particular, we will focus on two interacting QH edge channels and, finally, we will move towards a phenomenological approach to describe possible dissipative effects observed in recent experiments. From this Chapter to the end of the following thesis, we choose units in which $\hbar = k_B = 1$.

2.1 Introduction

Usually, in two and three dimensions, metals are well described by the Fermi liquid theory elaborated by L. Landau in the fifties [109, 110]. In this model the bare electrons are dressed by interactions and the problem can be described in terms of quasi-particles with renormalized parameters, which constitute the stable low-energy excitations of the system. These quasi-particles are essentially electrons dressed by density fluctuations around them and they interact very weakly with each other, even when the electron-electron Coulomb interaction is intense. This explains the success of Fermi liquid theory in describing several different materials.

However, in interacting 1D systems the Landau's theory fails. For example, in an 1D spinless lattice, with one electron on each site, the hopping of an electron from one site to the neighboring site forces every electron to jump forward. The Pauli principle forbids two electrons to be in the same state, thus each site can be at maximum singly occupied. Due to Coulomb repulsion, one electron hopping thus causes every other electrons hopping. Consequently, the only possible excitations in such a system are collective modes, which differ drastically from the original fermions.

During the fifties and sixties, new models to describe a 1D interacting electron gas were suggested by Tomonaga [111] and then Luttinger [112]. These models were then solved by Mattis and Lieb [113]. The underlying idea of those models is to linearize the spectrum in the vicinity of the Fermi energy. The new spectrum is then made out of two branches, corresponding to the electrons propagating towards opposite directions

along the 1D system.

The most striking feature of these models is that the elementary collective electron-hole excitations have a bosonic character. The Hamiltonian can then be expressed in terms of bosonic fields instead of the original fermionic ones. The point is that in this formulation the Hamiltonian is quadratic, which strongly simplifies the calculation of physical quantities. This technique is called bosonization. Later on, Haldane [114] showed that these models are way more general and can describe any 1D interacting fermions[1], as long as the spectrum respects a few conditions. Their validity has been verified in several instances, by observing exotic phenomena such as anomalous tunneling effects [115], spin-charge separation [116, 117] and charge fractionalization [118, 119, 120, 121] and the Tomonaga Luttinger Liquid (TLL) theory has been applied to a variety of systems, among which are carbon nanotubes, some organic conductors, or the edge states of the IQH and the FQH effects. In this latter examples, a direction of propagation is assigned to each edge state due to the magnetic field, and the Hamiltonian has only one branch. The TLL is then called chiral.

First, we will give a very brief introduction on the TLL theory, as many reviews are available [114, 122, 123, 124, 125]. The bosonization technique, which enables one to solve that model, will also be introduced. Finally, we will turn to the hydrodynamical model we use to describe the quantum Hall edge states.

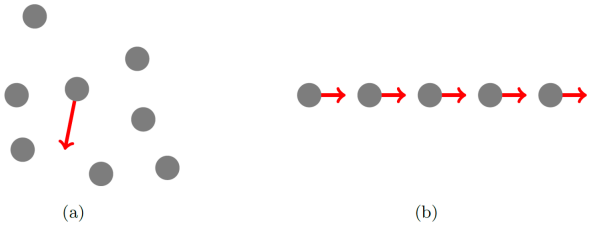

Figure 2.1: Comparison between interacting electrons in 1D and in higher dimensions. Left: in two or three dimensions, individual quasi-particle excitations are possible. Right: in 1D, the motion of an individual electron has an effect on all the others, thus resulting in a collective excitation. Image adapted from [125].

2.2 Tomonaga Luttinger liquid

Let us consider N spinless interacting fermions in a system of length L, subject to periodic boundary conditions. The Hamiltonian describing the system

$$H = H_0 + H_{int} \tag{2.1}$$

is composed of a free part

$$H_0 = \int_{-\frac{L}{2}}^{+\frac{L}{2}} dx\, \psi^\dagger(x)\varepsilon(-i\partial_x)\psi(x), \tag{2.2}$$

associated with the single particle spectrum $\varepsilon(k)$, and an interaction term

$$H_{\text{int}} = \int_{-\frac{L}{2}}^{+\frac{L}{2}} dx \int_{-\frac{L}{2}}^{+\frac{L}{2}} dy\, \psi^\dagger(x)\psi^\dagger(y)U(x-y)\psi(y)\psi(x), \tag{2.3}$$

[1]For sake of clarity, the bosonization can be used to describe both 1D bosonic and fermionic interacting systems [114].

$U(x-y)$ being the two-body interaction potential. In both previous formulas, $\psi(x)$ is a fermionic field operator annihilating an electron at position x as introduced in Section 1.4.3.

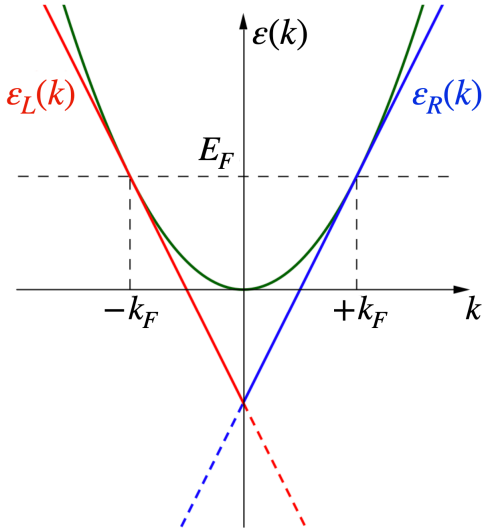

Figure 2.2: Linearization of the spectrum around the Fermi points $k = \pm k_F$. Starting from a generic dispersion (green curve), right (blue curve) and left (red curve) energy branches are obtained. Dashed lines indicate the addition of unphysical states, which naturally emerge in the bosonization technique.

2.2.1 Linearization of the spectrum

The explicit form of the dispersion relation $\varepsilon(k)$ is not very important, because the first key approximation of the Luttinger liquid model is to linearize the spectrum around the Fermi energy E_F, which is perfectly consistent in order to describe the low-energy physics of the system. The linearization procedure is sketched in Fig. 2.2 and defines the following two energy branches:

$$\varepsilon_r(k) = E_F + v_F(\xi_r k - k_F), \qquad v_F = \left.\frac{d\varepsilon}{dk}\right|_{k=k_F}, \tag{2.4}$$

with $r = R, L$, $\xi_{R,L} = \pm 1$ and k_F the Fermi momentum. In this way, two distinct fermionic species: right-moving electrons, with positive group velocity, and left-moving ones, with opposite group velocity. This is similar to what described in Section 1.2.1 however, for a generic 1D system, right and left movers are not spatially separated. At this stage the momentum k for the right (left) branch is restricted to positive (negative) values. However, in order for the bosonization technique to be applicable, the spectrum has to be unbounded [123]. Therefore, the second approximation of the model consists in extending the range of the momentum to $k \in (-\infty, +\infty)$ for both branches $\varepsilon_r(k)$. This operation introduces an infinite number of unphysical states, which are represented by the dashed lines in the spectrum of Fig. 2.2.

After the described procedure, the linearized free Hamiltonian becomes

$$H_0 = v_F \sum_{r=R,L} \int_{-\frac{L}{2}}^{+\frac{L}{2}} dx\, \psi_r^\dagger(x)\varepsilon(-i\xi_r\partial_x)\psi_r(x), \tag{2.5}$$

where the fields $\psi_r(x)$ annihilate an electron at position x on the branch r. These fields satisfy the canonical fermionic anticommutation relations

$$\begin{aligned} \{\psi_r(x), \psi'_r(x')\} &= \{\psi^\dagger_r(x), \psi^\dagger_{r'}(x')\} = 0 \\ \{\psi_r(x), \psi^\dagger_{r'}(x')\} &= \delta_{r,r'}\delta(x-x') \end{aligned} \tag{2.6}$$

and have the following plane-wave decomposition

$$\psi_r(x) = \frac{1}{\sqrt{L}} \sum_{k=-\infty}^{+\infty} e^{i\xi_r k x} c_{k,r}, \tag{2.7}$$

where the operator $c_{k,r}$ annihilates an electron with momentum $\xi_r k$ on the branch r. By exploiting this relation, H_0 is rewritten as

$$H_0 = v_F \sum_{r=R,L} \sum_{k=-\infty}^{+\infty} k c^\dagger_{k,r} c_{k,r}, \tag{2.8}$$

from which we immediately recognize that the expectation value of this operator on its ground state (all levels with energy below E_F filled) is divergent. This is an unphysical effect due to the introduction of an infinite number of negative-energy states and we can deal with this issue by considering normal ordered operators, obtained from the bare ones by subtracting their expectation value on a reference state, which is usually the ground state $|\mathrm{GS}\rangle$. For instance, the normal ordered number operator is

$$N_r = \sum_{k=-\infty}^{+\infty} :c^\dagger_{k,r} c_{k,r}: = \sum_{k=-\infty}^{+\infty} \left[c^\dagger_{k,r} c_{k,r} - \langle GS| c^\dagger_{k,r} c_{k,r} |GS\rangle\right] \tag{2.9}$$

and counts the number of electrons on the branch r, with respect to the ground state. In the same way, the expression for H_0 has to be normal ordered to obtain meaningful results in calculations.

2.2.2 Bosonization

The bosonization procedure consists in expressing the Hamiltonian and all other operators in terms of newly introduced bosonic operators. These operators will obey bosonic statistics, even though they are originally written using fermionic fields. According to this, the free Hamiltonian H_0 in Eq. (2.5) can be converted in a different but completely equivalent language, by using the bosonization identity [114, 123, 126], which expresses fermionic operators in terms of bosonic ones:

$$\psi_r(x) = \frac{F_r}{\sqrt{2\pi a}} e^{i\xi_r k_F x} e^{-i\phi_r(x)}. \tag{2.10}$$

Here, $a \sim k_F^{-1}$ is a short length cut-off, F_r are called Klein factors[2] and bosonic fields $\phi_r(x)$ are represented as[3]

$$\phi_r(x) = \frac{i}{\sqrt{L}} \sum_{q>0} \frac{e^{-aq/2}}{\sqrt{q}} \left(b_{q,r} e^{iq\xi_r x} - b^\dagger_{q,r} e^{-iq\xi_r x}\right) = \phi^\dagger_r(x) \tag{2.11}$$

[2] We are going to discuss their role in the following.

[3] From the exponential factor $e^{-aq/2}$ in Eq. (2.11), we see that the inverse of the cutoff, a^{-1}, plays the role of an upper bound to the momentum q associated with particle-hole pairs created by operators $b^\dagger_{q,r}$; see also Eq. (2.13).

with creation and annihilation operators satisfying

$$\begin{aligned}[b_{q,r}, b_{q',r'}] &= [b^\dagger_{q,r}, b^\dagger_{q',r'}] = 0 \\ [b_{q,r}, b^\dagger_{q',r'}] &= \delta_{q,q'}\delta_{r,r'}.\end{aligned} \tag{2.12}$$

They are related to the fermionic operators by

$$\begin{aligned}b^\dagger_{q,r} &= \sqrt{\frac{2\pi}{Lq}} \sum_{k=-\infty}^{+\infty} c^\dagger_{k+q,r} c_{k,r} \\ b_{q,r} &= \sqrt{\frac{2\pi}{Lq}} \sum_{k=-\infty}^{+\infty} c^\dagger_{k-q,r} c_{k,r}\end{aligned} \tag{2.13}$$

which show that $b^\dagger_{q,r}$ creates a superposition of particle-hole pairs with momentum q on the branch r. From the definition (2.11) and the commutators (2.12), the following commutation rules for fields $\phi_r(x)$ can be obtained

$$[\phi_r(x), \phi_{r'}(x')] = i\xi_r \pi \delta_{r,r'} \mathrm{sgn}(x - x'). \tag{2.14}$$

We now discuss the role of Klein factors F_r appearing in the bosonization identity (2.10). They are essential for a proper representation of fermionic fields in terms of bosonic ones. As a matter of fact, $\psi_r(x)$ removes an electron from the system, whereas $\phi_r(x)$ cannot modify the particle number because

$$\begin{aligned}[b^\dagger_{q,r}, N_r] &= \sqrt{\frac{2\pi}{Lq}} \sum_{k,k'} [c^\dagger_{k+q,r} c_{k,r} : c^\dagger_{k',r} c_{k',r} :] = \\ &= \sqrt{\frac{2\pi}{Lq}} \sum_{k,k'} \left(c^\dagger_{k+q,r} [c_{k,r}, c^\dagger_{k',r}] c_{k',r} + c^\dagger_{k',r} [c^\dagger_{k+q,r}, c_{k',r}] c_{k,r} \right) = \\ &= \sqrt{\frac{2\pi}{Lq}} \sum_{k} \left(c^\dagger_{k+q,r} c_{k,r} - c^\dagger_{k+q,r} c_{k,r} \right) = 0.\end{aligned} \tag{2.15}$$

This is why Klein factors are needed in (2.10). They are unitary operators, $F^\dagger_r F_r = F_r F^\dagger_r = \mathbb{1}$, which obey the algebra [125]

$$\begin{aligned}\left\{F_r, F^\dagger_{r'}\right\} &= 2\delta_{r,r'} \\ \left\{F_r, F_{r'}\right\} &= \left\{F^\dagger_r, F^\dagger_{r'}\right\} = 0 \qquad \text{for } r \neq r'\end{aligned} \tag{2.16}$$

and ensure that the canonical anticommutation relations (2.6) are satisfied. Moreover, Klein factors commute with operators $b_{q,r}$, $b^\dagger_{q,r}$ and

$$\left[F^\dagger_r, N_{r'}\right] = -\delta_{r,r'} F^\dagger_r \qquad [F_r, N_{r'}] = \delta_{r,r'} F_r, \tag{2.17}$$

showing that $F^\dagger_r$ (F_r) adds (remove) a particle to (from) the branch r. Notice, however, that they are not fermionic operators because $F^2_r \neq 0$. By using the above introduced machinery, we can rewrite all fermionic operators in a bosonized form. In what follows we focus on three of them which are particularly relevant.

Density operator The particle density operator of the branch r is defined as[4]

$$\rho_r(x) =: \psi_r^\dagger(x)\psi_r(x) : \tag{2.18}$$

By using Eq. (2.7) we can write

$$\begin{aligned}\rho_r(x) &= \frac{1}{L}\sum_{k,k'} : c_{k',r}^\dagger c_{k,r} : e^{i\xi_r(k-k')x} = \\ &= \frac{N_r}{L} + \frac{1}{L}\sum_{q>0}\sum_{k}\left(c_{k+q,r}^\dagger c_{k,r} e^{-iq\xi_r x} + c_{k-q,r}^\dagger c_{k,r} e^{iq\xi_r x}\right).\end{aligned} \tag{2.19}$$

Thus, from Eqs. (2.11) and (2.13), follows the representation in terms of the bosonic field $\phi_r(x)$

$$\rho_r(x) = \frac{N_r}{L} - \frac{\xi_r}{2\pi}\partial_x\phi_r(x) \tag{2.20}$$

which describes density fluctuations on top of a constant background term.

Free Hamiltonian The bosonization identity provides a new representation in terms of the Luttinger bosonic fields. It allows to re-write the kinetic Hamiltonian given by Eq. (2.22) in this new representation. But first, we compute the commutators of H_0 with the density operators on each branch

$$\left[H_0, \rho_r(k)\right] = \xi_r v_F k \rho_r(k). \tag{2.21}$$

Then, the free Hamiltonian H_0 can be written as [124, 125]

$$\begin{aligned}H_0 &= v_F \sum_{r=R,L}\int_{-\frac{L}{2}}^{+\frac{L}{2}} dx\ : \psi_r^\dagger(x)(-i\xi_r\partial_x)\psi_r(x) := \\ &= \frac{v_F}{4\pi}\sum_{r=R,L}\int_{-\frac{L}{2}}^{+\frac{L}{2}} dx\ : [\partial_x\phi_r(x)]^2 : + \frac{v_F\pi}{L}\sum_{r=R,L} N_r(N_r+1).\end{aligned} \tag{2.22}$$

The second term is usually referred to as the zero-mode contribution, while the first one is associated with bosonic excitations at fixed particle number. In the zero-mode part, the linear term in N_r can be reabsorbed in a shift of the chemical potential and will thus be dropped, yielding

$$H_0 = \frac{v_F}{4\pi}\int_{-\frac{L}{2}}^{+\frac{L}{2}} dx\left[(\partial_x\phi_R)^2 + (\partial\phi_L)^2\right]. \tag{2.23}$$

Thus, the kinetic part of the Hamiltonian is both quadratic and diagonal in terms of the bosonic fields. The problem becomes more interesting when interactions are taken into account.

Interaction Hamiltonian The purpose of the TLL theory is to deal with electron-electron interactions. The great advantage of the bosonization technique is that it allows to express the four-fermion-operator Hamiltonian (2.3) as a quadratic form of the bosonic fields. In particular, by assuming a point-like interaction potential

$$U(x-y) = U_0\delta(x-y), \tag{2.24}$$

[4] We use the notation $\rho_r(x)$ for the particle density operator in order to distinguish it from the charge density operator $\rho_r'(x) = -e\rho_r(x)$.

it can be shown that the only terms, for the present spinless case, are such that Eq. (2.3) becomes $H_{\text{int}} = H_2 + H_4$, where H_2 and H_4 are density-density couplings [123, 124, 125]:

$$\begin{aligned} H_2 &= g_2 \int_{-\frac{L}{2}}^{+\frac{L}{2}} dx \ :\rho_R(x)\rho_L(x):, \\ H_4 &= \frac{g_4}{2} \sum_{r=R,L} \int_{-\frac{L}{2}}^{+\frac{L}{2}} dx \ :[\rho_r(x)]^2: \ . \end{aligned} \tag{2.25}$$

Here, the notation for the coupling constants is chosen according to the conventional classification of interaction processes knows as the g-ology [125]. The two terms H_2 and H_4 describe inter- and intra-channel interactions respectively. By using the relation (2.20) into (2.25) and taking (2.22) into account, the complete Hamiltonian assumes the form

$$H = H_0 + H_2 + H_4 = H_N + H_B \tag{2.26}$$

with

$$H_N = \frac{v_F \pi}{L}\left[\left(1 + \frac{g_4}{2\pi v_F}\right) \sum_{r=R,L} N_r^2 + \frac{g_2}{v_F \pi} N_R N_L\right] \tag{2.27}$$

and

$$H_B = \int_{-\frac{L}{2}}^{+\frac{L}{2}} dx \left[\left(\frac{v_F}{2} + \frac{g_4}{4\pi}\right) \sum_{r=R,L} :[\partial_x \phi_r(x)]^2: + \frac{g_2}{2\pi} :\partial_x \phi_R(x) \partial_x \phi_L(x):\right]. \tag{2.28}$$

Here, H_B describes bosonic excitations, while H_N is the zero-mode Hamiltonian. As we can see, the intra-channel coupling g_4 simply results in a renormalization of the Fermi velocity and, in the absence of g_2, the model describes a system of free fermions with a velocity $v_F + g_4/(2\pi)$.

Just as the kinetic Hamiltonian in Eq. (2.23), the total Hamiltonian is quadratic in terms of the bosonic fields. This property is absolutely essential, insofar as it guarantees that it is diagonalizable. This can be done through a Bogoliubov transformation

$$\begin{pmatrix} \phi_R(x) \\ \phi_L(x) \end{pmatrix} = \begin{pmatrix} \cosh\gamma & \sinh\gamma \\ \sinh\gamma & \cosh\gamma \end{pmatrix} \begin{pmatrix} \phi_+(x) \\ \phi_-(x) \end{pmatrix}. \tag{2.29}$$

This is a canonical transformation and preserves the commutation rules of bosonic fields. By substituting Eq. (2.29) into (2.28), one finds that the condition for the Hamiltonian H_B to be diagonal with respect to the new fields $\phi_\pm$ is given by

$$\tanh 2\gamma = \frac{g_2}{2\pi v_F + g_4} \rightarrow \gamma = -\frac{1}{2}\ln K, \tag{2.30}$$

where we introduced the Luttinger parameter

$$K = \sqrt{\frac{2\pi v_F - g_2 + g_4}{2\pi v_F + g_2 + g_4}} \tag{2.31}$$

which measures the inteaction strength. Notice that in the case of free fermions one has $K = 1$, while for repulsive (attractive) interactions $K < 1$ ($K > 1$).

The Hamiltonian H_B in diagonal form reads

$$H_B = \frac{u'}{2} \sum_{\eta=\pm} \int_{-\frac{L}{2}}^{+\frac{L}{2}} dx : \left[\partial_x \phi_\eta(x)\right] : \tag{2.32}$$

where u' is a renormalized velocity

$$u' = \frac{1}{2\pi} \sqrt{(2\pi v_F + g_4)^2 - g_2^2} \tag{2.33}$$

which simplifies to $u' = v_F/K$ if $g_2 = g_4$. For completeness, we also diagonalize the zero mode term H_N in Eq. (2.27), even if it will be not considered for the forthcoming analysis. This is achieved by introducing the operators $N_\pm = N_R \pm N_L$, such that

$$H_N = \frac{\pi u'}{2L} \left(\frac{1}{K} N_+^2 + K N_-^2 \right). \tag{2.34}$$

2.3 Wen's hydrodynamical model

Until now, we have understood how to deal with TLL theory and, subsequently, how bosonization procedure works. However, throughout this thesis, we will consider the edge channels of the QH effect. Here, a simpler but equivalent way to understand the dynamics of the edge excitations is to use the hydrodynamical approach. In this approach, one use the fact that QH (IQH or FQH) states are incompressible irrotational liquid that contain no low energy bulk excitations. Therefore the only low lying excitations (below the bulk energy gap) are surface waves of the HQ droplet. These surface waves are identified as edge excitations of the QH state. This empirical model was developed by X.G. Wen in 1992 [127]. We will see that it can be mapped onto a TLL, with the peculiarity that its spectrum is only composed of one branch, instead of two.

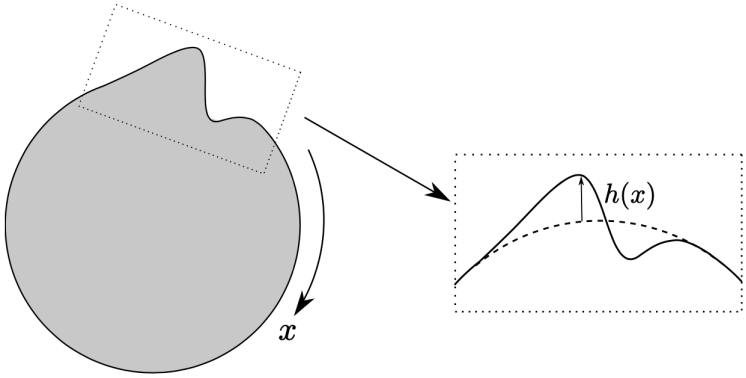

Figure 2.3: A quantum Hall fluid droplet. It undergoes deformations which propagate along the 1D boundary of the droplet.

In the hydrodynamical approach we first study the classical theory of the surface wave on the QH droplet. Then we quantize this model to obtain the quantum description of the edge excitations. It is amazing that the simple model obtained from the classical theory provides a complete description of the edge excitations at low energies.

2.3.1 Incompressibility of the QH fluid

Let us consider a QH liquid droplet. It is an incompressible fluid which has a fixed bidimensional electronic density n_e. In such a system, excitations are deformation waves which propagate along the edge in one direction (see Fig. 2.3). Thus the propagation is both one-dimensional and chiral. Let us note $h(x)$ the height of the deformation. The linear density along the edge is then defined as $\rho(x) = n_e h(x)$. Propagation is finally ruled by the continuity equation

$$\partial_t \rho - v\, \partial_x \rho = 0 \tag{2.35}$$

with v the propagation velocity of the excitations along the edge. The only contribution to the Hamiltonian is then the electrostatic term, that is to say the potential times the total charge

$$H = \frac{1}{2} \int_{-\frac{L}{2}}^{+\frac{L}{2}} dx\, V(x) e \rho(x). \tag{2.36}$$

When subject to the Hall effect, the electric field of a system is linked to the magnetic field by the relation

$$E = \frac{B}{e n_e} J \tag{2.37}$$

with J the current density. On the edge, one has $J = e n_e v$, and the previous relation becomes $E = vB$. Finally, the energy can be written as

$$\begin{aligned} H &= \frac{ev}{2} B \int_{-\frac{L}{2}}^{+\frac{L}{2}} dx\, h(x)\rho(x) \\ &= \frac{1}{2} \frac{evB}{n_e} \int_{-\frac{L}{2}}^{+\frac{L}{2}} dx\, \rho^2(x). \end{aligned} \tag{2.38}$$

This Hamiltonian is quadratic in terms of the electronic density. It is useful to recall the flux quantum, carried by each electron by surface unit, $\varphi_0 = h/e$ and that the filling factor ν is defined as the ratio between the electronic density and the flux quanta density from Eq. (1.7). Consequently, the Hamiltonian can be written using the filling factor rather than the electronic density, as

$$H = \frac{1}{2} \frac{hv}{\nu} \int_{-\frac{L}{2}}^{+\frac{L}{2}} dx\, \rho^2(x). \tag{2.39}$$

In the k-space the Hamiltonian reads

$$H = \frac{1}{2} \frac{hv}{\nu} \sum_k \rho(k)\rho(-k) \tag{2.40}$$

and the continuity relation in Eq. (2.35) becomes

$$\dot{\rho}(k) = -ivk\rho(k). \tag{2.41}$$

By comparing Eq. (2.41) with the standard Hamiltonian equations

$$\dot{q} = \frac{\partial H}{\partial p} \qquad \dot{p} = -\frac{\partial H}{\partial q} \tag{2.42}$$

we find that, if we identify $\rho(k > 0)$ as the generalized coordinate q, the corresponding canonical momenta can be identified as

$$p(k) = -i \frac{h}{\nu k} \rho(-k). \tag{2.43}$$

2.3.2 Quantization

Knowing the generalized coordinates and this canonically conjugate momentum, the classical theory can be quantized. We simply view $\rho(k)$ and $p(k)$ as canonically conjugate operators, which obey the commutation relation

$$\big[p(k), \rho(k')\big] = i\delta_{k,k'}. \tag{2.44}$$

Replacing $p(k)$ by its expression in Eq. (2.43) one gets the Kac-Moody algebra [128]

$$\begin{aligned} \big[\rho(k), \rho(k')\big] &= -\frac{\nu k}{2\pi}\delta_{k,-k'} \\ \big[H, \rho(k)\big] &= vk\rho(k), \end{aligned} \tag{2.45}$$

with $k, k' = s(2\pi)/L$ ($s \in \mathbb{Z}$). Notice that the second line of Eq. (2.45) is similar to Eq. (2.21). It is thus licit to apply the bosonization technique, described in Section 2.2.2, defining the bosonic field

$$\phi(x) = \frac{\pi}{\sqrt{\nu L}} \sum_k i \frac{e^{-a|k|/2}}{k} e^{-ikx} \rho(k). \tag{2.46}$$

Notice that Eq. (2.45) describes a collection of decoupled harmonic oscillators, generated by $\big(\rho(k), \rho(-k)\big)$. Thus, this is an one dimensional free phonon theory, with only a single branch of phonon, and it is exactly solvable providing a complete description of the low lying edge excitations of the QH state. The low lying charge excitations correspond to adding (removing) electrons to (from) the edge. Those charged excitations carry integer charges and are created by electron operators $\psi^\dagger$. The operator $\psi(x)$ can be expressed in terms of $\phi(x)$ as

$$\psi(x) = \frac{\mathcal{F}}{\sqrt{2\pi a}} e^{-i\frac{1}{\sqrt{\nu}}\phi(x)}. \tag{2.47}$$

In order to identify this as an electron operator we need to show that $\psi(x)$ is a fermionic operator. Using the Kac-Moody algebra (2.45) we find that

$$\psi(x)\psi(x') = (-1)^{\frac{1}{\nu}} \psi(x')\psi(x). \tag{2.48}$$

We see that the electron operator $\psi(x)$ is fermionic only when $1/\nu = m$ is an odd integer in which case the QH state is a Laughlin state [129] described in Section 1.2. This assumption is not generally true. We have assumed that the incompressible QH liquid contain only one component of incompressible fluid which leads to one branch of edge excitations. The above result implies that, when $\nu \neq 1/m$, the edge theory with only one branch do not contain fermionic operators and therefore it is not self consistent. We conclude that QH states with $\nu \neq 1/m$ may contain more than one branch of edge excitations [127, 129].

2.4 Theoretical model for filling factor $\nu = 2$

Thanks to the results derived in the previous Sections, we are now able to deal with interactions in the IQH regime. In this Section we present the TLL theory describing interactions in copropagating chiral channels based on bosonic collective excitations called Edge-MagnetoPlasmons (EMPs). The system we have in mind is sketched in

Fig. 2.4, representing the IQH state at filling factor $\nu = 2$ where two copropagating edge channels are present on each edge. This is useful since the majority of the EQO experiments have been performed at this filling factor, where, for a given carrier density, the QH effect is the most stable. In this state, two Landau levels are filled and, therefore, two channels are present at each edge of the sample. There is only one possible direction of propagation along the edges, which is determined by the sign of the applied orthogonal magnetic field B needed to bring the system in the IQH regime. The copropagating edge channels are spatially separated and we will refer to them as inner and outer channels. Since these channels are very close, Coulomb interaction among them is far from being negligible. It has indeed been proven experimentally [15] that the charges are fractionalized as a consequence of inter-edge coupling. The theory we are going to present was proposed in Ref. [130, 131, 132].

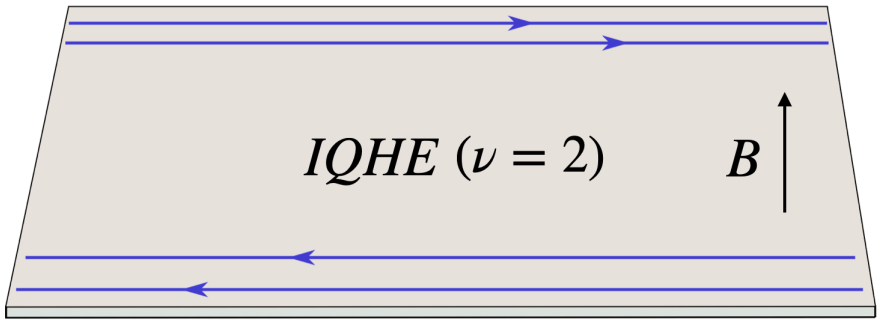

Figure 2.4: The IQH state at filling factor $\nu = 2$. Two chiral edge channels emerge at the edges of the sample, their propagation direction is determined by the sign of the applied magnetic field B. To fix the notation here, we place the right-moving channels on the upper edge.

2.4.1 The model and its diagonalization

Let us now discuss the model, which is based on the TLL theory discussed above. For the sake of simplicity, here we will just focus on a single edge: in particular, we describe the right-moving channels in the upper edge of Fig. 2.4. The starting point is the linear-dispersion Hamiltonian

$$H_0 = \sum_{j=1,2} v_j \int_{-\frac{L}{2}}^{+\frac{L}{2}} dx \ : \psi_j^\dagger(x)(-i\partial_x)\psi_j(x) :, \tag{2.49}$$

where the index $j = 1$ ($j = 2$) labels the inner (outer) channel on the edge and ψ is again the fermionic field operator annihilating an electron at position x on channel j. Moreover, the velocities v_j are assumed to be already renormalized by possible intra-channel density-density interactions. Next, we consider a density-density short-range inter-channel interaction term of the form

$$H_{\text{int}} = 2\pi u \int_{-\frac{L}{2}}^{+\frac{L}{2}} dx \ : \rho_1(x)\rho_2(x) : \tag{2.50}$$

where u is the coupling constant between the two channels and

$$\rho_j(x) =: \psi_j^\dagger(x)\psi_j(x) : \tag{2.51}$$

is the particle density operator on channel j. Notice that, the interaction term is introduced as a local capacitive coupling, via a Coulomb interaction, of the two edge channels. For this reason no net charge is transferred between copropagating channels as well observed in experiments [133].

As discussed in the previous Section (see Eq. (2.10)), bosonic fields $\phi_j(x)$ are introduced via the bosonization identity

$$\psi_j(x) = \frac{F_j}{\sqrt{2\pi a}} e^{ik_F x} e^{-i\phi_j(x)}. \tag{2.52}$$

Bosonic fields can be used to express the particle density operators, which become

$$\rho_j(x) = \frac{N_j}{L} - \frac{1}{2\pi}\partial_x \phi_j(x). \tag{2.53}$$

If we compare this expression with Eq. (2.20), we notice that here the sign is the same for both channels $j = 1, 2$, while a sign difference was present in the former case. This is because we are now dealing with copropagating channels. This difference is also reflected in the commutator

$$[\phi_j(x), \phi_{j'}(x')] = i\pi\delta_{j,j'}\mathrm{sgn}(x - x'), \tag{2.54}$$

where, again, the sign of the r.h.s. is the same for both values of j, unlike in (2.14).

The bosonized version of the full Hamiltonian $H = H_0 + H_{\mathrm{int}}$ reads

$$\begin{aligned} H = \frac{1}{4\pi}\int_{-\frac{L}{2}}^{+\frac{L}{2}} dx \; :\big\{ & v_1\big[\partial_x\phi_1(x)\big]^2 + v_2\big[\partial_x\phi_2(x)\big]^2 + \\ & + u\big[\partial_x\phi_1(x)\partial_x\phi_2(x) + \partial_x\phi_2(x)\partial_x\phi_1(x)\big]\big\} : \end{aligned} \tag{2.55}$$

where the off-diagonal terms are obtained directly by substituting (2.53) into (2.50), while the diagonal ones follow from the bosonized form (2.22) discussed in the previous Sections. The Hamiltonian can be straightforwardly diagonalized by the following transformation

$$\begin{pmatrix} \phi_\rho(x) \\ \phi_\sigma(x) \end{pmatrix} = \begin{pmatrix} \cos\theta & \sin\theta \\ -\sin\theta & \cos\theta \end{pmatrix} \begin{pmatrix} \phi_1(x) \\ \phi_2(x) \end{pmatrix}, \tag{2.56}$$

which introduces two new bosonic fields $\phi_{\rho,\sigma}(x)$ satisfying the commutation relations

$$[\phi_\eta(x), \phi_{\eta'}(x')] = i\pi\delta_{\eta,\eta'}\mathrm{sgn}(x - x') \qquad (\eta = \rho, \sigma). \tag{2.57}$$

The parameter θ is called the mixing angle and it is determined by the requirement that the Hamiltonian is diagonal in the basis of the new fields. This leads to the equation

$$\tan 2\theta = \frac{2u}{v_1 - v_2}. \tag{2.58}$$

The mixing angle ranges in $\theta \in [0, \pi/4]$; in the non-interacting case $\theta = 0$ and $\phi_{1,2}(x) = \phi_{\rho,\sigma}(x)$ so the two edge channels do not mix, as expected. On the contrary, the maximal mixing is achieved at $\theta = \pi/4$, which is usually referred to as the strongly interacting limit and seems to be the relevant case in different experimental implementations [2, 102, 134]. However, the stability of the model, namely, the request that both eigenvelocities are positive [135], imposes a constraint on the maximum admissible value of u, therefore, strictly speaking this limit can be properly obtained

only for $v_1 = v_2$ by keeping u fixed [136]. Experimentally, values of θ ranging from $\theta \approx \pi/6$ [133, 137] to $\pi \approx \pi/4$ [15] have been reported, indicating that this parameter strongly depends on the specific details of the considered set-ups.

The Hamiltonian in diagonal form reads

$$H = \frac{1}{4\pi} \sum_{\eta=\rho,\sigma} v_\eta \int_{-\frac{L}{2}}^{+\frac{L}{2}} dx \; :[\partial_x \phi_\eta(x)]^2 :, \tag{2.59}$$

where the renormalized velocities are given by

$$\begin{aligned} v_{\rho,\sigma} &= \frac{v_1 + v_2}{2} \pm \frac{1}{\cos 2\theta} \left(\frac{v_1 - v_2}{2} \right) = \frac{v_1 + v_2}{2} \pm \frac{u}{\sin 2\theta} \\ &= \frac{1}{2} \left[v_1 + v_2 \pm \sqrt{(v_1 - v_2)^2 + 4u^2} \right]. \end{aligned} \tag{2.60}$$

Here $v_\rho > v_\sigma$, so the Hamiltonian (2.59) describes slow and fast bosonic modes, propagating at velocities v_σ and v_ρ respectively. Moreover, from the chirality of the system, we have the constraint $v_{\rho,\sigma} > 0$ as all excitations must propagate in the right direction. This gives the following bound on the inter-channel coupling strength [135]

$$u \leq \sqrt{v_1 v_2}. \tag{2.61}$$

This relation further strengthen the previous comment about the strongly interacting limit ($\theta = \pi/4$): it is a situation which cannot arise from an arbitrarily strong inter-channel interaction and, for this reason, we prefer to refer to it as maximal mixing. In the following, for notational convenience and without loss of generality, we will consider $v_2 = v$ and $v_1 = \alpha' v$ (with $\alpha' > 1$) so that Eq. (2.60) can be rewritten as

$$v_{\rho/\sigma} = v f'_{\rho/\sigma}(\alpha', \theta) = v \left[\left(\frac{\alpha' + 1}{2} \right) \pm \frac{1}{\cos(2\theta)} \left(\frac{\alpha' - 1}{2} \right) \right]. \tag{2.62}$$

2.4.2 Edge-magnetoplasmon scattering matrix

Let us now discuss the physics of two edge channels capacitively coupled along a finite region of length L. In order to describe this situation, one can proceed as in Refs. [131, 138, 139], where the edge channels are divided into three parts: a non-interacting injection region, an interacting propagating region, and a non-interacting region of detection (see Fig. 2.5). Notice that this separation is not an oversimplification of the problem. Indeed, the chirality guarantees that the interacting region can be made arbitrarily close both to the injection and the detection regions without loss of generality.

In the incoming region, where no interactions occur (*i.e.* $u = 0$), the Hamiltonian can be written in terms of Wen's hydrodynamical model

$$H^{(1)} = \sum_{j=1,2} \frac{v_j}{4\pi} \int_{-\infty}^{+\frac{L}{2}} dx \left[\partial_x \phi_{j,in}(x) \right]^2. \tag{2.63}$$

Therefore, the chiral bosonic fields are related to the charge density along each channel according to the conventional prescription in Eq. (2.53). These bosonic fields propagate freely according to the equation of motion deduced from Eq. (2.63)

$$(\partial_t + v_j \partial_x) \phi_{j,in}(x,t) = 0. \tag{2.64}$$

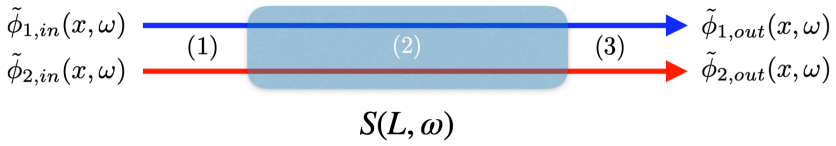

Figure 2.5: Model for a QH edge state at filling factor $\nu = 2$. According to the chirality, one can identify the incoming (injection) region (1), the interacting region (2) (shaded area of length L), and the outgoing (detection) region (3). In regions (1) and (3), the dynamics of the bosonic fields are well described in terms of free equations of motion ($u = 0$). Moreover, the outgoing fields, written in the Fourier space ($\tilde{\phi}_{j,out}(x,\omega)$ with $j = 1, 2$), are connected to the incoming ones ($\tilde{\phi}_{j,in}(x,\omega)$) through the EMP scattering matrix $S(L,\omega)$, which encodes the information of the inter-channel interaction acting over a length L and at a given frequency (energy) ω.

By moving into Fourier transform with respect to time, they become

$$(-i\omega + v_j\partial_x)\tilde{\phi}_{j,in}(x,\omega) = 0, \tag{2.65}$$

with $\tilde{\phi}_{j,in}(x,\omega)$ are the field amplitudes in the frequency space defined as

$$\tilde{\phi}_j(x,\omega) = \int_{-\infty}^{+\infty} d\omega\, e^{i\omega t}\, \phi_j(x,t). \tag{2.66}$$

In the interacting region, the Hamiltonian is the one in Eq. (2.59). According to the discussion in Section 2.4.1, the bosonic fields $\phi_{1/2}$ are no longer eigenstates of the Hamiltonian, and the system is diagonalized in terms of two new modes $\phi_{\rho/\sigma}$. In this case, the equations of motion are

$$(\partial_t + v_\eta\partial_x)\phi_\eta(x,t) = 0, \tag{2.67}$$

with $\eta = \rho, \sigma$. Again, by doing a Fourier transform in time, the previous equations become

$$(-i\omega + v_\eta\partial_x)\tilde{\phi}_\eta(x,\omega) = 0. \tag{2.68}$$

Then, the solution of the equations of motion in this region reads

$$\tilde{\phi}_\eta(x,\omega) = e^{i\frac{\omega}{v_\eta}x}\tilde{\phi}_\eta(0,\omega) \tag{2.69}$$

where, following the rotation (2.56), in the frequency space we have

$$\begin{aligned}\tilde{\phi}_\rho(0,\omega) &= \cos\theta\,\tilde{\phi}_{1,in}(0,\omega) + \sin\theta\,\tilde{\phi}_{2,in}(0,\omega)\\ \tilde{\phi}_\sigma(0,\omega) &= -\sin\theta\,\tilde{\phi}_{1,in}(0,\omega) + \cos\theta\,\tilde{\phi}_{2,in}(0,\omega)\end{aligned} \tag{2.70}$$

and the, possibly frequency-dependent, amplitudes are achieved by imposing the continuity of the fields at $x = 0$ which is the boundary between regions (1) and (2).

Analogously to what was discussed for region (1), in the outgoing region the inter-channel interaction is negligible and the equations of motion are written as in Eq. (2.64). Here, imposing the continuity of the fields at the boundary between regions (2) and (3) in $x = L$, we observe that the outgoing field amplitudes are related to the incoming ones through the relations

$$\begin{aligned}\tilde{\phi}_{1,out}(0,\omega) &= \cos\theta\,\tilde{\phi}_\rho(0,\omega) - \sin\theta\,\tilde{\phi}_\sigma(0,\omega)\\ \tilde{\phi}_{2,out}(0,\omega) &= \sin\theta\,\tilde{\phi}_\rho(0,\omega) + \cos\theta\,\tilde{\phi}_\sigma(0,\omega).\end{aligned} \tag{2.71}$$

According to this analysis and proceeding as in [139], we obtain the EMP scattering matrix connecting the incoming (injected) and the outgoing (detected) bosonic fields, namely

$$\begin{pmatrix} \tilde{\phi}_{1,out}(L,\omega) \\ \tilde{\phi}_{2,out}(L,\omega) \end{pmatrix} = S(L,\omega) \begin{pmatrix} \tilde{\phi}_{1,in}(0,\omega) \\ \tilde{\phi}_{2,in}(0,\omega) \end{pmatrix}, \tag{2.72}$$

with

$$S(L,\omega) = \begin{pmatrix} \cos^2\theta e^{i\omega\tau_\rho} + \sin^2\theta e^{i\omega\tau_\sigma} & \sin\theta\cos\theta\left(e^{i\omega\tau_\rho} - e^{i\omega\tau_\sigma}\right) \\ \sin\theta\cos\theta\left(e^{i\omega\tau_\rho} - e^{i\omega\tau_\sigma}\right) & \sin^2\theta e^{i\omega\tau_\rho} + \cos^2\theta e^{i\omega\tau_\sigma} \end{pmatrix}, \tag{2.73}$$

having introduced the short-hand notation

$$\tau_{\rho,\sigma} = \frac{L}{v_{\rho,\sigma}} \tag{2.74}$$

for the times of flight associated with the propagation velocity of the charge and dipolar eigenmodes along the interacting region.

2.4.3 Charge fractionalization

A charge fractionalization process is predicted to occur in copropagating channels as a consequence of the interaction [16, 140, 141]. In order to understand how this comes from, we recall Eqs. (2.72) and (2.73) of the previous Section. By explicitly writing the outgoing bosonic fields in terms of the incoming one, in the time domain, we have

$$\begin{aligned} \phi_{1,out}(L,t) &= \cos^2\theta\,\phi_{1,in}(0,t-\tau_\rho) + \sin^2\theta\,\phi_{1,in}(0,t-\tau_\sigma) + \\ &+ \sin\theta\cos\theta\big[\phi_{2,in}(0,t-\tau_\rho) - \phi_{2,in}(0,t-\tau_\sigma)\big] \\ \phi_{2,out}(L,t) &= \sin\theta\cos\theta\big[\phi_{1,in}(0,t-\tau_\rho) - \phi_{1,in}(0,t-\tau_\sigma)\big] + \\ &+ \sin^2\theta\,\phi_{2,in}(0,t-\tau_\rho) + \cos^2\theta\,\phi_{2,in}(0,t-\tau_\sigma). \end{aligned} \tag{2.75}$$

In order to visualize the charge fractionalization, consider now an electron injected only in the inner channel 1. The outgoing fields are then rewritten as

$$\begin{aligned} \phi_{1,out}(L,t) &= \cos^2\theta\,\phi_{1,in}(0,t-\tau_\rho) + \sin^2\theta\,\phi_{1,in}(0,t-\tau_\sigma) \\ \phi_{2,out}(L,t) &= \sin\theta\cos\theta\big[\phi_{1,in}(0,t-\tau_\rho) - \phi_{1,in}(0,t-\tau_\sigma)\big]. \end{aligned} \tag{2.76}$$

From these equations it is clear that, as a result of the interaction between the edge channels, two new different bosonic excitations propagate at different velocities on both the outer and the inner channel. They carry a fraction of the initial electron charge, which can be read directly from Eq. (2.76)

$$\begin{aligned} f_{1,\rho} &= \cos^2\theta \qquad & f_{1,\sigma} &= \sin^2\theta, \\ f_{2,\rho} &= \frac{\sin 2\theta}{2} \qquad & f_{2,\sigma} &= -\frac{\sin 2\theta}{2}. \end{aligned} \tag{2.77}$$

Here, $f_{j,\eta}$ denotes the fraction carried by the excitation propagating at velocity v_η on channel j. The above equations correctly reproduce the non-interacting limit when $\theta = 0$, in which case we have $f_{1,\rho} = 1$ and $f_{1,\sigma} = f_{2,\rho/\sigma} = 0$, as expected because the channels are decoupled. It is worth noting that $f_{1,\sigma} + f_{1,\rho} = 1$ for every value of the mixing angle. This is of course due to charge conservation, because these excitations originate from the electron injected at $x = x_0$. Likewise, $f_{2,\rho} = -f_{2,\sigma}$, meaning that no net charge is transferred from the outer to the inner channel. Indeed, the two channels

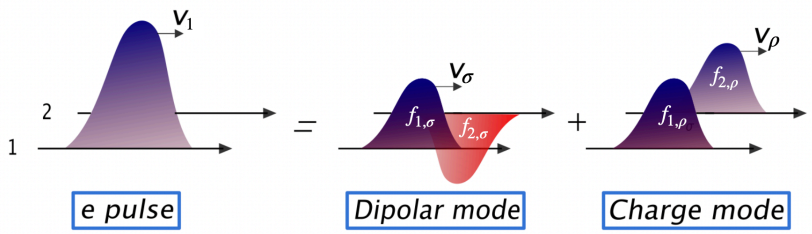

Figure 2.6: Charge fractionalization in copropagating channels for maximal coupling $\theta = \pi/4$. An electron injected into the inner channel at position x_0 splits into fractional excitations, propagating in the same direction (due to the chirality of the system) but with different velocities.

are capacitively coupled via Coulomb interactions, which cannot lead to a variation of the particle number on each channel.

We also note that at maximal mixing ($\theta = \pi/4$) the injected electron splits into two identical excitations as the fractionalization factors for the inner channel reduce to $f_{1,\rho} = f_{1,\sigma} = 1/2$. Moreover, the situation is the same also on the outer channel: $f_{2,\rho/\sigma} = \pm 1/2$. As a consequence, the mode made of the two fast excitations (those propagating with velocity v_ρ) has exactly the same charge as the injected electron, while the slow mode (made of the two excitations propagating at v_σ) carries no charge. This is why in the literature it is common to encounter the terms charged and neutral modes [15], or dipolar if the coupling is not maximal, associated with fractionalization in integer quantum Hall channels: they refer precisely at the scenario depicted in Fig. 2.6 at the mixing angle $\theta = \pi/4$. Last, but not least, evidence for the presence of fractional charges in copropagating quantum Hall channels has been recently reported by different groups [15, 134, 137, 142], demonstrating that the LL theory for copropagating quantum Hall edge states is successful in explaining experimental results [143].

2.5 Dissipative effects in integer quantum Hall edge channels

As stated in the first Chapter, the 1D, chiral edge channels of the QH effect are a promising platform in which to implement EQO experiments. In Section 2.4, we have dealed with interactions for a QH sample with filling factor $\nu = 2$ through a bosonization approach. However, interactions between the two edge channels and the external environment have been shown to lead to decoherence as well as energy relaxation [131, 138, 144] for the injected particle. Such dissipation effects are crucial in order to properly describe both the dynamics of integer QH states [145] and the evolution of the peak height of energy-resolved wave-packets injected into them [133]. Remarkably enough, the predicted functional form of the dissipation as a function of the energy seems to depend on the considered set-up. Therefore, the subject of the dominant microscopic dissipation processes at different propagation lengths is still an open issue and a more detailed analysis is needed in order to improve our understanding of this topic.

In this Section, we want to tackle this subject and to do so we refer to Ref. [146]. Assuming a phenomenological approach, we start from the hydrodynamic model, pre-

viously introduced, where the two edge channels are capacitively coupled through a short-range interaction. In addition, we compare two possible phenomenological dissipation regimes: an ohmic dissipation linear in the injection energy of the electronic wave-packet and a quadratic dissipation. We observe that the linear dependence provides the best fit for the experimental data of the evolution of the experimental peak height at small enough propagation lengths [133]. Conversely, at greater propagation lengths, a dissipation quadratic in the injection energy dominates [145].

2.5.1 Dissipative effects on the elastic scattering amplitude

Experimental observations [133, 145] suggest a relevant role played by energy dissipation towards additional degrees of freedom in the transport along QH edge channels. The simplest way to phenomenologically include this effect is by adding a real frequency-dependent energy loss rate $\gamma(\omega)$ (assumed here to be equal for both channels for the sake of simplicity) at the level of the equations of motion in the interacting region (see Eq. (2.68)). According to this, they become

$$\big(-i\omega\gamma(\omega)+v_\eta\partial_x\big)\tilde{\phi}_\eta(x,\omega)=0. \tag{2.78}$$

Due to this additional contribution, the solution of the equations of motion acquires a frequency-dependent damping

$$\tilde{\phi}_\eta(x,\omega)=e^{i[\omega+i\gamma(\omega)]\frac{x}{v_\eta}}\tilde{\phi}_\eta(0,\omega) \tag{2.79}$$

and, consequently, the dissipative effects are taken into account in the scattering matrix of Eq. 2.73 by substituting $\omega\to(\omega+i\gamma(\omega))$. In the following we will focus only on the top left entry of the scattering matrix in Eq. (2.73), which represents the amplitude probability for the EMP to be transmitted along the first channel (assumed as the injection/detection channel), namely

$$t(\omega)=\cos^2\theta e^{i[\omega+i\gamma(\omega)]\tau_\rho}+\sin^2\theta e^{i[\omega+i\gamma(\omega)]\tau_\sigma}. \tag{2.80}$$

Moreover, we will analyze three possible behaviours for $\gamma(\omega)$: a non-dissipative case $\gamma=0$ (discussed in Section 2.4.3), a linear dissipation case $\gamma(\omega)=\gamma_1\omega$ (γ_1 real adimensional parameter) [135], and a dissipation quadratic in the energy $\gamma(\omega)=\gamma_2\omega^2$ (γ_2 real parameter with the dimension of a time) [145]. Notice that this additional dissipation parameter can be phenomenologically accounted for by adding an imaginary term to the EMP velocities [147].

In order to catch the effects of dissipation on the evolution of the peak height of energy-resolved electronic wave-packets propagating along the two QH edge channels, we study the elastic scattering amplitude for the fermionic excitations evaluated at different injection energies. As we will show later, our theoretical results [146] are compared to the experimental data of Ref. [133].

As discussed in Ref. [144], assuming a very peaked (ideally δ-like) injected wave-packet in energy, the relative height of this peak as a function of the energy is given, at zero temperature, by

$$\mathcal{V}(\varepsilon)=\frac{|\mathcal{Z}(\varepsilon)|^2}{|\mathcal{Z}(0)|^2} \tag{2.81}$$

with

$$\mathcal{Z}(\varepsilon)=\int_{-\infty}^{+\infty}d\tau\, e^{i\varepsilon\tau}\exp\left\{\int_0^{+\infty}\frac{d\omega}{\omega}\big[t(\omega)e^{-i\omega\tau}-1\big]e^{-\omega/\omega_c}\right\} \tag{2.82}$$

which is the elastic scattering amplitude (see Appendix B for more details of the calculation). The converging factor ω_c, corresponding to the greatest energy scale in the systems, is sent to $\omega_c \to +\infty$ for our purposes.

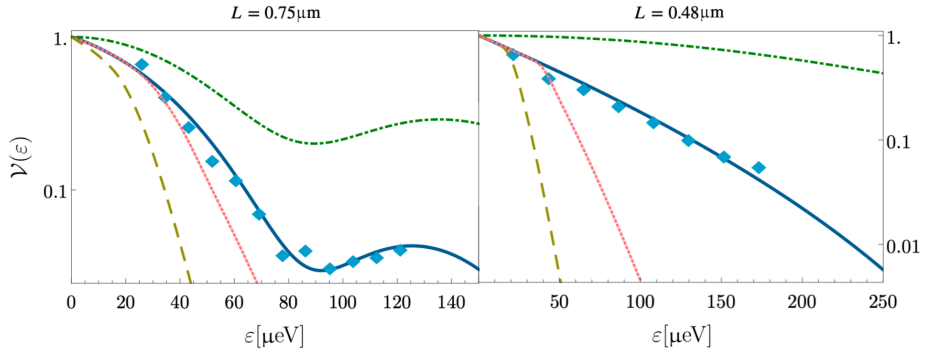

Figure 2.7: Relative peak height as a function of the injection energy (measured in μeV) for two samples of different lengths: $L = 0.75\mu$m (left panel) and $L = 0.48\mu$m (right panel). The non-dissipative case (green dash-dotted curve); the linear dissipative case (blue full curve) with $\gamma_1 = 0.13$ for the left panel and $\gamma_1 = 0.43$ for the right panel; quadratic dissipation with $\gamma_2\varepsilon_0 = 0.03$ for both panels (red dotted curve) and with $\gamma_2\varepsilon_0 = 0.13$ for the left panel and $\gamma_2\varepsilon_0 = 0.23$ for the right one (bronze dashed curve). Recalling Eq. (2.62), other parameters are: $\alpha' = 2.1$, $v = 4 \times 10^4$ m/s and $\theta = 0.17\pi$ (left panel) and $\alpha' = 1.6$, $v = 5 \times 10^4$ m/s and $\theta = 0.16\pi$ (right panel). Light-blue diamonds indicate the experimental data taken from Ref. [133].

In Fig. 2.7, we show the relative peak height $\mathcal{V}(\varepsilon)$ versus the injection energy ε for two different cases corresponding to experimental length, such that $L < 1\mu$m, and for various possible dissipations behaviors. The analytical expressions for $\mathcal{V}$ are given in Appendix B. In both panels, the parameters for the three different dissipative regimes are fixed in order to compare the theoretical expressions with the experimental data (light-blue diamonds). In absence of energy losses towards external degrees of freedom ($\gamma(\omega) = 0$ and dash-dotted green line), the curve stays above the experimental data due to the absence of exponential overall decay. The observed behavior is better explained through a linear dissipation model ($\gamma(\omega) = \gamma_1\omega$ and blue full line). The quadratic dissipation cases considered strongly deviate from the experimental situation because the decay of the relative peak height is more pronounced than the linear one. The discrepancy with the experimental data is more evident for strong dissipation (brown dashed curve) than with weak dissipation (red dotted line). It is interesting to notice that for small values of ε both the two dissipation behavior approach the data. According to these observations, the linear dissipation model can be considered as the best candidate for describing the experimental data, at least in this case of relatively short propagation lengths $L < 1\,\mu$m. It is worth remarking that different experiments [145] carried out in a regime of longer propagation lengths $L > 3\,\mu$m require a quadratic dissipation to properly reconcile theory and experiments.

Chapter 3

Collisional interferometry of levitons in interacting quantum Hall edge channels

In this Chapter, we study a HOM interferometer for Lorentzian voltage pulses applied to quantum Hall edge channels in the IQH regime at filling factor $\nu = 2$, in the presence of interactions between the two edge channels. Based on what discussed in Sec. 2.4.3, we expect that the injected electronic wavepackets fractionalize before partitioning at a QPC. Remarkably enough, differently from what was theoretically predicted and experimentally observed by using other injection techniques [108, 134, 148], we demonstrate that when the injection occurs through time-dependent voltage pulses arbitrarily shaped, the HOM noise signal always vanishes for a symmetric device and that a mismatch in the distances between the injectors and the point of collision is needed to reduce the visibility of the dip. Finally, we also show that by properly tuning these distances or by applying different voltages on the two edge channels in each arm of the interferometer, it is possible to estimate the intensity of the interedge interaction. The material presented in this Chapter includes our original findings discussed in Ref. [149].

3.1 Context

As introduced in the previous Chapter, the EQO experiments are mainly carried out in QH edge channels at filling factor $\nu = 2$ (or higher), where interchannel interactions cannot be neglected [15]. The effect of electron-electron interaction emerges dramatically in HOM experiments realized with a driven mesoscopic capacitor in the nonadiabatic regime [107, 150, 151], where the visibility of the predicted dip in the autocorrelated noise as a function of the injection delay, a signature of the antibunching of electrons (see Section 1.6.4), is strongly reduced [108, 134, 148].

In Ref. [148], A. Marguerite and coworkers have used the HOM experiment to analyze quantitatively the decoherence of a single electron along its propagation within the outer edge channel of the IQH sample at filling factor $\nu = 2$ and to demonstrate how EQO techniques provide a powerful probe to investigate strong interaction effects in ballistic conductors. Following the experimental set-up in Fig. 3.1(a) two mesoscopic capacitors are used for the injection of controlled electrons into the channels. Both sources are approximately equally distant from the QPC ($L \approx 3\,\mu$m).

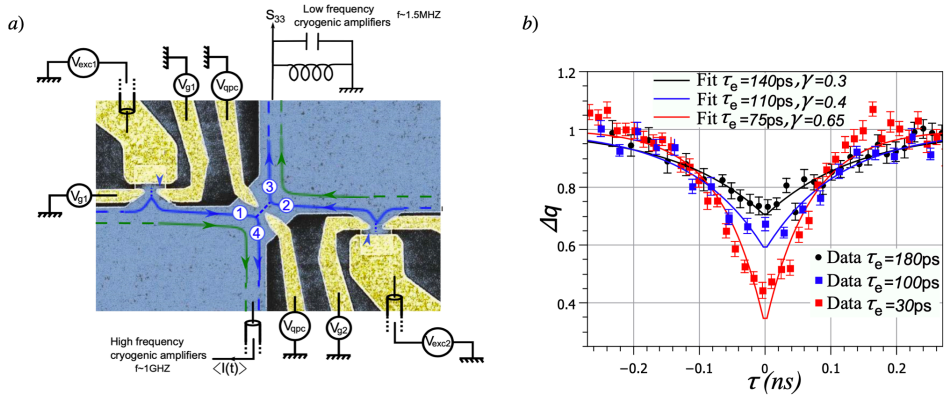

Figure 3.1: (a) HOM interferometry: modified scanning electronic microscope picture of the sample. The 2DEG is represented in blue, the edge channels by blue (outer channel) and green (inner channel) lines, metallic gates are in gold. The emitters inject particles in channels 1 and 2. (b) HOM experiment: HOM noise signal Δq as a function of the time delay between the sources τ for three values of the emission time τ_e. With respect to Chapter 1, we have that the time delay $\tau = \delta$ and the emission time $\tau_e = \gamma/2$. Figures taken from [148].

Figure 3.1(b) presents the HOM noise for three values of the source emission time which sets the temporal size of the emitted wavepackets (see Eq. (1.20)). A dip is observed for three curves around syncronized emission (*i.e.* $\tau = 0$), revealing the reduction of random partition noise by two electron interferences. Moreover, the width of the dip increases by increasing the escape time corresponding to progressively wider wavepackets. Surprisingly, none of the dips reaches the full suppression showing the failure of the free electron picture based on the collision of perfectly indistinguishable wavepackets (see Setion 1.6.4).

Several possibilities could have been envisioned in order to explain the reduction in the dip's minimum. A first hypothesis is that the emission of undistinguishable electrons is prevented by differences between the two sources, either from sample construction or related to environmental noise leading to random fluctuations in the energy at which electrons are emitted [152]. In a second hypothesis, the contrast reduction could be related to an energy dependence of the beamsplitter reflection [153]. However, authors identify the inter-channel Coulomb interaction as the dominant source of such reduction. Indeed, Coulomb interaction leads to decoherence [108, 138] along propagation as the quasiparticle gets entangled with the neighboring edge channel acting as an external environment [134], this effect allows to properly explain the experimental HOM traces.

An alternative protocol for the injection of electrons consists of the application of a train of well-designed time-dependent voltage pulses as we have introduced in Sec. 1.4.2. Some theoretical works have addressed the case of injection at $\nu = 2$ via voltage pulses, focusing on the evolution of excitations due to interactions on the HBT noise signal [102, 138, 154, 155]. However the following is the first detailed theoretical analysis of collisional HOM setups for voltage pulses and in particular for Levitons in QH edge channels at $\nu = 2$. This analysis will be relevant for the interpretation of forthcoming experiments.

3.2 Model of the system

For our purpose, we consider a QH bar at filling factor $\nu = 2$. The two copropagating edge channels are assumed to interact along a region of finite length L via a screened (δ-like) Coulomb repulsion (see Section 2.4.1) which correctly reproduces the experimental observations at low enough energies [15, 142, 143]. The system is described according to the TLL model for copropagating channels presented in Chapter 2. We recall that the kinetic and the interaction contributions to the total Hamiltonian density are written as

$$\mathcal{H}_0 = \sum_{i=1,2} \frac{v_i}{4\pi} \big[\partial_x \phi_i(x)\big]^2 \tag{3.1}$$

$$\mathcal{H}_{\text{int}} = \frac{u}{2\pi} \big[\partial_x \phi_1(x)\big] \big[\partial_x \phi_2(x)\big], \tag{3.2}$$

where the index $i = 1, 2$ labels inner and outer channels respectively (see Fig. 3.2) while the bosonic fields ϕ are related to the particle density through Eq. (2.53) and obey the statistics in Eq. (2.54).

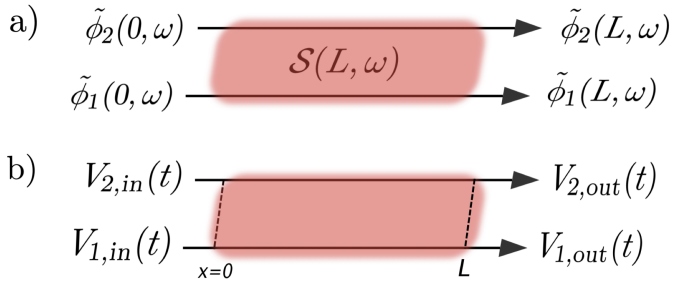

Figure 3.2: Schematic view of QH channels at integer filling factor $\nu = 2$. The shaded red area represents the interaction region, which has a finite length L and is described by the scattering matrix $S(L,\omega)$. (a) After passing this region, the incoming bosonic fields $\tilde{\phi}_{1,2}(0,\omega)$ are transformed into the outgoing ones $\tilde{\phi}_{1,2}(L,\omega)$. (b) The input voltages $V^{\text{in}}_{1/2}$ are applied to the edge channels. Due to interactions, the excitations emerging after the propagation from $x = 0$ to $x = L$ are equivalent to those that would be generated by the output voltages $V^{\text{out}}_{1/2}$ applied to the channels directly at the end of the interaction region. These output voltages are related to the incoming ones by Eq. (3.6).

The full interacting problem can be diagonalized through a rotation in the bosonic field space by the angle θ, introduced in Sec. 2.4.1, which is related to the velocities of the two edge channels and to the intensity of the coupling through Eq. (2.58). We remind that this parameter encodes the interaction strength, $\theta = 0$ being the non-interacting limit and $\theta = \pi/4$ representing the strong interacting regime. The rotation of Eq. (2.56) leads to two new bosonic fields ϕ_ρ and ϕ_σ in terms of which the full diagonalized Hamiltonian density becomes

$$\mathcal{H} = \sum_{\beta=\rho,\sigma} \frac{v_\beta}{4\pi} \big[\partial_x \phi_\beta(x)\big]^2. \tag{3.3}$$

This new fields are associated to the two new collective modes, known as EMP, presented in Sec. 2.4.3: a slow dipolar and a fast charge mode propagating, respectively, with velocities v_σ and v_ρ related to the previous $v_{1/2}$ through Eq. (2.62).

Recalling Section 2.4.2 and looking to Fig. 3.2(a), the fields outgoing from the interacting region L are related to the incoming ones through the EMP scattering matrix $S(L,\omega)$ of Eq. (2.73).

Following Refs. [13, 105, 106] and referring to Sec. 1.4.2, we can consider an electron source modeled as an ohmic contact coupling each channel to a time-dependent voltage source and allowing us to control the injection of electrons through voltages $V_{1,\mathrm{in}}(t)$ and $V_{2,\mathrm{in}}(t)$ applied to the inner and the outer channels, respectively, according to the conventional coupling Hamiltonian

$$\mathcal{H}_U = -e \int \rho_i(x) U_{1,\mathrm{in}}(x,t)\, dx \tag{3.4}$$

where $i = 1(2)$ labels the inner (outer) channel and $-e$ ($e > 0$) is the electron charge and $U_{i,\mathrm{in}}(x,t)$ describes the effect of the voltage source connected to the channels. We write it as $U_{i,\mathrm{in}}(x,t) = \Theta(-x)V_{i,\mathrm{in}}(t)$, where $V_{i,\mathrm{in}}(t)$ is the time-dependent voltage of the source and the Heaviside step function $\Theta(-x)$ specifies the region where this potential is applied [156, 157].

This classical potential, coupled to the charge density along the edge according to the above equation, can then be seen as an external classical forcing for a quantum harmonic oscillator leading to the generation of a coherent state of the EMPs along the edge channels. The displacement parameter associated to this coherent state is derived by solving the equations of motion for the bosonic fields (considering the complete Hamiltonian $\mathcal{H} + \mathcal{H}_U$) and is proportional to the Fourier transform of the voltages $\tilde{V}_{i,\mathrm{in}}(\omega)$ [102, 158]. In the frequency domain, the interacting region acts as a beamsplitter for this coherent state through the EMP scattering matrix $S(L,\omega)$ in exactly the same way as for the bosonic modes in absence of voltage, namely,

$$\begin{pmatrix} \tilde{V}_{1,\mathrm{out}}(\omega) \\ \tilde{V}_{2,\mathrm{out}}(\omega) \end{pmatrix} = \mathcal{S}(L,\omega) \begin{pmatrix} \tilde{V}_{1,\mathrm{in}}(\omega) \\ \tilde{V}_{2,\mathrm{in}}(\omega) \end{pmatrix}. \tag{3.5}$$

In the time domain (see Fig. 3.2(b)) this leads to

$$\begin{aligned} V_{1,\mathrm{out}}(t) &= \cos^2\theta\, V_{1,\mathrm{in}}(t-\tau_\rho) + \sin^2\theta\, V_{1,\mathrm{in}}(t-\tau_\sigma) \\ &\quad + \sin\theta\cos\theta[V_{2,\mathrm{in}}(t-\tau_\rho) - V_{2,\mathrm{in}}(t-\tau_\sigma)] \\ V_{2,\mathrm{out}}(t) &= \sin\theta\cos\theta[V_{1,\mathrm{in}}(t-\tau_\rho) - V_{1,\mathrm{in}}(t-\tau_\sigma)] \\ &\quad + \sin^2\theta\, V_{2,\mathrm{in}}(t-\tau_\rho) + \cos^2\theta\, V_{2,\mathrm{in}}(t-\tau_\sigma) \end{aligned} \tag{3.6}$$

clearly showing that, at the end of the interaction region, the two incoming voltages are mixed. We remind that $\tau_{\rho/\sigma} = L/v_{\rho/\sigma}$ are the times of flight associated with fast and slow modes, respectively.

3.3 General aspects of HOM interferometry

In this Section we will extend the mathematical analysis anticipated in Sec. 1.6.2 for the electronic HOM interferometer. For this reason, some definitions, as the ones for the correlators (Eq. (1.96)) or for the coefficients (Eq. (1.105)) will be recalled for sake of clarity since we now consider the effects of interaction in a HOM experiment where electronic wave-packets, generated by means of applied voltage pulses, collide at a QPC with a controlled delay in time.

Fig. 3.3 shows the HOM interferometer. Here, excitations emitted by the voltage sources A and B fractionalize when going through the interacting regions and are then

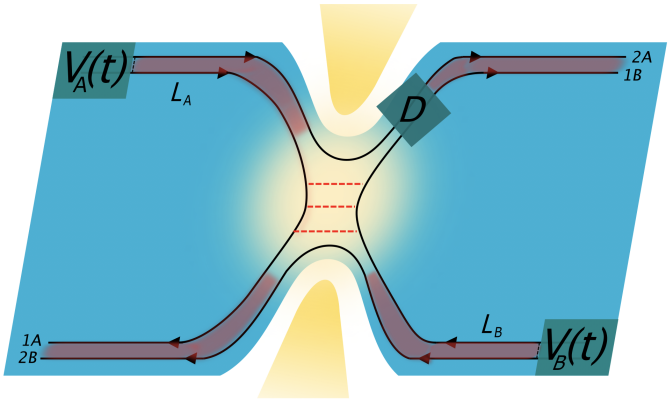

Figure 3.3: Schematic view of the HOM interferometer. Two pairs of copropagating and interacting edge states, on opposite sides of a QH bar, meet at a QPC. The electron sources A and B are modeled as ohmic contacts which are used to drive each edge with time-dependent voltages (here $V_{A/B}(t)$ is a compact notation to indicate $V^{A/B}_{1/2,\mathrm{in}}(t)$, which are the voltages shown in Fig. 3.2(b) and that are mixed by the interaction region indicated with the shaded red area). A detector D is placed just after the QPC to measure current correlations. Notice that the region of the QPC is brighter to indicate the fact that here the electron-electron interaction is screened.

partitioned at a QPC. For the moment, we assume that the injection only occurs into the inner channels of each edge, postponing the analysis of a more general case to Sec. 3.5. Therefore we set $V^{A/B}_{2,\mathrm{in}}(t) = 0$, where the notation now takes into account the fact that one can apply a voltage both to the A and the B source. It is worth noting that, as far as QH edge states in the integer regime are concerned, the different edge channels can be addressed independently by means of additional upstream QPCs [159, 18] or quantum dots with high transparency [145]. Moreover, we assume that the partitioning at the QPC involves the inner channels only, which we label as $1A$ (right-moving) and $1B$ (left-moving), related to the incoming fermionic fields $\psi_{1A,\mathrm{I}}$ and $\psi_{1B,\mathrm{I}}$ that are evaluated immediately before the QPC. Such a situation can be implemented by properly tuning the QPC transparency in such a way that the outer channels are completely transmitted, while the inner ones are also partially reflected [108, 145, 148]. Thus, the brighter region of the QPC (see Fig. 3.3) is not included in the interacting region and fermions are locally free at this location. According to this and assuming a local tunneling, the free fermionic fields, outgoing from the QPC, are related to the incoming ones through a scattering matrix (similarly to Eq. (1.90)) as

$$\begin{pmatrix} \psi_{1A}(t) \\ \psi_{1B}(t) \end{pmatrix}_{\mathrm{O}} = \begin{pmatrix} \sqrt{\mathsf{R}} & i\sqrt{\mathsf{T}} \\ i\sqrt{\mathsf{T}} & \sqrt{\mathsf{R}} \end{pmatrix} \begin{pmatrix} \psi_{1A}(t) \\ \psi_{1B}(t) \end{pmatrix}_{\mathrm{I}} \tag{3.7}$$

where we recall T and $\mathsf{R} = 1 - \mathsf{T}$ are positive real parameters describing the probability for a particle to be transmitted or reflected, respectively. This scattering approach for fermionic fields is justified, in our specific case of interacting channels at $\nu = 2$, as long as both the inter-edge interaction and the tunneling are local (see for example Supplementary Material of Ref. [108]). According to the chirality and locality of the coupling we can consider the interaction region extending from just after the injection point to just before the QPC [131, 138, 139]. This mathematical description is physically motivated by the fact that both the contacts used to apply the voltage and the gates that

realize the QPC locally enhance the screening of the interaction, that can be therefore assumed as negligible in these two regions. This theoretical approach already showed a very good agreement with the experimental observation for HOM interferometers realized using driven mesoscopic capacitors as single electron sources [15, 148].

Following what is usually investigated in EQO experiments, we focus our attention on the zero-frequency auto-correlated noise $S_{\rm HOM}$ evaluated just after the QPC. From Eq. (1.52), this quantity is defined as [74, 79]

$$S_{\rm HOM} = \int \left[\langle I_D(t) I_D(t')\rangle - \langle I_D(t)\rangle \langle I_D(t')\rangle\right] dtdt', \tag{3.8}$$

where $I_D(t)$ is the total current arriving at the detector D (see Fig. 3.3) and it is composed of the currents flowing in the channels $2A$ and $1B$:

$$I_D(t) = I_{2A}(t) + I_{1B}(t)\,. \tag{3.9}$$

The current operator on a given channel $j = 2A, 1B$ reads

$$I_j(t) = -ev_F : \psi_j^\dagger(t)\psi_j(t) :, \tag{3.10}$$

where $: \cdots :$ denotes the normal ordering with respect to the Fermi sea and fermionic fields are evaluated at the level of the detector D.

In full generality, the HOM noise can be expressed as

$$S_{\rm HOM} = S_{2A,2A} + S_{2A,1B} + S_{1B,2A} + S_{1B,1B}\,, \tag{3.11}$$

where $(i, j = 2A, 1B)$

$$S_{ij} = \int \left[\langle I_i(t) I_j(t')\rangle - \langle I_i(t)\rangle \langle I_j(t')\rangle\right] dtdt'\,. \tag{3.12}$$

The notation $S_{\rm HOM}$ is chosen to emphasize that we are dealing with the zero-frequency noise in the HOM configuration, *i.e.* when both sources are on. We note that in Eq. (3.11) the first contribution $S_{2A,2A}$ consists only of the current auto-correlations of the totally transmitted external channel but this does not affect the measurements because its contribution is zero. Also the terms $S_{2A,1B}$ and $S_{1B,2A}$ do not contribute, due to the fact that averages involving current operators in different channels factorize because no interaction occurs at the level of the QPC. Therefore, the only relevant contribution in Eq. (3.11) is $S_{1B,1B}$ which involves terms referring to both inner channels. This is because, according to Eq. (3.7), the fermionic field $\psi_{1B,\rm O}$ at the output of the QPC is expressed in terms of both incoming fields $\psi_{1A,\rm I}$ and $\psi_{1B,\rm I}$. In order to simplify the notation, in the following discussion we will refer to the inner channels $1A$ and $1B$ just as A and B.

By using Eqs. (3.7) and (3.8) we can express the total noise $S_{\rm HOM}$ as [103]

$$S_{\rm HOM} = -(ev_F)^2\, \mathsf{RT} \int \Delta Q(t,t') dtdt' \tag{3.13}$$

where

$$\begin{aligned}\Delta Q(t,t') =& \Delta\mathcal{G}_A^{(e)}(t',t)\Delta\mathcal{G}_B^{(h)}(t',t) + \Delta\mathcal{G}_A^{(h)}(t',t)\Delta\mathcal{G}_B^{(e)}(t',t)\\ &+\Delta\mathcal{G}_A^{(e)}(t',t)\mathcal{G}_{F,B}^{(h)}(t',t) + \Delta\mathcal{G}_A^{(h)}(t',t)\mathcal{G}_{F,B}^{(e)}(t',t)\\ &+\mathcal{G}_{F,A}^{(e)}(t',t)\Delta\mathcal{G}_B^{(h)}(t',t) + \mathcal{G}_{F,A}^{(h)}(t',t)\Delta\mathcal{G}_B^{(e)}(t',t).\end{aligned} \tag{3.14}$$

In Eq. (3.14), $\Delta\mathcal{G}^{(e/h)}_{A/B}$ are the non-equilibrium excess first order coherence functions [160, 161, 162] for electrons and holes

$$\Delta\mathcal{G}^{(e/h)}_{A/B}(t',t) = \mathcal{G}^{(e/h)}_{A/B}(t',t) - \mathcal{G}^{(e/h)}_{F,A/B}(t'-t)\,, \tag{3.15}$$

where the correlators $\mathcal{G}^{(e/h)}_{A/B}$, already defined in Eq. (1.96), are evaluated over the non-equilibrium state induced by the voltage injection, whereas $\mathcal{G}^{(e/h)}_{F,A/B}$ are the correlation functions for the equilibrium states (*i.e.* when no drive is applied) and are evaluated over the Fermi sea. The channel label (A/B) will be dropped in the following when referring to the equilibrium correlation functions, as they are assumed identical for both channels. The effect of the external voltage drive can be properly taken into account with a phase factor [102, 103], see Eq. (1.36), in such a way that Eq. (3.15) is rewritten as

$$\Delta\mathcal{G}^{(e/h)}_{A/B}(t',t) = \mathcal{G}^{(e/h)}_{F}(t'-t)\left(e^{\mp i\varphi_{A/B}(t,t')} - 1\right) \tag{3.16}$$

where

$$\varphi_{A/B}(t,t') = e\int_{t'}^{t} V^{A/B}_{1,\mathrm{out}}(\tau)d\tau \tag{3.17}$$

is the phase contribution due to the time dependent voltage, carrying information about interaction effects according to Eq. (3.6). It is worth noting that, limited to the injection through voltage and under the assumption of local interaction acting over a finite length, the coherence functions can be written as the free fermionic ones times phase factors encoding the effect of the applied voltage and the interaction. Therefore, our system can be mapped onto a free fermion problem subject to a modified voltage which takes into account the fractionalization effects [102]. Incidentally this fact can be seen as a further validation of Eq. (3.7).

By replacing Eq. (3.16) into Eq. (3.14), the correlation function $\Delta Q(t,t')$ can be expressed as

$$\Delta Q(t,t') = 2\mathcal{G}^{(e)}_{F}(t'-t)\mathcal{G}^{(h)}_{F}(t'-t)\big[1-\cos(\varphi_A(t,t')-\varphi_B(t,t'))\big]\,. \tag{3.18}$$

If one of the two sources is switched off, the above formula simplifies and the HBT noise associated with the partitioning of excitations incoming only in one arm of the interferometer is recovered $(i = A, B)$ [103]:

$$S_{\mathrm{HBT},i} = -2(ev_F)^2\,\mathsf{RT}\int dt\,dt'\mathcal{G}^{(e)}_{F}(t'-t)\mathcal{G}^{(h)}_{F}(t'-t)\left[1-\cos(\varphi_i(t,t'))\right]\,. \tag{3.19}$$

In the following, according to what is usually done in conventional HOM experiments with voltage pulses [13, 106], we consider the two sources A and B to be driven by identical signals apart from a controlled time delay δ, namely

$$V^{B}_{1,\mathrm{in}}(t) = V^{A}_{1,\mathrm{in}}(t+\delta). \tag{3.20}$$

An important consequence arises when we consider the interaction strengths and the distances between the sources and the QPC to be equal in both arms of the interferometer (symmetric configuration with $\theta^A = \theta^B = \theta$ and $L_A = L_B = L$). In this case, the voltages $V^{A/B}_{1,\mathrm{out}}$ after the interacting regions are the same for both arms. This can be easily seen from Eq. (3.6) where it is clear how these voltages depend on the interaction strength θ and on the interaction length L (via the times of flight $\tau_{\rho/\sigma}$). As a result, at zero injection delay $\delta = 0$ one has $\varphi_A(t,t') = \varphi_B(t,t')$, leading to $\Delta Q(t,t') = 0$.

Therefore we arrive at the consequence that, even in the presence of interactions, the HOM noise in a symmetric configuration always vanishes for a synchronized emission in the two incoming channels ($\delta = 0$), regardless of the particular form of the signal used for the time-dependent voltage injection. Notice that these considerations still hold also in the case of a long-range interaction [102, 134, 154] as long as it preserves the symmetry of the set-up.

The injection via the mesoscopic capacitor occurs at a well defined energy above the Fermi level and it has been shown [138] that in this case the emitted wave-packets undergo a relaxation towards low-energy degrees of freedom before the process of fractionalization takes place. On the contrary, voltage-generated excitations are robust in this respect, as the energy relaxation does not occur for them [138, 154] and they are only affected by the fractionalization process during their propagation through the interacting region.

This qualitative difference is consistent with our results, showing that the excitations injected via voltage pulses are robust and do not display any suppression of the HOM dip at zero delay.

We recall that the standard experimental procedure consists in normalizing the measured HOM signal with respect to the HBT ones [15], thus defining the ratio

$$\mathcal{R}(\delta) = \frac{S_{\rm HOM}(\delta)}{S_{{\rm HBT},A} + S_{{\rm HBT},B}}, \tag{3.21}$$

where we have taken into account the fact that the HOM noise contribution is the only one which depends on the time delay δ. The noise in Eq. (3.13) can be rewritten in terms of the average time $\bar{t} = (t + t')/2$ and of the time difference $\tau = t - t'$ as (adapting the definition to the case of a periodic drive [105])

$$S_{\rm HOM} = -(ev_F)^2 \mathsf{RT} \int_{-\frac{\mathcal{T}}{2}}^{+\frac{\mathcal{T}}{2}} \frac{d\bar{t}}{\mathcal{T}} \int_{-\infty}^{+\infty} d\tau \Delta Q \left(\bar{t} + \frac{\tau}{2}, \bar{t} - \frac{\tau}{2}\right). \tag{3.22}$$

These integrals are performed analytically in Appendix C by introducing the Fourier decomposition of Eq. (1.104) and by using the definition of the period in Eq. (1.100).

By using this approach, the ratio (3.21) can be written as

$$\mathcal{R}(\delta) = \sum_{l=-\infty}^{+\infty} \frac{|\mathcal{P}_l(q;\delta)|^2 |\Omega l|}{|\widetilde{p}_{l,A}(q)|^2 |\Omega(l+q)| + |\widetilde{p}_{l,B}(q)|^2 |\Omega(l+q)|}, \tag{3.23}$$

where $\widetilde{p}_{l,A/B}(q)$ and $\mathcal{P}_l(q;\delta)$ are new photoassisted coefficients defined in Appendix C (Eqs. (C.4) and (C.8)) and they can be expressed as functions of amplitudes p_l introduced in Eq. (1.105). They are related to the phases $\varphi_A - \varphi_B$ and $\varphi_{A/B}$, respectively, and fully take into account the effects of interactions. It is worth noting that Eq. (3.23) together with the following results is obtained in the zero temperature limit, thermal corrections being marginal in realistic experimental conditions [13, 15, 106, 148].

In the next Section, we specify the above general analysis to the case of Lorentzian pulses (see Sec. 1.4.2) considering symmetric and asymmetric configurations. Both of them are analyzed by relying on the general expression (3.23), where the proper photoassisted coefficients (see Eq. (C.6)) will be used.

3.4 HOM interferometry for Levitons

In the previous Section, we have proved that the excess noise in a symmetric HOM configuration, is always zero for simultaneous injection from the the sources, indepen-

dently of the shape of the voltage and of the interactions occurring along the channels. Here, recalling Sec. 1.4.2, we will focus on the injection of a periodic train of Levitons [8, 10, 13]. Then, the injected voltage pulse assumes the form

$$V^A_{1,\mathrm{in}}(t) \equiv V(t) = -\frac{2q}{e}\sum_{j\in\mathbb{Z}} \frac{\tau_0}{\tau_0^2 + (t - j\mathcal{T})^2}\,, \tag{3.24}$$

with $q \in \mathbb{N}$. When $q = 1$, one electron per period $\mathcal{T}$ is emitted. In Eq. (3.24) τ_0 represents the width in time of each Lorentzian pulse of the periodic train.

3.4.1 Symmetric setup

In this Section we analyze what happens to the noise ratio $\mathcal{R}$, in Eq. (3.23), when identical Lorentzian voltage pulses with unitary charge ($q = 1$) are applied to both contacts. We consider a symmetrical configuration for the interferometer, meaning that the lengths of the two interacting regions are equal ($L_A = L_B = L$), as well as the inter-edge interaction strength ($\theta^A = \theta^B = \theta$) in the two incoming channels. It is worth noticing that in this situation the photoassisted coefficients $\widetilde{p}_{l,A}(q)$ and $\widetilde{p}_{l,B}(q)$ entering in Eq. (3.23) are equal.

Due to interactions, as the time delay δ between the right and the left moving electrons is varied, we find three characteristic features in the noise profile (see Fig. 3.4). At $\delta = 0$ a central dip appears while two symmetrical side-dips emerge at positions $\delta_{\mathrm{sd}} = \pm|\tau_\rho - \tau_\sigma|$. The shape of these three dips is Lorentzian reflecting the overall form of the applied voltage pulses, while their width depends on the timescale τ_0. According to this the dips are more pronounced for a smaller ratio $\tau_0/\mathcal{T}$.

This interference pattern is interpreted in terms of the different excitations emerging after the interacting region. Indeed, after the injection, the electronic wave-packet fractionalizes into a slow and a fast mode carrying different charges. According to Eq. (3.18), the central dip, which corresponds to the situation of simultaneous injection from the two sources, goes exactly to zero because these identical excitations interfere destructively. This is in striking contrast with what has been observed in a HOM experiment at $\nu = 2$ where the injection was achieved by means of driven mesoscopic capacitors [15, 148], where the visibility of the central dip is always reduced (see Fig. 3.1) by interactions [108].

The destructive interference is also responsible for the side-dip structures appearing when fractionalized excitations with different velocities collide (see Fig. 3.4). For instance, at a delay $\delta_{\mathrm{sd}} = \tau_\sigma - \tau_\rho$ the fast right moving excitation and the slow left moving one reach the QPC at the same time. Furthermore, Fig. 3.4 also shows as a reference the behavior of the noise ratio in absence of interactions ($\theta = 0$) which always reaches zero (at $\delta = 0$) but does not show any side dip because no fractionalization occurs in this case. Our numerical curve (black) perfectly coincide with the theoretical analytical formula (gray dots) derived for the HOM noise ratio $\mathcal{R}$ of colliding Levitons with unitary charge in the absence of interactions ($\theta = 0$) [105, 156]

$$\mathcal{R}_0(\delta) = \frac{\sin^2\left(\pi\frac{\delta}{\mathcal{T}}\right)}{\sinh^2\left(2\pi\frac{\tau_0}{\mathcal{T}}\right) + \sin^2\left(\pi\frac{\delta}{\mathcal{T}}\right)}. \tag{3.25}$$

We have used this reference result as a check for the validity of our numerical calculations.

In view of possible future experimental validations of our theoretical analysis, the plots of $\mathcal{R}$ as a function of $\delta/\mathcal{T}$ for different values of θ have been obtained by fixing

the ratio between the pulse width and the period to be $\tau_0/\mathcal{T} = 0.05$, compatible with state of the art experiments carried out in narrow constrictions [13, 106], while the time of flight of both slow and fast modes are of the order of $10 \div 100$ ps, interaction lengths are $L \sim \mu m$ and velocities are $v_{\rho/\sigma} \sim 10^4 \div 10^5 m/s$. This makes our prediction observable in nowadays EQO experiments.

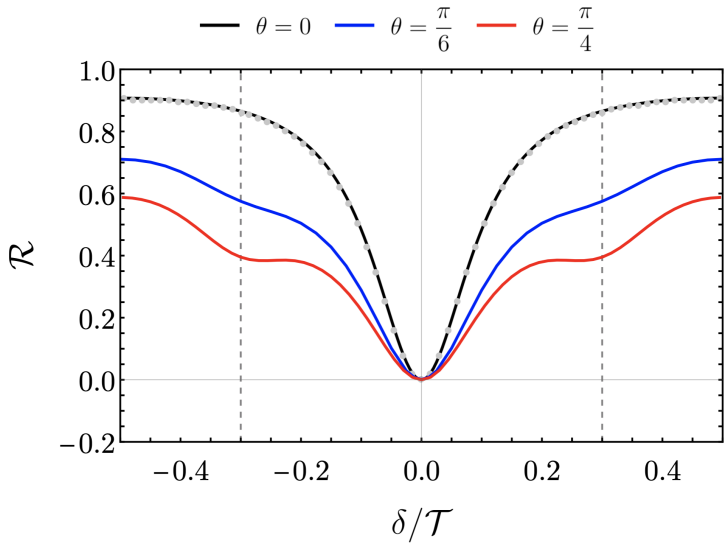

Figure 3.4: Ratio $\mathcal{R}$ in Eq. (3.23), for Lorentzian pulses, as a function of time delay over period ($\delta/\mathcal{T}$) for a symmetric setup. The HOM noise generated by the collision of periodical trains of Lorentzian pulses is shown for different interaction parameters: $\theta = 0$ (black curve), $\theta = \pi/6$ (blue curve) and $\theta = \pi/4$ (red curve). Gray dots represent the analytical prediction in Eq. (3.25) for the non-interacting case. Other parameters are: $\tau_0/\mathcal{T} = 0.05$, $v_\rho = 4 \cdot 10^5$ m/s and $v_\sigma = 1.8 \cdot 10^5$ m/s, with $L_\mathrm{A} = L_\mathrm{B} = 2\,\mu$m. Notice that the positions of side dips occur at $\delta_\mathrm{sd} = \pm|\tau_\rho - \tau_\sigma|$ (gray dotted vertical lines).

3.4.2 Asymmetric setup

We now examine the HOM noise ratio in Eq. (3.23) for an asymmetric configuration where the distances between the injection contacts and the QPC are different ($L_A \neq L_B$), still assuming the same inter-edge interaction on both arms ($\theta_A = \theta_B = \theta$). Notice that our general result in Eq. (3.23) can be directly used also to investigate the case $\theta_A \neq \theta_B$ even if this condition is more difficult to be controlled experimentally. We did not include this situation in the paper in order to keep the discussion more focused. In any case, we expect different interaction strengths to give a similar qualitative behavior as the presence of different lengths.

Differently from the symmetric case, when $L_A \neq L_B$ the photoassisted coefficients in Eq. (3.23) are no longer equal ($\widetilde{p}_{l,A} \neq \widetilde{p}_{l,B}$) because of the different interaction lengths. A new scenario thus emerges in this case as now the right-moving modes and the left-moving ones do not have the same times of flight even if they have the same velocities due to the same interaction strengths. For this reason we denote the times of flight of right-moving modes as $\tau^A_{\rho,\sigma} = L_A/v_{\rho,\sigma}$ and those of the left-moving ones as $\tau^B_{\rho,\sigma} = L_B/v_{\rho,\sigma}$.

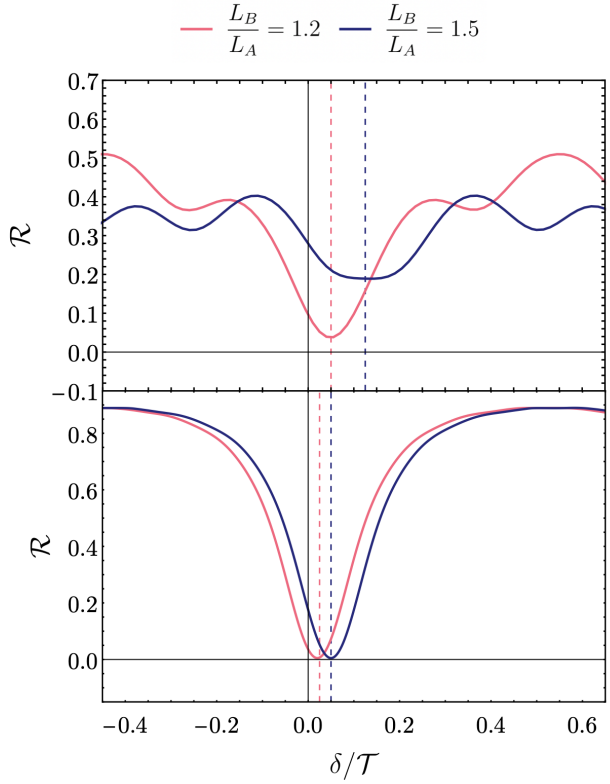

Figure 3.5: Ratio $\mathcal{R}$ in Eq. (3.23), for Lorentzian pulses, as a function of time delay over period ($\delta/\mathcal{T}$) for an asymmetric setup. In the upper panel, the two curves refer to the strong coupling regime ($\theta = \pi/4$) for two different length ratios: $L_B/L_A = 1.2$ (red curve), $L_B/L_A = 1.5$ (blue curve). In the lower one, the curves refer to the noninteracting case ($\theta = 0$) for the same length ratios as before (red and blue). It is worth noticing that, if no interaction occurs, the ratio $\mathcal{R}$ goes to zero and the positions of the minima depend on both the length ratios and the velocity propagation of the free fermions along the channel of the injection (here assumed to be $v_1 = v_\rho$). Other parameters are $\tau_0/\mathcal{T} = 0.05$, $v_\rho = 4 \cdot 10^5$ m/s and $v_\sigma = 1.8 \cdot 10^5$ m/s, with $L_A = 2\,\mu$m. Notice that the positions of the central dip are indicated, respectively, by the red and blue dashed vertical lines.

As before, we consider the noise ratio $\mathcal{R}$ as a function of the time delay δ focusing on the strong coupling regime ($\theta = \pi/4$) and considering different values of the length ratio L_B/L_A. From Fig. 3.5 (upper panel) one can outline that the three dips described before are still present, but now the overall profiles are very different with respect to the symmetric case. Indeed, here the central dip does not reach anymore zero (loss of visibility) and its position is shifted with respect to the origin by a time delay

$$\delta_{\rm cd} = \frac{\tau_\sigma^B + \tau_\rho^B - \tau_\sigma^A - \tau_\rho^A}{2} \tag{3.26}$$

which increases with to the length ratio L_B/L_A. This means that the total suppression of HOM noise is not achieved because the different interaction lengths result in different times of flight ($\tau^A_{\rho,\sigma} \neq \tau^B_{\rho,\sigma}$) in such a way that the charge and neutral parts of the incoming signals do not reach the QPC at the same time. The distances of the side

dips from the central one satisfy

$$|\delta_{\rm cd} - \delta_{\rm sd}| = \frac{\tau_\sigma^B - \tau_\rho^B + \tau_\sigma^A - \tau_\rho^A}{2} \tag{3.27}$$

clearly showing the effect of the asymmetric lengths of interacting regions on the noise ratio $\mathcal{R}$.

Notice that in absence of interactions (lower panel of Fig. 3.5) we recover the same behavior of the symmetric case in Fig. 3.4 up to a simple shift in the delay direction. This is a direct consequence of the lack of fractionalization of the incoming excitations.

An additional comment on Eq. (3.26) is worthwhile. In the symmetric setup, the central dip corresponds to the situation where the two charged (or dipolar) modes incoming from the two sources arrive simultaneously at the QPC. In the asymmetric case, at a delay $\delta_1 = \tau_\rho^B - \tau_\rho^A$ ($\delta_2 = \tau_\sigma^B - \tau_\sigma^A$) the charged (dipolar) modes reach the QPC at the same time, but the dipolar (charged) ones do not. As a result, instead of a single central dip as appearing in Fig. 3.5 (upper panel), two distinct dips located at δ_1 and δ_2 should be expected (for additional details see Appendix D). However, for realistic values for $\tau_0/\mathcal{T}$, these two dips are not resolved (because the wavepackets are not narrow enough) and merge into a broader one, located at an average delay $\delta_{\rm cd} = (\delta_1 + \delta_2)/2$.

In Section 3.4.1 we have shown that the HOM noise goes exactly to zero when we are in a symmetric situation and the excitations are injected simultaneously in the QH edge channels. This time one may wonder whether the signal periodicity affects the visibility of the central dip ($\mathcal{R}(\delta_{\rm cd})$) in an asymmetric setup when the lengths ratio is varied. In Fig. 3.6 we show the behavior of the minimum of the HOM ratio ($\mathcal{R}(\delta_{\rm cd})$) as a function of L_B/L_A in the presence of a periodical Lorentzian source (main plot) and compare it to the single Lorentzian pulse case (inset). Also in this case we focus on the strong coupling $\theta = \pi/4$ regime. The biggest difference between the two situations lies in the fact that for the periodic drive the red curve goes to zero three times in the considered range of the ratio L_B/L_A, including the starting point (where $L_B/L_A = 1$), while for the single pulse no other zero occurs apart the one corresponding to equal lengths. Therefore, the occurrence of additional zeros is a remarkable consequence of the periodicity of the drive and can be used to extract information about the interaction parameter θ.

In order to better understand the behavior in Fig. 3.6 we must start from Eq. (3.18), for a generic case with $\delta \neq 0$. Therein, the phases φ_A and φ_B must be equal in order to have a perfect superposition of colliding excitations and a consequent maximal visibility of the HOM central dip. The expression giving the lengths ratios at which the central dip is maximally visible in the case of a periodical injection is

$$\frac{L_{\rm B}}{L_{\rm A}} = \frac{2(k-k')\mathcal{T}}{\tau_\sigma^A - \tau_\rho^A} + 1 \tag{3.28}$$

with $k, k' \in \mathbb{N}$ and $k > k'$ (see Appendix D for more details). The previous relation describes the zero located at $L_{\rm B}/L_{\rm A} \approx 7.6$ in Fig. 3.6, for $k - k' = 1$. We also point out that the presence of a second zero, located at $L_{\rm B}/L_{\rm A} \approx 5.6$, is a direct consequence of the maximal coupling $\theta = \pi/4$. Indeed, as shown in Appendix D, in this condition additional zeros appear for a length ratio

$$\frac{L_{\rm B}}{L_{\rm A}} = \frac{2(k-k')\mathcal{T}}{\tau_\sigma^A - \tau_\rho^A} - 1\,. \tag{3.29}$$

However, as soon as the coupling departs from the maximal value ($\theta < \pi/4$) the second zero is lifted and turns into a local minimum (see Appendix D for more details). This is a signature of the different weight of charge and dipole contributions to the fractionalized wave-packet and can be use to extract information about the mismatch in the time of flight and consequently about the inter-edge coupling θ.

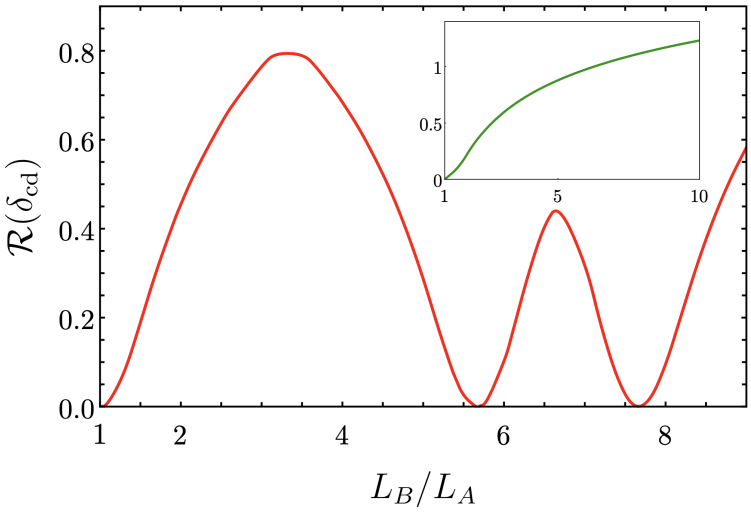

Figure 3.6: Behavior of $\mathcal{R}(\delta_{\rm cd})$ as a function of the length ratio L_B/L_A. The red curve is obtained for a periodic Lorentzian pulse ($\tau_0/\mathcal{T} = 0.05$) while the green inset shows the case of a single pulse. Other parameters are $\theta = \pi/4$, $L_A = 2\,\mu$m, $v_\rho = 1.5\cdot10^5$ m/s and $v_\sigma = 1.8\cdot10^5$ m/s. Notice that here we have chosen propagation velocities different with respect to the other figures with the only aim of magnifying the features discussed in the main text.

The possibility for the HOM central dip to reach zero at different values of the lengths ratio is a direct consequence of the periodicity of the applied signal. In terms of electronic density we can think of what is happening as follows: one Leviton is injected for every period, it crosses the interacting region where it fractionalizes into two modes with different velocities. If the interacting region has the proper length, the fast mode of a given period will reach the slow mode of the previous one. By properly calibrating the ratio between the lengths into the two arms it is possible to achieve a situation where the colliding objects, the fast and slow modes coming from both arms, at the QPC are identical leading to a vanishing HOM noise.

3.5 Measuring the interaction

Until now, we have considered a setup where the injection takes place on the inner channels of QH bar only. A more general analysis consists in considering a case where the excitations are also injected in the outer channels. This configuration can be achieved for example by further exploiting an open quantum dot coupled to the outer channels [15]. As we will demonstrate, in this case a collisional HOM experiment allows to extract information on the interaction strength between the edge channels as long as it can be assumed as short-range. In Section 3.4.2 we have shown how the dependence of the visibility of the central dip as a function of the lengths ratio can be used to indirectly estimate interactions. Here, we consider a more direct way to

measure the interaction intensity encoded in the parameter θ.

Let us start by considering two different input voltages $V_{1/2}^{A/B}$ at the entrance of the interaction region, where 1 stands for the inner channels and 2 for the outer ones. Without loss of generality we consider the two drives to be proportional, namely $V_{2,\mathrm{in}}^{A/B} = \alpha V_{1,\mathrm{in}}^{A/B}$. In what follows we only consider a symmetric configuration for the interferometer even if similar results can be obtained for an asymmetric case. This implies that Eq. (3.6) can be written as

$$\begin{aligned} V_{1,\mathrm{out}}^{A/B}(t) &= \cos^2\theta\, V_{1,\mathrm{in}}^{A/B}(t-\tau_\rho) + \sin^2\theta\, V_{1,\mathrm{in}}^{A/B}(t-\tau_\sigma) \\ &\quad +\alpha \sin\theta\cos\theta[V_{1,\mathrm{in}}^{A/B}(t-\tau_\rho) - V_{1,\mathrm{in}}^{A/B}(t-\tau_\sigma)] \\ V_{2,\mathrm{out}}^{A/B}(t) &= \sin\theta\cos\theta[V_{1,\mathrm{in}}^{A/B}(t-\tau_\rho) - V_{1,\mathrm{in}}^{A/B}(t-\tau_\sigma)] \\ &\quad +\alpha \sin^2\theta\, V_{1,\mathrm{in}}^{A/B}(t-\tau_\rho) + \alpha\cos^2\theta\, V_{1,\mathrm{in}}^{A/B}(t-\tau_\sigma). \end{aligned} \tag{3.30}$$

From the above equation, we can identify two relevant situations involving two different values of the proportionality parameter: $\alpha = \tan\theta$ and $\alpha = -\cot\theta$. For these two values $(V_{1,\mathrm{in}}^{A/B}, \alpha V_{1,\mathrm{in}}^{A/B})^T$ is an eigenvector of the scattering matrix $S(L,\omega)$ in Eq. (2.73). In the time domain, this results in

$$\begin{pmatrix} V_{1,\mathrm{out}}^{A/B}(t) \\ V_{2,\mathrm{out}}^{A/B}(t) \end{pmatrix} = \begin{pmatrix} V_{1,\mathrm{in}}^{A/B}(t-\tau_\rho) \\ V_{2,\mathrm{in}}^{A/B}(t-\tau_\rho) \end{pmatrix} \quad \text{for } \alpha = \tan\theta \tag{3.31}$$

and

$$\begin{pmatrix} V_{1,\mathrm{out}}^{A/B}(t) \\ V_{2,\mathrm{out}}^{A/B}(t) \end{pmatrix} = \begin{pmatrix} V_{1,\mathrm{in}}^{A/B}(t-\tau_\sigma) \\ V_{2,\mathrm{in}}^{A/B}(t-\tau_\sigma) \end{pmatrix} \quad \text{for } \alpha = -\cot\theta\,. \tag{3.32}$$

Therefore, for these values of α, the input voltages are not mixed by interactions and are transferred unaffected to the output of the interacting region. This feature is quite surprising because it means that, by properly tuning α, one can inject two input excitations which effectively propagate freely along the edge channels without undergoing any fractionalization process, despite the presence of an interacting region in the system. Therefore, it is possible to regard α as a tunable parameter with which one can switch off interaction effects on the HOM noise ratio $\mathcal{R}$. As a possible experimental way to implement such kind of voltage configuration one can apply the same voltage $V_{1,\mathrm{in}}^{A/B}(t)$ to both channels, further adding a voltage $(\alpha-1)V_{1,\mathrm{in}}^{A/B}(t)$ properly synchronized with the first one only to channel 2 by means of a quantum dot [15].

In order to illustrate this effect we compare in Fig. 3.7 the case where the injection only occurs in the inner channels ($\alpha = 0$) with the situation when both inner and outer channels are driven ($\alpha \neq 0$). The former scenario is represented by the dashed curves, showing the side dips structure already discussed in Section 3.4.1. The latter case is represented by full lines and clearly shows that, for the particular value $\alpha = \tan\theta$, the side dips disappear and one perfectly recovers the same behavior as in the absence of interactions, described by Eq. (3.21) and shown by black dots in Fig. 3.7.

As a final remark we mention that, for $\alpha > \tan\theta$ (not shown), the side dips become side peaks as a consequence of the fact that excitations with opposite charge reach the QPC [107, 108].

According to the above considerations it is clear that the study of the evolution of the side dips as a function of α can be used as a way to estimate the value of the inter-edge interaction as long as it can be assumed as short range. Indeed, by tuning

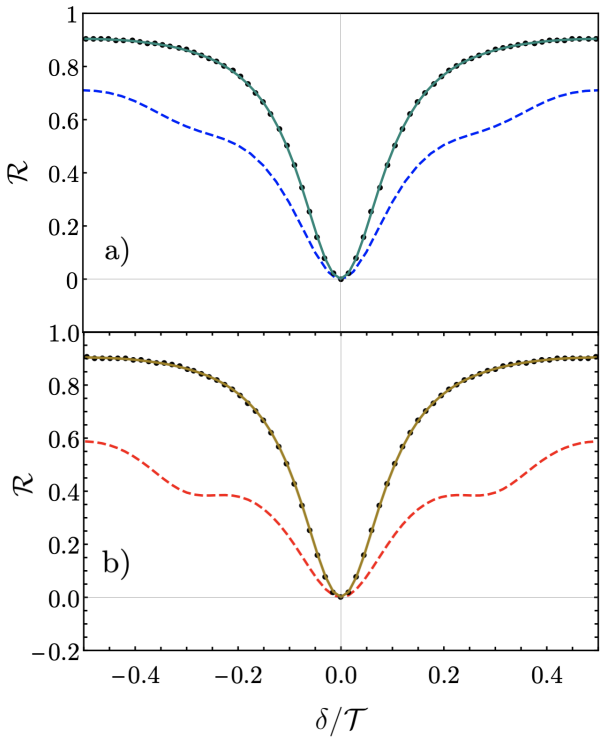

Figure 3.7: Ratio $\mathcal{R}$ as a function of time delay over period ($\delta/\mathcal{T}$). The full lines describe HOM collisions at finite values of α. In a) we set $\theta = \frac{\pi}{6}$ and $\alpha = \tan\left(\frac{\pi}{6}\right) \approx 0.58$ while in b) $\theta = \frac{\pi}{4}$ and $\alpha = \tan\left(\frac{\pi}{4}\right) = 1$. The dashed lines describe the corresponding curves for an injection only in inner channels ($\alpha = 0$) for both a) $\theta = \frac{\pi}{6}$ and b) $\theta = \frac{\pi}{4}$). The black dots show the ratio $\mathcal{R}$ in the absence of interactions ($\theta = 0$). Other parameters are: $\tau_0/\mathcal{T} = 0.05$, $v_\rho = 4 \cdot 10^5 m/s$ and $v_\sigma = 1.8 \cdot 10^5 m/s$, with $L_\mathrm{A} = L_\mathrm{B} = 2\mu m$.

α in such a way to eliminate the side dips in the HOM signal knowing that this occurs precisely at $\alpha = \tan\theta$, the mixing angle can be obtained from this relation.

3.6 Summary

In this Chapter, we have theoretically investigated a HOM experiment where periodic time-dependent voltage pulses are injected with a tunable delay into QH edge channels at filling factor $\nu = 2$ and collide at a QPC. As a consequence of the screened Coulomb interactions between the edge channels, the injected electrons fractionalize and the noise measured just outside the QPC is characterized by the emergence of side dips as a function of the delay in the injection. Differently from what happens in the case of injection using driven mesoscopic capacitors, the visibility of the central dip remains maximal independently of the interaction for a symmetric device regardless of the form of the voltage used for the injection. This fact is a signature of the robustness of voltage drives with respect to interaction effects. Then, focusing on Lorentzian voltage pulses and by inducing an asymmetry in the device, for example, by considering different distances between the injectors and the QPC, the visibility can be reduced. In addition, from the peculiar dependence of the visibility on the ratio between these distances, it is possible to extract information about the intensity

of the interaction along the edge. Along this direction, we have also proposed a more direct measurement of the interaction based on the application of different voltages on the two edge channels along each arm of the interferometer. In this case, by properly tuning the ratio between these voltages, it is possible to prevent the fractionalization with a consequent disappearance of the side dip in the HOM noise profile. Therefore, the study of the evolution of the side dips in this configuration can provide a direct measurement of the strength of interedge interactions.

Chapter 4

Radiation squeezing in interacting quantum Hall edge channels

In this Chapter, which is based on Ref. [163], we investigate the quantum fluctuations of the electromagnetic radiation emitted by a QH device at filling factor $\nu = 2$ in a QPC geometry. In particular, we connect the quantum features of the emitted microwave radiation, mainly focusing on the squeezing, to the electric current fluctuations measured at finite frequency, accessible through a two-filters set-up placed after the QPC. We compare two different periodic drives, a cosine and a train of Lorentzian pulses (see Section 3.4) respectively, focusing our attention on the role played by the unavoidable electron–electron interactions between the two edge channels. In both cases quantum features are reduced due to the interactions, however the Lorentzian drive is characterized by a more robust squeezing effect which can have important application in the quantum information framework. Finally, we will comment on experimental results about the squeezing in tunnel junctions and QH conductors [27, 29].

4.1 Introduction

Significant experimental and theoretical efforts have been deployed to find sources of quantum light. An electromagnetic radiation with properties beyond that of classical physics is indeed essential in the development of quantum information technology [164, 165] and has direct applications in metrology [166]. Many systems have been invented to produce squeezed light, based for example on non-linear crystals, atomic transitions and non-linear cavities in optics [167] but also with parametric amplifier and qubits in the microwave domain [168, 169, 170, 171]. Moreover, the study of electric current fluctuations at finite frequency, carried out in presence of tunnel [27, 28] and Josephson junctions [172], has underlined the deep connection between this quantity and the fluctuations of the microwave radiation emitted by driven mesoscopic devices. This radiation shows quantum features such as squeezing and entanglement of photons in the frequency domain, which can be properly engineered by controlling the form of the applied periodic drive. In particular it has been shown that very narrow voltage pulses can maximize the single- and two-photon squeezing of the radiation emitted in the microwave range [173, 174]. Above all, a key ingredient in order to obtain squeezed radiation is the presence of non-linearities which allows to beat vacuum fluctuations along one quadrature.

Along this direction, electron–electron interactions naturally lead to non-linearities in the current–voltage characteristics in a QPC geometry and, as lengthy discussed

above, their effect cannot be avoided in realistic experimental conditions.

In this Chapter we will theoretically investigate the dynamical response of the current fluctuations, which are associated to the photo-assisted finite frequency noise. This will allow us to carry out a detailed analysis of the effect of inter-edge coupling on the quantum properties of the emitted radiation. Setting the proper theoretical framework is needed in order to pave the way towards new experiments devoted to the control of the quantum behaviour of the electromagnetic field emitted by interacting electronic devices.

The importance of our analysis is testified by the fact that, very recently, H. Bartolomei and coworkers [29] have experimentally achieved the generation of squeezed EMP states at the output of a QPC in a GaAs QH conductor, as we have discussed in Ref. [163]. These squeezed states will allow for quantum enhanced measurements in EMP interferometers [175] implemented in mesoscopic QH conductors. Squeezed EMP states could also be used to extend the study of low dimensional quantum conductors in the regime where they are driven by quantum voltage sources [176], exploiting the strong coupling of high impedance transmission lines to high impedance low-dimensional quantum circuits.

4.2 Model

We adopt a model similar to the one used in Section 3.2 of the previous Chapter and shown schematically in Fig. 4.1, with the addition of few different ingredients. For completeness, and for a better readability of the present Chapter, we summarize the main points of the model below highlighting the new ones.

As in Chapter 3, we consider the edge states of the upper part of a QH bar at filling factor $\nu = 2$. The excitations are injected through a time-dependent voltage source, presented in Section 1.4.2. We consider the injection only from one arm instead of two recalling the HBT configuration of Section 1.6.3. The coprapagating edge channels interact via a short range capacitive coupling which is described according the TLL model presented in Chapter 2. Inter-edge interactions lead to a charge fractionalization process, as discussed in Section 2.4.3, before the QPC where the current is partitioned and enters a two-filters set-up. This set-up allows to measure the dynamical response of the noise (see below).

Similarly to what done in Section 3.2 of the previous Chapter, the total Hamiltonian density is $\mathcal{H} = \mathcal{H}_0 + \mathcal{H}_{\rm int}$, consisting of edge states and of an interaction contribution. The free Hamiltonian density modeling the two copropagating edge states is given by Eq. (3.1), while the interacting one is described by Eq. (3.2). The diagonalization is made possible through a bosonization approach (see Section 2.4.1) and by means of a rotation of an angle θ in the field space. Then, the dynamics of the edge channels is solved within the EMP scattering matrix as in Eq. (2.73).

The Hamiltonian density $\mathcal{H}_U$ modeling the time-dependent voltage source is the same as the one in Eq. (3.4) but now, differently from Chapter 3, we will consider the voltage source connected only to the inner channel where the notation $V_{\rm in}(t) \equiv V^{(A)}_{1,\rm in}(t)$, has been adopted to relate this Chapter with the previous one. We also consider the decomposition of the voltage in terms of DC and AC part

$$V_{\rm in}(t) = V_{\rm DC} + V_{\rm AC}(t) \tag{4.1}$$

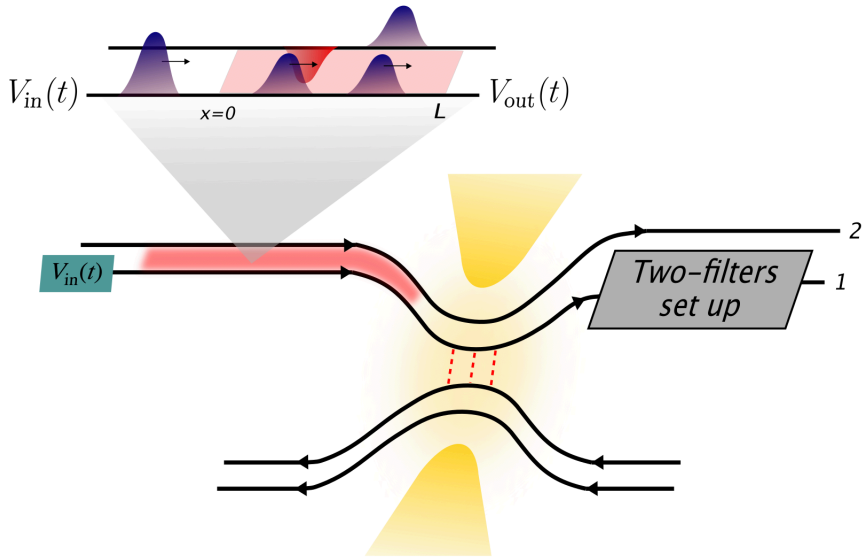

Figure 4.1: Schematic view of a QH bar at $\nu = 2$ in the QPC geometry. Here, the Hall channels are capacitively coupled through a short range interaction (red) which lead to a separation of the electronic excitation, injected through the voltage source $V_{\rm in}(t)$ in the inner channel, into a fast charge and a slow neutral modes propagating with velocities v_ρ and v_σ respectively, defined in Eq. (2.62). The outgoing voltage is indicated as $V_{\rm out}(t)$ and it contains a DC and AC parts. By means of gates (yellow), which create the QPC, the current is partitioned and reaches a two-filters set-up placed just outside the QPC region. Notice that the region of the QPC is yellow to indicate the fact that here the electron–electron interaction is negligible.

with

$$\frac{1}{\mathcal{T}}\int_{-\frac{\mathcal{T}}{2}}^{+\frac{\mathcal{T}}{2}} dt\, V_{\rm AC}(t) = 0 \tag{4.2}$$

being $\mathcal{T}$ the period of the drive. In the following we will focus on both a cosine drive with

$$V_{\rm AC}^{(c)}(t) = -\tilde{V}\cos\left(\frac{2\pi t}{\mathcal{T}}\right) \tag{4.3}$$

or a periodic train of Lorentzian pulses, from Section 3.4, with width $\tau_0 = \eta\mathcal{T}$

$$V_{\rm AC}^{(l)}(t) = \frac{\tilde{V}}{\pi}\sum_j \frac{\eta}{\eta^2 + \left(\frac{t}{\mathcal{T}} - j\right)^2} - \tilde{V}. \tag{4.4}$$

In both cases $\tilde{V}$ is the amplitude of the AC part of the drive. Recalling the scattering picture for the voltages of Eqs. (3.5) and (3.6), the voltage outgoing from the interacting region along the inner channel is

$$V_{\rm out}(t) = V_{\rm DC} + \cos^2\theta\, V_{\rm AC}(t-\tau_\rho) + \sin^2\theta\, V_{\rm AC}(t-\tau_\sigma) \tag{4.5}$$

where the times of flight $\tau_{\rho/\sigma}$ have been defined in Eq. (2.74). Finally, by looking at Fig. 4.1, the outgoing fractionalized excitation are then partitioned at a QPC where only inner channels are involved in the tunneling. Following the same considerations of Section 3.3 about the QPC region which is non-interacting and taking into account

the chirality of the propagation and to the locality of the coupling, the inner free fermionic fields outgoing from the QPC are related, from Eq. (1.90), to the incoming ones through[1]

$$\begin{pmatrix}\psi_R(t)\\ \psi_L(t)\end{pmatrix}_{\mathrm{O}} = \begin{pmatrix}\sqrt{\mathsf{T}} & i\sqrt{\mathsf{R}}\\ i\sqrt{\mathsf{R}} & \sqrt{\mathsf{T}}\end{pmatrix}\begin{pmatrix}\psi_R(t)\\ \psi_L(t)\end{pmatrix}_{\mathrm{I}}. \tag{4.6}$$

Then, the inner channel of the upper edge enter into a two-filters set-up which is placed immediately after the QPC in such a way that the interactions between the outgoing channels are there negligible. In the following Sections we will investigate the current and the associated fluctuations.

4.3 Current and photo-assisted noise at finite frequency

In this Section, we focus our attention on the evaluation of the finite frequency noise $S(\omega_1,\omega_2)$ which is defined, from Section 1.5, as [74, 79]

$$S(\omega_1,\omega_2) = \int_{-\infty}^{+\infty} dt \int_{-\infty}^{+\infty} dt'\, e^{i\omega_1 t} e^{i\omega_2 t'} C(t,t') \tag{4.7}$$

where, following Eq. (1.50), the current-current correlator is

$$C(t,t') = \langle \Delta I_1(t)\Delta I_1(t')\rangle \equiv \langle I_1(t) I_1(t')\rangle_c. \tag{4.8}$$

Here the notation $\langle ...\rangle_c$ stands for the connected zero temperature quantum mechanical correlator and the current operator of the inner channel $I_1(t)$ is defined as in Eq. (3.10).

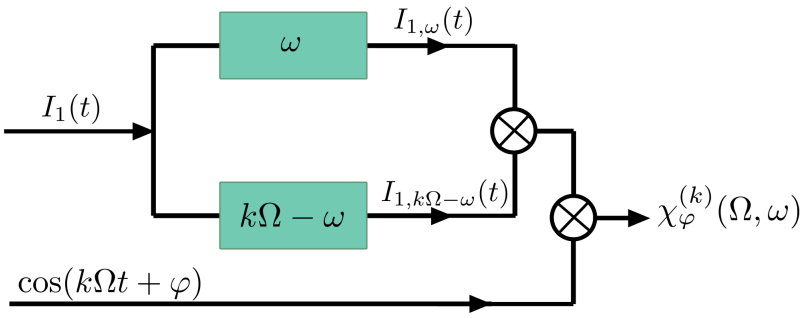

Figure 4.2: Schematic view of a set-up designed to measure the dynamical response of the noise $\mathcal{X}_\varphi^{(k)}$. The current of the inner channel outgoing from the QPC (associated to the operator $I_1(t)$) of the Hall bar is further split into two at the level of the detector. The resulting contributions are filtered at the two frequencies ω ($I_{1,\omega}(t)$) and $|k\Omega-\omega|$ ($I_{1,k\Omega-\omega}(t)$) respectively (green boxes). They are then multiplied among themselves and with a cosine signal ($\otimes$ symbols) with a tunable phase shift φ. The final output is then averaged over time.

In order to access the stationary component of the photo-assisted noise at finite frequency [74, 79, 177, 178] (zero-th order harmonic) and the more general dynamical response of the outgoing current fluctuations [174, 179], corresponding to the higher order harmonics at a frequency $k\Omega$ ($k\in\mathbb{N}$), we consider a two-filter measurement

[1] Notice that this scattering matrix is slightly different to the one in Eq. (3.7) due to the geometrical differences of the set-up considered in this Chapter.

device, placed immediately after the QPC (see Fig. 4.1). As depicted in Fig. 4.2, the current of the inner channel (associated to the operator $I_1(t)$), incoming the set-up, is filtered at two different frequencies, ω and $|k\Omega - \omega|$ respectively. By considering one of the two filter, for example the one in ω, the outgoing current becomes

$$I_1(t) \to I_{1,\omega}(t) \approx I_1(\omega)e^{i\omega t} + I_1(-\omega)e^{-i\omega t}. \tag{4.9}$$

The filtered contributions are then multiplied among themselves and further with a cosine signal with frequency $k\Omega$ and phase φ.

According to the described set-up and to the symmetrized correlators of the current operators [174, 179], the k-th harmonics of the dynamical response of the noise measured at a frequency ω is given by

$$\mathcal{X}_{\varphi}^{(k)}(\Omega,\omega) = \lim_{\mathcal{T}_m\to+\infty} \frac{1}{\mathcal{T}_m}\int_{-\frac{\mathcal{T}_m}{2}}^{+\frac{\mathcal{T}_m}{2}} dt\langle I_{1,\omega}(t)I_{1,k\Omega-\omega}(t)\cos(k\Omega t+\varphi)\rangle_c, \tag{4.10}$$

with $I_{1,\omega}(t)$ defined in Eq. (4.9) and Ω related to the injection period $\mathcal{T}$ through Eq. (1.100). Notice that, consistently to what typically done in experiments, we consider an averaging over a given measurement time $\mathcal{T}_m$ longer with respect to all the other time scales involved in the dynamics of the system. Therefore, keeping only the non zero terms in the average, the expression in Equation (4.10) reduces to

$$\mathcal{X}_{\varphi}^{(k)}(\Omega,\omega) = \frac{1}{2}\big[\langle I_1(\omega)I_1(k\Omega-\omega)e^{-i\varphi}\rangle_c + \langle I_1(-\omega)I_1(-k\Omega+\omega)e^{i\varphi}\rangle_c\big]. \tag{4.11}$$

According to this and to the reality constraint $I_1^\dagger(\omega) = I_1(-\omega)$, for the current operator, one can write

$$\mathcal{X}_{\varphi}^{(k)}(\Omega,\omega) = \frac{1}{2}\left[\Re\left\{\mathcal{X}_{+,\varphi}^{(k)}(\Omega,\omega)\right\} + \Re\left\{\mathcal{X}_{+,\varphi}^{(-k)}(\Omega,-\omega)\right\}\right] \tag{4.12}$$

with

$$\mathcal{X}_{+,\varphi}^{(k)}(\Omega,\omega) = e^{i\varphi}\langle I_1(\omega)I_1(k\Omega-\omega)\rangle_c \tag{4.13}$$

and $\Re\{...\}$ indicating the real part. From now on we will consider only $k > 0$. The expression for the dynamical response of the noise $\mathcal{X}_{\varphi}^{(k)}(\Omega,\omega)$, evaluated explicitly in Appendix E when a periodic drive is applied to the inner edge channel (see Fig. 4.1), becomes

$$\begin{aligned}\mathcal{X}_{\varphi}^{(k)}(\Omega,\omega) = \frac{\cos\varphi}{2}\Re\Bigg\{&\sum_{n=-\infty}^{+\infty}\widetilde{p}_n(z)\widetilde{p}_{n+k}^*(z)S_0(q'+1+n\lambda)+\\ &+\sum_{n=-\infty}^{+\infty}\widetilde{p}_n(z)\widetilde{p}_{n-k}^*(z)S_0(q'-1+n\lambda)\Bigg\}.\end{aligned} \tag{4.14}$$

Notice that, in the above expression we have kept separated the DC and the AC amplitude in such a way to consider the parameters $q' = eV_{DC}/\omega$ and $z = e\tilde{V}/\Omega$ as totally independent with $\lambda = \Omega/\omega$. The quantity

$$S_0(\xi) = \mathcal{A}(\omega)|\xi| \tag{4.15}$$

represents the shot noise [74, 79], in the zero temperature limit, with

$$\mathcal{A}(\omega) = G\mathsf{R}\mathsf{T}\omega \tag{4.16}$$

where $G = e^2/2\pi$ is the linear conductance of the considered channel and RT comes from the QPC scattering matrix in Eq. (4.6). From this quantity, it is also possible to tackle the effects of the temperature. Moreover, according to the general definition reported in Eq. (C.5), one has

$$\widetilde{p}_l(z) = \sum_n p_{l-n}(z_1) p_n(z_2) e^{i\Omega\tau_\rho(l-n)} e^{i\Omega\tau_\sigma(n)} \tag{4.17}$$

where $z_1 = z\cos^2\theta$ and $z_2 = z\sin^2\theta$. Thus, the coefficients $\widetilde{p}_l(z)$ are completely specified once the expression of $p_n(z)$ is known. These are the photo-assisted amplitudes defined in Eq. (1.105).

It is worth to note that for $k = 0$ and $\varphi = 0$, the expression in Eq. (4.12) reduces to

$$\mathcal{X}_0^{(0)}(\Omega,\omega) = \frac{1}{2}\sum_{n=-\infty}^{+\infty} |\widetilde{p}_n(z)|^2 \big[S_0(q'+1+n\lambda) + S_0(q'-1+n\lambda)\big], \tag{4.18}$$

which represents the photo-assisted noise measured at finite frequency ω [27].

In order to proceed, we need to recall the functional form of the photo-assisted amplitudes $p_n(z)$ for the considered voltage drives. In the case of the cosine drive in Eq. (4.3) the coefficients $p_n^{(c)}(z)$ assume the expression in Eq. (C.7) while, by looking at Eq. (C.6), we obtain the coefficients $p_n^{(l)}(z)$ in the case of the Lorentzian voltage pulse from Eq. (4.4).

4.4 Current fluctuations and electromagnetic quadratures

The outgoing current operator I_1 can be also related to the emitted electromagnetic field annihilation operator $\widetilde{a}$ through the relation[2] [180]

$$\widetilde{a}(\omega) = -i\frac{I_1(\omega)}{\sqrt{2\mathcal{A}(\omega)}}. \tag{4.19}$$

According to this, the electromagnetic field can be written as [27, 173]

$$\begin{aligned} A_\varphi(\omega) &= \frac{1}{\sqrt{2}}\left[e^{i\varphi} I_1(\omega) + e^{-i\varphi} I_1(-\omega)\right] \\ &= i\sqrt{\mathcal{A}(\omega)}\left[e^{i\varphi}\widetilde{a}(\omega) - e^{-i\varphi}\widetilde{a}^\dagger(\omega)\right] \end{aligned} \tag{4.20}$$

where the phase φ between a and $a^\dagger$ allows to span the whole phase space. By using the Robertson formulation of the Heisenberg principle for two generic operators

$$\Delta A \Delta B \geq \frac{1}{2}|\langle [A,B]\rangle| \tag{4.21}$$

the fluctuations of the quadratures of the electromagnetic field satisfy the uncertainty relation

$$\Delta A_{2\varphi} \Delta A_{2\varphi+\pi} \geq \mathcal{A}(\omega), \tag{4.22}$$

[2] It is worth to point out that, in an interacting one dimensional chiral channel, an analogous relation (up to a numerical prefactor) can be derived connecting the current with the EMP creation (annihilation) operator (Eq. (2.11)). Therefore the conclusion derived in the following can be generalized also to this bosonic operator as recently reported in Ref. [29].

with $\Delta A_{2\varphi} = \sqrt{\langle A_{2\varphi}^2\rangle - \langle A_{2\varphi}\rangle^2}$, which naturally link the quantum fluctuations of the electromagnetic field quadrature at a given frequency ω with the current fluctuations (see Eq. (4.23)) and can be detected by the experimental scheme previously presented. The effect of the radiation squeezing results from the previous Eq. (4.22): when the value of the fluctuations of one quadrature decreases below the quantum vacuum the other must increases in order to preserve the uncertainty relation. This means that if we know with a great precision $\Delta A_{2\varphi}$ we must give hope of knowing precisely the value of the other ($\Delta A_{2\varphi+\pi}$). Furthermore it can be observed, from the definition in the second line of Eq. (4.20), in terms of creation and annihilation operator, that the expectation value $\langle A_{2\varphi}\rangle$ on the equilibrium state is always zero.

In order to bind the dynamical response of the noise, measurable through the two-filters set-up shown above, to the quadrature fluctuations we use the first line of Equation (4.20) to calculate

$$\begin{aligned}\langle A_{2\varphi}^2(\omega)\rangle &= \frac{1}{2}\langle\Big[I_1(\omega)e^{i\varphi} + I_1(-\omega)e^{-i\varphi}\Big]\Big[I_1(\omega)e^{i\varphi} + I_1(-\omega)e^{-i\varphi}\Big]\rangle = \\ &= \frac{1}{2}\langle\Big[I_1(\omega)I_1(-\omega) + I_1(-\omega)I_1(\omega) + e^{2i\varphi}I_1(\omega)I_1(\omega) + e^{-2i\varphi}I_1(-\omega)I_1(-\omega)\Big]\rangle.\end{aligned} \tag{4.23}$$

We immediately notice that the first two terms, in the second line, correspond to the photo-assisted noise $\mathcal{X}_0^{(0)}(\Omega,\omega)$ at finite frequency while the other two are equal, up to a proportional term in the phase, to the expression in Eq. (4.12) once fixed $k\Omega = 2\omega$. In the following we will focus of the case $k = 1$ where a greater squeezing can be achieved [27, 174]. Furthermore, since we are dealing with a low energy theory for the bosonic modes and the high-frequency noise generated by the stream of single electrons gets suppressed with increasing frequency [68, 151], we have to consider as an upper limit for the possible frequencies the energy gap E_g of the QH state. Therefore, in order to efficiently investigate the squeezing of the emitted microwave radiation using fluctuations of an electric current we cannot exceed few GHz in the drive frequency Ω.

Following Eq. (4.23), the quadratures of the emitted electromagnetic field can be written in a more general way as

$$\langle A_{2\varphi}^2(\omega)\rangle = \mathcal{X}_0^{(0)}(2\omega,\omega) + \mathcal{X}_{2\varphi}^{(1)}(2\omega,\omega) \tag{4.24}$$

where φ is the phase of the cosine signal of the measurement set-up in Figure 4.2. In the following we will focus on the two orthogonal quadratures $\langle A_0^2\rangle$ and $\langle A_\pi^2\rangle$. Furthermore this configuration leads to the maximal squeezing in the non interacting case [27].

4.5 Suppression of the radiation squeezing

In this Section we will show how the effects of Coulomb interactions affect the squeezing of the emitted electromagnetic field through the study of the quadratures $\langle A_{2\varphi}^2\rangle$ and the related fluctuations $\Delta A_{2\varphi}$. In this context, the squeezing property offers the possibility to beat the vacuum fluctuations along one quadrature at the expense of the other in order to preserve the inequality in Eq. (4.22). Due to these considerations the squeezing of the electromagnetic field is achieved for $\langle A_{2\varphi}^2\rangle/\mathcal{A}(\omega) < 1$.

In Figure 4.3 and Figure 4.4, we present the two orthogonal quadratures $\langle A_0^2\rangle$ and $\langle A_\pi^2\rangle$ of the emitted electromagnetic field for the cosine drive, considered in Eq. (4.3), and for the Lorentzian one, in Eq. (4.4). The two panels of both figures allow us to

compare the behaviour of the quadratures in the non-interacting case (dashed curves in the left panels) with the interacting one (full curves in the right panels). It can be immediately observed that, for both the considered AC voltage drives, the effects of interactions lead to a reduction of the value of the minima of the two orthogonal quadratures due to the neutral-charge modes separation and the consequently rising of the quantum noise outgoing from the QPC.

In the cosine case for a non-zero θ (right panel of Fig. (4.3)), it is evident the almost total suppression of the squeezing because the minimum of the quadrature $\langle A_0^2 \rangle$ ($\langle A_\pi^2 \rangle$) is only slightly below the quantum vacuum (horizontal gray dashed line) while the other stays well above. Concerning Figure 4.3, the symmetry between the two quadratures for ($q' \to -q'$), observed in the non-interacting case [174], is still preserved in the interacting one according to the general properties of the photo-assisted amplitudes [13].

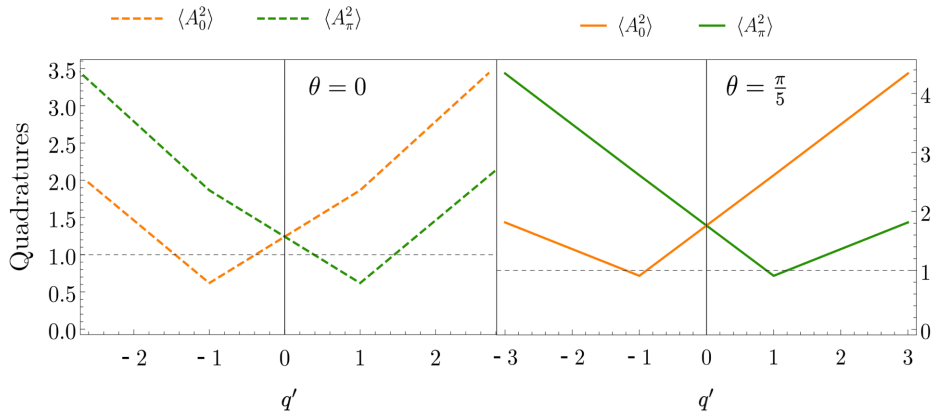

Figure 4.3: Quadratures of the emitted electromagnetic field in units of $\mathcal{A}(\omega)$ as a function of q' for a cosine drive. Both panels represent the two orthogonal quadratures $\langle A_0^2 \rangle$ (orange) and $\langle A_\pi^2 \rangle$ (green): the non-interacting case ($\theta = 0$) with $z = 0.706$ is described in the left panel (dashed curves). The right one (full curves) describes the quadratures in presence of interactions ($\theta = \pi/5$) and for $z = 1.32$. The dashed gray horizontal line indicates the vacuum fluctuations. The choice of the parameters z in the two cases is motivated by a numerical minimization of the noise. Other parameters are: $L = 2.5\,\mu$m, $v = 2.8 \times 10^4$ m/s, $\alpha' = 2.1$ (from Eqs. (2.62) and (2.74)) and $\lambda = 2$.

When we turn our attention to the Lorentzian case, in Fig. 4.4, the situation appears quite different. First of all, the mirror symmetry encountered for the cosine drive is absent here [13]. Then, the interactions still increase the values of the quadratures' minima but $\langle A_\pi^2 \rangle$, for $q' = 1$, continues to stay well below the quantum vacuum limit. It is a clear sign that even in the presence of electron-electron interactions the squeezing effect is not suppressed when the injection is done with a Lorentzian drive which appears more robust and remains better with respect to the cosine one, in order to maximize the squeezing (minimizing the noise). Furthermore, the correspondent conjugate quadrature $\langle A_0^2 \rangle$ is well above this limit as expected from a generic squeezed state where the fluctuations along one quadrature are suppressed while the others are enhanced in order to obey the Heisenberg's uncertainty relation. The presented results, for all panels in Figures 4.3 and 4.4, have been obtained by numerically minimizing the noise as a function of z which is the amplitude of the AC drive. This procedure is done on the one hand because the interactions deform the pulse of the AC drive and

these effects have to be properly compensated and one the other hand in order to find the amplitude of the drive leading to the optimal squeezing. It is worth noting that by considering the optimal value of z for the cosine drive, the squeezing associated to the Lorentzian drive is still slightly better. This comparison has been done in [163]. Hence it follows that we have used different values of z for the considered drive in the non-interacting case with respect to the interacting one.

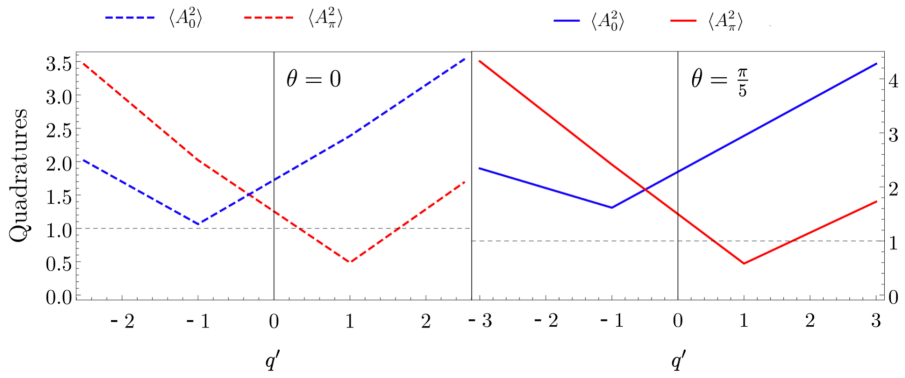

Figure 4.4: Quadratures of the emitted electromagnetic field in units of $\mathcal{A}(\omega)$ as a function of q'. The two panels describe the orthogonal quadratures $\langle A_0^2 \rangle$ (blue) and $\langle A_\pi^2 \rangle$ (red) for a Lorentzian voltage drive with $\eta = 0.1$. The left panel (dashed curves) represents the quadratures in absence of interactions and with $z = 0.856$. The right one (full curves) describes the quadratures in presence of interactions ($\theta = \pi/5$) and for $z = 1.21$. The dashed gray horizontal line indicates the vacuum fluctuations. The choice of the parameters z in the two cases is motivated by a numerical minimization of the noise. Other parameters are: $L = 2.5\,\mu$m, $v = 2.8 \times 10^4$ m/s, $\alpha' = 2.1$ (from Eqs. (2.62) and (2.74)) and $\lambda = 2$.

Figure 4.5 shows the behaviour of the minimum (*i.e.* for $q' = 1$) of $\langle A_\pi^2 \rangle$ as a function of the interaction coupling strength θ for the two drives considered previously. We observe that, by increasing the interactions, the minimum of the quadrature increases its value for both cosine drive (light blue diamonds) and Lorentzian one (red circles). However, the squeezing effect is always better if we consider the injection of Levitons with respect to a cosine drive and it can be seen for all the considered interaction strengths. It is worth to notice that for all points we have chosen a value for z which minimize the noise.

Until now, recalling Fig. 4.2, we have considered a fixed value of φ for both quadratures respectively $\langle A_0^2 \rangle$ ($\varphi = 0$) and $\langle A_\pi^2 \rangle$ ($\varphi = \pi/2$). We remind that this is the phase of the cosine signal which is multiplied with the filtered current in the two-filters set-up. From this point of view, we can consider the phase as an experimentally tunable parameter and we might ask what happens to the quantum fluctuations $\Delta A_{2\varphi}$ when φ changes.

In Figure 4.6 it is shown the evolution of $\Delta A_{2\varphi}$, for $q' = 1$, when the phase φ is varied in a polar plot. In the left panel we consider the periodic injection of Levitons in the non-interacting case (blue) and for $\theta = \pi/5$ (red) while in the right one we consider a cosine drive for $\theta = 0$ (blue) and $\theta = \pi/5$ (red). From both panels, when we consider a fixed φ, we obtain the values for the fluctuations of the two orthogonal quadratures $\Delta A_{2\varphi}$ and $A_{2\varphi+\pi}$ of the emitted electromagnetic field. In the left panel (Lorentzian voltage pulses), for the specific case of $\varphi = 0$ and for $q' = 1$ we immediately

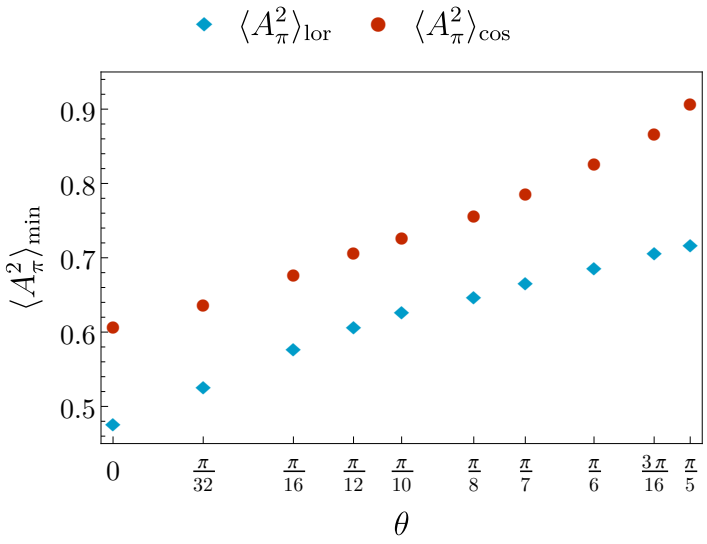

Figure 4.5: Evolution of the minimum of the $\langle A_\pi^2 \rangle$ quadrature, in units of $\mathcal{A}(\omega)$, as a function of the interaction parameter θ for the two different voltage drives evaluated at $q' = 1$. The light blue diamonds describe the behavior of $\langle A_\pi^2 \rangle$ when a Lorentzian drive is applied while the red circles are referred to a cosine drive. In presence of interactions, the minimum of the quadrature increases for both drives. However, a train of Lorentzian pulses is still a better candidate in order to maximize the squeezing. Notice that, for all points, the z values are chosen in order to numerically minimize the noise. Other parameters are: $L = 2.5\,\mu$m, $v = 2.8 \times 10^4\,$m/s, $\alpha' = 2.1$ (from Eqs. (2.62) and (2.74)) and $\lambda = 2$.

observe that the quantum fluctuation ΔA_π reaches its minimum value at the expense of ΔA_0. Thanks to the particular "peanut shape" of the left panel's Fig. 4.6, it is clear that the maximum squeezing effect is obtained for the previous considered condition where ΔA_π is well below the value of quantum vacuum at the expenses of ΔA_0. This happens in order to preserve the Heisenberg's uncertainty relation in Eq. (4.22). The same considerations about the shape of the curves can be done for both the non-interacting and interacting cases. The latter case leads to greater values of the quadratures' fluctuations but the squeezing property is still present even in the presence of interactions. This is in perfect agreement with what observed in Fig. 4.4 where even if $\langle A_\pi^2 \rangle$, for $\theta = \pi/5$ and $q' = 1$, is bigger than $\langle A_\pi^2 \rangle$ (for $\theta = 0$ and $q' = 1$) the squeezing effects still remains. The right panel of Fig. 4.6 shows the polar plot of $\Delta A_{2\varphi}$ for a cosine drive, considered in Eq. (4.3). In this panel, the shape of both non-interacting (blue) and interacting (red) cases is no longer similar to the "peanut" one. We can observe that for non-interacting channels the maximum squeezing is achieved for a fixed $\varphi = 0$ while in the interacting case this quantum property is quite totally suppressed. According to this, we can remark that the Lorentzian shape of injection voltage is a better drive, even in the presence of interactions, in order to obtain a squeezed state of the emitted microwave radiation. Until now, we have assumed $\eta = 0.1$ for the Lorentzian case.

Now, in Fig. 4.7 we compare the polar plot of quantum fluctuations $\Delta A_{2\varphi}$ for a Lorentzian drive ($q' = 1$) with different values of the ratio η between the width of the Lorentzian τ_0 and the period $\mathcal{T}$. In the left panel we show the fluctuations in the non-

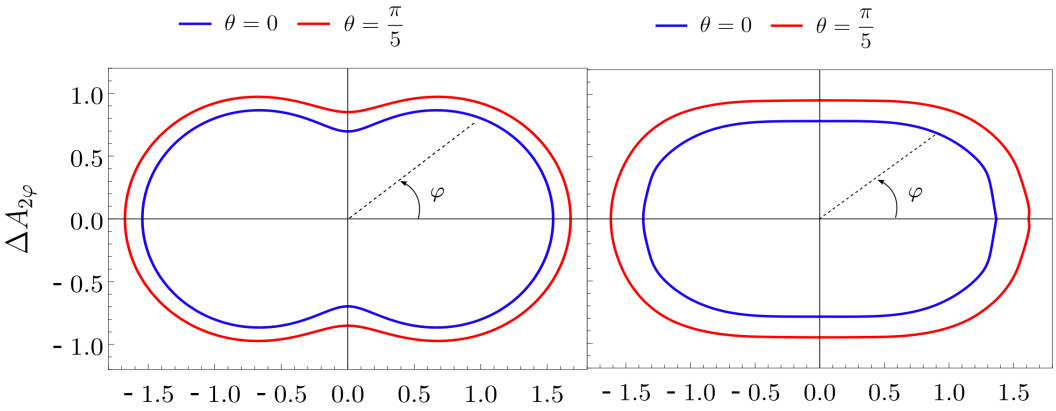

Figure 4.6: Left panel: polar plot of the quadratures fluctuations $\Delta A_{2\varphi}$, in unit of $\mathcal{A}(\omega)$ and for $q' = 1$, with respect to the phase φ, according to Eq. (4.24). The injection of particles is done by means of a Lorentzian voltage drive with $\eta = 0.1$. The blue line describes the non interacting case ($\theta = 0$) while the red one stands for $\theta = \pi/5$. Right panel: polar plot of the quadratures fluctuations $\Delta A_{2\varphi}$ in the case of injection of particles through cosine voltage drives, in unit of $\mathcal{A}(\omega)$ and for $q' = 1$, with respect to the phase φ. The blue line describes the non interacting case ($\theta = 0$) while the red one stands for $\theta = \pi/5$. Other relevant parameters are: $L = 2.5\,\mu$m, $v = 2.8 \times 10^4$ m/s, $\alpha' = 2.1$ (from Eqs. (2.62) and (2.74)) and $\lambda = 2$.

interacting case while in the right one we consider the interaction $\theta = \pi/5$ between edge channels. If we consider an experimentally more challenging situation where the Lorentzian pulses are very narrow (purple curve with $\eta = 0.05$), we get a more pronounced "peanut shape" (violet and gold line in both panels), but the squeezing effect doesn't improve with respect to the case $\eta = 0.1$. Conversely, by increasing the ratio (yellow and light blue curves with $\eta = 0.2$), the "peanut shape" disappears. In this last situation the effects of the squeezing is evidently reduced and tends to disappear in the interacting case with respect to the non-interacting one, similarly to what happens for a cosine drive.

4.6 Experimental signatures

In this Section, we report different experimental signatures of the squeezing of the emitted electromagnetic radiation by a mesoscopic device.

Starting from Ref. [27], Gasse and co-workers exploited the discreteness of the electron charge as a source of non-linearity in the free electron case. The authors considered a tunnel junction, obtained through two metallic contacts separated by a thin insulating layer, which has a linear current-voltage characteristics at low voltage and thus cannot be used as a non-linear element to mix signals. This kind of system shows no photo-assisted DC transport, *i.e.* no rectification. However, it exhibits shot noise, in other words the variance of the current fluctuations generated by the junction depends on the voltage bias. Thus, in the presence of an AC excitation, the junction exhibits photo-assisted noise [177, 178, 181] as well as a dynamical modulation of its noise [179]. This modulation due to the external AC excitation is then used to generate squeezed light. Recalling Section 4.5, the squeezing effect can be seen in Fig. 4.8 where the fluctuations ΔA^2 of the amplitude $A\cos(\omega t)$ can beat vacuum fluctuations at the

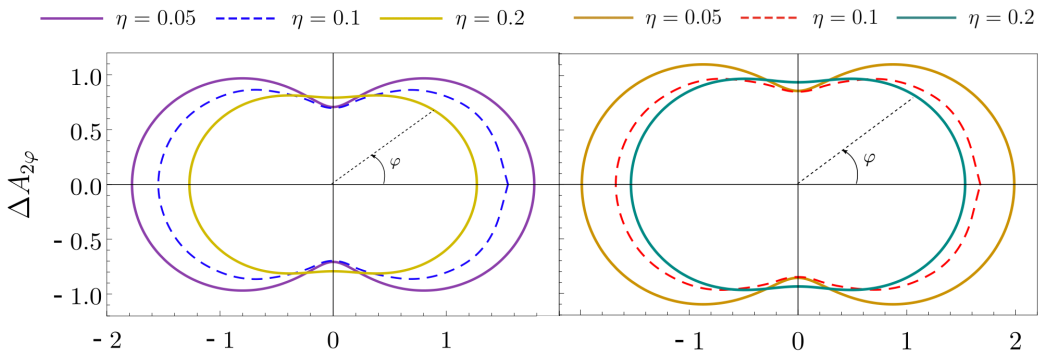

Figure 4.7: Polar plot of the quadratures fluctuations $\Delta A_{2\varphi}$ with respect to the angle φ, in unit of $\mathcal{A}(\omega)$. The voltage drive considered for the injection is a train of Lorentzian pulses with $q' = 1$. In the left we consider the non interacting case $\theta = 0$ while in the right one we consider the interaction parameter $\theta = \pi/5$. The three different curves (in both panels) stand for three values of the ratio η: the purple (left) and gold (right) lines describes the case at $\eta = 0.05$, the blue (left) and red (right) dashed lines are obtained for $\eta = 0.1$ and the yellow (left) and light blue (right) represent the fluctuations for $\eta = 0.2$. Other relevant parameters are: $L = 2.5\mu$m, $v = 2.8 \times 10^4$ m/s, $\alpha' = 2.1$ (from Eqs. (2.62) and (2.74)) and $\lambda = 2$.

expense of the others fluctuations ΔB^2 of the amplitude of $B\sin(\omega t)$.

Very recently, the generation of squeezed EMP states has been surprisingly achieved at the output of a QPC in a GaAs QH conductor [29], whose characteristic impedance is set by the quantum of resistance ($R_K \approx 25\,\mathrm{k}\Omega$) much larger than the 50 Ohms used in previous experiments [27, 28]. This could offer the possibility of a strong coupling to low dimensional quantum conductors of high impedance [182].

The principle of the experiment is represented in Fig. 4.9(a). The outer edge channel of a QH conductor at filling factor $\nu = 3$ is partitioned at the central QPC. A DC current is generated at input 1 while an AC sinusoidal source $V_{\mathrm{AC}}(t) = V_{\mathrm{AC}}\cos(4\pi f t)$ is applied at input 2, with frequency $f = \Omega/4\pi = 7.75\,\mathrm{GHz}$. The high frequency noise $\Delta S_{\Omega,\varphi}(V_{\mathrm{DC}}, V_{\mathrm{AC}})$ is measured by weakly transmitting the EMPs propagating at output 4 to a coaxial cable. The signal is then amplified and $S_{\Omega,\varphi}$ is measured by multiplying the output signal with a local oscillator $V_l(t) = V_l\cos(\Omega t + \varphi)$ using high frequency mixers. The local oscillator is locked in phase with the pump $V_{\mathrm{AC}}(t)$ and the phase φ of the measured quadrature can be continuously varied. Finally, $S_{\Omega,\varphi}$ is measured using a diode which integrates the power at the output of the mixer.

Turning on the V_{AC} pump, the high frequency noise measurements are performed and their results are plotted in Fig. 4.9(b). It can be seen that $\Delta S_{\Omega,\varphi}(V_{\mathrm{DC}}, V_{\mathrm{AC}})$ depends strongly on the phase φ as shown by the strong differences between $\varphi = 0$ (red points) and $\varphi = \pi/4$ (yellow points). Notice that yellow plot is symmetric for positive and negative biases V_{DC} while the red one looks completely different because of its asymmetry with respect to V_{DC}. It shows that for this combination of DC and AC voltages, the squeezing of the EMP mode at frequency f is obtained since the red plot goes below the black dashed line which represents the vacuum fluctuations. Interestingly enough, the red and yellow dashed lines, which represent the theoretical predictions, don't fit perfectly experimental data since it is possible to observe less noise than the theoretical model for negative bias on the red curve. Moreover, it is

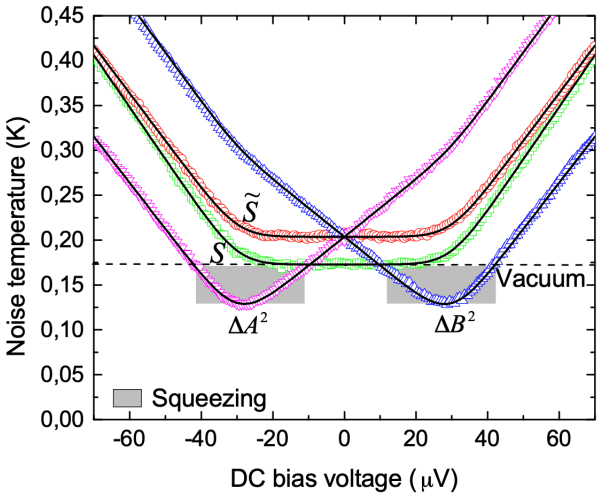

Figure 4.8: Measurements of the fluctuations of the two quadratures (ΔA^2 and ΔB^2) of the emitted electromagnetic field as a function of the DC voltage bias at $T = 28\,\mathrm{mK}$. When the AC voltage is turned on ($V_{AC} = 46\,\mu\mathrm{V}$) then the emitted radiation is squeezed (shaded region). The dotted line corresponds to vacuum fluctuations. Figure taken from [27].

worth noticing that both experiments have been obviously performed at very low, but not zero, temperatures which are well approximated by our theoretical predictions. In fact, the most relevant effect of a non-zero temperature involves a smoothing of the curves in the quadratures' plots.

4.7 Perspectives

To conclude, starting from an overview on early works about the quantum properties of the emitted electromagnetic radiation by a mesoscopic device, we have theoretically investigated the dynamical response of the outgoing current fluctuations, which are associated to the photo-assisted finite frequency noise, in a QPC geometry for a QH bar at filling factor $\nu = 2$ in presence of electron-electron interactions between the two edge channels.

We have considered the periodic injection of excitations (in the GHz range) in the mesoscopic system by means of two different time dependent voltage drives, respectively a cosine and a train of Lorentzian pulses, and a short-range coupling between edge channels. We have shown that the effects of interaction lead to an unavoidable reduction of the squeezing of the electromagnetic quadratures for both drives. However, the Lorentzian case still remain a better candidate in order to achieve a relevant squeezing also in presence of interaction. We have investigated the quantum properties of the emitted light by studying how the quantum fluctuations vary in terms of the experimental tunable phase φ. Furthermore, we have shown the connection between the shape of the squeezed quantum state and the different regimes in the two filters set-up accessible in experiments. In addition to this analysis, experimental results [29] involving the demonstration of the squeezing of EMP modes at a frequency in GHz range by using two-particle interferences, have been presented at the end of this Chapter.

Squeezed states could be used in EMP interferometers for quantum enhanced sen-

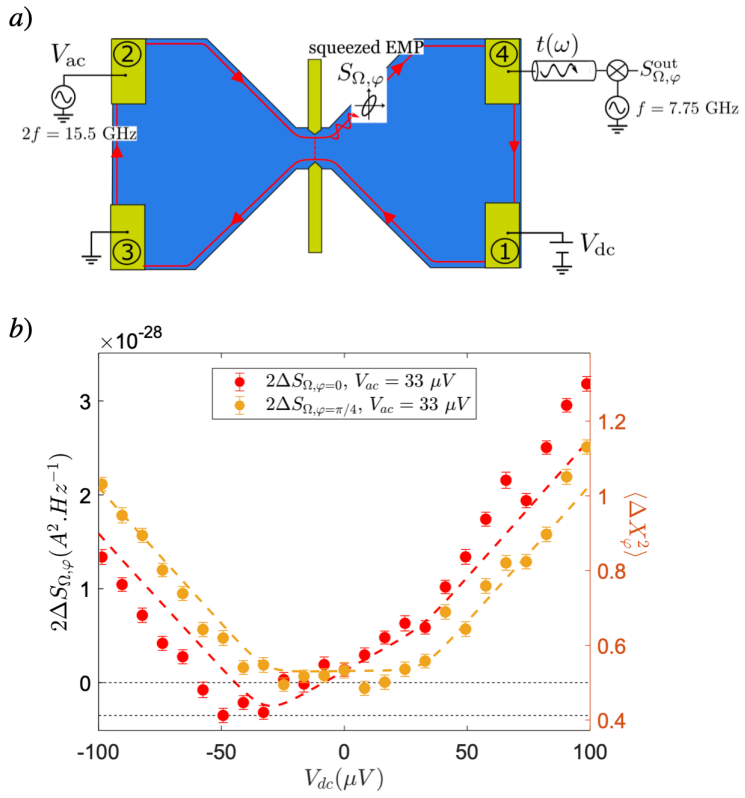

Figure 4.9: (a) Principle of the experiment by Bartolomei *et al.* [29]: EMP squeezing is generated at the QPC level by partitioning a DC drive and a sinusoidal AC voltage at frequency $2f = \Omega/\pi$. Squeezing is characterized by measuring the high frequency noise $S^{\text{out}}_{\Omega,\varphi}$ at the output. The phase φ of the measured quadrature is set by using a high frequency mixer fed by a local oscillator at frequency f and with a controllable phase φ locked in phase with the pump V_{AC}. (b) Measurements of $\Delta S_{\Omega,\varphi}$, for $\varphi = 0$ (red points) and $\varphi = \pi/4$ (yellow points) as a function of the DC bias voltage for $V_{\text{AC}} = 33\,\mu$V. The red and yellow dashed lines represent the theoretical predictions for $V_{\text{AC}} = 33\,\mu$V. Best agreement is obtained using the electronic temperature $T_{el} = 30\,$mK. Figures are taken from [29].

sors or in EMP cavities used as quantum buses to transmit quantum states between distant mesoscopic samples. For practical applications, it will be necessary to increase the degree of squeezing which could be achieved by replacing the sinusoidal temporal dependence of the AC drive by Lorentzian shaped current pulses.

Chapter 5

Delta-T noise for fractional quantum Hall states

In this final Chapter, starting from what introduced in Sections 1.2.2 and 1.5.4, we analyze the current fluctuation in a system where two different FQH edge states, belonging to the Laughlin sequence and coupled through a QPC, are connected to reservoirs placed at different temperatures. We solve exactly the problem for all couplings and for any set of temperatures in the specific case of $(1/3, 1)$ junction and we see that linear contributions in the temperature difference are predominant. This motivates us to focus on a situation where a small mismatch in temperatures is considered, which turns out to also be the most relevant for possible experimental implementations. Here, we derive a universal analytical expression which connects the delta-T noise to the equilibrium one valid for all generic pairs (ν_L, ν_R) up to the first order in the temperature difference. Results presented here are based on Ref. [183].

5.1 Introduction

As presented in Sec. 1.2.2, the FQHE takes its roots in the strong correlations among electrons due to Coulomb interaction. These edge states provide an interesting alternative with respect to the channels of the IQHE for the realization of EQO waveguides as seen for example in [184, 185]. From Chapter 1 we have understood that noise measurements are fundamental tools for the understanding of mesoscopic devices. As introduced in Sec. 1.5.4, systems connected to reservoirs kept at different temperatures have been experimentally [26, 92, 93, 94] and theoretically [95, 96, 97, 98, 99, 100, 101, 186] considered in recent years. The presence of a temperature gradient leads to a non-equilibrium contribution to the charge current noise known as delta-T noise which is expected to carry additional information on quantum correlations inside the systems, since it allows to address directly the tunneling density of states.

In this context, the delta-T noise was recently studied for FQH systems in a QPC geometry. Here, the delta-T contribution to the noise is quadratic, due to the symmetry of the considered set-up under the exchange of reservoirs, and it was found that the tunneling of quasiparticles is associated with negative values of the delta-T noise [96]. In other words, the non-equilibrium noise induced by the temperature mismatch between the two channels of this correlated state turns out to be smaller than the equilibrium one. Conversely, when electrons tunnel from one edge to the other, the delta-T noise becomes positive. While it was shown that interactions alone could not account for such negative delta-T noise, it was put forward that, in several recent

works, negative contributions to the noise were attributed to braiding effects, albeit in different configurations [187, 188]. More recently, this connection was further explored [100], and shown to be merely a byproduct of the true physical mechanism at play [101]. It was shown that the sign of the delta-T noise was uniquely determined by the scaling dimension of the tunneling operator.

It follows that the study of the delta-T noise can thus be exploited in order to investigate the properties of strongly interacting systems, in a way that cannot be addressed by the usual voltage-induced noise. Moreover, the absence of any bias voltage allows one to discard some of the non-universal effects (changes in the electrostatic properties of the point contact, slight modifications of the edge confining potential) that typically make the comparison with experimental data all the more difficult.

5.2 Model of the junction

In this Chapter, we consider two FQH bars at different filling factors ν_α ($\alpha = L, R$) belonging to the Laughlin sequence introduced in Sec. 1.2.2. They are kept at different temperatures T_L and T_R and coupled through a point-like tunneling region as depicted in Fig. 5.1. Since we are dealing with strong interacting systems, the edge states are described in terms of the hydrodynamical model, introduced in Sec. 2.3, by a chiral Luttinger liquid with free Hamiltonian of the form

$$H^{(0)} = H_L^{(0)} + H_R^{(0)} = \sum_{\alpha=L,R} \frac{v_\alpha}{4\pi} \int dx \left[\partial_x \phi_\alpha(x)\right]^2, \qquad \alpha = L, R \tag{5.1}$$

which comes from Eq. (2.23). Quite generally, the velocities $v_{L,R}$ along the two edges can be different. However, in what follows, we focus on the situation where the tunneling occurs at a specific point, allowing us to rescale the position coordinates independently for the two bosonic fields. This in turn enables us to alter the velocities at will, so that, for sake of simplicity, we will assume the same propagation velocity for the two edges ($v_L = v_R = v$). The bosonic fields ϕ_α satisfy the commutators in Eq. (2.54) and are related to the particle density through the relation

$$\rho_\alpha(x) = \frac{\sqrt{\nu_\alpha}}{2\pi} \partial_x \phi_\alpha(x). \tag{5.2}$$

Then, the electron annihilation operator $\psi_\alpha(x)$ is expressed in terms of $\phi_\alpha(x)$ following Eq. (2.47).

We assume that the two QH systems are coupled via a QPC, placed at position $x = 0$, which allows local tunneling between the two counter-propagating edges. In practice, there is no bulk Hall fluid in between the two edge states, so that the only allowed tunneling process involves electrons [189]. This configuration, where only electrons can locally tunnel from one lead to the other, is described by the tunneling Hamiltonian

$$\begin{aligned} H_\Lambda &= \Lambda \int dx\, \delta(x)\, \psi_R^\dagger(x) \psi_L(x) + \text{H.c.} = \\ &= \frac{\Lambda}{2\pi a} e^{i\frac{1}{\sqrt{\nu_R}}\phi_R(0)} e^{-i\frac{1}{\sqrt{\nu_L}}\phi_L(0)} + \text{H.c.}, \end{aligned} \tag{5.3}$$

where the second line stands from Eq. (2.47) and Λ is a constant tunneling amplitude strength [189, 190, 191, 192]. Notice that the QPC description conventionally used

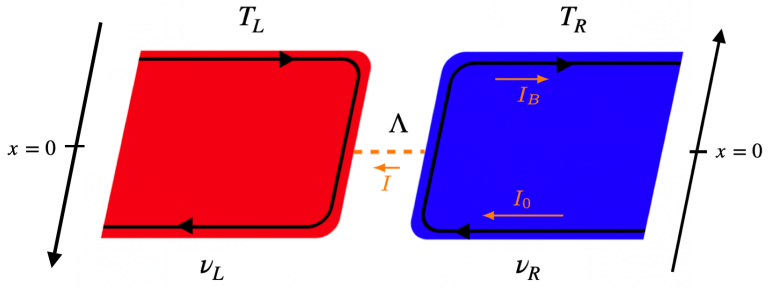

Figure 5.1: Sketch of two fractional quantum Hall systems with different filling factors (ν_L and ν_R) belonging to Laughlin sequence and at different temperatures (T_L and T_R). Counter-propagating edge states are coupled via a point-like tunneling (orange dashed line) placed in $x = 0$ with Λ being the constant tunneling amplitude strength. Notice that the x-axis follows the chirality of the channels. In orange, we have highlighted the impinging current on the QPC I_0, related to the quantized Hall conductance, the tunneling current I and the backscattering one I_B.

to model the tunneling between QH edge states is valid as long as the width of the tunneling region is of the order of the magnetic length. This situation is typically quite well achieved in experiments devoted to noise measurement in quantum Hall systems [193]. Generalization of this picture towards extended contacts have been considered [194, 195]. In this situation additional effects such as disorder at the level of the contact or interferences due to the formation of Aharonov-Bohm loops could come into play and need to be properly taken into account.

The current operator $I(t)$ describing the tunneling current flowing from one edge state to the other is obtained from the tunneling Hamiltonian and reads

$$\begin{aligned} I(t) &= -e\dot{N}_R = ie[N_R, H_\Lambda] = ie\Lambda\psi_R^\dagger(t)\psi_L(t) + \text{H.c.} \\ &= ie\frac{\Lambda}{2\pi a}e^{i\frac{1}{\sqrt{\nu_R}}\phi_R(t)}e^{-i\frac{1}{\sqrt{\nu_L}}\phi_L(t)} + \text{H.c.}, \end{aligned} \tag{5.4}$$

with $N_\alpha = \int dx \rho_\alpha(x)$ the particle numbers on each edge and where the notation only keeps track of the time dependence of the field operators omitting the fact that they are evaluated at the QPC in $x = 0$. Notice that in the second line, we have rewritten the fermionic operators in terms of the bosonic ones following the prescription in Eq. (2.47). The current operator can be rewritten as

$$I(t) = -e\dot{N}_R = -e\int_{-\infty}^{+\infty} dx\ \partial_t\rho_R(x,t) = ie\int_{-\infty}^{+\infty} dx\ \left[\rho_R(x,t), H_\Lambda\right]. \tag{5.5}$$

Since H_Λ only involves fields at the position of the QPC, the resulting commutator is nonzero only close to $x = 0$. This allows to write

$$I(t) = ie\int_{0^-}^{0^+} dx\ \left[\rho_R(x,t), H_\Lambda\right] = -e\int_{0^-}^{0^+} dx\ \partial_t\rho_R(x,t). \tag{5.6}$$

Exploiting the chirality and linear dispersion of edge states, one can readily write the continuity relation of Eq. (2.35) for $\rho_R(x)$, so that the current can be expressed in terms of the densities right before ($x = 0^-$) and right after ($x = 0^+$) the QPC as

$$I(t) = ev\left[\rho_R(0^+,t) - \rho_R(0^-,t)\right]. \tag{5.7}$$

5.2.1 From different to identical chiral Luttinger liquids

We now consider, differently from Eq. (2.56), another suitable rotation in the bosonic field space [196]

$$\begin{pmatrix}\varphi_L(x)\\ \varphi_R(x)\end{pmatrix} = \begin{pmatrix}\cos\zeta & \sin\zeta\\ -\sin\zeta & \cos\zeta\end{pmatrix}\begin{pmatrix}\phi_L(x)\\ \phi_R(x)\end{pmatrix}, \tag{5.8}$$

with angle satisfying

$$\sin 2\zeta = \frac{\nu_R - \nu_L}{\nu_R + \nu_L}. \tag{5.9}$$

The total Hamiltonian $H = H^{(0)} + H_\Lambda$ is then rewritten as

$$H = \sum_{\alpha=L,R}\frac{v}{4\pi}\int dx\big[\partial_x\varphi_\alpha(x)\big]^2 + \frac{\Lambda}{2\pi a}e^{i\frac{1}{\sqrt{g}}\left[\varphi_R(0)-\varphi_L(0)\right]} + \text{H.c.} \tag{5.10}$$

which corresponds to the tunneling between two identical chiral Luttinger liquids with effective filling factor

$$g^{-1} = \frac{1}{2}\left(\frac{1}{\nu_L}+\frac{1}{\nu_R}\right). \tag{5.11}$$

In this way we map the problem of electron tunneling between different FQH edges into the problem of electron tunneling between two identical chiral Luttinger liquids with the same effective filling factor g. This mapping can be visualized passing from Fig. 5.2(a) to Fig. 5.2(b).

Moreover, a further transformation is introduced

$$\begin{aligned}\varphi_+(x) &= \frac{1}{\sqrt{2}}\big[\varphi_L(x)+\varphi_R(x)\big]\\ \varphi_-(x) &= \frac{1}{\sqrt{2}}\big[\varphi_L(x)-\varphi_R(x)\big].\end{aligned} \tag{5.12}$$

According to this, the free Hamiltonians become

$$\begin{aligned}H^{(0)}_{L/R} = \frac{v}{4\pi}\int dx\Big\{&\frac{1}{2}(\cos\zeta\mp\sin\zeta)^2[\partial_x\varphi_+(x)]^2 +\\ &+\frac{1}{2}(\sin\zeta\pm\cos\zeta)^2[\partial_x\varphi_-(x)]^2 \pm(\cos^2\zeta-\sin^2\zeta)[\partial_x\varphi_+(x)][\partial_x\varphi_-(x)]\Big\}\end{aligned} \tag{5.13}$$

and their sum depends on the new fields $\varphi_\pm$ separately

$$H^{(0)}_L + H^{(0)}_R = \frac{v}{4\pi}\int dx\,\big\{\,[\partial_x\varphi_+(x)]^2 + [\partial_x\varphi_-(x)]^2\,\big\}. \tag{5.14}$$

Then, the total Hamiltonian of Eq. (5.10) is rewritten as

$$H = \frac{v}{4\pi}\int dx\big[\partial_x\varphi_+(x)\big]^2 + \frac{v}{4\pi}\int dx\big[\partial_x\varphi_-(x)\big]^2 + \left[\frac{\Lambda}{2\pi a}e^{i\sqrt{\frac{2}{g}}\varphi_-(0)} + \text{H.c.}\right] \tag{5.15}$$

The transformation of Eq. (5.12) allows us to decouple the problem of the two FQH liquids with same g into two separate ones (see Fig. 5.2(c)): the first depending only on the free field φ_+ and the second one which includes the tunneling contribution and that can be written only in terms of the field φ_-.

From a physical point of view, by looking at Fig. 5.2(a), when the two systems are totally decoupled (*i.e.* $\Lambda = 0$) if an electron is sent from one of the two QH bars, it is perfectly reflected at the contact and there is no net current flowing through the junction. However, if we consider a weak coupling limit, for which the two edges are almost decoupled (*i.e.* Λ is small but non-zero), the electrons are allowed to jump from one side to the other.

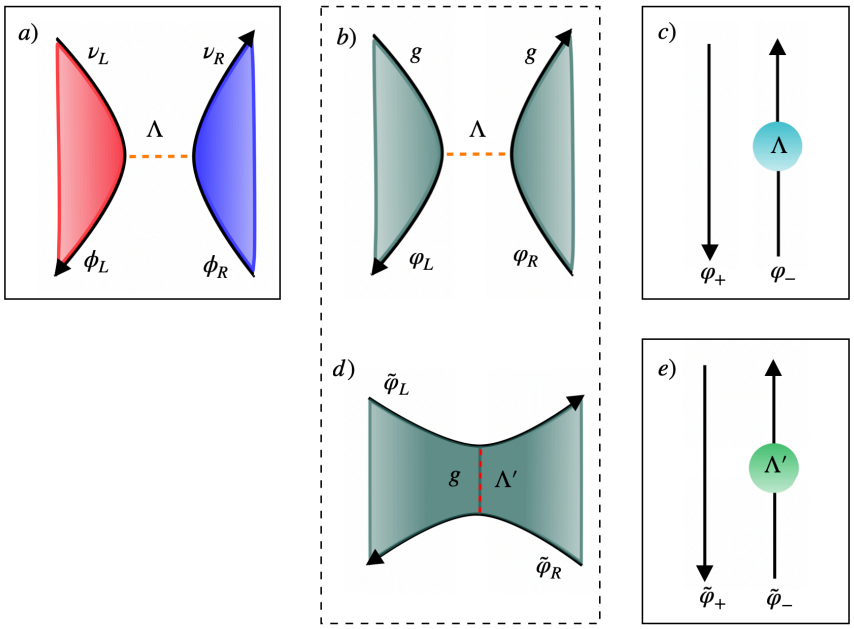

Figure 5.2: (a) Scheme of the two FQH systems with filling factors $\nu_{L/R}$ whose edges are described by the bosonic fields $\phi_{L/R}$. (b) This panel is obtained through the rotation in Eq. (5.8) which maps the original junction, with tunneling parameter Λ, between two different FQH liquids to one between FQH with the same effective filling factor g. (c) The rotation in Eq. (5.12) decouples the problem into two separate ones: one free channel and the other describing a channel with the QPC referred as a localized impurity. (d) The duality relation in Eq. (5.20) allows to map the problem of two FQH liquids in the weak coupling regime, where electrons can tunnel, to the strong coupling one described by a single FQH liquid, with filling factor g and tunneling parameter Λ'. In this configuration, the quasi-particles provide the dominant contribution to the tunneling. (e) The further rotation in Eq. (5.23) decouples the problem into two separate ones in analogy with (c).

5.2.2 Delta-T noise

The expectation value of the current operator in Eq. (5.4) is given by

$$\langle I(t)\rangle \equiv \mathcal{I} = \frac{1}{Z}\,\mathrm{Tr}\left\{\exp\left[-\sum_{\alpha=L,R}\frac{H_\alpha^{(0)}}{T_\alpha}\right] I(t)\right\}, \tag{5.16}$$

with

$$Z = \mathrm{Tr}\left\{\exp\left[-\sum_{\alpha=L,R}\frac{H_\alpha^{(0)}}{T_\alpha}\right]\right\}. \tag{5.17}$$

Here, we are assuming that, at the time $t \to -\infty$, the tunneling is switched-off and the two bars are at thermal equilibrium. This leads to the initial density matrix $\varrho_0 = (1/Z)\exp\big[-\sum_\alpha H_\alpha^{(0)}/T_\alpha\big]$ [197]. The tunneling is then turned-on establishing a stationary current. Moreover, since we are considering no voltage bias and local tunneling, the total net current $\mathcal{I}$ is zero independently of the respective temperatures of the two edges. This is due to the fact that the transmission function is energy independent and electrons and holes contribute equally [198, 199]. However, since

the finite temperature always leads to a non-zero contribution to the noise, through thermal fluctuations [23, 24], the current-current fluctuations do not vanish. This charge current noise induced by the mismatch in the temperatures has been dubbed delta-T noise. As already discussed in Section 1.5.4, it has a purely thermal origin, but it is only generated in non-equilibrium situations [26, 93, 94, 96].

As in Equation (1.52), the zero-frequency current noise is written as

$$\begin{aligned} S\left(T_L, T_R\right) &= 2\int_{-\infty}^{+\infty} d\tau \left\langle \Delta I(\tau)\Delta I(0)\right\rangle = \\ &= 2\int_{-\infty}^{+\infty} d\tau \left[\frac{1}{Z}\,\mathrm{Tr}\left\{\exp\left[-\sum_{\alpha=L,R}\frac{H_\alpha^{(0)}}{T_\alpha}\right]\Delta I(\tau)\Delta I(0)\right\}\right] \end{aligned} \tag{5.18}$$

where $\Delta I(t)$ is defined in Eq. (1.49).

As already introduced in Eq. (1.70), we will also consider, for the following, the temperature parametrization

$$T_R = T \qquad T_L = T_R + \Delta T, \tag{5.19}$$

which is convenient from an experimental point of view. Here, the temperature of one of the two FQH sample is kept fixed at T, while the other can be varied with ΔT either positive or negative.

5.3 Duality relation

Let us focus now on the configuration of Fig. 5.2(b), after the change of basis introduced in Eq. (5.8), where we move from an inhomogeneous QH junction to two separate FQH liquids at the same filling factor g. In this effective picture, as the tunneling amplitude increases up to the limit value $\Lambda \to \infty$ (*i.e.* strong coupling), we switch from the two identical, but separate, FQH liquids to a unique one [see Fig. 5.2(d)]. In analogy to what happens for the Laughlin states, the dynamics of the point contact evolves from being dominated by electron tunneling at weak coupling, where the fluid is pinched off, to a strong coupling regime where quasiparticle tunneling dominates [193, 200]. This process is embodied by a powerful electron-quasiparticle duality [189, 201] which reflects the duality relation between the weak- and strong-coupling limits. In particular, the strong coupling limit is accessible through a weak-strong duality transformation [202, 203, 204]. This fact is graphically described in Fig. 5.2 by the central panels surrounded by a dashed line. In this limit, the fields $\varphi_{L,R}$ can be written in terms of dual fields $\widetilde{\varphi}_{L,R}$ defined as

$$\begin{aligned} \varphi_L(x) &= \widetilde{\varphi}_L(x)\Theta(-x) + \widetilde{\varphi}_R(x)\Theta(x) \\ \varphi_R(x) &= \widetilde{\varphi}_L(x)\Theta(x) + \widetilde{\varphi}_R(x)\Theta(-x) \end{aligned} \tag{5.20}$$

with $\Theta(\pm x)$ the step function. This dual transformation can be geometrically understood by thinking about the fact that in the strong coupling limit the previous bosonic states φ_L and φ_R are mixed since now there is only one QH liquid. This non-local relation, due to the step function, recall the starting point of two different QH sample separated by a QPC.

Due to the above considerations the total Hamiltonian describing the dynamics and the coupling of these fields is now

$$\widetilde{H} = \sum_{\alpha=L,R}\frac{v}{4\pi}\int dx\,[\partial_x\widetilde{\varphi}_\alpha(x)]^2 + \frac{\Lambda'}{2\pi a}e^{i\sqrt{g}\left[\widetilde{\varphi}_R(0)-\widetilde{\varphi}_L(0)\right]} + \text{H.c.} \tag{5.21}$$

Notice that this last Hamiltonian is the dual of the one in Eq. (5.10) where we have considered the substitution $g \to 1/g$ due to the electron-quasiparticle mapping and we have introduced an effective coupling parameter Λ'. However, the two tunneling strengths Λ and Λ' are not independent as they are connected by the relation [205]

$$\left(\frac{\Lambda'}{\omega_c a}\right) = \left[2^{-2g+1}\,\Gamma^g\left(1+\frac{1}{g}\right)\Gamma(1+g)\right]\left(\frac{\Lambda}{\omega_c a}\right)^{-g} \tag{5.22}$$

where $\omega_c = v/a$ is related to the short-distance cut-off a and $\Gamma(x)$ is the Euler Gamma function of a given argument x. Due to the inverse proportionality between Λ and Λ', focusing on the $\Lambda \to \infty$ limit is equivalent to consider $\Lambda' \to 0$ and vice versa, consistently with the discussed weak-strong coupling duality. The previous relation has been obtained in Ref. [205] by considering an expansion of the non-linear conductance in the two different regimes in terms of the weak and strong coupling parameters.

The formulation of the problem in terms of the dual fields $\widetilde{\varphi}_{L/R}$ in the strong coupling limit ($\Lambda \to \infty$ or $\Lambda' \to 0$) has the advantage that these are now free fields. The quasi-particles which tunnels are non-interacting and carry a charge $e^* = ge$. Quite remarkably, these effective fractionally charged excitations correspond neither to electrons nor to quasiparticles of the isolated Hall fluids, but instead to complicated nonlocal objects emerging from the dynamics of the two strongly coupled edge channels as a whole.

By introducing the fields

$$\widetilde{\varphi}_{\pm}(x) = \frac{1}{\sqrt{2}}\big[\widetilde{\varphi}_L(x) \pm \widetilde{\varphi}_R(x)\big], \tag{5.23}$$

the Hamiltonian of Eq. (5.21) leads again to two decoupled systems (see Fig. 5.2(e)) with total Hamiltonian $\widetilde{H} = \widetilde{H}_+ + \widetilde{H}_-$ where

$$\begin{aligned} \widetilde{H}_+ &= \frac{v}{4\pi}\int dx\big[\partial_x\widetilde{\varphi}_+(x)\big]^2 \\ \widetilde{H}_- &= \frac{v}{4\pi}\int dx\big[\partial_x\widetilde{\varphi}_-(x)\big]^2 + \left[\frac{\Lambda'}{2\pi a}e^{i\sqrt{2g}\widetilde{\varphi}_-(0)} + \text{H.c.}\right]. \end{aligned} \tag{5.24}$$

5.4 Exact solution for tunneling in a $\left(\frac{1}{3},1\right)$ junction

In this Section we focus on a junction between a normal metal ($\nu_R = 1$) and a FQH state with filling factor $\nu_L = 1/3$ in the presence of a temperature difference between the Hall bars. This case can be exactly solved via refermionization for the entire range of couplings and temperatures allowing us to evaluate the delta-T noise exactly.

5.4.1 Refermionization

The case $\nu_R = 1$ and $\nu_L = 1/3$ leads to a description, in terms of an effective filling factor $g = 1/2$ (see Eq. (5.11)). In the rotated basis, and taking into account the duality, one can consider a tunneling Hamiltonian proportional to the factor $e^{i\widetilde{\varphi}_-}$ (see Eq. (5.24)), which looks like an electronic operator. It thus becomes possible to introduce a new fermionic field and re-express the tunneling term accordingly, ultimately allowing us to diagonalize exactly the Hamiltonian, and therefore account for tunneling at all orders.

This idea of refermionization was first introduced in Ref. [206] in the framework of quantum dissipative systems, and subsequently applied to the case FQH states [207]. It amounts to refermionize the bosonic field $\widetilde{\varphi}_-$ so that the tunneling term of the Hamiltonian $\widetilde{H}_-$ in Eq. (5.24) now takes the form

$$\frac{\Lambda'}{2\pi a}e^{i\widetilde{\varphi}_-(0)} + \text{H.c.} \longrightarrow \frac{\Lambda'}{\sqrt{2\pi a}} f\psi^\dagger(0) + \text{H.c.}\,, \tag{5.25}$$

where we remind that $x = 0$ is the position of the QPC. Here f is an auxiliary (Majorana) fermion field which arises from the proper handling of the zero modes of the bosonic fields. In particular, the new fields $\psi(x)$ and f satisfy the following set of equations of motion

$$\begin{aligned} -i\partial_t\psi(x,t) =& iv\partial_x\psi(x,t) + \frac{\Lambda'}{\sqrt{2\pi a}} f(t)\delta(x) \\ -i\partial_t\psi^\dagger(x,t) =& iv\partial_x\psi^\dagger(x,t) - \frac{\Lambda'}{\sqrt{2\pi a}} f(t)\delta(x) \\ -i\partial_t f(t) =& 2\frac{\Lambda'}{\sqrt{2\pi a}}\left[\psi(0,t) - \psi^\dagger(0,t)\right]. \end{aligned} \tag{5.26}$$

From this, one can map the problem into the scattering of the right-mover ψ on a localized impurity. These equations are then solved by introducing a plane-wave decomposition of the fermionic field ψ as

$$\psi(x,t) = \begin{cases} \int d\omega A_\omega e^{i\omega\frac{x}{v}} e^{-i\omega t} & \text{for } x < 0 \\ \int d\omega B_\omega e^{i\omega\frac{x}{v}} e^{-i\omega t} & \text{for } x > 0 \end{cases} \tag{5.27}$$

$$\psi^\dagger(x,t) = \begin{cases} \int d\omega A^\dagger_{-\omega} e^{i\omega\frac{x}{v}} e^{-i\omega t} & \text{for } x < 0 \\ \int d\omega B^\dagger_{-\omega} e^{i\omega\frac{x}{v}} e^{-i\omega t} & \text{for } x > 0. \end{cases} \tag{5.28}$$

Substituting these back into the equations of motion, using the definition

$$\psi(0) = \frac{1}{2}\left[\psi(0^+) + \psi(0^-)\right] \tag{5.29}$$

and integrating around the $\delta(x)$ function, one is left with

$$\begin{aligned} 0 =& iv\int d\omega\big(B_\omega - A_\omega\big)e^{-i\omega t} + \frac{\Lambda'}{\sqrt{2\pi a}} f(t) \\ 0 =& iv\int d\omega\big(B^\dagger_{-\omega} - A^\dagger_{-\omega}\big)e^{-i\omega t} - \frac{\Lambda'}{\sqrt{2\pi a}} f(t) \\ -i\partial_t f(t) =& \frac{\Lambda'}{\sqrt{2\pi a}}\left[\int d\omega\big(B_\omega + A_\omega\big)e^{-i\omega t} + \right. \\ & \left. - \int d\omega\big(B^\dagger_{-\omega} + A^\dagger_{-\omega}\big)e^{-i\omega t}\right]. \end{aligned} \tag{5.30}$$

Combining these equations to get rid of f and $B^\dagger$, one obtains

$$B_\omega = \frac{-i\omega}{\mathcal{T}_k - i\omega} A_\omega + \frac{\mathcal{T}_k}{\mathcal{T}_k - i\omega} A^\dagger_{-\omega}, \tag{5.31}$$

where we introduced the crossover energy scale

$$\mathcal{T}_k = \frac{4\pi a}{v}\left(\frac{\Lambda'}{2\pi a}\right)^2 \tag{5.32}$$

which is set by the tunneling amplitude Λ'. Following Ref. [205], the previous relation can be generalized for all filling factors taking the form

$$\mathcal{T}_k = \frac{2\omega_c}{g}\left(\frac{1}{2\Gamma(g)}\frac{\Lambda'}{a\omega_c}\right)^{\frac{1}{1-g}}. \tag{5.33}$$

Performing the Fourier transform back to the time domain one finally obtains the following relation between the Fourier components of the fermionic field ψ before (A) and after (B) the QPC as

$$B(t) = A(t) - \mathcal{T}_k \int_{-\infty}^{t} e^{-\mathcal{T}_k(t-t')}\left[A(t') - A^\dagger(t')\right]. \tag{5.34}$$

In Refs. [196] and [207], all relevant transport quantities are then written down only in terms of averages of this newly defined fermionic A field, which is free by construction. The corresponding propagator was naturally assumed to be trivially given by a Fermi function, corresponding to the reservoirs at equilibrium, *i.e.* equal temperature.

However, as we can see from Eq. (5.27), the new fermion ψ is actually made of combined quasiparticles from the right and left reservoirs which, in our present case, correspond to different temperatures. One therefore needs to be particularly careful in expressing the propagator. One way of doing this is to revert to the bosonic description and to write ψ in terms of the bosonic fields $\phi_{R,L}$, taken at a position before the QPC, which are then uncoupled from each other. The full calculation of the propagator is detailed in Appendix F, here we report the final result for a $(1/3,1)$ junction which reads

$$\langle A^\dagger(t)A(t')\rangle = \langle \psi^\dagger(0^-,t)\psi(0^-,t')\rangle = \frac{1}{2\pi a} e^{\frac{3}{4}\mathcal{G}_L(t-t')} e^{\frac{1}{4}\mathcal{G}_R(t-t')} \tag{5.35}$$

where, since A is only defined at a position before the QPC, the quantum averaging is performed on the state where the two edge states are decoupled and at their respective temperature T_α. Following Eq. (1.96), the bosonic Green's function is written as [79]

$$\mathcal{G}_\alpha(\tau) = -\log\left[\frac{\sinh\left(\pi T_\alpha(\frac{i}{\omega_c}-\tau)\right)}{\sinh\left(\frac{i}{\omega_c}\pi T_\alpha\right)}\right]. \tag{5.36}$$

In practice, we will be needing two types of correlators, which we express from their Fourier transform as

$$\langle A^\dagger(t)A(t')\rangle = \int \frac{d\omega}{2\pi v} e^{i\omega(t-t')} n_\omega \tag{5.37}$$

$$\langle A(t)A^\dagger(t')\rangle = \int \frac{d\omega}{2\pi v} e^{-i\omega(t-t')}(1-n_\omega) \tag{5.38}$$

where according to Eq. (5.35), one has

$$n_\omega = \int d\tau e^{-i\omega\tau}\frac{\omega_c}{2\pi} e^{\frac{3}{4}\mathcal{G}_L(\tau)} e^{\frac{1}{4}\mathcal{G}_R(\tau)}. \tag{5.39}$$

Note that although n_ω is not, in all generality, a Fermi distribution, the field A is a fermionic field and thus satisfies the standard anti-commutation relations (see Eq. (2.6)).

5.4.2 General expression of the delta-T noise for $\left(\frac{1}{3},1\right)$ junction

In order to evaluate the noise in Eq. (5.18) we need to consider the fluctuations of the tunneling current. The latter, in Eq. (5.7), is expressed in terms of the imbalance of the right densities before and after the QPC which are related to the Fourier components of the fermionic field ψ before (A) and after (B) the QPC (see Appendix G for more details), namely

$$I(t) = ev\big[\rho_R(0^+,t) - \rho_R(0^-,t)\big] = \frac{ev}{2}\Big[B^\dagger(t)B(t) + A^\dagger(t)A(t)\Big]. \tag{5.40}$$

This expression can readily be understood from a current conservation perspective as the current tunneling between edges naturally corresponds to the difference of the current impinging on and the one outgoing from the QPC.

From Eqs. (1.50) and (5.40), the fluctuations of the tunneling current are then readily given by

$$C(t_1,t_2) = \left(\frac{ev}{2}\right)^2 \big\langle \big[B^\dagger(t_1)B(t_1) + A^\dagger(t_1)A(t_1)\big]\cdot\big[B^\dagger(t_2)B(t_2) + A^\dagger(t_2)A(t_2)\big]\big\rangle \tag{5.41}$$

where one should only keep the connected contributions of the thermal average.

Since we are interested in the zero-frequency current noise given in Eq. (5.18), the final result reads

$$\begin{aligned} S(T_L,T_R) = 2\int_{-\infty}^{+\infty} d\tau\, C(0,\tau) = 2\left(\mathcal{T}_k\frac{e}{2}\right)^2 \int \frac{d\omega}{2\pi}\Bigg\{2\big[n_\omega n_{-\omega} + \\ + (1-n_\omega)(1-n_{-\omega})\big]\left(\frac{\omega}{\mathcal{T}_k^2+\omega^2}\right)^2 + n_\omega(1-n_\omega)\left(\frac{2}{\mathcal{T}_k}\frac{\omega^2}{\mathcal{T}_k^2+\omega^2}\right)^2\Bigg\} \end{aligned} \tag{5.42}$$

where all the detailed calculations are reported in Appendix H. It is worth noticing that, since we are considering the noise induced by a temperature difference, the distribution function n_ω depends on both temperatures as

$$n_\omega = \int d\tau e^{-i\omega\tau}\frac{\omega_c}{2\pi}\left[\frac{\sinh(\frac{i}{\omega_c}\pi T_L)}{\sinh(\pi T_L(\frac{i}{\omega_c}-\tau))}\right]^{3/4}\left[\frac{\sinh(\frac{i}{\omega_c}\pi T_R)}{\sinh(\pi T_R(\frac{i}{\omega_c}-\tau))}\right]^{1/4}. \tag{5.43}$$

Using that $n_\omega + n_{-\omega} = 1$, the noise can be written under a much simpler form as

$$S(T_L,T_R) = e^2\int\frac{d\omega}{2\pi}n_\omega(1-n_\omega)\left(1-\frac{\mathcal{T}_k^2-\omega^2}{\mathcal{T}_k^2+\omega^2}\right). \tag{5.44}$$

The noise can be obtained numerically for any set of temperatures T_L, T_R and the information on the coupling strength is encoded in the energy crossover $\mathcal{T}_k$ which allows to scan for the entire range of tunneling regimes.

In Fig. 5.3, we show the full delta-T noise (as defined in Eq. (5.18)) as a function of the temperature difference, in unit of $\mathcal{T}_k$, for six different cuts. It comes out that in the weak to moderate temperature bias regime, the leading contribution to the noise is linear in ΔT, a feature that can be readily confirmed analytically as we show in Appendix H. This leading linearly-ΔT behavior survives even if one changes the temperature parametrization, introducing the average temperature $\bar{T} = (T_R + T_L)/2$. This may come as a surprise as it is in stark contrast with the results obtained for the homogeneous case ($\nu_R = \nu_L = \nu$) [96] where the dominant term was quadratic in the

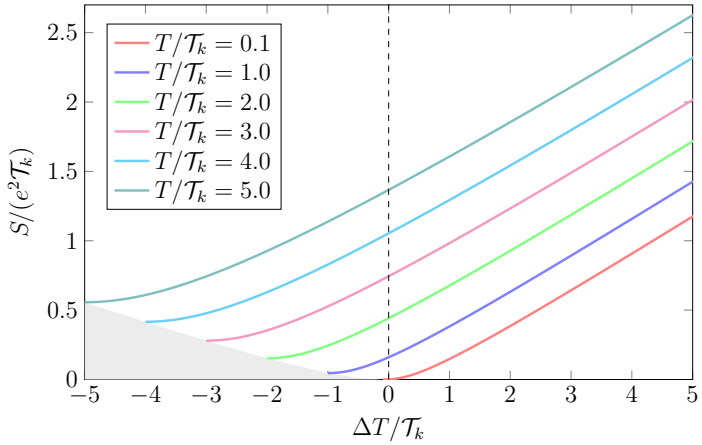

Figure 5.3: Full noise S for the $(1/3, 1)$ junction, as a function of the temperature difference ΔT (given in units of the energy scale $\mathcal{T}_k$) for different values of the right lead temperature, $T/\mathcal{T}_k = 0.1, 1, 2, 3, 4$ and 5. The gray area corresponds to the unphysical region where $T_L = T + \Delta T < 0$.

temperature difference. Indeed, in this latter situation, one is protected from such a linear contribution because of the symmetry of the system under the exchange of right and left leads, ensuring that only even terms in ΔT survive. The inhomogeneous case considered here breaks this symmetry, thus enabling linear contributions which then dominate the noise in the regime of weak temperature bias.

Notice that in presence of an extended contact, disorder effects could lead to asymmetries also in in homogeneous case. This could lead to a noise contribution linear in the temperature mismatch. However, we expect this contribution to be sample dependent and not universally related to the scaling dimension of the tunneling operators differently from the one we are investigating (see below). From the experimental standpoint, the emergence of a linear correction as a function of the temperature difference constitutes a major improvement compared to the homogeneous case as it makes the delta-T noise a lot easier to probe.

In this Section we have been able to solve exactly the problem of tunneling between a QH junction with the only constraint on filling factors, being $\nu_L = 1/3$ and $\nu_R = 1$. This interesting result can be enriched by extending to a general dependence of the noise on filling factors without specifying their values *a priori*. Moreover, in addition to the numerical evaluation, it could be interesting to work out an analytic expression for the delta-T noise. As we will see below, this can be achieved for comparable temperatures of the two QH bars, as this approach relies on an expansion in the temperature difference ΔT. Nevertheless, considering small temperature differences allows us to be closer to the experimentally realistic situation, where large temperature gradients between reservoirs are difficult to control.

5.5 Universal expression for the delta-T noise

In this Section, we derive a universal formula for the first order expansion of the noise in Eq. (5.18) that applies to all orders in the tunneling amplitude Λ and for any set of filling factors (ν_L, ν_R).

Since we are considering different temperatures between the two QH bars, parametrized

as in Eq. (5.19), and according to the rotations introduced in previous Sections, we can expand the noise $S(T_L, T_R)$ up to the first order in the ratio $\Delta T/T$. Following the calculations given in Appendix I, one has

$$\begin{aligned} S(T_L, T_R) = S_0(T) + \frac{\Delta T}{T^2} \int_{-\infty}^{+\infty} d\tau \, \frac{1}{Z} \times \\ \times \mathrm{Tr}\Big\{ e^{-\beta(H_+^{(0)}+H_-^{(0)})} H_{+,-} I(\varphi_-(\tau)) I(\varphi_-(0)) \Big\} + O(\Delta T^2) \end{aligned} \tag{5.45}$$

where $\beta = T^{-1}$ and the mixed term $H_{+,-}$ due to the expansion in ΔT is given by

$$\begin{aligned} H_{+,-} = & \frac{v}{4\pi} \int dx \Big[\frac{\cos^2\zeta}{2} (\partial_x \varphi_+ + \partial_x \varphi_-)^2 + \\ & - \sin\zeta \cos\zeta (\partial_x \varphi_+ + \partial_x \varphi_-)(\partial_x \varphi_+ - \partial_x \varphi_-) + \frac{\sin^2\zeta}{2} (\partial_x \varphi_+ - \partial_x \varphi_-)^2 \Big]. \end{aligned} \tag{5.46}$$

In Eq. (5.45), $S_0(T)$ is the equilibrium noise at $\Delta T = 0$, namely

$$\begin{aligned} S_0(T) &= S(T_L, T_R)\Big|_{\Delta T=0} = \\ &= \frac{1}{Z_+^{(0)} Z_-^{(0)}} \int_{-\infty}^{+\infty} d\tau \, \mathrm{Tr}\Big\{ e^{-\beta(H_+^{(0)}+H_-^{(0)})} I(\varphi_-(\tau)) I(\varphi_-(0)) \Big\}, \end{aligned} \tag{5.47}$$

with

$$Z_\pm^{(0)} = \mathrm{Tr}\Big\{ e^{-\beta H_\pm^{(0)}} \Big\}. \tag{5.48}$$

Furthermore, in Eq. (5.45) one needs to consider also the first order expansion of Z which reads

$$Z = \mathrm{Tr}\Big\{ e^{-\beta(H_+^{(0)}+H_-^{(0)})} \Big(1 + \frac{\Delta T}{T^2} H_{+,-} \Big) \Big\}. \tag{5.49}$$

Finally, putting everything together, the delta-T noise of Eq. (5.18), expanded to first order in ΔT, reads

$$S(T_L, T_R) = S_0(T) + \Sigma(\nu_L, \nu_R, T)\, \Delta T + O(\Delta T^2) \tag{5.50}$$

with

$$\Sigma(\nu_L, \nu_R, T) = -\Big(\frac{\nu_R}{\nu_R + \nu_L} \Big) \frac{1}{T^2} \frac{\partial S_0}{\partial \beta}. \tag{5.51}$$

We underline the relevance of this result which enables to calculate the first order correction to the noise in the temperature gradient only by knowing the expression for the equilibrium noise $S_0(T)$. In particular, our derivation does not require any assumption concerning the strength of the tunneling between the two QH bars. This allows us to obtain the out-of-equilibrium delta-T noise in various tunneling regimes, provided that one is able to compute the corresponding thermal noise at equilibrium. Since Eqs. (5.50) and (5.51) are valid for all values of Λ, it is worth noticing that they can be exploited for describing both the weak-coupling regime and the dual strong-coupling model.

5.6 Explicit results for the delta-T noise

In the previous Section, we have showed that it is possible to obtain a universal expression for the delta-T noise at first order in $\Delta T/T$, without specifying the tunneling strength between the two QH systems.

Here, we investigate in details the two opposite regimes of weak and strong coupling between the two Hall fluids. We start by applying our universal formula, Eq. (5.50), to the specific case of the ($\nu_L = 1/3$, $\nu_R = 1$) junction. There, an exact expression of the equilibrium noise can be derived at all orders in the tunnel coupling [196], following the refermionization procedure introduced in the previous Section. Then, we generalize this approach for a system with generic filling factor combinations, concentrating on the two opposite regimes of the coupling strength. It is worth emphasizing that, although our focus is on the weak and strong coupling regimes, in principle, our approach allows us to calculate the full noise for any value of the tunneling parameter, provided that we have the corresponding expression of the equilibrium noise.

5.6.1 Exact solution for a $\left(\frac{1}{3}, 1\right)$ junction

By exploiting the exact refermionization procedure, given in the previous Section, we are able to evaluate the equilibrium noise $S_0(T)$ in the case ($\nu_L = 1/3$, $\nu_R = 1$), recovering the result from Ref. [196] at zero voltage. The final expression, whose derivation is given in Appendix J, reads

$$S_0(T) = \frac{1}{2}\left(\frac{e^2}{2\pi}\right)\mathcal{T}_k\left[4\frac{T}{\mathcal{T}_k} - \frac{2}{\pi}\psi'\left(\frac{1}{2} + \frac{\mathcal{T}_k}{2\pi T}\right)\right], \tag{5.52}$$

with $\mathcal{T}_k$ defined in Eq. (5.33). Then, according to Eq. (5.51), one can write the coefficient of the first order correction to the delta-T noise

$$\Sigma\left(\frac{1}{3}, 1, T\right) = \left(\frac{e^2}{2\pi}\right)\left[\frac{3}{2} + \frac{3}{8\pi^2}\psi''\left(\frac{1}{2} + \frac{\mathcal{T}_k}{2\pi T}\right)\left(\frac{\mathcal{T}_k}{T}\right)^2\right] \tag{5.53}$$

with ψ'' the second derivative of the digamma function. The behavior of this quantity as a function of $T/\mathcal{T}_k$ is reported in Fig. 5.4.

We can now consider two interesting limits of Eq. (5.53): the weak coupling limit described by $\Lambda \to 0$ or equivalently, due to Eq. (5.22), $\Lambda' \to \infty$ (*i.e.* $\mathcal{T}_k \to \infty$ from Eq. (5.32)) and the strong coupling limit where $\Lambda \to \infty$ and consequently Λ' and $\mathcal{T}_k$ go to zero. This means that, in terms of the ratio $T/\mathcal{T}_k$, in the weak coupling regime ($T \ll \mathcal{T}_k$) one has

$$\Sigma^{(wc)}\left(\frac{1}{3}, 1, T\right) = \left(\frac{e^2}{2\pi}\right)\frac{3\pi^2}{2}\left(\frac{T}{\mathcal{T}_k}\right)^2 \tag{5.54}$$

while in the strong coupling limit ($T \gg \mathcal{T}_k$) one obtains

$$\Sigma^{(sc)}\left(\frac{1}{3}, 1, T\right) = \left(\frac{e^2}{2\pi}\right)\frac{3}{2}. \tag{5.55}$$

It is worth noting that Eqs. (5.54) and (5.55) are related to the slope of the curves shown in Fig. 5.3 near the value of $\Delta T = 0$. When the ratio $T/\mathcal{T}_k$ is small, meaning that we are considering the weak coupling limit, we see that the plot has a non-linear behavior, near $\Delta T = 0$, reflecting the quadratic dependence of $\Sigma^{(wc)}$ on $T/\mathcal{T}_k$ in Eq. (5.54). However, for the strong coupling regime, where bigger ratios $T/\mathcal{T}_k$ have

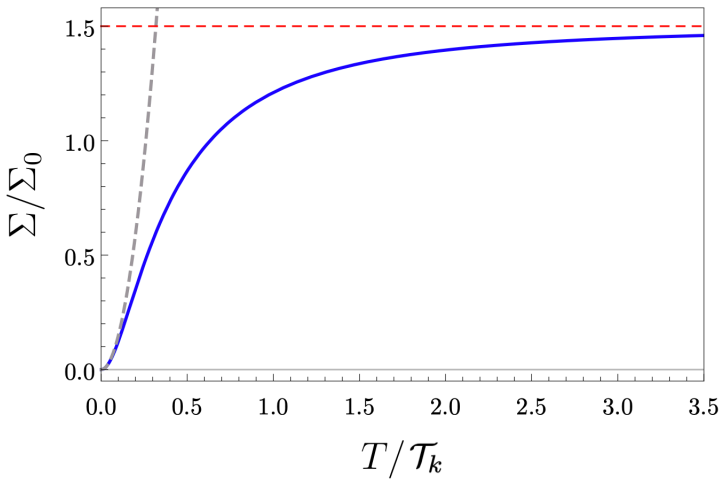

Figure 5.4: Behavior of the linear coefficient $\Sigma \equiv \Sigma(1/3, 1, T)$ in Eq. (5.53) in units of $\Sigma_0 = e^2/2\pi$ as a function of $T/\mathcal{T}_k$. The dashed gray line stands for the weak coupling limit (see Eq. (5.54)) when $T \ll \mathcal{T}_k$ ($\Lambda \to 0$, $\Lambda' \to \infty$). The horizontal dashed red line describes the strong coupling limit for $T \gg \mathcal{T}_k$ ($\Lambda \to \infty$, $\Lambda' \to 0$) [see Eq. (5.55)].

been considered, the slope of the plot is linear according to Eq. (5.55), where $\Sigma^{(sc)}$ is independent of $T/\mathcal{T}_k$.

Moreover, in Fig. 5.3 we observe the behavior of the linear coefficient in Eq. (5.53) for a $(1/3, 1)$ junction in terms of the ratio between temperature T and the energy scale $\mathcal{T}_k$, related to the tunneling amplitude. This coefficient vanishes at zero temperature then evolves quadratically, consistently with Eq. (5.54). As temperature increases further, Σ continuously increases before saturating as it gets closer to the limiting value of $3/2$ (in units of $e^2/2\pi$) which corresponds to the strong coupling value of Eq. (5.55). This latter value represents the maximum reachable one for the linear order correction in the considered case.

5.6.2 Perturbative regimes

In this Subsection, we write the explicit expression for the equilibrium noise $S_0(T)$ due to the tunneling current, starting from the weak-coupling regime for all filling factors ν_L and ν_R. We then switch to the strong-coupling limit by exploiting the duality relation discussed in Section 5.3.

In the weak-coupling regime, the explicit form for the equilibrium noise $S_0(T)$ is obtained through a perturbative expansion up to the second order in the tunneling Hamiltonian H_Λ, from Eq. (5.10), by using the Keldysh formalism [79, 208]

$$S_0^{(wc)}(T) = \left(\frac{e\Lambda}{\pi a}\right)^2 \int_{-\infty}^{+\infty} d\tau \; e^{\frac{2}{g}\mathcal{G}(\tau)} \tag{5.56}$$

with the bosonic Green's function given in Eq. (5.36) with $T_\alpha = T$ and $g = 2(\nu_L\nu_R)/(\nu_L + \nu_R)$.

Then the equilibrium noise in the weak-coupling regime reads [185, 209]

$$S_0^{(wc)}(T) = \left(\frac{e^2}{2\pi}\right)\left(\frac{2\Lambda}{\omega_c a}\right)^2 \left(\frac{2\pi}{\omega_c}\right)^{\frac{2}{g}-2} T^{\frac{2}{g}-1} \frac{\Gamma^2(\frac{1}{g})}{\Gamma(\frac{2}{g})}. \tag{5.57}$$

In the case of free fermions $\nu_L = \nu_R = 1$, Eq. (5.57) yields the Johnson-Nyquist linearity of the equilibrium noise as a function of temperature. Furthermore, if we consider equal filling factors $\nu_L = \nu_R$ we recover the result reported in Ref. [96] for the thermal noise calculated in the tunneling regime. It is worth noticing that the expression in (5.57) only depends on g which is the sum of the inverse filling factors [196] which does not allow us to discriminate between configurations such as ($\nu_R = 1$, $\nu_L = 1/5$) or ($\nu_R = \nu_L = 1/3$) only by looking at the equilibrium noise.

The equilibrium noise of Eq. (5.57) in the weak coupling regime for all filling factors can be rewritten in terms of the crossover energy scale instead of the tunneling amplitude by exploiting Eqs. (5.22) and (5.33), namely

$$S_0^{(wc)}(T) = \frac{1}{4}\left(\frac{e^2}{2\pi}\right)(4\pi)^{\frac{2}{g}-2}\frac{\Gamma^4(\frac{1}{g})}{\Gamma(\frac{2}{g})}\left(\frac{T}{\mathcal{T}_k}\right)^{\frac{2}{g}-1}\mathcal{T}_k \tag{5.58}$$

and consequently from Eq. (5.51) the linear coefficient for a generic (ν_L, ν_R) junction as

$$\Sigma^{(wc)}(\nu_L, \nu_R, T) = \frac{1}{4}\left(\frac{e^2}{2\pi}\right)\left(\frac{\nu_R}{\nu_R+\nu_L}\right)\left(\frac{2}{g}-1\right)(4\pi)^{\frac{2}{g}-2}\frac{\Gamma^4(\frac{1}{g})}{\Gamma(\frac{2}{g})}\left(\frac{T}{\mathcal{T}_k}\right)^{\frac{2}{g}-2}. \tag{5.59}$$

Notice that for $\nu_R = 1$ and $\nu_L = 1/3$, this last equation reduces to the result derived in Eq. (5.54) for the weak coupling limit $T \ll \mathcal{T}_k$.

Now, the strong coupling limit can be studied using the weak-strong duality transformation, introduced in Section 5.3, where we consider the electron-quasiparticle substitution for the charge $e \to e^* = ge$ and for the filling factor $g \to 1/g$. By focusing on the strong coupling limit we consider Λ' instead of Λ as depicted in Fig. 5.2(d). According to this, Eq. (5.57) leads to

$$S_B^{(sc)}(T) = \left(\frac{e^{*2}}{2\pi}\right)\left(\frac{2\Lambda'}{\omega_c a}\right)^2\left(\frac{2\pi}{\omega_c}\right)^{2g-2}T^{2g-1}\frac{\Gamma^2(g)}{\Gamma(2g)}. \tag{5.60}$$

It is worth mentioning that the weak-strong duality transformation amounts to consider a dual system which can be treated in the weak coupling limit, i.e. perturbatively in Λ'. According to this, at equilibrium, the tunneling current noise maps into a backscattered current noise, hence the notation S_B.

Using the expression for $\mathcal{T}_k$ from Eq. (5.33), we can rewrite the equilibrium backscattering noise in the strong coupling regime for all filling factors as

$$S_B^{(sc)}(T) = (4g)^2\left(\frac{e^2}{2\pi}\right)\left(\frac{4\pi}{g}\right)^{2g-2}\frac{\Gamma^4(g)}{\Gamma(2g)}\left(\frac{T}{\mathcal{T}_k}\right)^{2g-1}\mathcal{T}_k. \tag{5.61}$$

The noise associated with the tunneling current is then readily obtained from its backscattering counterpart by accounting for a bare equilibrium noise contribution linear in temperature which ends up dominating the transport for temperatures $T \gg \mathcal{T}_k$.

In the end, it leads to the total equilibrium tunneling noise in the strong coupling regime

$$S_0^{(sc)}(T) = \left(\frac{e^2}{2\pi}\right)4gT - S_B^{(sc)}(T). \tag{5.62}$$

In this case, the linear coefficient of the ΔT noise can be written as

$$\Sigma^{(sc)}(\nu_L,\nu_R,T)=\left(\frac{e^2}{2\pi}\right)\left(\frac{\nu_R}{\nu_R+\nu_L}\right)\Bigg[4g+ \\ +(4g)^2(1-2g)\left(\frac{4\pi}{g}\right)^{2g-2}\frac{\Gamma^4(g)}{\Gamma(2g)}\left(\frac{\mathcal{T}_k}{T}\right)^{2-2g}\Bigg] \tag{5.63}$$

which then reduces to Eq. (5.55) for the $(1,1/3)$ junction.

Notice that the analysis carried out so far is proper of the case of inhomogeneous Hall junction with filling factors belonging to the Laughlin sequence. Here, clearly emerge the role played by the scaling dimension associated to the different FQH states involved in the tunneling (related to the filling factors ν_L and ν_R). In more general composite FQH states the emergence of neutral modes affects the scaling dimension of the tunneling operators and need to be carefully taken into account [210].

As a final remark we notice that the first order contribution to the delta-T noise in the temperature bias cannot be solely expressed in terms of the effective filling factor g. This is true for both the weak and strong coupling regimes as can be readily seen from Eqs. (5.59) and (5.63). Since the linear in ΔT coefficient depends separately on ν_L and ν_R, this specific signature allows us to distinguish between different filling factor combinations which nevertheless have the same effective filling factor g, and consequently the same equilibrium noise, such as ($\nu_R=1$, $\nu_L=1/5$) or ($\nu_R=\nu_L=1/3$). This further highlights the importance of the low order delta-T noise as a relevant probe of the transport mechanisms at play in the general (ν_R,ν_L) junction.

5.7 Summary

As introduced in Section 1.2.2, FQH systems host topologically protected chiral modes at their edge which can be relevant for a generalization of EQO to the fractional regime. Along this direction, the study of the current noise is essential in the EQO framework for the understanding of transport mechanisms in mesoscopic systems.

In this Chapter we devote our attention to the study of the non-equilibrium noise generated by a temperature gradient between two FQH systems, known as delta-T noise. We have considered an inhomogeneous QH junction and we have demonstrated the predominant contribution to the noise is linear in the temperature gradient, differently from an homogeneous junction where the first non-zero contribution is quadratic [96]. Moreover, we have considered the two Hall bars characterized by strong interaction in the FQH regime, with filling factors belonging to the Laughlin sequence, focusing on a coupling between the two edges whose intensity can be either considered in a weak or strong coupling regime thanks to a weak-strong duality transformation.

We have solved exactly the problem of the delta-T noise for the $(1/3,1)$ junction, demonstrating that this regime enables to explore the full range of tunnel coupling and to consider any set of temperatures T_R and T_L without restrictions. In addition, we have reported on a universal expression, in terms of the tunneling parameter for a completely generic junction, for the linear correction to the full delta-T noise in the temperature gradient starting from the knowledge of the equilibrium noise. Furthermore, we have demonstrated that we are able again to move from the weak-coupling regime to the strong-coupling one by applying a duality transformation and we have reported on the asymptotic behavior of the linear coefficient of this expansion for generic values of the filling factors (ν_L,ν_R). Finally, our approach shows the relevance

of delta-T noise in better understanding the transport properties of such strongly correlated systems, unlike previously considered noise contributions, since it depends on both filling factors separately rather than the sole effective filling factor describing the junction.

This analysis offers many interesting perspectives, essentially related to practical realizations of such temperature-biased inhomogeneous junctions. Indeed, junctions between different Hall fluids are notoriously difficult to implement experimentally and the careful investigation of their transport properties remain largely unexplored. As the magnetic field is constant everywhere across the two-dimensional electron gas, regions of different filling factors require different electron density, which is typically achieved via electrostatic gates whose close proximity leads to a severe risk of shorting each other. Several solutions have been envisioned to circumvent this issue. However, these raise several challenging problems for theoretical modeling. One aspect that could be explored in forthcoming studies is the effect of local charge depletion at the QPC, as a consequence of electrostatic effects. This leads to a local filling factor in the region of the point contact, whose importance for transport properties has been previously underlined [211, 212]. Moreover, interesting new perspectives in this field could be opened by the study of composite FQH edge state, where the emergence of co- and counter-propagating neutral modes could complicate the presented picture [138, 189, 210, 213]. Another fascinating direction to explore is the case of long junctions, where Andreev reflection-like processes have been observed recently [214]. This would theoretically involve multiple, randomly distributed, quantum point contacts and brings about the importance of coherence effects.

Conclusions and perspectives

In this Thesis, we have investigated the effects of electron-electron interactions on current fluctuations in quantum Hall systems. These kind of systems provide topologically protected edge states where electrons can propagate ballistically. The discovery of these new states of matter and their protected edge states has triggered a huge number of theoretical proposals and cutting-edge experiments. In these context several analogies can be drawn between the propagation of electrons in quantum Hall edge channels and photons in vacuum. This observation opened the way to a new research field, known as electron quantum optics. The main purpose of electron quantum optics is to reproduce conventional optics experiments using electrons propagating in condensed matter systems instead of photons traveling along waveguides. In the first part of **Chapter 1**, we revised the main concept of electron quantum optics in non-interacting systems. Here, we introduced the idea of single-electron sources, that can be exploited to emit purely electronic excitations into quantum Hall edge states. In particular, we focused on the case of Lorentzian voltage pulses carrying an integer number of electronic excitations, the so-called levitons, which are one of the main building blocks of electron quantum optics. By partitioning a periodic train of levitons traveling along quantum Hall edge states by means of a quantum point contact, which is the analogue of a photonic beam splitter for electrons, we showed that levitons are minimal excitation states for integer filling factors. Finally, we discussed different sources of noise through the scattering formalism focusing on the Hanbury Brown-Twiss and Hong-Ou-Mandel interferometry with levitons, where electrons impinge on the opposite side of a quantum point contact with a tunable delay. By performing such interferometric experiments, it is possible to observe the anti-bunching effect typical of particle obeying Fermi statistics.

Despite having considered non-interacting systems, the crucial difference between conventional quantum optics and electron quantum optics is the fact that electrons are charged interacting particles. This leads to many-body effects which strongly affect the dynamics of excitations and play a major role in various experimental situations. In particular, this is true when experiments are carried out in quantum Hall edge channels at filling factor $\nu = 2$ or at fractional filling factor belonging to the Laughlin sequence where electron-electron interactions cannot be neglected. In **Chapter 2** we introduced the Tomonaga Luttinger liquid theory which allowed us to treat Coulomb interactions in quantum Hall systems through the bosonization procedure. Here, we showed a theoretical model for a quantum Hall sample at filling factor $\nu = 2$ where the dynamics along edge channels, which interact via a short-range capacitive coupling, is solved through the edge-magnetoplasmon scattering matrix. Interedge interactions led to a charge fractionalization process for copropagating edge channels which will play a fundamental role in the next Chapters. Interactions between the two edge channels and the external environment have been shown to lead to decoherence as well as energy relaxation. The edge-magnetoplasmon approach allowed us to deal

with these effects and we showed what happens to an injected electrons in the inner channel of an interacting $\nu = 2$ QH sample where interaction and dissipation effects are taken into account.

The electron quantum optics experiments are mainly carried out in quantum Hall edge channels at filling factor $\nu = 2$ where interchannel interactions cannot be neglected. The effect of electron-electron interaction emerges dramatically in Hong-Ou-Mandel experiments. **Chapter 3** is devoted to the study of interactions on the current correlations in an electronic Hong-Ou-Mandel interferometer. Here, two identical stream of particles, injected through a properly engineered time-dependent voltage pulse, impinge at a quantum point contact with a given time delay. We demonstrate the Hong-Ou-Mandel noise signal always vanishes for a symmetric device and that a mismatch in the distances between the injectors and the point of collision is needed to reduce the visibility of the dip. We also showed that, by properly tuning these distances or by applying different voltages on the two edge channels in each arm of the interferometer, it is possible to estimate the intensity of the interedge interaction.

In **Chapter 4**, starting from the set-up presented in the previous Chapter, we studied the connection between the current fluctuations and the electromagnetic radiation emitted by a mesoscopic device. In particular, we focused on the effects of interacting edge channels on the squeezing of the emitted microwave radiation when particles are injected into the system by means of time-dependent voltage sources. We compared a cosine pulse with a Lorentzian one and we realized that in both cases quantum features are reduced due to the interactions, however the Lorentzian drive is characterized by a more robust squeezing effect. We finally reported recent experimental results which supported the edge-magnetoplasmon squeezing in a quantum point contact geometry.

Finally, in **Chapter 5**, we moved into a different platform where, however, interactions play a significant role: the ones governed by the fractional quantum Hall effect. Here, we investigated a thermal activated non-equilibrium noise which is known as delta-T noise. We considered an inhomogeneous quantum Hall junction, coupled through a quantum point contact, and we demonstrated that the predominant contribution to the noise is linear in the temperature gradient, differently from an homogeneous junction where the first non-zero contribution is quadratic. Moreover, we solved exactly the problem of delta-T noise for a $(1/3, 1)$ junction demonstrating that this regime enables to explore the full range of tunnel coupling and to consider any set of temperatures without restrictions. In addition, we reported on a universal expression, in terms of the tunneling parameter for a completely generic junction, for the linear correction to the full delta-T noise in the temperature gradient starting from the knowledge of the equilibrium noise. Finally, we demonstrated that we can cross from the weak-coupling regime to the strong-coupling showing the relevance of delta-T noise in better understanding the transport properties of such strongly correlated systems, unlike previously considered noise contributions.

Possible extensions of this Thesis could address the consequences of inter-edge interactions on the quantum coherence of the injected electrons in an electronic Mach-Zehnder interferomer. It would be extremely interesting going beyond the simple understanding of the consequences of in interactions in such an interferometer by studying the possibility to obtain squeezed light even in this configuration. However, a first step in this direction should be to better understand experimental results in non-interacting quantum Hall system where the edge-magnetoplasmon squeezing does not seem to overlap with theoretical predictions. Furthermore, another interesting research perspective could extend the study of delta-T noise to states with filling factors other

than Laughlin where fascinating effects should manifest themselves as a consequence of the more complex structure of the edge states.

Appendix A

Time evolution of fermionic and bosonic operators

In this Appendix we evaluate the time evolution of fermionic and bosonic operators due to the effect of a voltage drive in the non interacting case. The free Hamiltonian for a single channel is

$$H_0 = \int_{-\infty}^{+\infty} dx\, \psi^\dagger(x)(-iv_F\partial_x)\psi(x). \tag{A.1}$$

Next, we consider a time-dependent voltage $V(t)$ applied in the region $x \in (-\infty, 0)$. This is described by the Hamiltonian

$$H_U = -e\int_{-\infty}^{+\infty} dx\, U(x,t)\psi^\dagger(x)\psi(x)$$

with $U(x,t) = \Theta(-x)V(t)$.

The equations of motion determining the time evolution $\psi(x,t)$ operators are obtained in the Heisenberg picture by calculating the commutator $[H_0 + H_U, \psi]$. This is easily done by using the identity $[A, BC] = \{A, B\}C - B\{A, C\}$, as well the canonical anticommutation. relations. We have

$$\begin{aligned}[\psi(x), H_0] &= -iv_F\partial_x\psi(x)\\ [\psi(x), H_U] &= -eU(x,t)\psi(x)\end{aligned} \tag{A.2}$$

resulting in the equation of motion

$$i(\partial_t + v_F\partial_x) = -eU(x,t)\psi(x,t). \tag{A.3}$$

This equation can be solved by the Green function method as follows: define the differential operator $\mathcal{L} = i(\partial_t + v_F\partial_x)$ and look for a solution of the form

$$\psi(x,t) = \psi(x,t)e^{\beta(x,t)} \tag{A.4}$$

such that $\mathcal{L}(x,t) = 0$. Then Eq. (A.3) is converted in an equation for the function $\beta(x,t)$

$$\begin{aligned}\mathcal{L}\psi(x,t) = \psi(x,t)e^{\beta(x,t)}\mathcal{L}\beta(x,t) &= -eU(x,t)\psi(x,t)e^{\beta(x,t)},\\ \rightarrow \mathcal{L}\beta(x,t) &= -eU(x,t).\end{aligned} \tag{A.5}$$

By introducing the Green function $G(x,x';t,t')$ of the operator $\mathcal{L}$, satisfying

$$\mathcal{L}G(x,x';t,t') = \delta(x-x')\delta(t-t'), \tag{A.6}$$

we can write the solution to (A.5) in the form

$$\beta(x,t) = -e\int_{\mathbb{R}^2} dx'dt' G(x,x';t,t')U(x',t'). \tag{A.7}$$

Indeed, by acting with $\mathcal{L}$ on this expression and using the property (A.6), we readily obtain (A.5). The Green function for $\mathcal{L}$ is

$$G(x,x';t,t') = -i\Theta(t-t')\delta[v_F(t-t') - (t-t')]. \tag{A.8}$$

As a matter of fact

$$\begin{aligned}\mathcal{L}G(x,x';t,t') &= \delta(t-t')\delta(x-x') + \Theta(t-t')\partial_t\delta[v_F(t-t') - (t-t')] \\ &\quad + v_F\Theta(t-t')\partial_x\delta[v_F(t-t') - (t-t')] \\ &= \delta(t-t')\delta(x-x').\end{aligned} \tag{A.9}$$

By using (A.8) into (A.7) we obtain

$$\beta(x,t) = ie\int_{-\infty}^{t} dt'\, U[x - v_F(t-t'), t']. \tag{A.10}$$

The last ingredient is the solution to the homogeneous equation $\mathcal{L}\psi(x,t) = 0$, which is any function of the form $\psi(x - v_F t, 0)$. Therefore we conclude

$$\psi(x,t) = \psi(x - v_F t, 0)e^{ie\int_{-\infty}^{t} dt' U[x - v_F(t-t'), t']}, \tag{A.11}$$

which reduces to Eq. (1.35). In particular, by expliciting the $U(x,t) = \Theta(-x)V(t)$, we find

$$\psi(x,t) = \psi(x - v_F t, 0)e^{i\alpha\left(t - \frac{x}{v_F}\right)} \tag{A.12}$$

with the function $\alpha(t)$ defined as

$$\alpha(\tau) = e\int_{-\infty}^{\tau} dt' V(t'). \tag{A.13}$$

The above result reduces to Eq. (1.36).

Appendix B

Calculation of the elastic scattering amplitude

We start by considering an electronic wave-packet injected in channel 1 of Fig. 2.5 in such a way that

$$|\text{in}\rangle = \int_{-\infty}^{+\infty} dy\, \varphi(y)\psi^\dagger(y)|\text{F}\rangle_1 \otimes |\text{F}\rangle_2 \tag{B.1}$$

with $|\text{F}\rangle_i$ $(i = 1, 2)$ the Fermi sea associated to the i-th channel, $\psi^\dagger$ the electronic creation operator and $\varphi(y)$ its wave-packet.

In the following we will focus on an energy resolved wave-packet with

$$\varphi(y) = \frac{e^{i\varepsilon y}}{\sqrt{N_t}} \tag{B.2}$$

where the normalization N_t represents the longest time scale in the system and ε the energy.

According to the hydrodynamic approach discussed in Section 2.3 one can write the fermionic operator acting on the Fermi sea as a coherent state of edge-magnetoplasmons (up to a Klein factor that plays no role in what follows) [215]. This leads to

$$|\text{in}\rangle = \int_{-\infty}^{+\infty} dy \frac{e^{i\varepsilon y}}{\sqrt{\mathcal{T}}} \left(\bigotimes_{\omega>0} |-\lambda_\omega(y)\rangle_1 \right) \otimes \left(\bigotimes_{\omega>0} |0_\omega\rangle_2 \right) \tag{B.3}$$

with

$$\lambda_\omega(y) = -\frac{1}{\sqrt{\omega}} e^{i\omega y} \tag{B.4}$$

and 0_ω the EMP vacuum.

The analogous expression

$$|\text{out}\rangle = \int_{-\infty}^{+\infty} dy' \frac{e^{i\varepsilon y'}}{\sqrt{\mathcal{T}}} \left(\bigotimes_{\omega>0} |-\lambda_\omega(y')\rangle_1 \right) \otimes \left(\bigotimes_{\omega>0} |0_\omega\rangle_2 \right) \tag{B.5}$$

holds for the state in the outgoing region.

Expressing the incoming EMPs in terms of the outgoing ones requires to take into account the entries of the matrix $\hat{S}$ in Eq. (2.73) in such a way that

$$|\text{in}\rangle \to |\text{in}\rangle' = \int_{-\infty}^{+\infty} dy \frac{e^{i\varepsilon y}}{\sqrt{\mathcal{T}}} \left(\bigotimes_{\omega>0} |-S_{11}(\omega)\lambda_\omega(y)\rangle_1 \right) \otimes \left(\bigotimes_{\omega>0} |-S_{12}(\omega)\lambda_\omega(y)\rangle_2 \right). \tag{B.6}$$

The elastic scattering amplitude is then given by

$$\mathcal{Z}(\varepsilon) = \langle \text{out}|\text{in}\rangle' \tag{B.7}$$

that, taking into account the general relation for coherent states

$$\bigotimes_{\omega>0} \langle \alpha_\omega | \beta_\omega \rangle = e^{-\frac{1}{2}\int_0^{+\infty} |\alpha_\omega - \beta_\omega|^2 d\omega} e^{i\int_0^{+\infty} \Im(\alpha_\omega^* \beta_\omega) d\omega} \tag{B.8}$$

with $\Im(...)$ representing the imaginary part, leads (in the limit $N_t \to +\infty$) to

$$\mathcal{Z}(\varepsilon) = \int_{-\infty}^{+\infty} d\tau e^{i\varepsilon\tau} \exp\left\{ \int_0^{+\infty} \frac{d\omega}{\omega} \left[t(\omega) e^{-i\omega\tau} - 1 \right] \right\} \tag{B.9}$$

which is the expression considered in Eq. (2.82).

B.1 Non-dissipative case

In absence of energy losses towards external degrees of freedom the EMP transmission amplitude is

$$t_{nd}(\omega) = p_\rho e^{i\omega\tau_\rho} + p_\sigma e^{i\omega\tau_\sigma} \tag{B.10}$$

with $p_\rho(\theta) = \cos^2\theta$ and $p_\sigma(\theta) = \sin^2\theta$. This leads, in the time domain, to

$$\begin{aligned} \mathcal{Z}_{nd}(t) &= \exp\left\{ p_\rho \int_0^{+\infty} \frac{d\omega}{\omega} \left[e^{-i\omega(t-\tau_\rho)} - 1 \right] e^{-\omega/\omega_c} \right\} \times \\ &\times \exp\left\{ p_\sigma \int_0^{+\infty} \frac{d\omega}{\omega} \left[e^{-i\omega(t-\tau_\sigma)} - 1 \right] e^{-\omega/\omega_c} \right\} = \\ &= \frac{-i}{\omega_c} \frac{1}{\left(t - \tau_\rho - \frac{i}{\omega_c}\right)^{p_\rho} \left(t - \tau_\sigma - \frac{i}{\omega_c}\right)^{p_\sigma}}. \end{aligned} \tag{B.11}$$

Its Fourier transform reads

$$\begin{aligned} \mathcal{Z}_{nd}(\varepsilon) &= \frac{-i}{\omega_c} \int_{-\infty}^{+\infty} dt \frac{e^{i\varepsilon t}}{\left(t - \tau_\rho - \frac{i}{\omega_c}\right)^{p_\rho} \left(t - \tau_\sigma - \frac{i}{\omega_c}\right)^{p_\sigma}} \\ &= \frac{2\pi}{\omega_c} e^{i\frac{\varepsilon}{\varepsilon_0 f'_\rho}} {}_1F_1\left[p_\rho, 1; -i\frac{\varepsilon}{\varepsilon_0}\left(\frac{1}{f'_\sigma} - \frac{1}{f'_\rho}\right) \right] \Theta(\varepsilon) \end{aligned} \tag{B.12}$$

with

$$\varepsilon_0 = \frac{v}{L}, \tag{B.13}$$

$\Theta(...)$ the Heaviside Theta function, ${}_1F_1$ indicates the Kummer confluent hypergeometric function and $f'_{\rho/\sigma}$ defined in Eq. (2.62).

In this case the relative height of the wave-packet evolves as

$$\mathcal{V}_{nd}(\varepsilon) = \left| {}_1F_1\left[p_\rho, 1; -i\frac{\varepsilon}{\varepsilon_0}\left(\frac{1}{f'_\sigma} - \frac{1}{f'_\rho}\right) \right] \right|^2 \Theta(\varepsilon). \tag{B.14}$$

In the strongly interacting limit ($\theta = \pi/4$), due the peculiar functional identities between hypergeometric and the zero-th order Bessel function J_0, the above expression reduces to [144]

$$\mathcal{Z}_{nd,strong}(\varepsilon) = \frac{2\pi}{\omega_c} e^{i\frac{\varepsilon}{2\varepsilon_0}\left(\frac{1}{f'_\rho}+\frac{1}{f'_\sigma}\right)} J_0\left[\frac{\varepsilon}{2\varepsilon_0}\left(\frac{1}{f'_\sigma}-\frac{1}{f'_\rho}\right)\right]\Theta(\varepsilon). \tag{B.15}$$

with visibility

$$\mathcal{V}_{nd,strong}(\varepsilon) = J_0^2\left[\frac{\varepsilon}{2\varepsilon_0}\left(\frac{1}{f'_\sigma}-\frac{1}{f'_\rho}\right)\right]\Theta(\varepsilon). \tag{B.16}$$

B.2 Linear dissipation

The analytic expressions in this case can be obtained from the non-dissipative one by taking into account the substitution (see Section 2.5)

$$\omega \to \omega + i\gamma_1\omega \tag{B.17}$$

at the level of the first integral. This leads to

$$\mathcal{Z}_l(\varepsilon) = \frac{2\pi}{\omega_c} e^{i\frac{\varepsilon}{\varepsilon_0 f'_\rho}} e^{-\frac{\gamma_1}{f'_\rho}\frac{\varepsilon}{\varepsilon_0}} {}_1F_1\left[p_\rho, 1; -\gamma_1\frac{\varepsilon}{\varepsilon_0}\left(\frac{1}{f'_\sigma}-\frac{1}{f'_\rho}\right) + i\frac{\varepsilon}{\varepsilon_0}\left(\frac{1}{f'_\sigma}-\frac{1}{f'_\rho}\right)\right]\Theta(\varepsilon) \tag{B.18}$$

and

$$\mathcal{V}_l(\varepsilon) = e^{-2\frac{\gamma_1}{f'_\rho}\frac{\varepsilon}{\varepsilon_0}}\left|{}_1F_1\left[p_\rho, 1; -\gamma_1\frac{\varepsilon}{\varepsilon_0}\left(\frac{1}{f'_\sigma}-\frac{1}{f'_\rho}\right) + i\frac{\varepsilon}{\varepsilon_0}\left(\frac{1}{f'_\sigma}-\frac{1}{f'_\rho}\right)\right]\right|^2\Theta(\varepsilon). \tag{B.19}$$

B.3 Quadratic dissipation

In this case the elastic scattering amplitude can be written, in the time domain, as

$$\begin{aligned}\mathcal{Z}_q(t) &= \exp\{\mathcal{W}_\rho(t)\}\exp\{\mathcal{W}_\sigma(t)\} = \\ &= \exp\left\{p_\rho\int_0^{+\infty}\frac{d\omega}{\omega}[e^{-i\omega(t-\tau_\rho-i\gamma_2\omega\tau_\rho)}-1]e^{-\omega/\omega_\rho}\right\}\times \\ &\times\exp\left\{p_\sigma\int_0^{+\infty}\frac{d\omega}{\omega}[e^{-i\omega(t-\tau_\sigma-i\gamma_2\omega\tau_\sigma)}-1]e^{-\omega/\omega_\rho}\right\}.\end{aligned} \tag{B.20}$$

This first integration can be done analytically and the exponents $\mathcal{W}_{\rho,\sigma}(t)$ take the following form

$$\begin{aligned}\mathcal{W}_{\rho,\sigma}(t) = 2p_{\rho,\sigma}\Bigg\{&\gamma - \log(\gamma_2\tau_{\rho,\sigma}\omega_c^2) + i\pi\,\mathrm{Erf}\left[\frac{i+(\tau_{\rho,\sigma}-t)\omega_c}{2\sqrt{\gamma_2\omega_c}}\right] + \\ &-\frac{(i+(\tau_{\rho,\sigma}-t)\omega_c)^2}{2\gamma_2\tau_{\rho,\sigma}\omega_c^2}\,{}_2F_2\left[1,1;\frac{3}{2},2;-\frac{(i+(\tau_{\rho,\sigma}-t)\omega_c)^2}{4\gamma_2\tau_{\rho,\sigma}\omega_c^2}\right]\Bigg\}\end{aligned} \tag{B.21}$$

where $\gamma \approx 0.577$ is the Euler's constant and Erf is the error function. Unfortunately, it is not possible to obtain an analytical solution for the Fourier transform $\mathcal{Z}_q(\varepsilon)$ and a numerical integration is needed.

Appendix C

Photoassisted amplitudes and HOM noise ratio

In this Appendix we evaluate the photoassisted amplitudes $\widetilde{p}_{l,A/B}(q)$ and $\mathcal{P}_l(q;\delta)$ in terms of amplitudes $p_l(q)$, introduced in Section 1.6.3, and we show how to obtain Eq. (3.23). The coefficients we want to determine, for a periodic voltage pulse source $V(\tau) = V(\tau + \mathcal{T})$, are defined by the Fourier series ($j = A, B$)

$$e^{-ie\int_0^t V^j_{1,\mathrm{out}}(\tau)d\tau} = e^{-iq\Omega t}\sum_l \widetilde{p}_{l,j}(q)e^{-il\Omega t} \tag{C.1}$$

where $\Omega = 2\pi/\mathcal{T}$ and

$$e^{-ie\int_0^t\left[V^A_{1,\mathrm{out}}(\tau)-V^B_{1,\mathrm{out}}(\tau)\right]d\tau} = \sum_l \mathcal{P}_l(q;\delta)e^{-il\Omega t}\,. \tag{C.2}$$

The explicit expressions of these coefficients in terms of p_l are then obtained by inverting the previous relations. Let us start with $\widetilde{p}_{l,j}(q)$. From Eq. (C.1) we have

$$\widetilde{p}_{l,j}(q) = \int_0^{\mathcal{T}} \frac{dt}{\mathcal{T}} e^{i(l+q)\Omega t} e^{-ie\int_0^t V^j_{1,\mathrm{out}}(\tau)d\tau}. \tag{C.3}$$

Next, with the help of Eqs. (3.20) and (3.30), the voltages $V^j_{1,\mathrm{out}}(t)$ are expressed in terms of the source drive $V(t)$ given in Eq. (3.24). In doing that, four different phase factors involving $V(t)$ are obtained, each of which containing a time shift and being differently weighted due to interactions. It is then possible to repeatedly use Eq. (1.104) to express these factors as Fourier series involving the photoassisted coefficients p_l. Finally, after performing the time integration in Eq. (C.3) we obtain the result (neglecting unimportant phases)

$$\begin{aligned}\widetilde{p}_{l,j}(q) = &\sum_{nrs} p_{l-n-r+s}(q_1)p_n(q_2)p_r(q_3)p^*_s(q_3)\\ &\times e^{i\Omega\tau^j_\rho(l-n+s)}e^{i\Omega\tau^j_\sigma(n-s)},\end{aligned} \tag{C.4}$$

where $q_1 = \cos^2\theta$, $q_2 = \sin^2\theta$ and $q_3 = \alpha\sin\theta\cos\theta$. In absence of the voltage source connected to the external channel (*i.e.* $\alpha = 0$) Eq. (C.4) becomes

$$\widetilde{p}_{l,j}(q) = \sum_n p_{l-n}(q_1)p_n(q_2)e^{i\Omega\tau^j_\rho(l-n)}e^{i\Omega\tau^j_\sigma n}. \tag{C.5}$$

Notice that in absence of interaction ($\theta = 0$) the photoassisted coefficients reduces to the results in Eq. (1.105) finding the condition of free fermions.

Thus, the coefficients $\widetilde{p}_{l,j}(q)$ are completely specified once the expression of p_l is known. In the following we will specify the form of these coefficients both for a Lorentzian drive and for a cosine one which will be useful for Chapter 4.

For a Lorentzian drive, the expression of $p_l(q)$ is generically given by [13, 102, 156]

$$p_l(t) = t\sum_{s=0}^{+\infty} \frac{(-1)^s \Gamma(t+l+s) e^{-2\pi\tau_0(2s+l)/\mathcal{T}}}{\Gamma(t+1-s)\Gamma(1+s)\Gamma(1+l+s)} \tag{C.6}$$

with $\Gamma(x)$ being the Euler's Gamma function.

For a cosine drive one has

$$p_l^{(c)}(t) = J_l(-t) \tag{C.7}$$

with $J_l(t)$ the l-th Bessel's function of the first kind.

Once $\widetilde{p}_{l,j}$ are known, it is easy to obtain the photoassisted coefficients $\mathcal{P}_l(q;\delta)$ that take into account the time delay δ between the two sources. Indeed, by inverting Eq. (C.2) and using Eq. (C.1) to express the phase factors involving the voltages $V^j_{1,\mathrm{out}}(t)$, we readily arrive at the expression

$$\mathcal{P}_l(q;\delta) = \sum_m \widetilde{p}_{l+m,A}(q)\widetilde{p}^*_{m,B}(q)\, e^{im\Omega\delta}, \tag{C.8}$$

where, again, unimportant phases have been neglected.

Now we have all the ingredients to evaluate the HOM ratio defined in Eq. (3.21). Recall that S_{HOM} is obtained by evaluating Eq. (3.22) and that the contributions $S_{\mathrm{HBT},j}$ are particular cases when one of the two sources is switched off. The first step is to express the phases $\varphi_j(t,t')$ by relying on the photoassisted coefficients we have determined in this Appendix. For instance,

$$\begin{aligned} e^{-i\varphi_A(\bar{t}+\frac{\tau}{2},\bar{t}-\frac{\tau}{2})} &= \left(\sum_l \widetilde{p}_{l,A}(q)\, e^{-il\Omega(\bar{t}+\frac{\tau}{2})} e^{-iq\Omega(\bar{t}+\frac{\tau}{2})}\right) \\ &\times \left(\sum_{l'} \widetilde{p}^*_{l',A}(q)\, e^{il'\Omega(\bar{t}-\frac{\tau}{2})} e^{iq\Omega(\bar{t}-\frac{\tau}{2})}\right) \\ &= \sum_{ll'} \widetilde{p}_{l,A}(q)\widetilde{p}^*_{l',A}(q)\, e^{i\Omega\bar{t}(l'-l)} e^{-i\Omega\frac{\tau}{2}(l+l'+2q)} \end{aligned} \tag{C.9}$$

and similarly for $e^{-i\varphi_B}$, where the time delay δ has to be taken into account. This expression is then used into Eq. (3.18) to obtain the function $\Delta Q(t+\tau/2, t-\tau/2)$. Finally, the two time integrations in Eq. (3.18) can be performed yielding (in the limit of zero temperature)

$$S_{\mathrm{HOM}} = -(ev_F)^2 \mathsf{RT}\left(\pi \sum_l |\mathcal{P}_l(q;\delta)|^2 |\Omega l|\right) \tag{C.10}$$

for the general HOM case and

$$S_{\mathrm{HBT},j} = -(ev_F)^2 \mathsf{RT}\left(\pi \sum_l |\widetilde{p}_{l,j}(q)|^2 |\Omega(l+q)|\right) \tag{C.11}$$

for the HBT contributions. From these expressions, the noise ratio $\mathcal{R}$ in Eq. (3.23) follows straightforwardly. All the above (infinite) sums are convergent and their value has been obtained numerically by summing over a finite number of coefficients until the desired precision is obtained.

Appendix D

Central dip in the asymmetric length case

D.1 Central dip resolution

In this Appendix we want to comment the resolution of the central dip in the asymmetric case $\theta_A = \theta_B$ and $L_A \neq L_B$.

In principle when the interferometer is asymmetric, one should expect four dips, whose positions would be indeed determined by two delay times only. At $\delta_1 = \tau_\rho^B - \tau_\rho^A$, the two charged modes arrive at the QPC simultaneously, but the dipolar ones do not. Similarly, at $\delta_2 = \tau_\sigma^B - \tau_\sigma^A$, the two dipolar modes arrive at the QPC at the same time while the charged ones do not. However, the proper visualization of those dips requires enough resolution, namely the wave-packets have to be narrow enough. This feature is simply not resolved in Fig. 3.5 (upper panel) where we have chosen a value for τ_0 (width of the Lorentzian voltage) and $\mathcal{T}$ (period of the source) in the typical range accessible for the experiments. As a result, the two expected dips at δ_1 and δ_2 merge into a broader one, located at δ_{cd} (Eq. (3.26)), which is the average delay between the previous two

$$\delta_{cd} = \frac{\delta_1 + \delta_2}{2}. \tag{D.1}$$

In Fig. D.1 we show how the ratio $\mathcal{R}$ should be if we consider unrealistically narrow pulses (for a period $\mathcal{T} = 100\tau_0$). Here the two dips are well resolved respectively at positions δ_1 and δ_2 symmetrically with respect to δ_{cd}, bringing the number of observed dips in the HOM ratio from three (as in Fig. 3.5) to four.

Concerning the sideband dips, they are located at $\delta = \tau_\sigma^B - \tau_\rho^A$ (coincidence between the dipolar mode incoming from B and the charged one incoming from A) and $\delta = \tau_\rho^B - \tau_\sigma^A$ (coincidence between the charged mode incoming from B and the dipolar one incoming from A). Therefore their positions are determined by two times only. In Eq. (3.27) we have expressed the location of these side dips relative to the broad central one.

It is worth noticing that in the symmetric situation when $L_A = L_B$ we have $\delta_1 = \delta_2 = \delta_{cd} = 0$ as expected.

D.2 Central dip visibility

The result in Eq. (3.28), relating the lengths ratio to the periodicity of the signal used for explanation of the minimum value for $\mathcal{R}(\delta_{\mathrm{cd}})$ in Fig. 3.6, is obtained starting from

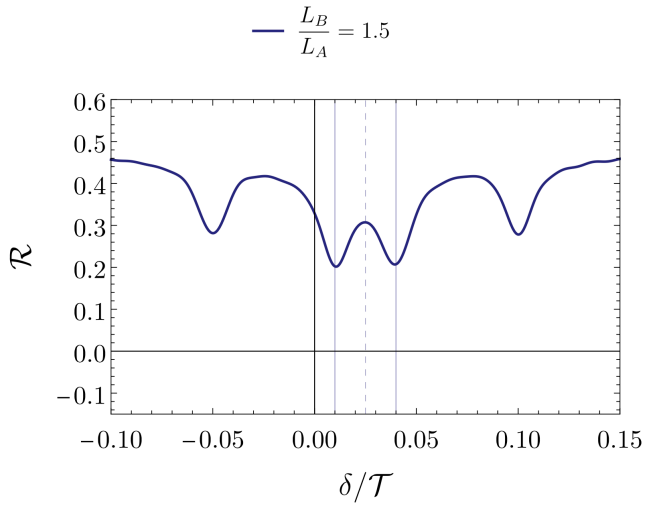

Figure D.1: Ratio $\mathcal{R}$ in Eq. (3.26), for Lorentzian pulses, as a function of time delay over period ($\delta/\mathcal{T}$) for an asymmetric set-up. The lengths ratio of the two arms is $L_B/L_B = 1.5$, the channel coupling strength is maximal ($\theta = \pi/4$) and one fix $\mathcal{T} = 100\tau_0$. Vertical solid lines correspond respectively to $\delta_1 = \tau_\rho^B - \tau_\rho^A$ and $\delta_2 = \tau_\sigma^B - \tau_\sigma^A$ while the dotted vertical one to δ_{cd} (in Eq. (3.26)). Other parameters are: $\tau_0/\mathcal{T} = 0.05$, $v_\rho = 4 \cdot 10^5 m/s$ and $v_\sigma = 1.8 \cdot 10^5 m/s$, with $L_\mathrm{A} = 2\mu m$.

the equality in Eq. (3.20), that is still true also for the phases $\varphi_j(t)$. The phases are (considering the injection only in one channel)

$$\begin{aligned} \varphi_A(t) &= \cos^2\theta\,\varphi(t-\tau_\rho^A) + \sin^2\theta\,\varphi(t-\tau_\sigma^A) \\ \varphi_B(t+\delta) &= \cos^2\theta\varphi(t-\tau_\rho^B+\delta) + \sin^2\theta\varphi(t-\tau_\sigma^B+\delta) \end{aligned} \tag{D.2}$$

where $\varphi(t) = \sum_{k\in\mathbb{Z}} \arctan\left(\frac{t-k\mathcal{T}}{\tau_0}\right)$ for Lorentzian periodic pulses. In order to solve $\varphi_\mathrm{A}(t) = \varphi_\mathrm{B}(t+\delta)$ we have to specify the interaction angle. Firstly considering $0 < \theta < \pi/4$, see Fig. D.2 (left panel), we know that $\sin\theta \neq \cos\theta$ and this means that Eq. (3.20) is satisfied when

$$\varphi(t-\tau_{\rho/\sigma}^A) = \varphi(t-\tau_{\rho/\sigma}^B+\delta). \tag{D.3}$$

These two conditions lead to the same result, therefore we can focus on the first one

$$\sum_k \tan^{-1}\left[\frac{t-k\mathcal{T}-\tau_\rho^A}{\tau_0}\right] = \sum_{k'} \tan^{-1}\left[\frac{t-k'\mathcal{T}-\tau_\rho^B+\delta}{\tau_0}\right] \tag{D.4}$$

which yields

$$(k'-k)\mathcal{T} = \tau_\rho^A - \tau_\rho^B + \delta. \tag{D.5}$$

Because we want to study how the minimum of central dip varies, the delay δ has to be fixed by

$$\delta_\mathrm{cd} = \frac{\tau_\rho^B + \tau_\sigma^B - \tau_\rho^A - \tau_\sigma^A}{2}. \tag{D.6}$$

By substituting this expression into Eq. (D.5) and recalling that $\tau_{\rho/\sigma}^B = \tau_{\rho/\sigma}^A\, L_B/L_A$, we arrive at the result in Eq. (3.28).

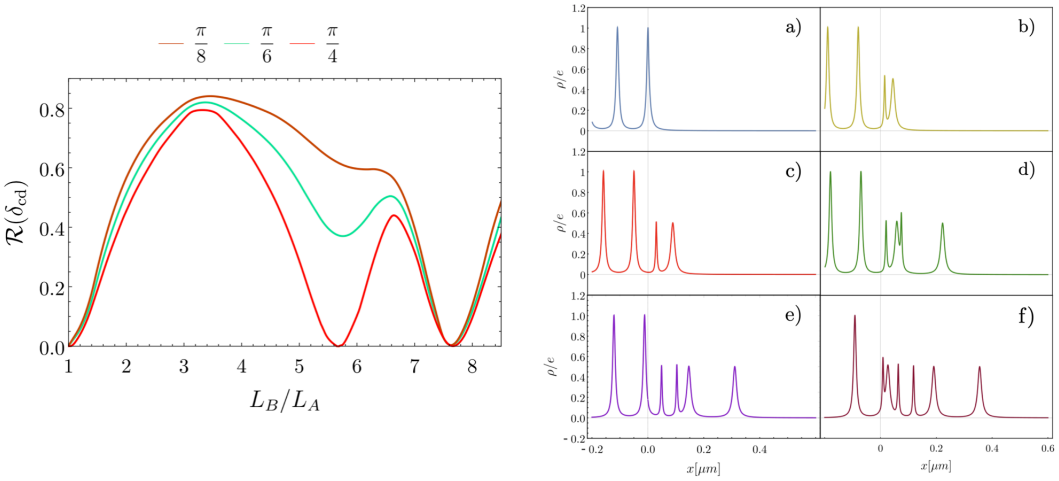

Figure D.2: Left panel: behavior of $\mathcal{R}(\delta_{\rm cd})$ with respect to lengths ratio $L_{\rm B}/L_{\rm A}$ for three different fixed value of the interaction angle: $\theta = \frac{\pi}{4}$ (red curve), $\theta = \frac{\pi}{6}$ (cyan curve) and $\frac{\pi}{8}$ (brown curve). Other parameters are: $\tau_0/\mathcal{T} = 0.05$, $L_A = 2\mu m$ $v_\rho = 1.5 \cdot 10^5 m/s$ and $v_\sigma = 2 \cdot 10^4 m/s$. Right panel: visualization of single electron charge density propagation along an edge channel. In a) a Leviton enter the interacting region $x > 0$, in b) it is clear how the Coulomb coupling mechanism works: the fast mode and the slow one start separating. The separtion continues in c). In d) the green curve describes the case when a second Leviton enter the interacting region: its fast mode reaches the slow mode of the previous period, recreating a purely electronic wave-packet. The process of entry and of charge fractionalization continues in e) and f). By repeating this mechanism for all the periods one can justify Eq. (3.28) and the relations between the lengths ratio and the periodic windows.

An interesting additional feature for $\mathcal{R}(\delta_{\rm cd})$ is obtained when $\theta = \pi/4$. Due to the fact that in this case $\sin\theta = \cos\theta$, there is another possibility to fulfill $\varphi_A(t) = \varphi_B(t+\delta)$, namely

$$\varphi(t - \tau^A_{\rho/\sigma}) = \varphi(t - \tau^B_{\sigma/\rho} + \delta). \tag{D.7}$$

Again, this two conditions lead to the same result, which reads

$$\frac{L_B}{L_A} = \frac{2(k'-k)\mathcal{T}}{\tau^A_\sigma - \tau^A_\rho} - 1. \tag{D.8}$$

This analysis clearly shows that the zeros in $\mathcal{R}(\delta_{\rm cd})$ described by Eq. (3.28) are stable with respect to the change of the interaction strength, while those described by Eq. (D.8) are only present at maximal coupling (see also Fig. D.2 (left panel)). In order to further characterize the physics behind this phenomenology we have reported in Fig. D.2 (right panel) some snapshots of the evolution of the particle density, showing how Levitons emitted in different periods of the drive can recombine due to the interaction-induced fractionalization process.

Appendix E

Calculation of the dynamical response of the noise

In this Appendix we evaluate explicitly the expression of the dynamical response of the noise $\mathcal{X}^{(k)}_{\varphi}(\Omega,\omega)$ appearing in Eq. (4.14) in the zero temperature limit, according to what happens in the experimental situations. In order to reach this goal we have to calculate the correlator in Eq. (4.13)

$$\begin{aligned}\mathcal{X}^{(k)}_{+,\varphi}(\omega_0,\omega) &= e^{i\varphi}\langle I_1(\omega)I_1(k\Omega-\omega)\rangle_c = \\ &= e^{i\varphi}\int_{-\infty}^{+\infty} dt\, e^{i\omega t}\int_{-\infty}^{+\infty} dt'\, e^{i(k\Omega-\omega)t'}\langle I_1(t)I_1(t')\rangle_c.\end{aligned} \tag{E.1}$$

By considering the following change of variables $\bar{t}=\frac{t+t'}{2}$ and $\tau=t-t'$, the previous equation can be rewritten as

$$\mathcal{X}^{(k)}_{+,\varphi}(\Omega,\omega) = e^{i\varphi}\int_{-\frac{T}{2}}^{+\frac{T}{2}}\frac{d\bar{t}}{T}\int_{-\infty}^{+\infty} d\tau e^{i\omega(\bar{t}+\frac{\tau}{2})}e^{i(k\Omega-\omega)(\bar{t}-\frac{\tau}{2})}\langle I_1(\bar{t}+\frac{\tau}{2})I_1(\bar{t}-\frac{\tau}{2})\rangle_c\,. \tag{E.2}$$

The effect of the external voltage drive $V_{\rm in}(t)$ can be properly taken into account with a phase factor [102, 103], see Eq. (1.36) for the fermionic field, in such a way that Eq. (3.15) is rewritten as

$$\begin{aligned}\mathcal{G}_1(\bar{t}+\frac{\tau}{2},\bar{t}-\frac{\tau}{2}) &= \langle\psi_1^\dagger(\bar{t}+\frac{\tau}{2})\psi_1(\bar{t}-\frac{\tau}{2})\rangle_c = \\ &= \mathcal{G}_{1,F}(\tau)(e^{-i\Phi_1(\bar{t}+\frac{\tau}{2},\bar{t}-\frac{\tau}{2})}-1)\end{aligned} \tag{E.3}$$

where $\mathcal{G}_{1,F}$ is the correlation function for the equilibrium state (*i.e.* when no drive is applied) and the phase factor follows Eq. (1.37)

$$\Phi_1(t,t') = e\int_{t'}^{t} V_{1,\rm out}(\tau)d\tau \tag{E.4}$$

with $V_{1,\rm out}$ takes the form in Eq. (4.5) and carry information about the effects of interactions. The fermionic operator $\psi_{R,\rm O}\equiv\psi_1$, outgoing from the QPC in the inner channel, is

$$\psi_{R,\rm O}(t) = \sqrt{\mathsf{T}}\,\psi_{R,\rm I}(t) + i\sqrt{\mathsf{R}}\,\psi_{L,\rm I}(t) \tag{E.5}$$

where $\psi_{R,\rm I}$ and $\psi_{L,\rm I}$ are the incoming inner ones. The previous relation descends directly from the scattering matrix in Eq. (4.6).

In the HBT geometry depicted in Fig. 4.1, after substituting (E.5) in Eq. (E.3) the HBT contribution to the correlation function is

$$\mathcal{G}_1(\bar{t}+\frac{\tau}{2},\bar{t}-\frac{\tau}{2}) = -i\sqrt{\mathsf{RT}}\mathcal{G}_{1,F}^{(R,L)}(e^{-i\Phi_1(\bar{t}+\frac{\tau}{2},\bar{t}-\frac{\tau}{2})}-1). \tag{E.6}$$

By substituting Equation (E.6) in (E.2), the current correlator becomes

$$\begin{aligned}\langle I_1(\bar{t}+\frac{\tau}{2})I_1(\bar{t}-\frac{\tau}{2})\rangle_c = (ev_1)^2\,\mathsf{RT}\,\mathcal{G}_{1,F}^{(R,L)}(\tau)\mathcal{G}_{1,F}^{(R,L)}(\tau)\times \\ \times\left[e^{-i\Phi_1(\bar{t}+\frac{\tau}{2},\bar{t}-\frac{\tau}{2})}+e^{+i\Phi_1(\bar{t}+\frac{\tau}{2},\bar{t}-\frac{\tau}{2})}-2\right].\end{aligned} \tag{E.7}$$

For a periodic voltage pulse source, considered here, the phase factor can be written in terms of the Fourier series as in Eq. (1.104) and Eq. (C.1). Then the explicit expression of the coefficients $\widetilde{p}_l$ is reported in Eq. (4.17) similarly to Eq. (C.5). Furthermore the form of the coefficients p_l is related to particular form of the drive considered (cosine or Lorentzian) and it is expressed in Equations (C.7) and (C.6). By substituting the Fourier series in (E.2) we have

$$\begin{aligned}\mathcal{X}_{+,\varphi}^{(k)}(\Omega,\omega) =&(ev_F)^2\mathsf{RT}e^{i\varphi}\int_{-\frac{T}{2}}^{+\frac{T}{2}}\frac{d\bar{t}}{T}\int_{-\infty}^{+\infty}d\tau\frac{1}{\tau^2}e^{i(\omega-\frac{k\Omega}{2})\tau}e^{ik\Omega\bar{t}}\times \\ &\times\sum_{ll'}\widetilde{p}_l(z)\widetilde{p}_{l'}^{*}(z)e^{-i\Omega(l-l')\bar{t}}e^{-i\Omega(l+l')\frac{\tau}{2}}e^{iq'\omega\tau}.\end{aligned} \tag{E.8}$$

After the first integration in $\bar{t}$ the previous Equation gives a $\delta(l-l'-k)$ and the expression becomes

$$\begin{aligned}\mathcal{X}_{+,\varphi}^{(k)}(\Omega,\omega) &= (ev_F)^2\mathsf{RT}e^{i\varphi}\int_{-\infty}^{+\infty}d\tau\frac{1}{\tau^2}\sum_l\widetilde{p}_l(z)\widetilde{p}_{l-k}^{*}(z)e^{-i\Omega\frac{\tau}{2}(2l-k)}e^{iq'\omega\tau}e^{-ik\Omega\tau/2}e^{i\omega\tau} \\ &= (ev_F)^2\mathsf{RT}e^{i\varphi}\sum_l(\pi|\Omega l+q'\omega-\omega|) \\ &= (ev_F)^2\mathsf{RT}e^{i\varphi}\sum_l(\pi\omega|\lambda l+q'-1|)\end{aligned} \tag{E.9}$$

where we have used the short hand notation $\lambda=\Omega/\omega$ and $|...|$ denotes the absolute value. The same steps can be followed in order to calculate the other term $\mathcal{X}_{+,\varphi}^{(-k)}(\Omega,-\omega)$ in Eq. (4.12). The above (infinite) sum is convergent and its value has been obtained numerically by summing over a finite number of coefficients until the desired precision is obtained.

Appendix F

Explicit evaluation of the correlator in Eq. (5.35)

In this Appendix, we compute explicitly the propagator $\langle A^\dagger(t)A(t')\rangle$ of Eq. (5.35). The latter only involves the fermionic field A, which is only defined at a position before the QPC, so that the quantum averaging is performed on the state where the two edge states are decoupled and at their respective temperature $T_{R,L}$.

We first recall the relation in Eq. (5.20) between the rotated fields $\varphi_{R/L}$ and the dual ones $\widetilde{\varphi}_{R/L}$. The idea in order to evaluate the propagator is to revert to the bosonic description, where

$$\begin{aligned}
\langle A^\dagger(t)A(t')\rangle &= \langle \psi^\dagger(0^-,t)\psi(0^-,t')\rangle = \frac{1}{2\pi a}\Big\langle e^{-i\widetilde{\varphi}_-(0^-,t)}e^{i\widetilde{\varphi}_-(0^-,t')}\Big\rangle = \\
&= \frac{1}{2\pi a}\Big\langle e^{-\frac{i}{\sqrt{2}}\widetilde{\varphi}_L(0^-,t)-\widetilde{\varphi}_R(0^-,t)}e^{\frac{i}{\sqrt{2}}\widetilde{\varphi}_L(0^-,t')-\widetilde{\varphi}_R(0^-,t')}\Big\rangle = \\
&= \frac{1}{2\pi a}\Big\langle e^{-\frac{i}{\sqrt{2}}\varphi_L(0^-,t)-\varphi_R(0^-,t)}e^{\frac{i}{\sqrt{2}}\varphi_L(0^-,t')-\varphi_R(0^-,t')}\Big\rangle = \\
&= \frac{1}{2\pi a}\Big\langle e^{-i\left[\frac{\cos\zeta+\sin\zeta}{\sqrt{2}}\phi_L(0^-,t)+\frac{\sin\zeta-\cos\zeta}{\sqrt{2}}\phi_R(0^-,t)\right]}e^{i\left[\frac{\cos\zeta+\sin\zeta}{\sqrt{2}}\phi_L(0^-,t')+\frac{\sin\zeta-\cos\zeta}{\sqrt{2}}\phi_R(0^-,t')\right]}\Big\rangle.
\end{aligned} \tag{F.1}$$

The bosonic fields $\phi_{R/L}$ are taken at a position before the QPC ($x = 0^-$) and are thus uncoupled from each other. For this reason we are able to rewrite the correlator as a product of averages evaluated at a fixed temperature $T_{R/L}$ of the considered right or left QH bar. Then, for the particular case of a QH junction with $\nu_L = 1/3$ and $\nu_R = 1$ we recover the result of Eq. (5.35) in the main text, namely

$$\begin{aligned}
\langle A^\dagger(t)A(t')\rangle &= \frac{1}{2\pi a}\Big\langle e^{-i\frac{\sqrt{3}}{2}\phi_L(0^-,t)}e^{i\frac{\sqrt{3}}{2}\phi_L(0^-,t')}\Big\rangle\Big\langle e^{i\frac{1}{2}\phi_R(0^-,t)}e^{-i\frac{1}{2}\phi_R(0^-,t')}\Big\rangle \\
&= \frac{1}{2\pi a}e^{\frac{3}{4}\mathcal{G}_L(t-t')}e^{\frac{1}{4}\mathcal{G}_R(t-t')}.
\end{aligned} \tag{F.2}$$

Appendix G

Particle densities relations in an inhomogeneous FQH junction

In this Appendix, we give a description of the junction in terms of the particle densities of the edge channels and we restore the equivalence in Eq. (5.40). This allows to compute the current noise for the specific case of $(1/3, 1)$ presented in Section 5.4.2.

The particle densities $\rho_{L/R}$ of the two edges of the inhomogeneous QH junction are defined in Eq. (5.2) and depend on the fields $\phi_{L/R}$. The first change of basis, which relates $\phi_{L/R}$ to $\varphi_{L/R}$ (see Eq. (5.8)), can be expressed in terms of the particle densities as follows

$$\begin{pmatrix} \rho_L \\ \rho_R \end{pmatrix} = \begin{pmatrix} \frac{\sqrt{\nu_L}+\sqrt{\nu_R}}{2} & \frac{\sqrt{\nu_L}-\sqrt{\nu_R}}{2} \\ \frac{\sqrt{\nu_R}-\sqrt{\nu_L}}{2\sqrt{\nu_L\nu_R}} & \frac{\sqrt{\nu_R}+\sqrt{\nu_L}}{2\sqrt{\nu_L\nu_R}} \end{pmatrix} \begin{pmatrix} \rho'_L \\ \rho'_R \end{pmatrix}. \tag{G.1}$$

After the introduction of the second rotation of Eq. (5.12), the new densities $\rho_{+/-}$ are related to $\rho'_{L/R}$ by

$$\begin{pmatrix} \rho'_L \\ \rho'_R \end{pmatrix} = \sqrt{\frac{g}{2}} \begin{pmatrix} 1 & 1 \\ 1 & -1 \end{pmatrix} \begin{pmatrix} \rho_+ \\ \rho_- \end{pmatrix}. \tag{G.2}$$

In terms of densities, the duality relates $\rho'_{L/R}$ to the dual ones $\widetilde{\rho}_{L/R}$. Notice, from the dual fields transformation in Eq. (5.20), that the densities in the incoming channels $\rho'_{L/R}(x<0)$ are the same as $\widetilde{\rho}_{L/R}(x<0)$ (*i.e.* from Eq. (5.20) for $x<0$ we have $\varphi_{L/R} = \widetilde{\varphi}_{L/R}$ and consequently for the densities). Furthermore, the matrices given in Eq. (G.1) and (G.2) can be used to express the original fields $\phi_{L/R}(x<0)$ in terms of the fields $\widetilde{\varphi}_{+/-}(x<0)$.

In order to write the original densities in the outgoing channels $\rho_{L/R}(x>0)$ in terms of the densities $\widetilde{\rho}_{+/-}(x>0)$ it is necessary to realize that the duality transformation of Eq. (5.20) exchanges φ_L and φ_R for $x>0$. As a consequence, for $x>0$ Eq. (G.1) reads

$$\begin{pmatrix} \rho_L \\ \rho_R \end{pmatrix} = \begin{pmatrix} \frac{\sqrt{\nu_L}+\sqrt{\nu_R}}{2} & \frac{\sqrt{\nu_L}-\sqrt{\nu_R}}{2} \\ \frac{\sqrt{\nu_R}-\sqrt{\nu_L}}{2\sqrt{\nu_L\nu_R}} & \frac{\sqrt{\nu_R}+\sqrt{\nu_L}}{2\sqrt{\nu_L\nu_R}} \end{pmatrix} \begin{pmatrix} \widetilde{\rho}_R \\ \widetilde{\rho}_L \end{pmatrix}. \tag{G.3}$$

It is thus useful to connect the corresponding $\pm$ density operators with their initial (L/R) counterparts. By using Eqs. (G.1), (G.2) and (G.3) the densities $\rho_{L/R}$ can be

written in terms of $\widetilde{\rho}_{+/-}$

$$\begin{aligned}\rho_L(x=0^-,t) &= \sqrt{\frac{g\nu_L}{2}}\widetilde{\rho}_+(0^-,t) + \sqrt{\frac{g\nu_R}{2}}\widetilde{\rho}_-(0^-,t)\\ \rho_R(x=0^-,t) &= \sqrt{\frac{g}{2\nu_L}}\widetilde{\rho}_+(0^-,t) - \sqrt{\frac{g}{2\nu_R}}\widetilde{\rho}_-(0^-,t)\end{aligned} \tag{G.4}$$

and

$$\begin{aligned}\rho_L(x=0^+,t) &= \sqrt{\frac{g\nu_L}{2}}\widetilde{\rho}_+(0^+,t) - \sqrt{\frac{g\nu_R}{2}}\widetilde{\rho}_-(0^+,t)\\ \rho_R(x=0^+,t) &= \sqrt{\frac{g}{2\nu_L}}\widetilde{\rho}_+(0^+,t) + \sqrt{\frac{g}{2\nu_R}}\widetilde{\rho}_-(0^+,t).\end{aligned} \tag{G.5}$$

Since the $\widetilde{\varphi}_+$ field is continuous through the QPC, we can drop the $\widetilde{\rho}_+$ contribution and the current operator is therefore given by

$$I(t) = ev\sqrt{\frac{g}{2}}[\widetilde{\rho}_-(0^+,t) + \widetilde{\rho}_-(0^-,t)]. \tag{G.6}$$

Exploiting the decomposition in Eqs. (5.27) and (5.28) for the specific case of the $(1/3,1)$ junction (*i.e.* $g=1/2$), the tunneling current can be rewritten in terms of the Fourier components of the fermionic field before (A) and after (B) the QPC leading to

$$I(t) = \frac{ev}{2}[A^\dagger(t)A(t) + B^\dagger(t)B(t)]. \tag{G.7}$$

This last equation is thus an equivalent definition of the current operator introduced in Eq. (5.4) and it is quoted in the main text as Eq. (5.40).

Appendix H

Delta-T noise for a $(1/3, 1)$ junction

H.1 Zero-frequency noise for a mismatched $(1/3, 1)$ QH junction

In this Appendix we derive the result of Eq. (5.42). To do this, we recall Eq. (5.34) where the fermionic fields B are written in terms of the A ones so that one has

$$\begin{aligned}
&B^\dagger(t)B(t) + A^\dagger(t)A(t) = \\
&= -\mathcal{T}_k \int_{-\infty}^{t} dt' e^{-\mathcal{T}_k(t-t')} A^\dagger(t)\big[A(t') - A^\dagger(t')\big] + \\
&- \mathcal{T}_k \int_{-\infty}^{t} dt' e^{-\mathcal{T}_k(t-t')} \big[A^\dagger(t') - A(t')\big] A(t) + 2A^\dagger(t)A(t) \\
&+ \mathcal{T}_k^2 \int_{-\infty}^{t} dt_1' \int_{-\infty}^{t} dt_2' e^{-\mathcal{T}_k(t-t_1')} e^{-\mathcal{T}_k(t-t_2')} \big\{A^\dagger(t_1'), A(t_2')\big\} \\
&= \frac{\mathcal{T}_k}{2v} + \mathcal{T}_k \int_{-\infty}^{t} dt' e^{-\mathcal{T}_k(t-t')} \big[A^\dagger(t)A^\dagger(t') - A^\dagger(t)A(t') + \\
&\qquad + A(t')A(t) - A^\dagger(t')A(t) + 2A^\dagger(t)A(t)\big].
\end{aligned} \tag{H.1}$$

Substituting this expression back into the definition for the noise, Eq. (5.41), one has

$$\begin{aligned}
\mathcal{S}(t_1, t_2) = &\left(\mathcal{T}_k \frac{ev}{2}\right)^2 \int_{-\infty}^{t_1} dt_1' \int_{-\infty}^{t_2} dt_2' e^{-\mathcal{T}_k(t_1 - t_1' + t_2 - t_2')} \\
&\big\langle \big[A^\dagger(t_1)A^\dagger(t_1') - A^\dagger(t_1)A(t_1') + A(t_1')A(t_1) \\
&\quad - A^\dagger(t_1')A(t_1) + 2A^\dagger(t_1)A(t_1)\big] \times \\
&\times \big[A^\dagger(t_2)A^\dagger(t_2') - A^\dagger(t_2)A(t_2') + A(t_2')A(t_2) \\
&\quad - A^\dagger(t_2')A(t_2) + 2A^\dagger(t_2)A(t_2)\big]\big\rangle
\end{aligned} \tag{H.2}$$

which becomes, after applying Wick's theorem,

$$\begin{aligned}
\mathcal{S}(t_1,t_2) = &\left(\mathcal{T}_k\frac{ev}{2}\right)^2\int_{-\infty}^{t_1}dt_1'\int_{-\infty}^{t_2}dt_2' e^{-\mathcal{T}_k(t_1-t_1'+t_2-t_2')}\times\\
&\Big\{\langle A^\dagger(t_1)A(t_2)\rangle\langle A^\dagger(t_1')A(t_2')\rangle - \langle A^\dagger(t_1)A(t_2')\rangle\langle A^\dagger(t_1')A(t_2)\rangle\\
&+\langle A^\dagger(t_1)A(t_2')\rangle\langle A(t_1')A^\dagger(t_2)\rangle + \langle A^\dagger(t_1)A(t_2)\rangle\langle A(t_1')A^\dagger(t_2')\rangle\\
&+\langle A(t_1')A^\dagger(t_2')\rangle\langle A(t_1)A^\dagger(t_2)\rangle - \langle A(t_1')A^\dagger(t_2)\rangle\langle A(t_1)A^\dagger(t_2')\rangle\\
&+\langle A^\dagger(t_1')A(t_2')\rangle\langle A(t_1)A^\dagger(t_2)\rangle + \langle A^\dagger(t_1')A(t_2)\rangle\langle A(t_1)A^\dagger(t_2')\rangle\\
&-2\big(\langle A^\dagger(t_1)A(t_2)\rangle\langle A(t_1')A^\dagger(t_2)\rangle + \langle A^\dagger(t_1')A(t_2)\rangle\langle A(t_1)A^\dagger(t_2)\rangle\\
&+\langle A^\dagger(t_1)A(t_2')\rangle\langle A(t_1)A^\dagger(t_2)\rangle + \langle A^\dagger(t_1)A(t_2)\rangle\langle A(t_1)A^\dagger(t_2')\rangle\big)\\
&+4\langle A^\dagger(t_1)A(t_2)\rangle\langle A(t_1)A^\dagger(t_2)\rangle\Big\}.
\end{aligned} \tag{H.3}$$

Using the Fourier transformed versions of the correlators from Eqs. (5.37) and (5.38), this is further rewritten as

$$\begin{aligned}
C(t_1,t_2) = &\left(\mathcal{T}_k\frac{ev}{2}\right)^2\int\frac{d\omega_1}{2\pi v}\int\frac{d\omega_2}{2\pi v}\\
&\times\Big\{e^{i(\omega_1+\omega_2)(t_1-t_2)}n_{\omega_1}n_{\omega_2}\left[\frac{1}{\mathcal{T}_k-i\omega_2}-\frac{1}{\mathcal{T}_k-i\omega_1}\right]\frac{1}{\mathcal{T}_k+i\omega_2}+\\
&+e^{-i(\omega_1+\omega_2)(t_1-t_2)}(1-n_{\omega_1})(1-n_{\omega_2})\left[\frac{1}{\mathcal{T}_k+i\omega_1}-\frac{1}{\mathcal{T}_k+i\omega_2}\right]\frac{1}{\mathcal{T}_k-i\omega_1}+\\
&+e^{i(\omega_1-\omega_2)(t_1-t_2)}n_{\omega_1}(1-n_{\omega_2})\left[\frac{1}{\mathcal{T}_k-i\omega_1}+\frac{1}{\mathcal{T}_k+i\omega_2}\right]\frac{1}{\mathcal{T}_k-i\omega_2}+\\
&+e^{i(\omega_1-\omega_2)(t_1-t_2)}n_{\omega_1}(1-n_{\omega_2})\left[\frac{1}{\mathcal{T}_k-i\omega_1}+\frac{1}{\mathcal{T}_k+i\omega_2}\right]\frac{1}{\mathcal{T}_k+i\omega_1}\\
&-2e^{i(\omega_1-\omega_2)(t_1-t_2)}n_{\omega_1}(1-n_{\omega_2})\left[\frac{2}{\mathcal{T}_k^2+\omega_2^2}+\frac{2}{\mathcal{T}_k^2+\omega_1^2}-\frac{2}{\mathcal{T}_k^2}\right]\Big\}
\end{aligned} \tag{H.4}$$

where we also performed the time integrals.

Since we want to consider the noise power $S(T_L,T_R)$ we need to perform an additional time integration over (t_1-t_2), leading to

$$\begin{aligned}
S(T_L,T_R) = 2\left(\mathcal{T}_k\frac{e}{2}\right)^2\int\frac{d\omega}{2\pi}\Bigg(&2\big[n_\omega n_{-\omega}+(1-n_\omega)(1-n_{-\omega})\big]\left[\frac{\omega}{\mathcal{T}_k^2+\omega^2}\right]^2+\\
&+n_\omega(1-n_\omega)\left\{\left[\frac{2\mathcal{T}_k}{\mathcal{T}_k^2+\omega^2}\right]^2-\frac{8}{\mathcal{T}_k^2+\omega^2}+\frac{4}{\mathcal{T}_k^2}\right\}\Bigg)
\end{aligned} \tag{H.5}$$

which then recovers the result of Eq. (5.42).

H.2 Delta-T noise of the $(1/3,1)$ junction: first order expansion in ΔT

Rather than a numerical evaluation, it could be more rewarding to try to work out an analytic expression for the ΔT noise of the $(1/3,1)$ junction. This, however, can only

be achieved for comparable temperatures, as this approach relies on an expansion in the temperature difference ΔT.

In practice, the calculation amounts to expanding the distribution function as

$$n_\omega = n_\omega^{(0)} + \frac{\Delta T}{T} n_\omega^{(1)} + O\left(\Delta T^2\right). \tag{H.6}$$

Substituting this back into the expression for the noise, Eq. (5.44), one has

$$S(T_R, T_L) = S_0(T) + \frac{\Delta T}{T} S_1(T) \tag{H.7}$$

with

$$S_0(T) = e^2 \int \frac{d\omega}{2\pi} n_\omega^{(0)} \left(1 - n_\omega^{(0)}\right) \left(1 - \frac{\mathcal{T}_k^2 - \omega^2}{\mathcal{T}_k^2 + \omega^2}\right) \tag{H.8}$$

$$S_1(T) = e^2 \int \frac{d\omega}{2\pi} n_\omega^{(1)} \left(1 - 2n_\omega^{(0)}\right) \left(1 - \frac{\mathcal{T}_k^2 - \omega^2}{\mathcal{T}_k^2 + \omega^2}\right). \tag{H.9}$$

The zero-th order contribution to the distribution n_ω trivially reduces to the Fermi distribution at temperature T which is given in Eq. (1.34) where we have now set $k_B = 1$ and $n_\omega^{(0)} \equiv f(\omega)$ for notational convenience.

The first order contribution can be worked out as

$$\begin{aligned} n_\omega^{(1)} &= \frac{3}{4} \int d\tau e^{-i\omega\tau} \frac{\omega_c}{2\pi} \frac{\sinh\left(i\pi \frac{T}{\omega_c}\right)}{\sinh\left(\pi T \left(i\frac{1}{\omega_c} - \tau\right)\right)} \left(\frac{i\pi \frac{T}{\omega_c}}{\tanh\left(i\pi \frac{T}{\omega_c}\right)} - \frac{\pi T (i\frac{1}{\omega_c} - \tau)}{\tanh\left(\pi T (i\frac{1}{\omega_c} - \tau)\right)} \right) \\ &= T \frac{3}{4} \partial_T \left[\int d\tau e^{-i\omega\tau} \frac{\omega_c}{2\pi} \frac{\sinh\left(i\pi \frac{T}{\omega_c}\right)}{\sinh\left(\pi T \left(i\frac{1}{\omega_c} - \tau\right)\right)} \right] = T \frac{3}{4} \partial_T n_\omega^{(0)}. \end{aligned} \tag{H.10}$$

It follows that

$$n_\omega^{(1)} \left(1 - 2n_\omega^{(0)}\right) = T \frac{3}{4} \partial_T n_\omega^{(0)} \left(1 - 2n_\omega^{(0)}\right) = T \frac{3}{4} \partial_T \left[n_\omega^{(0)} \left(1 - n_\omega^{(0)}\right) \right] \tag{H.11}$$

which allows us to readily write

$$S_1(T) = T \frac{3}{4} \partial_T S_0(T). \tag{H.12}$$

Here, we have obtained an analytical expression for the delta-T noise in a (1/3,1) junction. In the next Appendix we generalize this approach to a generic (ν_L,ν_R) junction.

Appendix I

Universal first order expansion of the noise in ΔT

In this Appendix we report on the calculation for the expansion of $S(T_L, T_R)$ at the first other in $\Delta T/T$. The noise can be written, taking into account the temperature parametrization in Eq. (5.19) and up to first order in $\Delta T/T$, as

$$S(T_L,T_R) = \frac{1}{Z}\int_{-\infty}^{+\infty} d\tau\, \mathrm{Tr}\Big\{ e^{-\beta(H_L^{(0)}+H_R^{(0)})}\Big[1+\frac{\Delta T}{T^2}H_L^{(0)}\Big] I(\tau)I(0)\Big\} + O(\Delta T^2), \tag{I.1}$$

with $\beta = T^{-1}$. Through the transformations in Eqs. (5.8) and (5.12) the noise can be rewritten as

$$\begin{aligned} S(T_L,T_R) = \frac{1}{Z}\int_{-\infty}^{+\infty} d\tau\, \mathrm{Tr}\Big\{ & e^{-\beta(H_+^{(0)}+H_-^{(0)})}\times \\ & \times\Big[1+\frac{\Delta T}{T^2}H_{+,-}\Big] I(\varphi_-(\tau))I(\varphi_-(0))\Big\} + O(\Delta T^2) \end{aligned} \tag{I.2}$$

with $H_{+,-}$ defined in Eq. (5.46) of the main text.

One needs also to consider the first order expansion of the partition function Z

$$Z = \mathrm{Tr}\Big\{ e^{-\beta(H_L^{(0)}+H_R^{(0)})}\Big[1+\frac{\Delta T}{T^2}H_L^{(0)}\Big]\Big\} + O(\Delta T^2). \tag{I.3}$$

In terms of the new fields $\varphi_\pm$ and taking into account the fact that the term $(\partial_x\varphi_+)(\partial_x\varphi_-)$ gives no contribution to the trace, one has

$$Z = \mathrm{Tr}\Big\{ e^{-\beta H_+^{(0)}} e^{-\beta H_-^{(0)}}\Big[1+\frac{\Delta T}{2T^2}\big(H_+^{(0)}+H_-^{(0)}+\sin 2\zeta(H_-^{(0)}-H_+^{(0)})\big)\Big]\Big\} + O(\Delta T^2) \tag{I.4}$$

where we recall that

$$\sin 2\zeta = \frac{\nu_R-\nu_L}{\nu_R+\nu_L}. \tag{I.5}$$

Then by exploiting the properties of the trace we have that

$$\begin{aligned} Z &= Z_+^{(0)}Z_-^{(0)} + \frac{\Delta T}{2T^2}\Big[-Z_-^{(0)}\frac{\partial Z_+^{(0)}}{\partial\beta} - Z_+^{(0)}\frac{\partial Z_-^{(0)}}{\partial\beta} + \sin 2\zeta\Big(-Z_+^{(0)}\frac{\partial Z_-^{(0)}}{\partial\beta} + Z_-^{(0)}\frac{\partial Z_+^{(0)}}{\partial\beta}\Big)\Big] = \\ &= Z_+^{(0)}Z_-^{(0)}\Big\{1+\frac{\Delta T}{2T^2}\Big[-\frac{\partial \ln(Z_+^{(0)}Z_-^{(0)})}{\partial\beta} + \sin 2\zeta\frac{\partial}{\partial\beta}\ln\Big(\frac{Z_+^{(0)}}{Z_-^{(0)}}\Big)\Big]\Big\} + O(\Delta T^2) \end{aligned} \tag{I.6}$$

with

$$Z_{\pm}^{(0)} = \mathrm{Tr}\left\{ e^{-\beta H_{\pm}^{(0)}} \right\}. \tag{I.7}$$

One can then define the equilibrium noise as in Eq. (I.1) with $\Delta T = 0$. Since the operator I only depends on φ_- [see Eq. (5.4)], the trace with respect to φ_+ is trivial leading to

$$S_0(T) = \frac{1}{Z_-^{(0)}} \int_{-\infty}^{+\infty} d\tau \, \mathrm{Tr}\left\{ e^{-\beta H_-^{(0)}} I(\varphi_-(\tau)) I(\varphi_-(0)) \right\}, \tag{I.8}$$

which only depends on the temperature T.

The expansion of the noise $S(T_L, T_R)$ up to first order in $\Delta T/T$ then reads

$$\begin{aligned} S(T_L, T_R) = S_0(T) + \frac{1}{Z_+^{(0)} Z_-^{(0)}} \int_{-\infty}^{+\infty} d\tau \mathrm{Tr}\Big\{ e^{-\beta(H_+^{(0)} + H_-^{(0)})} \times \\ \times \left[\frac{\partial \ln(Z_+^{(0)} Z_-^{(0)})}{\partial \beta} - \sin 2\zeta \, \frac{\partial}{\partial \beta} \ln\left(\frac{Z_+^{(0)}}{Z_-^{(0)}} \right) + 2H_{+,-} \right] I(\varphi_-(\tau)) I(\varphi_-(0)) \Big\} \frac{\Delta T}{2T^2} + O(\Delta T^2). \end{aligned} \tag{I.9}$$

By exploiting the properties of the $\mathrm{Tr}\{...\}$ and after some algebra we rewrite Eq. (I.9) as

$$\begin{aligned} S(T_L, T_R) = S_0(T) + \Bigg[S_0(T) \frac{\partial \ln(Z_+^{(0)} Z_-^{(0)})}{\partial \beta} - \sin 2\zeta \, S_0(T) \frac{\partial}{\partial \beta} \ln\left(\frac{Z_+^{(0)}}{Z_-^{(0)}} \right) + \\ - (1 - \sin 2\zeta) S_0(T) \frac{\partial \ln(Z_+^{(0)})}{\partial \beta} - (1 + \sin 2\zeta) \times \\ \times \int_{-\infty}^{+\infty} d\tau \, \frac{1}{Z_-^{(0)}} \frac{\partial}{\partial \beta} \mathrm{Tr}\left\{ e^{-\beta H_-^{(0)}} I(\varphi_-(\tau)) I(\varphi_-(0)) \right\} \Bigg] \frac{\Delta T}{2T^2} + O(\Delta T^2). \end{aligned} \tag{I.10}$$

Since the last term can be rewritten as

$$\int_{-\infty}^{+\infty} d\tau \, \frac{1}{Z_-^{(0)}} \frac{\partial}{\partial \beta} \mathrm{Tr}\left\{ e^{-\beta H_-^{(0)}} I(\varphi_-(\tau)) I(\varphi_-(0)) \right\} = \frac{\partial S_0}{\partial \beta} + S_0 \frac{\partial \ln Z_-^{(0)}}{\partial \beta} \tag{I.11}$$

one can finally rewrite Eq. (I.9) as

$$S(T_L, T_R) = S_0(T) - (1 + \sin 2\zeta) \frac{\partial S_0}{\partial \beta} \frac{\Delta T}{2T^2} + O(\Delta T^2). \tag{I.12}$$

Note that from this expression we recover the noise for the particular $(1/3, 1)$ junction reported in Eq. (H.12).

Appendix J

Recovering Equation (5.52)

We start from the general expression for the noise of the $(1, 1/3)$ junction, as obtained in Eq. (5.44), and write

$$S_0(T) = \frac{e^2}{4}\int \frac{d\omega}{2\pi}\left[1-\tanh^2\left(\frac{\omega}{2T}\right)\right]\left(2-\frac{2\mathcal{T}_k^2}{\mathcal{T}_k^2+\omega^2}\right) \tag{J.1}$$

where we focus on the equilibrium situation, allowing us to replace the distribution function n_ω with the standard Fermi distribution $n_\omega^{(0)}$ at temperature T, whose expression is made explicit in Eq. (1.34) where $n_\omega^{(0)} \equiv f(\omega)$. We recall that the crossover energy is set by the tunneling amplitude Λ'

$$\mathcal{T}_k = \frac{4\pi a}{v}\left(\frac{\Lambda'}{2\pi a}\right)^2. \tag{J.2}$$

The first term can be readily integrated out, while the second one is re-expressed through an integration by part, thus leading to

$$S_0(T) = \frac{e^2}{\pi}T - \frac{e^2}{\pi}T\mathcal{T}_k^2\int d\omega \tanh\left(\frac{\omega}{2T}\right)\frac{\omega}{\left(\mathcal{T}_k^2+\omega^2\right)^2}. \tag{J.3}$$

The resulting integral can then be evaluated following standard contour integration techniques, yielding

$$S_0(T) = \frac{e^2}{\pi}T - \frac{e^2\mathcal{T}_k}{4}\frac{1}{\cos^2\left(\frac{\mathcal{T}_k}{2T}\right)} + \frac{e^2}{\pi}T\left(\frac{\mathcal{T}_k}{T}\right)^2 4\pi\sum_{n=0}^{\infty}\frac{\pi(2n+1)}{\left(\frac{\mathcal{T}_k}{T}\right)^2-\pi^2(2n+1)^2} \tag{J.4}$$

which can further be rewritten as

$$\begin{aligned} S_0(T) &= \frac{e^2}{\pi}T - \frac{e^2\mathcal{T}_k}{4}\frac{1}{\cos^2\left(\frac{\mathcal{T}_k}{2T}\right)} + \frac{e^2}{4\pi^2}\mathcal{T}_k\left[\psi'\left(\frac{1}{2}-\frac{\mathcal{T}_k}{2\pi T}\right)-\psi'\left(\frac{1}{2}+\frac{\mathcal{T}_k}{2\pi T}\right)\right] \\ &= \frac{e^2}{\pi}T - \frac{e^2}{2\pi^2}\mathcal{T}_k\psi'\left(\frac{1}{2}+\frac{\mathcal{T}_k}{2\pi T}\right) \end{aligned} \tag{J.5}$$

where we used the properties of the derivatives of the digamma function.

This ultimately leads back to the expression from Eq. (5.52) quoted in the text, namely

$$S_0(T) = \frac{1}{2}\frac{e^2}{2\pi}\mathcal{T}_k\left[4\frac{T}{\mathcal{T}_k} - \frac{2}{\pi}\psi'\left(\frac{1}{2}+\frac{\mathcal{T}_k}{2\pi T}\right)\right]. \tag{J.6}$$

Bibliography

[1] S. Haroche and J. M. Raimond. *Exploring the quantum: atoms, cavities, and photons*. Oxford University Press, 2006.

[2] E. Bocquillon et al. "Electron quantum optics in ballistic chiral conductors". In: *Annalen der Physik* 526 (2014), pp. 1–30.

[3] R. Hanbury Brown and R. Q. Twiss. "Correlation between photons in two coherent beams of light". In: *Nature* 177 (1956), pp. 27–29.

[4] C. K. Hong, Z. Y. Ou, and L. Mandel. "Measurement of subpicosecond time intervals between two photons by interference". In: *Physical Review Letters* 59 (1987), pp. 2044–2046.

[5] K. V. Klitzing, G. Dorda, and M. Pepper. "New method for high-accuracy determination of the fine-structure constant based on quantized Hall resistance". In: *Physical Review Letters* 45 (1980), pp. 494–497.

[6] H. L. Stormer, D. C. Tsui, and A. C. Gossard. "The fractional quantum Hall effect". In: *Reviews of Modern Physics* 71 (1999), S298.

[7] G. Fève et al. "An on-Demand coherent single-electron source". In: *Science* 316 (2007), pp. 1169–1172.

[8] L. S. Levitov, H. Lee, and G. B. Lesovik. "Electron counting statistics and coherent states of electric current". In: *Journal of Mathematical Physics* 37 (1996), pp. 4845–4866.

[9] D. A. Ivanov, H. W. Lee, and L. S. Levitov. "Coherent states of alternating current". In: *Physical Review B* 56 (1997), pp. 6839–6850.

[10] J. Keeling, I. Klich, and L. S. Levitov. "Minimal excitation states of electrons in one-dimensional wires". In: *Physical Review Letters* 97 (2006), p. 116403.

[11] R. J. Glauber. "The quantum theory of optical coherence". In: *Physical Review* 130 (1963), p. 2529.

[12] C. Grenier et al. "Electron quantum optics in quantum Hall edge channels". In: *Modern Physics Letters B* 25 (2011), pp. 1053–1073.

[13] J. Dubois et al. "Minimal-excitation states for electron quantum optics using levitons". In: *Nature* 502 (2013), pp. 659–663.

[14] E. Bocquillon et al. "Electron quantum optics: partitioning electrons one by one". In: *Physical Review Letters* 108 (2012), p. 196803.

[15] E. Bocquillon et al. "Coherence and indistinguishability of single electrons emitted by independent sources". In: *Science* 339 (2013), pp. 1054–1057.

[16] I. Neder. "Fractionalization noise in edge channels of integer quantum Hall states". In: *Physical Review Letters* 108 (2012), p. 186404.

[17] I. P. Levkivskyi and E. V. Sukhorukov. "Energy relaxation at quantum Hall edge". In: *Physical Review B* 85 (2012), p. 075309.

[18] H. Le Sueur et al. "Energy relaxation in the integer quantum Hall regime". In: *Physical Review Letters* 105 (2010), p. 056803.

[19] D. C. Tsui, H. L. Stormer, and A. C. Gossard. "Two-dimensional magnetotransport in the extreme quantum limit". In: *Physical Review Letters* 48 (1982), pp. 1559–1562.

[20] D. C. Glattli et al. "Design of a single-shot electron detector with sub-electron sensitivity for electron flying qubit operation". In: *arXiv:2002.03947* (2020).

[21] V. Thiney et al. "In-flight detection of few electrons using a singlet-triplet spin qubit". In: *arXiv:2210.08831* (2022).

[22] K. Thibault et al. "Pauli-Heisenberg oscillations in electron quantum transport". In: *Physical Review Letters* 114 (2015), p. 236604.

[23] J. B. Johnson. "Thermal agitation of electricity in conductors". In: *Nature* 119 (1927), p. 97.

[24] H. Nyquist. "Thermal agitation of electric charge in conductors". In: *Physical Review* 32 (1928), p. 110.

[25] W. Schottky. "Über spontane Stromschwankungen in verschiedenen Elektrizitätsleitern". In: *Annalen der physik* 362 (1918), pp. 541–567.

[26] O. S. Lumbroso et al. "Electronic noise due to temperature differences in atomic-scale junctions". In: *Nature* 562 (2018), pp. 240–244.

[27] G. Gasse, C. Lupien, and B. Reulet. "Observation of squeezing in the electron quantum shot noise of a tunnel junction". In: *Physical Review Letters* 111 (2013), p. 136601.

[28] J. C. Forgues, C. Lupien, and B. Reulet. "Experimental violation of bell-like inequalities by electronic shot noise". In: *Physical Review Letters* 114 (2015), p. 130403.

[29] H. Bartolomei et al. "Observation of edge magnetoplasmon squeezing in a quantum Hall conductor". In: *arXiv:2210.04279* (2022).

[30] R. J. Glauber. "Photon correlations". In: *Physical Review Letters* 10 (1962), p. 84.

[31] D. Y. Sharvin and Y. V. Sharvin. "Magnetic flux quantization in a cylindrical film". In: *Journal of Experimental and Theoretical Physics Letters* 34 (1981), pp. 285–288.

[32] R. A. Webb et al. "Observation of h/e Aharonov-Bohm oscillations in normal-metal rings". In: *Physical Review Letters* 54 (1985), p. 2696.

[33] S. Washburn et al. "Temperature dependence of the normal-metal Aharonov-Bohm effect". In: *Physical Review B* 32 (1985), p. 4789.

[34] C. C. Dean and M. Pepper. "The transition from two- to one-dimensional electronic transport in narrow silicon accumulation layers". In: *Journal of Physics C: Solid State Physics* 15 (1982), p. L1287.

[35] B. J. Van Wees et al. "Quantized conductance of point contacts in a two-dimensional electron gas". In: *Physical Review Letters* 60 (1988), p. 848.

[36] R. Landauer and M. Büttiker. "Resistance of small metallic loops". In: *Physical Review Letters* 54 (1985), pp. 2049–2052.

[37] M. Büttiker. "Four-terminal phase-coherent conductance". In: *Physical Review Letters* 57 (1986), pp. 1761–1764.

[38] J. Gabelli et al. "Violation of Kirchhoff's laws for a coherent *RC* circuit". In: *Science* 313 (2006), pp. 499–502.

[39] D. C. Tsui. "Nobel lecture: interplay of disorder and interaction in two-dimensional electron gas in intense magnetic fields". In: *Reviews of Modern Physics* 71 (1999), p. 891.

[40] D. R. Nelson and J. M. Kosterlitz. "Universal jump in the superfluid density of two-dimensional superfluids". In: *Physical Review Letters* 39 (1977), p. 1201.

[41] D. J. Thouless et al. "Quantized Hall conductance in a two-dimensional periodic potential". In: *Physical Review Letters* 49 (1982), p. 405.

[42] F. D. M. Haldane. "Model for a quantum Hall effect without Landau levels: condensed-matter realization of the "parity anomaly"". In: *Physical Review Letters* 61 (1988), p. 2015.

[43] D. Tong. "Lectures on the quantum Hall effect". In: *arXiv:1606.06687* (2016).

[44] R. B. Laughlin. "Quantized Hall conductivity in two dimensions". In: *Physical Review B* 23 (1981), pp. 5632–5633.

[45] B. I. Halperin. "Quantized Hall conductance, current-carrying edge states, and the existence of extended states in a two-dimensional disordered potential". In: *Physical Review B* 25 (1982), pp. 2185–2190.

[46] R. E. Prange and S. M. Girvin. *The Quantum Hall effect*. Springer-Verlag, New York, 1990.

[47] M. O. Goerbig. "Quantum hall effects". In: *arXiv:0909.1998* (2009).

[48] L. D. Landau and E. M. Lifshitz. *Course of theoretical physics*. Elsevier, 2013.

[49] L. D. Landau and E. M. Lifshitz. *Quantum mechanics: non-relativistic Theory (Volume 3)*. Oxford, 1977.

[50] F. W. J. Olver et al. "NIST Digital Library of Mathematical Functions". In: *Release 1.1.6 of 2022-06-30* 1 (2016), p. 22.

[51] R. Landauer. "Spatial variation of currents and fields due to localized scatterers in Metallic Conduction". In: *IBM Journal of Research and Development* 1 (1957), pp. 223–231.

[52] M. Büttiker et al. "Generalized many-channel conductance formula with application to small rings". In: *Physical Review B* 31 (1985), pp. 6207–6215.

[53] R. Willett et al. "Observation of an even-denominator quantum number in the fractional quantum Hall effect". In: *Physical Review Letters* 59 (1987), pp. 1776–1779.

[54] R. B. Laughlin. "Nobel lecture: Fractional quantization". In: *Reviews of Modern Physics* 71 (1999), p. 863.

[55] H. L. Stormer. "Nobel lecture: the fractional quantum Hall effect". In: *Reviews of Modern Physics* 71 (1999), p. 875.

[56] E. Wigner. "On the interaction of electrons in metals". In: *Physical Review* 46 (1934), p. 1002.

[57] E. Andrei et al. "Observation of a magnetically induced Wigner solid". In: *Physical Review Letters* 60 (1988).

[58] R. B. Laughlin. "Anomalous quantum Hall effect: an incompressible quantum fluid with fractionally charged excitations". In: *Physical Review Letters* 50 (1983), pp. 1395–1398.

[59] R. Landauer. "Spatial variation of currents and fields due to localized scatterers in metallic conduction". In: *IBM Journal of Research and Development* 32 (1988), pp. 306–316.

[60] C. Bäuerle et al. "Coherent control of single electrons: a review of current progress". In: *Reports on Progress in Physics* 81 (2018).

[61] J. D. Fletcher et al. "Clock-controlled emission of single-electron wave packets in a solid-state circuit". In: *Physical Review Letters* 111 (2013), p. 216807.

[62] N. Johnson et al. "LO-phonon emission rate of hot electrons from an on-demand single-electron source in a GaAs/AlGaAs heterostructure". In: *Physical Review Letters* 121 (2018), p. 137703.

[63] T. Ota et al. "Spectroscopic study on hot-electron transport in a quantum Hall edge channel". In: *Physical Review B* 99 (2019).

[64] S. Hermelin et al. "Electrons surfing on a sound wave as a platform for quantum optics with flying electrons". In: *Nature* 477 (2011), pp. 435–438.

[65] R. P. G. McNeil et al. "On-demand single-electron transfer between distant quantum dots". In: *Nature* 477 (2011), pp. 439–442.

[66] A. Mahé et al. "Current correlations of an on-demand single-electron emitter". In: *Physical Review B* 82 (2010), p. 201309.

[67] S. E. Nigg and M. Büttiker. "Quantum to classical transition of the charge relaxation resistance of a mesoscopic capacitor". In: *Physical Review B* 77 (2008), p. 085312.

[68] F. D. Parmentier et al. "Current noise spectrum of a single-particle emitter: Theory and experiment". In: *Physical Review B* 85 (2012), p. 165438.

[69] M. Albert, C. Flindt, and M. Büttiker. "Accuracy of the quantum capacitor as a single-electron source". In: *Physical Review B* 82 (2010), p. 041407.

[70] J. Keeling, A. V. Shytov, and L. S. Levitov. "Coherent particle transfer in an on-demand single-electron source". In: *Physical Review Letters* 101 (2008), p. 196404.

[71] R. Landauer. "Johnson-Nyquist noise derived from quantum mechanical transmission". In: *Physica D: Nonlinear Phenomena* 38 (1989), pp. 226–229.

[72] T. Martin and R. Landauer. "Wave-packet approach to noise in multichannel mesoscopic systems". In: *Physical Review B* 45 (1992), p. 1742.

[73] R. Landauer. "The noise is the signal". In: *Nature* 392 (1998), pp. 658–659.

[74] Y. M. Blanter and M. Büttiker. "Shot noise in mesoscopic conductors". In: *Physics Reports* 336 (2000), pp. 1–166.

[75] A. C. Funk and M. Beck. "Sub-Poissonian photocurrent statistics: theory and undergraduate experiment". In: *American Journal of Physics* 65 (1997), pp. 492–500.

[76] L. Saminadayar et al. "Observation of the e/3 fractionally charged Laughlin quasiparticle". In: *Physical Review Letters* 79 (1997), p. 2526.

[77] A. Kumar et al. "Experimental test of the quantum shot noise reduction theory". In: *Physical Review Letters* 76 (1996), p. 2778.

[78] M. Büttiker. "Scattering theory of current and intensity noise correlations in conductors and wave guides". In: *Physical Review B* 46 (1992), p. 12485.

[79] T. Martin. "Nanophysics: coherence and transport". In: *Les Houches Session LXXXI* (2005).

[80] Y. V. Nazarov and Y. M. Blanter. *Quantum transport: introduction to nanoscience*. Cambridge University Press, 2009.

[81] G. B. Lesovik and I. A. Sadovskyy. "Scattering matrix approach to the description of quantum electron transport". In: *Physics-Uspekhi* 54 (2011), p. 1007.

[82] J. Sakurai and J. Napolitano. *Modern Quantum Mechanics*. Addison-Wesley, 2014.

[83] H. Bruus and K. Flensberg. *Many-body quantum theory in condensed matter physics: an introduction*. OUP Oxford, 2004.

[84] H. E. Van den Brom and J. M. Van Ruitenbeek. "Quantum suppression of shot noise in atom-size metallic contacts". In: *Physical Review Letters* 82 (1999), p. 1526.

[85] H. B. Callen and T. A. Welton. "Irreversibility and generalized noise". In: *Physical Review* 83 (1951), p. 34.

[86] R. A. Kamper and J. E. Zimmerman. "Noise thermometry with the Josephson effect". In: *Journal of Applied Physics* 42 (1971), pp. 132–136.

[87] R. A. Webb, R. P. Giffard, and J. C. Wheatley. "Noise thermometry at ultralow temperatures". In: *Journal of Low Temperature Physics* 13 (1973), pp. 383–429.

[88] F. Giazotto et al. "Opportunities for mesoscopics in thermometry and refrigeration: physics and applications". In: *Reviews of Modern Physics* 78 (2006), p. 217.

[89] M. Büttiker. "Scattering theory of thermal and excess noise in open conductors". In: *Physical Review Letters* 65 (1990), pp. 2901–2904.

[90] G. B. Lesovik. "Excess quantum noise in 2D ballistic point contacts". In: *Soviet Journal of Experimental and Theoretical Physics Letters* 49 (1989), p. 592.

[91] R. De-Picciotto et al. "Direct observation of a fractional charge". In: *Nature* 389 (1997), pp. 162–164.

[92] E. S. Tikhonov et al. "Local noise in a diffusive conductor". In: *Scientific Reports* 6 (2016), pp. 1–7.

[93] E. Sivre et al. "Electronic heat flow and thermal shot noise in quantum circuits". In: *Nature Communications* 10 (2019), pp. 1–8.

[94] S. Larocque et al. "Shot noise of a temperature-biased tunnel junction". In: *Physical Review Letters* 125 (2020), p. 106801.

[95] E. Zhitlukhina, M. Belogolovskii, and P. Seidel. "Electronic noise generated by a temperature gradient across a hybrid normal metal-superconductor nanojunction". In: *Applied Nanoscience* 10 (2020), pp. 5121–5124.

[96] J. Rech et al. "Negative delta-T noise in the fractional quantum Hall effect". In: *Physical Review Letters* 125 (2020), p. 086801.

[97] M. Hasegawa and K. Saito. "Delta-T noise in the Kondo regime". In: *Physical Review B* 103 (2021), p. 045409.

[98] H. Duprez et al. "Dynamical Coulomb blockade under a temperature bias". In: *Physical Review Research* 3 (2021), p. 023122.

[99] A. Popoff et al. "Scattering theory of non-equilibrium noise and delta-T current fluctuations through a quantum dot". In: *Journal of Physics: Condensed Matter* 34 (2022), p. 185301.

[100] N. Schiller, Y. Oreg, and K. Snizhko. "Extracting the scaling dimension of quantum Hall quasiparticles from current correlations". In: *Physical Review B* 105 (2022), p. 165150.

[101] G. Zhang, I. V. Gornyi, and C. Spånslätt. "Delta-T noise for weak tunneling in one-dimensional systems: Interactions versus quantum statistics". In: *Physical Review B* 105 (2022), p. 195423.

[102] C. Grenier et al. "Fractionalization of minimal excitations in integer quantum Hall edge channels". In: *Physical Review B* 88 (2013), p. 085302.

[103] D. Ferraro et al. "Wigner function approach to single electron coherence in quantum Hall edge channels". In: *Physical Review B* 88 (2013), p. 205303.

[104] W. D. Oliver et al. "Hanbury Brown and Twiss-type experiment with electrons". In: *Science* 284 (1999), pp. 299–301.

[105] J. Dubois et al. "Integer and fractional charge Lorentzian voltage pulses analyzed in the framework of photon-assisted shot noise". In: *Physical Review B* 88 (2013), p. 085301.

[106] D. C. Glattli and P. Roulleau. "Hanbury-Brown Twiss noise correlation with time controlled quasi-particles in ballistic quantum conductors". In: *Physica E: Low-dimensional Systems and Nanostructures* 76 (2016), pp. 216–222.

[107] T. Jonckheere et al. "Electron and hole Hong-Ou-Mandel interferometry". In: *Physical Review B* 86 (2012), p. 125425.

[108] C. Wahl et al. "Interactions and charge fractionalization in an electronic Hong-Ou-Mandel interferometer". In: *Physical Review Letters* 112 (2014), p. 046802.

[109] L. D. Landau. "Theory of the Fermi-liquids". In: *Soviet Physics JETP* 3 (1967), p. 1526.

[110] P. Nozières. *Theory of Interacting Fermi Systems*. W. A. Benjamin Inc., New York, 1964.

[111] S. Tomonaga. "Remarks on Bloch's method of sound waves applied to many-fermion problems". In: *Progress of Theoretical Physics* 5 (1951), pp. 544–569.

[112] J. M. Luttinger. "An exactly soluble model of a many fermion system". In: *Journal of Mathematical Physics* 4 (1963), p. 1154.

[113] E. H. Lieb and D. C. Mattis. "Exact solution of a many-fermjon system and its associated boson field". In: *Journal of Mathematical Physics* 6 (1965), p. 304.

[114] F. D. M. Haldane. "Luttinger liquid theory of one-dimensional quantum fluids: I. Properties of the Luttinger model and their extension to the general 1D interacting spinless Fermi gas". In: *Journal of Physics C: Solid State Physics* 14 (1981), p. 2585.

[115] M. Bockrath et al. "Luttinger-liquid behaviour in carbon nanotubes". In: *Nature* 397 (1999), pp. 27–29.

[116] O. M. Auslaender et al. "Spin-charge separation and localization in one dimension". In: *Science* 308 (2005), pp. 88–92.

[117] Y. Jompol et al. "Probing spin-charge separation in a Tomonaga-Luttinger liquid". In: *Science* 325 (2009), pp. 597–601.

[118] O. M. Auslaender et al. "Tunneling spectroscopy of the elementary excitations in a one-dimensional wire". In: *Science* 295 (2002), pp. 825–828.

[119] H. Steinberg et al. "Charge fractionalization in quantum wires". In: *Nature Physics* 4 (2008), pp. 116–119.

[120] H. Kamata et al. "Fractionalized wave packets from an artificial Tomonaga-Luttinger liquid". In: *Nature Nanotechnology* 9 (2014), pp. 177–181.

[121] P. Brasseur et al. "Charge fractionalization in artificial Tomonaga-Luttinger liquids with controlled interaction strength". In: *Physical Review B* 96 (2017), p. 081101.

[122] J. Sólyom. "The Fermi gas model of one-dimensional conductors". In: *Advances in Physics* 28 (1979), pp. 201–303.

[123] J. Von Delft and H. Schoeller. "Bosonization for beginners - refermionization for experts". In: *Annalen der Physik* 7 (1998), pp. 225–305.

[124] J. Voit. "One-dimensional Fermi liquids". In: *Reports on Progress in Physics* 58 (1995), p. 977.

[125] T. Giamarchi. *Quantum physics in one dimension*. Oxford University Press, 2003.

[126] R. Heidenreich, R. Seiler, and D. A. Uhlenbrock. "The Luttinger model". In: *Journal of Statistical Physics* 22 (1980), pp. 27–57.

[127] X. G. Wen and A. Zee. "Classification of Abelian quantum Hall states and matrix formulation of topological fluids". In: *Physical Review B* 46 (1992), pp. 2290–2301.

[128] V. G. Kac. "Integrable highest weight modules: the weight system, the contravariant Hermitian form and the restriction problem". In: *Infinite Dimensional Lie Algebras*. Springer, 1983, pp. 134–149.

[129] X. G. Wen. "Chiral Luttinger liquid and the edge excitations in the fractional quantum Hall states". In: *Physical Review B* 41 (1990), p. 12838.

[130] I. P. Levkivskyi and E. V. Sukhorukov. "Dephasing in the electronic Mach-Zehnder interferometer at filling factor $\nu = 2$". In: *Physical Review B* 78 (2008).

[131] P. Degiovanni et al. "Plasmon scattering approach to energy exchange and high-frequency noise in $\nu = 2$ quantum Hall edge channels". In: *Physical Review B* 81 (2010), p. 121302.

[132] E. V. Sukhorukov and V. V. Cheianov. "Resonant dephasing in the electronic Mach-Zehnder interferometer". In: *Physical Review Letters* 99 (2007), p. 156801.

[133] R. H. Rodriguez et al. "Relaxation and revival of quasiparticles injected in an interacting quantum Hall liquid". In: *Nature Communications* 11 (2020), pp. 1–8.

[134] V. Freulon et al. "Hong-Ou-Mandel experiment for temporal investigation of single-electron fractionalization". In: *Nature Communications* 6 (2015), pp. 1–6.

[135] A. Braggio et al. "Environmental induced renormalization effects in quantum Hall edge states due to 1/f noise and dissipation". In: *New Journal of Physics* 14 (2012), p. 093032.

[136] D. L. Kovrizhin and J. T. Chalker. "Relaxation in driven integer quantum Hall edge states". In: *Physical Review Letters* 109 (2012), p. 106403.

[137] H. Inoue et al. "Charge fractionalization in the integer quantum Hall effect". In: *Physical Review Letters* 112 (2014), p. 166801.

[138] D. Ferraro et al. "Real-time decoherence of Landau and Levitov quasiparticles in quantum Hall edge channels". In: *Physical Review Letters* 113 (2014), p. 166403.

[139] D. Ferraro and E. Sukhorukov. "Interaction effects in a multi-channel Fabry-Perot interferometer in the Aharonov-Bohm regime". In: *SciPost Physics* 3 (2017), p. 014.

[140] E. Berg et al. "Fractional charges on an integer quantum Hall edge". In: *Physical Review Letters* 102 (2009), p. 236402.

[141] M. Milletarì and B. Rosenow. "Shot-noise signatures of charge fractionalization in the $\nu = 2$ quantum Hall edge". In: *Physical Review Letters* 111 (2013), p. 136807.

[142] M. Hashisaka et al. "Waveform measurement of charge- and spin-density wavepackets in a chiral Tomonaga-Luttinger liquid". In: *Nature Physics* 13 (2017), pp. 559–562.

[143] M. Hashisaka and T. Fujisawa. "Tomonaga-Luttinger liquid nature of edge excitations in integer quantum Hall edge channels". In: *Reviews in Physics* 3 (2018), pp. 32–43.

[144] P. Degiovanni, C. Grenier, and G. Fève. "Decoherence and relaxation of single-electron excitations in quantum Hall edge channels". In: *Physical Review B* 80 (2009), p. 241307.

[145] E. Bocquillon et al. "Separation of neutral and charge modes in one-dimensional chiral edge channels". In: *Nature Communications* 4 (2013), pp. 1–7.

[146] G. Rebora et al. "Electronic wave-packets in integer quantum Hall edge channels: relaxation and dissipative effects". In: *Entropy* 23 (2021), p. 138.

[147] A. S. Goremykina and E. V. Sukhorukov. "Coherence recovery mechanisms of quantum Hall edge states". In: *Physical Review B* 97 (2018), p. 115418.

[148] A. Marguerite et al. "Decoherence and relaxation of a single electron in a one-dimensional conductor". In: *Physical Review B* 94 (2016), p. 115311.

[149] G. Rebora et al. "Collisional interferometry of levitons in quantum Hall edge channels at $\nu = 2$". In: *Physical Review B* 101 (2020), p. 245310.

[150] S. Ol'Khovskaya et al. "Shot noise of a mesoscopic two-particle collider". In: *Physical Review Letters* 101 (2008), p. 166802.

[151] M. Moskalets, G. Haack, and M. Büttiker. "Single-electron source: adiabatic versus non adiabatic emission". In: *Physical Review B* 87 (2013), p. 125429.

[152] E. Iyoda et al. "Dephasing in single-electron generation due to environmental noise probed by Hong-Ou-Mandel interferometry". In: *Physical Review B* 89 (2014), p. 205318.

[153] D. Marian, E. Colomés, and X. Oriols. "Time-dependent exchange and tunneling: detection at the same place of two electrons emitted simultaneously from different sources". In: *Journal of Physics: Condensed Matter* 27 (2015), p. 245302.

[154] C. Cabart et al. "Taming electronic decoherence in one-dimensional chiral ballistic quantum conductors". In: *Physical Review B* 98 (2018), p. 155302.

[155] M. Acciai et al. "Probing interactions via nonequilibrium momentum distribution and noise in integer quantum Hall systems at $\nu = 2$". In: *Physical Review B* 98 (2018), p. 035426.

[156] J. Rech et al. "Minimal Excitations in the Fractional Quantum Hall Regime". In: *Physical Review Letters* 118 (2017), p. 076801.

[157] L. Vannucci et al. "Minimal excitation states for heat transport in driven quantum Hall systems". In: *Physical Review B* 95 (2017).

[158] I. Safi. "A dynamic scattering approach for a gated interacting wire". In: *The European Physical Journal B-Condensed Matter and Complex Systems* 12 (1999), pp. 451–455.

[159] C. Altimiras et al. "Non-equilibrium edge-channel spectroscopy in the integer quantum Hall regime". In: *Nature Physics* 6 (2010), pp. 34–39.

[160] C. Grenier et al. "Single-electron quantum tomography in quantum Hall edge channels". In: *New Journal of Physics* 13 (2011), p. 093007.

[161] G. Haack, M. Moskalets, and M. Büttiker. "Glauber coherence of single-electron sources". In: *Physical Review B* 87.20 (2013), p. 201302.

[162] M. Moskalets and G. Haack. "Single-electron coherence: Finite temperature versus pure dephasing". In: *Physica E: Low-dimensional Systems and Nanostructures* 75 (2016), pp. 358–369.

[163] G. Rebora, D. Ferraro, and M. Sassetti. "Suppression of the radiation squeezing in interacting quantum Hall edge channels". In: *New Journal of Physics* 23 (2021), p. 063018.

[164] S. L. Braunstein and P. Van Loock. "Quantum information with continuous variables". In: *Reviews of Modern Physics* 77 (2005), p. 513.

[165] C. Weedbrook et al. "Gaussian quantum information". In: *Reviews of Modern Physics* 84 (2012), p. 621.

[166] C. M. Caves. "Quantum-mechanical noise in an interferometer". In: *Physical Review D* 23 (1981), p. 1693.

[167] R. Slusher et al. "Observation of squeezed states generated by four-wave mixing in an optical cavity". In: *Physical Review Letters* 55 (1985), p. 2409.

[168] B. Yurke et al. "Observation of 4.2 equilibrium-noise squeezing via a Josephson-parametric amplifier". In: *Physical Review Letters* 60 (1988), p. 764.

[169] R. Movshovich et al. "Observation of zero-point noise squeezing via a Josephson-parametric amplifier". In: *Physical Review Letters* 65 (1990), p. 1419.

[170] P. Nation et al. "Stimulating uncertainty: amplifying the quantum vacuum with superconducting circuits". In: *Reviews of Modern Physics* 84 (2012), p. 1.

[171] E. Flurin et al. "Generating entangled microwave radiation over two transmission lines". In: *Physical Review Letters* 109 (2012), p. 183901.

[172] M. Westig et al. "Emission of nonclassical radiation by inelastic Cooper pair tunneling". In: *Physical Review Letters* 119 (2017), p. 137001.

[173] U. C. Mendes and C. Mora. "Cavity squeezing by a quantum conductor". In: *New Journal of Physics* 17 (2015), p. 113014.

[174] D. Ferraro et al. "Enhancing photon squeezing one leviton at a time". In: *Physical Review B* 97 (2018), p. 155135.

[175] N. Hiyama, M. Hashisaka, and T. Fujisawa. "An edge-magnetoplasmon Mach-Zehnder interferometer". In: *Applied Physics Letters* 107 (2015), p. 143101.

[176] J. R. Souquet et al. "Photon-assisted tunnelling with nonclassical light". In: *Nature Communications* 5 (2014), pp. 1–9.

[177] G. B. Lesovik and L. S. Levitov. "Noise in an ac biased junction: nonstationary Aharonov-Bohm effect". In: *Physical Review Letters* 72 (1994), p. 538.

[178] R. J. Schoelkopf et al. "Observation of "photon-assisted" shot noise in a phase-coherent conductor". In: *Physical Review Letters* 80 (1998), p. 2437.

[179] J. Gabelli and B. Reulet. "Dynamics of quantum noise in a tunnel junction under ac excitation". In: *Physical Review Letters* 100 (2008), p. 026601.

[180] A. L. Grimsmo et al. "Quantum optics theory of electronic noise in coherent conductors". In: *Physical Review Letters* 116 (2016), p. 043602.

[181] A. A. Kozhevnikov, R. J. Schoelkopf, and D. E. Prober. "Observation of photon-assisted noise in a diffusive normal metal-superconductor junction". In: *Physical Review Letters* 84 (2000), p. 3398.

[182] F. D. Parmentier et al. "A high sensitivity ultralow temperature RF conductance and noise measurement setup". In: *Review of Scientific Instruments* 82 (2011), p. 013904.

[183] G. Rebora et al. "Delta-T noise for fractional quantum Hall states at different filling factor". In: *arXiv:2207.00454* (2022).

[184] F. Ronetti et al. "Crystallization of levitons in the fractional quantum Hall regime". In: *Physical Review B* 98 (2018), p. 075401.

[185] F. Ronetti et al. "Hong-Ou-Mandel heat noise in the quantum Hall regime". In: *Physical Review B* 99 (2019), p. 205406.

[186] M. Hübler and W. Belzig. "Light emission in delta-T-driven mesoscopic conductors". In: *arXiv:2210.04984* (2022).

[187] B. Rosenow, I. P. Levkivskyi, and B. I. Halperin. "Current correlations from a mesoscopic anyon collider". In: *Physical Review Letters* 116 (2016), p. 156802.

[188] B. Lee, C. Han, and H. S. Sim. "Negative excess shot noise by anyon braiding". In: *Physical Review Letters* 123 (2019), p. 016803.

[189] C. L. Kane and M. P. A. Fisher. "Impurity scattering and transport of fractional quantum Hall edge states". In: *Physical Review B* 51 (1995), p. 13449.

[190] C. de C. Chamon et al. "Two point-contact interferometer for quantum Hall systems". In: *Physical Review B* 55 (1997), p. 2331.

[191] U. Weiss, R. Egger, and M. Sassetti. "Low-temperature nonequilibrium transport in a Luttinger liquid". In: *Physical Review B* 52 (1995), p. 16707.

[192] F. Guinea et al. "Asymptotic tunnelling conductance in Luttinger liquids". In: *Europhysics Letters* 30 (1995), p. 561.

[193] A. M. Chang. "Chiral Luttinger liquids at the fractional quantum Hall edge". In: *Reviews of Modern Physics* 75 (2003), p. 1449.

[194] B. J. Overbosch and C. de C. Chamon. "Long tunneling contact as a probe of fractional quantum Hall neutral edge modes". In: *Physical Review B* 80 (2009), p. 035319.

[195] D. Chevallier et al. "Poissonian tunneling through an extended impurity in the quantum Hall effect". In: *Physical Review B* 82 (2010), p. 155318.

[196] N. P. Sandler, C. de C. Chamon, and E. Fradkin. "Noise measurements and fractional charge in fractional quantum Hall liquids". In: *Physical Review B* 59 (1999), p. 12521.

[197] A. Kamenev. *Field theory of non-equilibrium systems*. Cambridge University Press, 2011.

[198] C. L. Kane and M. P. A. Fisher. "Thermal transport in a Luttinger liquid". In: *Physical Review Letters* 76 (1996), p. 3192.

[199] L. Vannucci et al. "Interference-induced thermoelectric switching and heat rectification in quantum Hall junctions". In: *Physical Review B* 92 (2015), p. 075446.

[200] X. G. Wen. "Edge transport properties of the fractional quantum Hall states and weak-impurity scattering of a one-dimensional charge-density wave". In: *Physical Review B* 44 (1991), p. 5708.

[201] P. Fendley, A. W. Ludwig, and H. Saleur. "Exact conductance through point contacts in the $\nu = 1/3$ fractional quantum Hall effect". In: *Physical Review Letters* 74 (1995), p. 3005.

[202] A. Schmid. "Diffusion and localization in a dissipative quantum system". In: *Physical Review Letters* 51 (1983), p. 1506.

[203] M. P. A. Fisher and W. Zwerger. "Quantum Brownian motion in a periodic potential". In: *Physical Review B* 32 (1985), p. 6190.

[204] C. G. Callan and D. Freed. "Phase diagram of the dissipative Hofstadter model". In: *Nuclear Physics B* 374 (1992), pp. 543–566.

[205] U. Weiss. "Low-temperature conduction and DC current noise in a quantum wire with impurity". In: *Solid State Communications* 100 (1996), pp. 281–285.

[206] F. Guinea. "Dynamics of a particle in an external potential interacting with a dissipative environment". In: *Physical Review B* 32 (1985), p. 7518.

[207] C. de C. Chamon, D. E. Freed, and X. G. Wen. "Nonequilibrium quantum noise in chiral Luttinger liquids". In: *Physical Review B* 53 (1996), p. 4033.

[208] A. Kamenev. "Keldysh technique and non-linear σ-model: basic principles and applications". In: *Advanced Physics* 58 (2009), p. 7518.

[209] D. Ferraro et al. "Single quasiparticle and electron emitter in the fractional quantum Hall regime". In: *Physical Review B* 91 (2015), p. 205409.

[210] D. Ferraro et al. "Neutral modes' edge state dynamics through quantum point contacts". In: *New Journal of Physics* 12 (2010), p. 013012.

[211] S. Lal. "Transport through constricted quantum Hall edge systems: beyond the quantum point contact". In: *Physical Review B* 77 (2008), p. 035331.

[212] S. Roddaro et al. "Tuning nonlinear charge transport between integer and fractional quantum Hall states". In: *Physical Review Letters* 103 (2009), p. 016802.

[213] C. L. Kane, M. P. A. Fisher, and J. Polchinski. "Randomness at the edge: theory of quantum Hall transport at filling $\nu = 2/3$". In: *Physical Review Letters* 72 (1994), p. 4129.

[214] M. Hashisaka et al. "Andreev reflection of fractional quantum Hall quasiparticles". In: *Nature Communications* 12 (2021), pp. 1–7.

[215] X. G. Wen. "Topological orders and edge excitations in fractional quantum Hall states". In: *Advances in Physics* 44 (1995), pp. 405–473.